

# UC Riverside

## UC Riverside Electronic Theses and Dissertations

### Title

Carbonaceous Aerosol Study Using Advanced Particle Instrumentation

### Permalink

<https://escholarship.org/uc/item/9dn463p4>

### Author

Qi, Li

### Publication Date

2010

Peer reviewed|Thesis/dissertation

UNIVERSITY OF CALIFORNIA  
RIVERSIDE

Carbonaceous Aerosol Study Using Advanced Particle Instrumentation

A Dissertation submitted in partial satisfaction  
of the requirements for the degree of

Doctor of Philosophy

in

Chemical and Environmental Engineering

by

Li Qi

August 2010

Dissertation committee:  
Dr. David R. Cocker III, Chairperson  
Dr. Joseph M. Norbeck  
Dr. Paul J. Ziemann

Copyright by  
Li Qi  
2010

This Dissertation of Li Qi is approved:

---

---

---

Committee Chairperson

University of California, Riverside

## **Acknowledgements**

With my graduate study at UCR approaching the end, I would like to take this opportunity to appreciate those who have continuously given the professional guidance and personal support with generous patience during the past four and an half years. I would never have been able to go this far without them.

I would like to express my deepest gratitude to my advisor, Dr. David R. Cocker III, for his excellent guidance, caring, patience, and providing me with a flexible atmosphere for doing research. Not only did I gain technical knowledge and professional capability from him, but I also improved my skills in research, writing and presentation.

I would also like to thank the staff of the Atmospheric Processes Laboratory at CE-CERT who gave me timely assistance and courses from analytical techniques to instrument troubleshooting; from building reactors to wiring electronics. Special thanks to Kurt Bumiller; without his help I would not have been able to produce this body of work. Other people include, but are certainly not limited to, Charles Bufalino, Dennis Fitz, and Kathy Cocker.

Thanks must also be given to previous graduate students, Dr. Bethany Warren, and Dr. Quentin Malloy who gave me invaluable advice on research techniques and asked probing questions which further helped me. Current graduate students Shunsuke Nakao, who is always willing to help and give his best suggestions, should be acknowledged for his aid in developing technique for data processing and in resolving miscellaneous problems that the laboratory encountered. Lindsay Yee, Dylan Switzer, Rebecca Austin, Christina Zapata also proved helpful while conducting my research.

Finally, I would like to thank my advisory committee, Dr. Joseph Norbeck and Dr. Paul J. Ziemann for their time and valuable comments during developing this dissertation. In addition, thanks should be given to the W.M Keck Foundation and the National Science Foundation (NSF) who granted me the financial support under ATM-0449778 for this project.

Last but not least, I would also like to thank my loved parents and friends. They are always by my side, supporting me and encouraging me with their best wishes.

## ABSTRACT OF THE DISSERTATION

Carbonaceous Aerosol Study Using Advanced Particle Instrumentation

by

Li Qi

Doctor of Philosophy, Graduate Program in Chemical and Environmental Engineering  
University of California, Riverside, August 2010  
Dr. David R. Cocker III, Chairperson

A study of the evolution of carbonaceous aerosol in the atmosphere was conducted with special focus on primary biomass burning and secondary organic aerosol (SOA) processing. The work is broken down into two major components: the organic aerosol mass released from biomass burning and the evolution of SOA with special emphasis on formation routes. The biomass burning work explored the evolution of organic aerosol emissions as a function of modified combustion efficiency with correlations drawn between levoglucosan emissions and wood-type, combustion type (flaming, mixed, smoldering) using high resolution aerosol mass spectrometry. The SOA work includes insights into the mechanism for SOA formation from aromatics including the impacts of temperature and particle-aging. This work conclusively demonstrates that gas-particle partitioning theory combined with enthalpies of formation are insufficient to model the formation of SOA as a function of time; that the presence of secondary reactions, in both the particle and gas-phase continue to evolve the aerosol beyond that typically simulated in environmental chambers; and that current mechanisms for SOA

formation from aromatics fail to explain isotopically labeled experiments while conclusively ruling out the importance of organic nitrate products.



## Table of Contents

### Acknowledgements

### Abstract

<b>1. Introduction.....</b>	<b>1</b>
1.1 Introduction of the Dissertation .....	1
1.2 References .....	7
<b>2. Can secondary organic aerosol formed in an atmospheric simulation chamber continuously age? .....</b>	<b>12</b>
2.1 Introduction .....	12
2.2 Experimental Section .....	13
2.2.1 Facility Overview .....	13
2.2.2 Particle Analysis .....	14
2.2.3 Gas Analysis.....	17
2.2.4 Experiment Methods.....	17
2.2.5 Aging Pathways.....	17
2.3 Results and Discussion.....	18
2.3.1 SOA production .....	18
2.3.2 Hygroscopic Property Evolution.....	19
2.3.3 Particle Density Evolution .....	21

2.3.4 <i>Particle Volatility Evolution</i> .....	22
2.3.5 <i>Chemical Composition Evolution</i> .....	24
2.4 Conclusions .....	25
2.5 References .....	27
<b>3. Aging process from select chamber reaction systems-the role of additional reactants</b> .....	<b>40</b>
3.1 Introduction .....	40
3.2 Experimental Section .....	42
3.2.1 <i>Facility Overview</i> .....	42
3.2.2 <i>Particle and Gas Measurements</i> .....	42
3.2.3 <i>Experiment Methodology</i> .....	45
3.3 Results .....	45
3.3.1 <i><math>\alpha</math>-Pinene Reaction with Ozone</i> .....	45
3.3.2 <i><math>\alpha</math>-Pinene Reaction with Ozone + Additional Oxidants</i> .....	46
3.4 Discussions.....	49
3.5 Conclusions .....	51
3.6 References .....	52
<b>4. Temperature effect on physical and chemical properties of SOA from <i>m</i>-xylene photooxidation</b> .....	<b>69</b>

4.1. Introduction .....	69
4.2. Experimental Section .....	71
4.2.1 Facility Overview .....	71
4.2.2 Light Intensity.....	71
4.2.3 Particle and Gas Measurements .....	72
4.3. Results and Discussions .....	75
4.3.1 SOA production .....	75
4.3.2 SOA density .....	76
4.3.3 SOA hygroscopicity .....	77
4.3.4 SOA volatility .....	77
4.3.5 SOA chemical composition.....	78
4.3.6 System Reversibility.....	80
4.4 Conclusions .....	81
4.5 References .....	83
<b>5. Investiagtion of SOA formation from aromatic photooxidation reaction using isotopic (<sup>13</sup>C<sub>2</sub>)<i>m</i>-xylene and <sup>15</sup>NO .....</b>	<b>99</b>
5.1 Introduction .....	99
5.2 Experimental Section .....	101
5.2.1 Facility Overview .....	101

5.2.2 <i>Particle and Gas Measurements</i> .....	101
5.3 Results and Discussions .....	103
5.3.1 <i>(<sup>13</sup>C<sub>2</sub>)m-xylene and (<sup>12</sup>C<sub>2</sub>)m-xylene Reaction Comparison</i> .....	103
5.3.2 <i><sup>15</sup>NO and <sup>14</sup>NO Reaction Comparison</i> .....	105
5.4 Conclusions .....	107
5.5 References .....	108
<b>6. Chemical analysis of PM<sub>2.5</sub> from controlled burns of southwest biomass fuels using a high resolution time-of-flight aerosol mass spectrometer</b> .....	<b>121</b>
6.1 Introduction .....	121
6.2 Experimental Section .....	123
6.2.1 <i>Fuel selection and treatment</i> .....	123
6.2.2 <i>Facility and combustion</i> .....	125
6.2.3 <i>Real-time particle measurements</i> .....	126
6.2.4 <i>Real-time gas measurement</i> .....	127
6.3 Results .....	128
6.3.1 <i>Modified combustion efficiency</i> .....	128
6.3.2 <i>Mass spectra of different southwest fuel types</i> .....	128
6.3.3 <i>Bulk chemical composition</i> .....	130

6.3.4 Comparison of organic mass based on organic carbon using two methodologies.....	132
6.3.5 Levoglucosan analysis.....	133
6.4 Conclusions .....	135
6.5 References .....	137
<b>7. Conclusions</b> .....	<b>162</b>
<b>Appendices</b>	
Appendix A: Secondary Organic Aerosol Formation from Primary Aliphatic Amines with NO <sub>3</sub> Radical .....	166
Appendix B: Trimethylamine as precursor to secondary organic aerosol formation via nitrate radical reaction in the atmosphere .....	202
Appendix C: Real-Time Aerosol Density Determination Utilizing a Modified Scanning Mobility Particle Sizer – Aerosol Particle Mass Analyzer System .....	230

## List of Table

Table 2.1 Experimental conditions and results for the $\alpha$ -pinene and <i>m</i> -xylene oxidation systems.....	33
Table 3.1 Experimental conditions and results for the $\alpha$ -pinene oxidation systems.....	57
Table 4.1 Experimental conditions and results summary for the <i>m</i> -xylene photooxidation reactions .....	87
Table 5.1 Experimental conditions and results for the <i>m</i> -xylene photooxidation systems .....	111
Table 5.2 List of major ion peaks observed for the reaction of ( <sup>13</sup> C <sub>2</sub> ) <i>m</i> -xylene/NO in the smog chamber and their potential assignments .....	113
Table 6.1 Plant species that used as southwestern biomass fuels in this study .....	142
Table 6.2 Fuel bed properties for the 9 plant species .....	143
Table 6.3 Ratios of m/z 29, 43, 44, 60 and 73 for all nine fuels (a) flaming; (b) mixed; (c) smoldering.....	148
Table 6.4 Empirical formula for nine biomass fuels during flaming, mixed and smoldering phases.....	156

## List of Figures

Figure 2.1 Pathways of SOA formation and process .....	32
Figure 2.2 Aerosol volume concentration and peak mobility diameter evolution.....	34
Figure 2.3 The growth factor and the variations in RH in a typical operating scheme for (a) $\alpha$ -pinene ozonolysis experiment, (b) $\alpha$ -pinene photooxidation experiment and (c) <i>m</i> -xylene photooxidation experiment .....	35
Figure 2.4 The time evolution of particle density for three typical experiments: (a) $\alpha$ -pinene ozonolysis with hydroxyl radical scavenger (b) $\alpha$ -pinene photooxidation and (c) <i>m</i> -xylene photooxidation .....	36
Figure 2.5 The volume remaining fraction in typical operating schemes for: (a) $\alpha$ -pinene ozonolysis experiment (dry), $\alpha$ -pinene photooxidation experiment (dry) and <i>m</i> -xylene photooxidation experiment (dry) (b) an example of VRF variation on different selected single particle sizes.....	37
Figure 2.6 The average ratio comparison for <i>m</i> -xylene photooxidation experiment (dry) without thermal denuder and with thermal denuder set at 50, 100 and 150°C .....	38
Figure 2.7 Time series of average atomic O/C and OM/OC for experiments: (a) <i>m</i> -xylene photooxidation (dry) and (b) $\alpha$ -pinene photooxidation (dry).....	39
Figure 3.1 Wall-loss corrected aerosol volume concentration and diameter for dry non-seeded ozonolysis with and without CO .....	58
Figure 3.2 The growth factor and the variations in RH in a typical operating scheme for (a) $\alpha$ -pinene ozonolysis experiment with CO, (b) $\alpha$ -pinene ozonolysis experiment without CO.....	59
Figure 3.3 A typical temperature profile inside the reactor over the course of the experiment.....	60
Figure 3.4 Aerosol formation results for four experiments .....	61
Figure 3.5 The growth factor and the variations in RH in a typical operating scheme for (a) $\alpha$ -pinene ozonolysis with additional H <sub>2</sub> O <sub>2</sub> injection, (b) $\alpha$ -pinene ozonolysis with additional NO injection and (c) $\alpha$ -pinene ozonolysis with additional N <sub>2</sub> O <sub>5</sub> injection.....	62
Figure 3.6 The time evolution of particle density for two select experiments: (a) $\alpha$ -pinene ozonolysis with additional NO injection (b) $\alpha$ -pinene ozonolysis with additional H <sub>2</sub> O <sub>2</sub> injection .....	64
Figure 3.7 Time series of average atomic O/C for $\alpha$ -pinene/ozonolysis experiments with additional injection of: (a) NO; (b) N <sub>2</sub> O <sub>5</sub> ; (c) H <sub>2</sub> O <sub>2</sub> .....	65
Figure 3.8 Simplified mechanism of $\alpha$ -pinene ozonolysis .....	67
Figure 3.9 Example of explicit mechanism of •OH reaction with pinonaldehyde .....	67

Figure 3.10 A sample data set for time trace of $\text{NO}^+$ , and $\text{CH}_2\text{O}^+$ ions specifically in the additional injection of $\text{N}_2\text{O}_5$ reaction.....	68
Figure 4.1 Aerosol formation results for three selected temperature experiments.....	88
Figure 4.2 The time evolution of particle density for four selected temperature experiments.....	90
Figure 4.3 Growth factor and RH for <i>m</i> -xylene photooxidation experiments at two different temperatures.....	92
Figure 4.4 The volume remaining fraction in typical operating schemes for <i>m</i> -xylene photooxidation experiment at three temperatures.....	93
Figure 4.5 The normalized average mass spectra of total organics for <i>m</i> -xylene photooxidation experiment at two temperatures (278 K, 313 K).....	95
Figure 4.6 The time series of O/C ratio for <i>m</i> -xylene photooxidation experiment at cold and hot temperature.....	96
Figure 4.7 Wall-loss corrected volume concentration for <i>m</i> -xylene photooxidation reaction.....	97
Figure 4.8 Particle density evolution for <i>m</i> -xylene photooxidation reaction.....	98
Figure 5.1 UMR mass spectrum comparison for (a) ( $^{13}\text{C}_2$ ) <i>m</i> -xylene /NO and (b) ( $^{12}\text{C}_2$ ) <i>m</i> -xylene /NO.....	112
Figure 5.2 ( $^{13}\text{C}_2$ ) <i>m</i> -xylene-OH initial reaction split and details of abstraction path.....	114
Figure 5.3 Real time measurements of major gas-phase products from PTR-MS.....	115
Figure 5.4 Mechanism of <i>m</i> -xylene-OH reaction leading to the major gas-phase products.....	116
Figure 5.5 UMR mass spectrum comparison for ( $^{12}\text{C}_2$ ) <i>m</i> -xylene / $^{14}\text{NO}$ and ( $^{12}\text{C}_2$ ) <i>m</i> -xylene / $^{15}\text{NO}$ photooxidation reactions.....	117
Figure 5.6 Example of high resolution spectra of m/z 30 and 46.....	118
Figure 5.7 Contribution of organic nitrate to total organics for high and low $\text{HC}_x$ : NO cases.....	119
Figure 5.8 Reaction of $\text{NO}_2$ resulting from <i>m</i> -xylene-OH reaction leading to observed organic nitrate.....	120
Figure 6.1 Two pictures showing fuel and fuel bed before fire.....	144
Figure 6.2 Schematic of the US Forest Service Science Laboratory combustion facility at Missoula, MT.....	145
Figure 6.3 Schematic of online and offline sampling system.....	146
Figure 6.4 Averaged MCE for 9 fuel species during flaming, mixed and smoldering phases.....	147



Figure 6.5 Averaged normalized mass spectra for (a) flaming, (b) mixed and (c) smoldering phases of measured particle components from the combustion of different southwestern biomass fuels.....	150
Figure 6.6 The elemental ratio evolution of particles at different phases from Chamise burning.....	153
Figure 6.7 Averaged elemental ratios of organic carbonaceous aerosol from the combustion of different biomass fuels.....	154
Figure 6.8 Averaged OM/OC from the combustion of different biomass fuels.....	157
Figure 6.9 Molecular structure of levoglucosan.....	158
Figure 6.10 Peaks resolved for m/z 60 and 73 from Chamise burning.....	158
Figure 6.11 Time evolution of $C_2H_4O_2^+$ and $C_3H_5O_2^+$ ions vs. total organics of aerosol emissions for nine southwestern biomass fuels.....	159
Figure 6.12 The relationship between $C_2H_4O_2^+$ and $C_3H_5O_2^+$ fragment ions.....	161

## **Chapter 1**

### **1.1 Introduction of the Dissertation**

Particulate Matter is a general term used for the mixture of solid particles and liquid droplets in the air. Fine particles ( $PM_{2.5}$ ) refer specifically to particulate matter that is 2.5 microns in diameter or less. Sources of particulate matter are of both anthropogenic and natural origin. Natural sources include volcanoes, dust storms, forest and grassland fires, living vegetation, and sea spray. Anthropogenic include fossil fuel combustion and various industrial processes. Based on their origin, atmospheric aerosol can be classified as primary aerosol (directly emitted from sources) and secondary aerosol (formed via atmospheric chemical reaction of gaseous species).

SOA refers to organic aerosol formed from gas-phase oxidative processing of volatile organic compounds (VOCs) in the atmosphere (e.g., Kroll and Seinfeld, 2008). VOCs are emitted into the atmosphere from a variety of anthropogenic and biogenic sources such as industrial solvent evaporation, fuel combustion, and vegetation emissions (Seinfeld and Pandis, 1998). Examples of these compounds include alkanes, alkenes, aromatics and monoterpenes. Subsequently, atmospheric oxidation of these VOCs produces gas-phase and particle-phase pollutants. The semi-volatile gas-phase oxidation products then partition between the gas- and particle-phase onto pre-existing particles to form SOA.

SOA accounts for a majority of organic aerosol in the atmosphere. Turpin et al. (1995) estimated that SOA comprises up to 70% of all organic aerosol present using the

elemental carbon (EC)/organic carbon (OC) tracer method. More recently, Zhang et al., (2007) reported that SOA was a major fraction of organic aerosol in megacities based on a global data base acquired from aerosol mass spectrometer (AMS). SOA is also believed to contribute to climatic impacts, regional visibility reduction and potential health hazards (IPCC, 2007; Eldering and Cass, 1996; Davidson et al., 2005; Pope and Dockery, 2006).

Aromatics and monoterpenes are two important classes of atmospheric VOCs. Aromatic hydrocarbons are prevalent in the urban atmosphere; it is estimated that aromatic hydrocarbons contribute ~19% of atmospheric VOCs in the Los Angeles, California area (Calvert et al., 2002). It is further estimated that aromatic hydrocarbons can contribute up to 50-70% of the SOA formation in the urban atmosphere (Na et al., 2004). Biogenic sources dominate global VOC emissions with estimated annual non-methane emissions of 491-1150 Tg carbon (Müller, 1992; Guenther et al., 1995). Approximately 11% of biogenic VOCs are monoterpenes with  $\alpha$ -pinene contributing one-quarter of the total inventory of monoterpenes (Kanakidou et al., 2005). The ozonolysis of monoterpenes is reported to be one of the major contributors to global SOA (Griffin et al., 1999).

Traditionally, an environmental simulation chamber is used to investigate the atmospheric processes leading to ozone and SOA formation. This is done to limit the number of factors impacting ozone and SOA formation by utilizing a well-controlled environment not subject to processes involving atmospheric transport. Over the past several decades, a number of smog chamber studies have evaluated SOA formation potential from the photooxidation of alkyl-substituted aromatic hydrocarbons in the

presence of  $\text{NO}_x$  or  $\text{H}_2\text{O}_2$  (e.g., Izumi and Fukuyama, 1990; Odum et al., 1996; Odum et al., 1997; Kleindienst et al., 1999; Edney et al., 2000; Cocker et al., 2001a; Song et al., 2005; 2007a,b) and from dark ozonolysis of monoterpenes (e.g., Hoffmann et al., 1997; Griffin et al., 1999; Iinuma et al., 2005; Pathak et al., 2007; Shilling et al., 2008). Additional chamber experiments have focused on identifying particle-phase product compositions from SOA produced from aromatic and monoterpene precursors (e.g., Forstner et al., 1997; Jang and Kamens, 2001; Kleindienst et al., 2004; Alfarra et al., 2006; Hoffmann et al., 1998; Docherty et al., 2005; Ma et al., 2008; Camredon et al., 2010). SOA formation has been studied in the presence of additional water vapor, measured as relative humidity (RH) (e.g., Cocker et al., 2001a, Cocker et al., 2001b, Na et al., 2006, Na et al., 2007, Varutbangkul et al., 2006, Warren et al., 2009). Results have indicated that water vapor may participate in both the gas- and particle-phase chemistry, thereby altering the final SOA chemical composition. Further studies have explored the role of different oxidants including the importance of HC/ $\text{NO}_x$  ratio (e.g., Hurley et al., 2001; Song et al., 2005; Ng et al., 2007).

Environmental parameters such as temperature and light intensity also influence SOA formation. A few studies have investigated SOA formation at different temperatures, focusing on the final aerosol production yield dependence with temperature (Pathak, et al., 2007, Takekawa et al., 2003). The results showed a direct temperature dependence on SOA formation with the final aerosol mass formed decreasing with increasing temperature. Changing light source and intensity has also been reported to influence SOA production. For example, Warren et al., (2009) reported that less SOA

production was observed as the rate of NO<sub>2</sub> photolysis was decreased in the *m*-xylene/NO photooxidation reaction systems.

Early studies by our group provided a large, accurate experimental data base for SOA formation under different environmental parameters for *m*-xylene photooxidation and cyclohexene and  $\alpha$ -pinene ozonolysis. This previous research mainly focused on the effects of these environmental parameters on SOA yield in the absence of physical and chemical product information.

This study provides insight into the physical and chemical properties of SOA formed from photooxidation of aromatic and mono-terpene hydrocarbons and ozonolysis of mono-terpene hydrocarbon under widely varying conditions.

Chapter 2 investigates the aging processes of SOA formed in the *m*-xylene and  $\alpha$ -pinene photooxidation systems as well as in the  $\alpha$ -pinene ozonolysis system. A series of experiments are performed with varying reactants inputs and concentrations for up to sixteen hours. The results clearly demonstrate that aerosol produced from these systems age with increased functionalization of the SOA in terms of particle hygroscopicity, volatility and elemental composition, but at a lower rate compared to the ambient particle aging. The results indicate that the hydroxyl radical plays a significant role in aerosol aging.

Chapter 3 expands on the Chapter 2 study of SOA aging by adding additional reactants (NO, nitrate radical, hydrogen peroxide) to SOA generated from  $\alpha$ -pinene ozonolysis. This chapter provides evidence that the particle-phase product distribution changes (aerosol ages) with the injection of additional reactants. This aging may occur

either through modification of the particle-phase chemical composition via further oxidation of gas-phase products (followed by condensation) or via heterogeneous reaction at the gas-particle interface.

Chapter 4 expands the current knowledge of temperature influences on SOA formation from dark cyclohexene and  $\alpha$ -pinene ozonolysis reaction systems to the *m*-xylene photooxidation system. Temperature is found to have a clear and dramatic effect on the SOA formation not only in terms of particle volume but also chemical composition. This chapter demonstrates that aerosol formation as a function of temperature is not fully described using estimated product enthalpies and traditional gas-particle theory. Rather, the temperature dependence and resulting measured bulk chemical and physical characterization indicate additional SOA formation mechanisms that must be accounted for to fully characterize SOA formation dependence on system temperature.

Chapter 5 explores the possible mechanism for aerosol formation from *m*-xylene photooxidation by using the isotopic ( $^{13}\text{C}_2$ ) *m*-xylene and  $^{15}\text{NO}$ . High-resolution time-of-flight aerosol mass spectrometer (HR-ToF-AMS) provides chemical information that fragmented ions shift by only +1 (only one of two  $^{13}\text{C}$  atoms remains) and the presence of products resulting from ring open reactions. It also confirms that the organic nitrate formation is not as significant by the fact that little contribution of  $^{15}\text{NO}$  and  $^{15}\text{NO}_2$  addition was observed. Several major gas-phase products were observed using Proton Transfer Reaction Mass Spectrometer (PTR-MS) which are tentatively identified as di-carbonyl compounds and may partially account for the SOA formation.

Chapter 6 moves from chamber SOA studies towards primary organic aerosol studies by investigating organic aerosol originating from prescribed burns of southwest biomass fuels. This chapter summarizes the chemical characterization of PM<sub>2.5</sub> emissions collected for flaming, mixed and smoldering phases using a HR-ToF-AMS for a total of nine southwest biomass fuels. Real time elemental ratios and levoglucosan content with respect to modified combustion efficiency (MCE) are reported.

Chapter 7 summarizes the results of these studies, presents the conclusions, and provides suggestions for future study.

In addition to the above sections, located in the appendix are three papers, which I contributed to significantly and appear on the paper as co-author. Appendix A describes a systematic study of nitrate radical oxidation of a series of primary amines (Malloy et al., 2009). Appendix B describes the laboratory study of SOA formation from nitrate radical reaction with trimethylamine (Silva et al., 2008). Appendix C describes the development of a novel technique for real-time aerosol density measurement which all the experiments from this dissertation used to obtain particle density (Malloy et al., 2009).

## 1.2 References

- Alfarra, M.R., Paulsen, D., Gysel, M., Garforth, A.A., Dommen, J., Pr  t, A.S.H., Worsnop, D.R., Baltensperger, U., Coe, H., 2006. A mass spectrometric study of secondary organic aerosols formed from the photooxidation of anthropogenic and biogenic precursors in a reaction chamber. *Atmos. Chem. Phys.* 6, 5279-5293.
- Calvert, J.G., Atkinson, R., Becker, K.H., Kamens, R.M., Seinfeld, J.H., Wallington, T.J., Yarwood, G., 2002. *The Mechanisms of Atmospheric Oxidation of Aromatic Hydrocarbons*. Oxford University Press, London.
- Cocker III, D.R., Mader, B.T., Kalberer, M., Flagan, R.C. and Seinfeld, J.H., 2001a. The effect of water on gas-particle partitioning of secondary organic aerosol: II. *m*-xylene and 1,3,5-trimethylbenzene photooxidation systems. *Atmospheric Environment* 35, 6073-6085.
- Cocker, D.R., Whitlock, N.E., Flagan, R.C., Seinfeld, J.H., 2001b. Hygroscopic properties of Pasadena, California aerosol. *Aerosol Science and Technology* 35, 637-647.
- Davidson, C.I., Phalen, R.F., Solomon, P.A., 2005. Airborne Particulate Matter and Human Health: A Review. *Aerosol Science and Technology* 39, 737-749.
- Docherty, K. S., Wu, W., Lim, Y. B., and Ziemann, P. J., 2005. Contributions of organic peroxides to secondary aerosol formed from reactions of monoterpenes with O<sub>3</sub>, *Environ. Sci. Technol.*, 39, 4049-4059.
- Edney, E.O., Driscoll, D.J., Speer, R.E., Weathers, W.S., Kleindienst, T.E., Li, W., Smith, D.F., 2000. Impact of aerosol liquid water on secondary organic aerosol yields of irradiated toluene/propylene/NO<sub>x</sub>/(NH<sub>4</sub>)<sub>2</sub>SO<sub>4</sub>/air mixtures. *Atmospheric Environment* 34, 3907-3919.
- Eldering, A., Cass, G.R., 1996. Source-oriented model for air pollutant effects on visibility. *Journal of Geophysical Research-Atmospheres* 101, 19343-19369.
- Forstner, H.J.L., Flagan, R.C., Seinfeld, J.H., 1997. Secondary organic aerosol from the photooxidation of aromatic hydrocarbons: molecular composition. *Environ. Sci. Technol.* 31, 1345-1358.
- Griffin, R. J., Cocker, D. R., Flagan, R. C., and Seinfeld, J. H., 1999. Organic aerosol formation from the oxidation of biogenic hydrocarbons, *Journal of Geophysical Research-Atmosphere* 104, 3555-3567.



- Guenther, A., Hewitt, C. N., Erickson, D., Fall, R., Geron, C., Graedel, T., Harley, P., Klinger, L., Lerdau, M., McKay, W. A., Pierce, T., Scholes, B., Steinbrecher, R., Tallamraju, R., Taylor, J., and Zimmerman, P., 1995. A Global-Model of Natural Volatile Organic-Compound Emissions, *J. Geophys. Res.-Atmos.*, 100, 8873–8892.
- Hoffmann, T., Bandur, R., Marggraf, U., and Linscheid, M., 1998. Molecular composition of organic aerosols formed in the  $\alpha$ -pinene/  $O_3$  reaction: Implications for new particle formation processes, *J. Geophys. Res.*, 103, 25569–25578.
- Hoffmann, T., Odum, J. R., Bowman, F., Collins, D., Klockow, D., Flagan, R. C., and Seinfeld, J. H., 1997. Formation of organic aerosols from the oxidation of biogenic hydrocarbons, *J. Atmos. Chem.*, 26, 189–222.
- Hurley, M. D., Sokolov, O., Wallington, T. J., Takekawa, H., Karasawa, M., Klotz, B., Barnes, I., Becker, K. H., 2001. Organic aerosol formation during the atmospheric degradation of toluene. *Environ. Sci. Technol.*, 35, 1358–1366.
- Iinuma, Y., Boge, O., Miao, Y., Sierau, B., Gnauk, T., and Hermann, H., 2005. Laboratory studies on secondary organic aerosol formation from terpenes, *Faraday Discuss.*, 130, 279–294.
- Intergovernmental Panel on Climate Change (IPCC) Fourth Assessment Report: Climate Change 2007.
- Izumi, K. and Fukuyama, T., 1990. Photochemical aerosol formation from aromatic hydrocarbons in the presence of  $NO_x$ . *Atmospheric Environment* 24A, No. 6, 1433-1441.
- J. E. Shilling, Q. Chen, S. M. King, T. Rosenoern, J. H. Kroll, D. R. Worsnop, K. A. McKinney, and S. T. Martin, 2008. Particle mass yield in secondary organic aerosol formed by the dark ozonolysis of  $\alpha$ -pinene. *Atmos. Chem. Phys.*, 8, 2073–2088.
- Kanakidou, M., Seinfeld, J. H., Pandis, S. N., Barnes, I., Dentener, F. J., Facchini, M. C., Van Dingenen, R., Ervens, B., Nenes, A., Nielsen, C. J., Swietlicki, E., Putaud, J. P., Balkanski, Y., Fuzzi, S., Horth, J., Moortgat, G. K., Winterhalter, R., Myhre, C. E. L., Tsigaridis, K., Vignati, E., Stephanou, E. G., and Wilson, J., 2005. Organic aerosol and global climate modelling: a review, *Atmos. Chem. Phys.*, 5, 1053–1123.
- Kleindienst, T.E., Smith D.F., Li W., Edney E.O., Driscoll D.J., Speer R.E. and Weathers, W.S., 1999. Secondary organic aerosol formation from the oxidation of

- aromatic hydrocarbons in the presence of dry submicron ammonium sulfate aerosol. *Atmospheric Environment* 33, 3669-3681.
- Kroll, J.H., Seinfeld, J.H., 2008. Chemistry of secondary organic aerosol: Formation and evolution of low-volatility organics in the atmosphere. *Atmospheric Environment* 42, 3593-3624.
- M. Camredon, J. F. Hamilton, M. S. Alam, K. P. Wyche, T. Carr, I. R. White, P. S. Monks, A. R. Rickard, and W. J. Bloss, 2010. Distribution of gaseous and particulate organic composition during dark  $\alpha$ -pinene ozonolysis, *Atmos. Chem. Phys.* 10, 2893-2917.
- Ma, Y., Russell, A. T., and Marston, G., 2008. Mechanisms for the formation of secondary organic aerosol components from the gasphase ozonolysis of  $\alpha$ -pinene, *Phys. Chem. Chem. Phys.*, 10, 4294-4312.
- Malloy, Q.G.J., Nakao, S., Qi, L., Austin, R., Stothers, C., Hagino, H., Cocker, D.R., 2009. *Aerosol Science and Technology* 43, 673-678.
- Malloy, Q.G.J., Qi, L., Warren, B., Cocker, D.R., Erupe, M. Silva, P., 2009. Secondary organic aerosol formation from primary aliphatic amines with  $\text{NO}_3$  radical. *Atmospheric Chemistry and Physics* 9, 2367–2388.
- Müller, J. F., 1992. Geographical-Distribution and Seasonal-Variation of Surface Emissions and Deposition Velocities of Atmospheric Trace Gases, *J. Geophys. Res.-Atmos.*, 97, 3787–3804.
- Ng, N.L., Kroll, J.H., Chan, A.W., Chhabra, P.S., Flagan, R.C. and Seinfeld, J.H., 2007. Secondary organic aerosol formation from *m*-xylene, toluene, and benzene. *Atmos. Chem. Phys.*, 7, 3909-3922.
- Na, K., Song, C., Cocker, D.R., 2006. Formation of secondary organic aerosol from the reaction of styrene with ozone in the presence and absence of ammonia and water. *Atmospheric Environment* 40, 1889–1900.
- Na, K., Song, C., Switzer, C., Cocker, D.R., 2007. Effect of ammonia on secondary organic aerosol formation from alpha-pinene ozonolysis in dry and humid conditions. *Environ. Sci. Technol.* 41, 6096–6102.
- Na, K., Swant, A.A., Song, C. and Cocker III, D.R., 2004. Primary and secondary carbonaceous species in the atmosphere of Western Riverside County, California. *Atmospheric Environment* 38, 1345-1355.

- Odum, J.R., Hoffmann, T., Bowman, F., Collins, D., Flagan, R.C. and Seinfeld, J.H., 1996. Gas/particle partitioning and secondary organic aerosol yields. *Envir. Sci. Technol.*, 30, 2580-85.
- Odum, J.R., Jungkamp, T.P.W., Griffin, R.J., Forstner, H.J.L., Flagan, R.C. and Seinfeld, J.H., 1997. Aromatics, reformulated gasoline, and atmospheric organic aerosol formation. *Envir. Sci. Technol.*, 31, 1890-97.
- Pathak, R. K., Presto, A. A., Lane, R. E., Stanier, C. O., Donahue, N. M., and Pandis, S. N., 2007. Ozonolysis of  $\alpha$ -pinene: Parameterization of secondary organic aerosol mass fraction, *Atmos. Chem. Phys.*, 7, 3811–3821.
- Pathak, R. K., Stanier, C. O., Donahue, N. M., and Pandis, S. N.: Ozonolysis of  $\alpha$ -pinene at atmospherically relevant concentrations: temperature dependence of aerosol mass fractions (yields), *Journal of Geophysical Research-Atmospheres* 112, D03201, 2007.
- Pope, C.A., Dockery, D.W., 2006. Health effects of fine particulate air pollution: lines that connect, *Journal of the Air and Waste Management Association* 56, 709-742.
- Seinfeld, J.H. and Pandis, S.N., 1998. *Atmospheric Chemistry and Physics: From Air Pollution to Climate Change*. John Wiley, New York.
- Song, C., Na, K., Warren, B., Malloy, Q. and Cocker, D.R., 2007a. Secondary organic aerosol formation from *m*-xylene in the absence of NO<sub>x</sub>. *Environmental Science & Technology* 41, 7409-7416.
- Song, C., Na, K., Warren, B., Malloy, Q. and Cocker, D.R., 2007b. Secondary organic aerosol formation from the photooxidation of *p*- and *o*-xylene. *Environmental Science & Technology* 41, 7403-7408.
- Song, C., Na, K.S. and Cocker, D.R., 2005. Impact of the hydrocarbon to NO<sub>x</sub> ratio on secondary organic aerosol formation. *Envir. Sci. Technol.*, 39, 3143-3149.
- Takekawa, H., Minoura, H., and Yamazaki, S.: Temperature dependence of secondary organic aerosol formation by photo-oxidation of hydrocarbons, *Atmospheric Environment* 37, 3413-3424, 2003.
- Turpin, B.J. and Huntzicker, J.J., 1991. Secondary formation of organic aerosol in the Los-angeles basin – a descriptive analysis of organic and elemental carbon Concentrations. *Atmospheric Environment* 25A, No. 2, 207-215.
- Varutbangkul, V., Brechtel, F.J., Bahreini, R., Ng, N.L., Keywood, M.D., Kroll, J.H., Flagan, R.C., Seinfeld, J.H., Lee, A., Goldstein, A.H., 2006. Hygroscopicity of secondary organic aerosols formed by oxidation of cycloalkenes, monoterpenes,

sesquiterpenes, and related compounds. *Atmospheric Chemistry and Physics* 6, 2367–2388.

Warren, B., Malloy, Q., Yee, L., Cocker, D.R., 2009. Secondary organic aerosol formation from cyclohexene ozonolysis in the presence of water vapor and dissolved salts. *Atmospheric Environment* 43, 1789–1795.

Warren, B., Song, C., Cocker, D.R., 2008. Light intensity and light source influence on secondary organic aerosol formation for the *m*-xylene/NO<sub>x</sub> photooxidation system. *Environ. Sci. Technol.* 42, 5461–5466.

Zhang, Q., Jimenez, J. L., Canagaratna, M. R., Allan, J. D., Coe, H., Ulbrich, I. et al., 2007. Ubiquity and dominance of oxygenated species in organic aerosols in anthropogenically-influenced Northern Hemisphere midlatitudes, *Geophysical Research Letters* 34, L13801, doi:10.1029/2007GL029979.

## Chapter 2

### 2.1 Introduction

Secondary Organic Aerosol (SOA) refers to organic aerosol formed from gas-phase oxidative processing of volatile organic compounds (VOCs) in the atmosphere (e.g., Kroll and Seinfeld, 2008). SOA accounts for a majority of organic aerosol in the atmosphere. It comprises up to 80% of all organic aerosol present (Turpin, et al., 1995; Zhang et al., 2007) and contributes to climatic impacts, regional visibility reduction and potential health hazards (IPCC, 2007; Eldering and Cass, 1996; Davidson et al., 2005; Pope and Dockery, 2006).

Once formed, organic aerosol particles in the atmosphere may undergo further physical and chemical processing, altering the physiochemical properties of aerosol, including its hygroscopic property (Broekhuizen et al., 2004; Asad et al., 2004), density (Katrib et al., 2005; Bahreini et al., 2005), chemical composition (Mmereki et al., 2004), toxicity (Rudich et al., 2007), optical property (Rudich et al., 2007), and their cloud condensation nuclei (CCN) activity (Shilling et al., 2007). Several pathways have been proposed for SOA aging processes: 1) heterogeneous reactive uptake of gas-phase oxidants such as  $O_3$ , OH and  $NO_3$  by the condensed-phase molecules (Ellison et al., 1999); 2) further gas-phase oxidation of semi-volatile products that repartition between the gas and particle phase (Robinson et al., 2007); 3) organic semi-volatile monomers in the interior of SOA particles to form large molecular weight oligomeric compounds (Rudich, 2003; Ziemann, 2005); or 4) other heterogeneous processes leading to SOA

formation (e.g., Kalberer et al., 2004, 2006; Tolocka et al., 2004; Baltensperger et al., 2005; Gao et al., 2004a,b; Gross et al., 2006).

As chemical and physical aging should vary locally with ambient concentrations of oxidants and condensates, a more detailed understanding of the hydrophobic-to-hydrophilic aging mechanism of secondary organic aerosol particles is necessary before a more accurate representation can be included in atmospheric chemistry models. Previous experiments conducted in the UC Riverside/CE-CERT environment chamber have shown little changes in hygroscopic property from  $\alpha$ -pinene ozonolysis system within time scale of fifteen hours ( $G_f=1.1\pm 0.02$  at  $83.3\pm 0.5\%$  RH) (Warren et al., 2009).

This paper focuses on the evolution of particle hygroscopicity and density as well as C:O:H ratios estimated from aerosol mass spectra. It evaluates whether the processing of chamber SOA can lead to sufficiently high oxygen/carbon ratios to be congruent with ambient SOA observations. Chemical aging processes of SOA derived from  $\alpha$ -pinene and *m*-xylene utilizing the UC Riverside/CE-CERT environmental chamber are discussed correspondingly.

## **2.2 Experimental Section**

### **2.2.1 Facility Overview**

Experiments are conducted in the UC Riverside/CE-CERT indoor environmental chamber, which is described in detail elsewhere (Carter et al., 2005). Dual 90m<sup>3</sup> Teflon reactors are suspended by a rigid steel framework in a temperature-controlled enclosure which is continuously flushed with purified air. The rigid framework slowly collapses the

reactors during the experiments to minimize leaks and diffusion of contaminants into the reactors by maintaining a positive 0.03" H<sub>2</sub>O differential pressure between the reactors and enclosure. Eighty 115 W Sylvania 350 black lights are used as light sources for photooxidation reactions. All ozonolysis experiments are conducted under dark conditions. A known volume of high purity liquid hydrocarbon precursor ( $\alpha$ -pinene: Sigma-Aldrich,  $\geq 99.0\%$ ; *m*-xylene: Sigma-Aldrich,  $\geq 99.5\%$ ) and 50 % wt hydrogen peroxide are injected through a heated glass injection manifold system and flushed into the chamber with pure N<sub>2</sub>. NO is introduced by flushing pure N<sub>2</sub> through a calibrated glass bulb filled to a predetermined partial pressure of pure NO. Ozone is made using two Dalton ozone generators (Model Type: OZG-UV-01) and injected the same way with pure N<sub>2</sub> flushing. CO is directly introduced as OH radical scavenger from a certified known concentration gas cylinder with flow rate set at 900 cc/min, and then flushed into the chamber with pure N<sub>2</sub>.

### **2.2.2 Particle Analysis**

Particle size distributions between 28 and 700 nm are monitored with scanning mobility particle sizers (SMPS). Particle sizing is validated with a suite of polystyrene latex spheres (PSL) (Duke Scientific Corp., Palo Alto, CA).

Real-time particle density is measured using an Aerosol Particle Mass Analyzer (APM) (Kanomax model 3600) and SMPS in series. Details of the instruments and theory are described elsewhere (Malloy et al., 2009; Ehara et al., 1996). A custom Labview program determines mode diameter peak from a parallel SMPS and then actively

configures the APM-SMPS to optimize instrument response. Density is acquired approximately every 75 s.

The hygroscopicity of chamber derived SOA is continuously monitored with a custom-built Hygroscopic Tandem Differential Mobility Analyzer (HTDMA). The instrument follows the original design of Radar and McMurry with the configuration similar to that illustrated in Cocker et al. (2001b). The particle diameter transmitted through the first SMPS was selected to match the peak size distribution measured by a parallel SMPS. Hygroscopic growth factor ( $G_f$ ) is reported as the ratio of the modal diameter of humidified aerosol (85.0%~95.0%±1.0%),  $D_{p,\text{humidified}}$ , to that of classified aerosol,  $D_{p,\text{dry}}$ , i.e.,  $G_f = D_{p,\text{humidified}}/D_{p,\text{dry}}$ . Both size distributions are fitted to log-normal distributions to get  $D_{p,\text{humidified}}$  and  $D_{p,\text{dry}}$  for calculation. The residence time of the humidification system is approximately 1 minute. The HTDMA measurement is validated with ammonium sulfate, the growth factor of which as a function of RH is well-known. The  $G_f$  is found to agree within 1.0% of theoretically calculated result using Köhler model at similar RH level (Brechtel and Kreidenweis, 2000). Parallel to the humidification system is a thermal denuder system (residence time ~17 sec) that can be alternatively operated to evaluate SOA volatility.

The evolution of particle elemental composition of aerosol particles was tracked using an Aerodyne High Resolution Time-of-Flight Aerosol Mass Spectrometry (HR-ToF-AMS) operating in the high resolution mode (Jayne et al., 2000; Jimenez et al., 2003). The HR-ToF-AMS has been described in detail previously (Jayne et al., 2000) and improves on mass resolution by using a custom high-resolution ToFMS (Tofwerk,



Switzerland). As a result of both the extensive fragmentation caused by electron impact ionization and the thermal decomposition of molecules by the vaporizer, most of the signal intensity occurred below mass to charge ratio ( $m/z$ ) 100; parent molecular peaks were weak or unobserved. Therefore,  $m/z$  values of fragment ions were interpreted as tracers of the parent species and the change in contribution fraction of signal intensities could be attributed to evolution of aerosol species (e.g., change in signal intensity ratio of  $m/z$  44/43). A relative increase in the signal intensity at  $m/z$  44, which is a common fragment of oxo- and dicarboxylic acids ( $\text{CO}_2^+$ ) and a relative decrease at  $m/z$  43, which is a fragment of oxidized organic molecules containing carbonyl groups ( $\text{C}_2\text{H}_3\text{O}^+$ ) could be expected as further oxidation. More recently, a new elemental analysis (EA) technique was developed coupled with HR-ToF-AMS sampling data (Aiken et al., 2007; 2008). The method is based on the property of electron ionization (EI) for molecules containing small atoms such as C, H, N, O and S that the sum of the ion signal intensities from all fragments is approximately proportional to the mass concentration of the original organic species. Thus, if the elemental composition of each fragment ion signal in a mass spectrum can be identified (as with HR mass spectra), the average composition of the ions can be calculated. For a complex spectrum from an unknown molecule or mixture, the best estimate of the composition can then be found by summing up the ion contributions across the entire mass spectrum, which represented as estimated ratios of oxygen-to-carbon (O/C), hydrogen-to-carbon (H/C), and nitrogen-to-carbon (N/C). Estimated atomic ratios are used to calculate Organic Matter (OM)/Organic Carbon (OC). In this study, the C:O:H ratio of the total aerosol was determined using the high

resolution capabilities of the HR-ToF-AMS following the Peak Integration by Key Analysis (PIKA) and Analytical Procedure for Elemental Separation (APES) templates (DeCarlo et al., 2006, Aiken et al., 2008).

### **2.2.3 Gas Analysis**

Decay of the parent hydrocarbon species was monitored with gas chromatography (GC-FID, Agilent 6890, Palo Alto, CA) equipped with a flame ionization detector. A Thermal Environmental Instruments Model 42C was used to measure NO, NO<sub>x</sub> and (NO<sub>x</sub> – NO) concentration. O<sub>3</sub> was monitored with a Dasibi Environmental Corp. Model 1003-AH O<sub>3</sub> analyzer.

### **2.2.4 Experiment Methods**

A series of *m*-xylene photooxidation and  $\alpha$ -pinene dark ozonolysis and photooxidation experiments were designed (Table 2.1) to evaluate the chemical aging of SOA. Thirteen experiments were conducted under dry conditions (RH<0.5%) in the absence of inorganic seed aerosol and one experiments under low humidity conditions (RH~25%). All the experiments were conducted as long as the reactor would permit.

### **2.2.5 Aging Pathways**

Chemical aging of secondary organic aerosol can occur through gas-phase, surface, and subsurface reactions (Fig. 2.1). Immediately after nucleation, the gas-to-particle phase partition of one or more generations of oxidation products may dominate aerosol growth (routes I and II). After this rapid growth, particle-phase semi-volatiles can

evaporate back to gas-phase, oxidize into low-volatility compounds, and then re-condense back into the particle-phase (route III). There is also the possibility that gaseous oxidants attack the particle surface and convert some of the semi-volatile species into less volatile products (route IV). Particle-phase reactions can also be promoted and oligomeric species formed over the experiment duration (route V). Recent studies suggest that surface reaction on preexisting SOA may also occur; Criegee intermediates with carboxylic acid and carbonyl functional groups may produce high-molecular-weight, oligomers and humic-like-substances (Hearn et al., 2005, Reynolds et al., 2006, Katrib et al., 2005). Ziemann et al. (2005) hypothesized that oligomeric species may form within particles through monomer reactions leading to linkage of an O-O bond. Several groups have reported observations of oligomeric or polymeric structures within chamber SOA experiments from oxidation of 1, 3, 5-trimethylbenzene (TMB) (Kalberer et al. 2004, Baltensperger et al., 2005) and  $\alpha$ -pinene (Gao et al., 2004a, Iinuma et al., 2005, Tolocka et al., 2004). Previous studies have been unable to definitively identify which reaction routes dominate particle evolution within an environmental chamber; it is likely that many of these routes occur simultaneously with each process contributing to a different extent at different stages of an experiment.

## **2.3 Results and Discussion**

### **2.3.1 SOA production**

A typical plot of the wall-loss-corrected aerosol volume and aerosol electrical mobility diameter versus time for select experiments is displayed in Fig. 2.2. The aerosol

production for the *m*-xylene photooxidation and  $\alpha$ -pinene ozonolysis experiments are consistent with earlier *m*-xylene (Song et al., 2005) and  $\alpha$ -pinene work (Cocker et al., 2001a) after accounting for differences in reacted hydrocarbon, hydroxyl radical scavenger, and reactor temperatures. Similar to the plots seen in Fig. 2.2, the final amounts of aerosol formed from  $\alpha$ -pinene dark ozonolysis for both dry and humid conditions without initial seeds remain constant for up to fourteen hours *after* completion of the initial aerosol growth phase. Similar aerosol formation plateaus, albeit after a longer aerosol growth-phase period due to the slower consumption of the parent compound, are seen for *m*-xylene photooxidation experiments.

Additional experiments were conducted to tentatively examine whether further functionalization of the aerosol could be enhanced by introduction of NO, O<sub>3</sub> or H<sub>2</sub>O<sub>2</sub> followed by photolysis. A typical experimental result with a second NO injection and UV irradiation (Fig. 2.2) only yielded small particle growth of suspended particles (~30nm) translating to an increase of wall loss corrected volume of only 2.9%. The small increase in aerosol volume is likely attributable to a slight increase in oxidation of gaseous products that subsequently condense onto the particle surface (routes I and II). The results on the additional injections of reactants will be described in detail in another paper (Qi et al., in prep).

### **2.3.2 Hygroscopic Property Evolution**

Particle hydrophilicity is influenced by the molecular weight and extent of functionalization of the organic molecules (Varutbangkul et al., 2006). Homogeneous reactions forming larger oligomer molecules within the particle phase (route V) or loss of

highly functionalized semi-volatile compounds will decrease particle hydrophilicity. Conversely, heterogeneous surface reactions or further gas-phase oxidation of semi-volatile products (either evaporated from the particle or already in the gas-phase) increases the functionalization of the organic molecules thereby increasing the hydrophilicity of the particle (route IV). Additionally, gas-phase reactions can lead to the distribution of different condensing species throughout the reaction (route I, II, III). The observed temporal variation in particle hygroscopicity is governed by competing effects (Varutbankul et al., 2006).

Real-time hygroscopic growth factors for select experiments are shown in Fig. 2.3.  $\alpha$ -Pinene ozonolysis experiments did not show increases in water uptake throughout the experiment (Fig. 2.3a). The  $G_f$  of the aerosol was constant ( $\sim 1.09$ , RH  $93.6\% \pm 0.4\%$ ) during and after SOA formation. Therefore, either processes influencing particle hydrophilicity were offset throughout the experiment or little processing (aging) of the SOA occurred. This is in contrast to other studies that report continuous increases in  $G_f$  with time for the ozonolysis of  $\alpha$ -pinene (Virkkula et al., 1999; Cocker et al., 2001a). However, the hygroscopicity of  $\alpha$ -pinene and *m*-xylene photooxidation aerosol shows a continuous increase of  $G_f$  for the entire experiment (1.04 to 1.11 for  $\alpha$ -pinene in Fig. 2.3b, 1.07 to 1.17 for *m*-xylene in Fig. 2.3c). The increased hydrophilicity is attributed to continued functionalization of semi-volatile compounds.

$G_f$  is observed to decrease with increasing particle diameter for the photooxidation experiments (Fig. 2.3c). Larger particles within the chamber undergo longer processing times and have smaller surface area-to-volume ratios, while smaller

particles are more representative of condensing species that is supposed to be less functionalized. The size dependent particle hydrophilicity is consistent with either 1) more highly functionalized semi-volatile species (multigeneration products) forming and condensing at later times in the reaction, 2) heterogeneous surface oxidation, or 3) reduction in relative particle hydrophilicity due to oligomeric reactions. It is noted that the hydrophilicity is not solely attributable to oligomeric reactions as the overall particle hydrophilicity increases throughout the experiment. The lack of size dependent particle hydrophilicity for the experiment is consistent with the stable  $G_f$  measured throughout the experiment. Our results are also supported by previous findings that show  $\alpha$ -pinene dark ozonolysis systems are dominated by first generation products.

### 2.3.3 Particle Density Evolution

The evolution of aerosol effective density for  $\alpha$ -pinene ozonolysis (with CO as OH scavenger) and  $\alpha$ -pinene and *m*-xylene photooxidation reaction are presented in Fig. 4. Effective density remains constant ( $1.24 \text{ g/cm}^3$ ) for the dry  $\alpha$ -pinene ozonolysis reaction (with CO) throughout the course of the experiment. Similar trends were observed for  $\alpha$ -pinene and *m*-xylene photooxidations ( $1.31 \text{ g/cm}^3$  and  $1.35 \text{ g/cm}^3$ , respectively, shown in Fig. 2.4b and Fig. 2.4c) after the initial nucleation burst; however, the measured density is  $\sim 8\%$  higher during initial aerosol formation than later in the experiment. These density trends are consistent with earlier work on  $\alpha$ -pinene dark ozonolysis and *m*-xylene photooxidation by Malloy et al., 2009. The constant density profiles for the systems (after nucleation) indicate that aerosol composition, as inferred from density, does not change appreciably. Or the reason could be that the sensitivity of

this instrument is insufficient to identify the chemical composition change compared to other techniques used in this paper to evaluate SOA aging processes.

### 2.3.4 Particle Volatility Evolution

Measurement of SOA volatility can provide indirect information about its chemical composition (Philippin et al., 2003, Kalberer et al., 2004). Baltensperger et al. (2005) reported that 65%, 25% and 10% of SOA from  $\alpha$ -pinene/NO<sub>x</sub> photooxidation after 10 hours irradiation remained in the particle phase after heating at 100, 150, and 200 °C, respectively. Similarly, they also reported the volume remaining fraction (VRF) from TMB photooxidation as 80%, 60% and 10% at 100, 150, and 200 °C, respectively, after 24 hours of photochemical aging. The thermodenuder used for these studies had relatively short aerosol residence times (~1.5 s) within the heated zone. The small residence time and the potential resistance to mass transfer of material from the particle-phase to the gas-phase may have resulted in an underestimation of SOA volatility. Therefore, for this study, we utilized a Dekati thermodenuder (model WAN 5912-4, Dekati Ltd., Finland) with a 17s residence time in the heating zone (0.25 LPM flow rate) set to 100°C.

The SOA VRF for the  $\alpha$ -pinene dark ozonolysis and the  $\alpha$ -pinene and *m*-xylene photooxidation experiments are shown in Fig. 2.5a. The VRF of the initial SOA formed is 6% and 18% for  $\alpha$ -pinene and *m*-xylene photooxidation, respectively. These VRFs increased to 44% and 47% for  $\alpha$ -pinene and *m*-xylene, respectively, by the end of experiments. However, the VRF for  $\alpha$ -pinene dark ozonolysis remained stable over the course of the experiment (61%±2%). The VRF time traces are consistent with HTDMA

observations that the chemical composition, inferred from these techniques, changes with SOA age for the photooxidation experiments but remains stable for the  $\alpha$ -pinene dark ozonolysis experiments. The remaining mass loading of the *m*-xylene photooxidation SOA measured by AMS drops to nearly zero after passing the aerosol through the thermodenuder set at 150°C (Fig. 2.6). The near complete evaporation of the aerosol at 150°C indicates that only a small fraction, if any, of the SOA is oligomeric as these larger molecules would be expected to remain condensed at these temperatures. Therefore, it is likely that the VRF is increasing in these systems due to increased functionalization of the semi-volatile compounds. No size dependence, within the resolution of the instrument, is observed in the VRF of the SOA (Fig 2.5b).

It is clear that SOA formation may highly depend on the experimental conditions, such as temperature, RH, seed particles presence and light intensity. The experiments normally carried out under different conditions between laboratories even though the reaction system may be very similar. This makes the need for inter-comparison between different chamber facilities a necessity. To facilitate comparison we took our measurements in the same TMB/NO<sub>x</sub> system at residence time of 1.5 seconds in the thermodenuder set at 100°C. The measurements reported by Kalberer et al., (2004) for the same system at 12h are quite different even if our experiment was performed at similar conditions. The VRF of particles only increased from about 20% to 40% over the course of 13 hours. In contrast, Kalberer et al. (2004) found that the VRF for TMB increased to 80% for comparable times. An et al., 2007 also performed VTDMA analyses on SOA produced for  $\alpha$ -pinene ozonolysis with particle number mode diameters



decreasing from 210 nm to 35 nm when the aerosol was heated to 100°C. The volatility of SOA for  $\alpha$ -pinene/NO<sub>x</sub> photooxidation reactions in this work was similar to those reported by Baltensperger et al. (2005) and An et al. (2007).

### 2.3.5 Chemical Composition Evolution

Organic elemental analysis (EA) was applied to HR-ToF-AMS SOA data collected during select experiments. Time series for O/C, H/C and OM/OC ratios for  $\alpha$ -pinene and *m*-xylene photooxidation are presented in Fig. 2.7. Values are not presented for aerosol mass loadings less than 2.0  $\mu\text{g m}^{-3}$  to reduce scatter at low mass loadings. Empirical formulas of  $\text{C}_1\text{H}_{1.50\pm 0.08}\text{O}_{0.40\pm 0.02}$  and  $\text{C}_1\text{H}_{1.46\pm 0.01}\text{O}_{0.25\pm 0.01}$  were observed for SOA derived from *m*-xylene and  $\alpha$ -pinene photooxidations. Chamber SOA from photooxidation of both compounds have intermediate O/C values (0.25-0.40), similar to results from observed Biomass Burning Organic Aerosol (BBOA) near the ground. The O/C ratios are also comparable to, but lower than the OOAI factors (0.52-0.64) and much lower than OOAI (0.83-1.02) that Aiken et al., (2008) identified through PMF analyses of AMS data from ambient organic aerosol in Mexico City. The results are consistent with the fact that the ratio of  $\text{C}_2\text{H}_3\text{O}^+$  (*m/z* 43) to  $\text{CO}_2^+$  (*m/z* 44) is typically observed to be larger for chamber SOA (Zhang et al., 2005) than ambient SOA. In other words, this suggests that the chamber SOA is less oxidized than both ambient OOAI and OOAI.

Somewhat surprisingly, the average O/C and  $\text{CO}_2^+/\text{OA}$  values increase very slowly during the course of the experiment indicating that further aging of the aerosol

under these environmental conditions are insufficient to achieve the O/C observed for OOAI and OOAI within the normal chamber experiment duration. O/C ratio is seen to marginally increase after aerosol formation is complete, consistent with increasing organic functionalization of the suspended aerosol inferred from the HTDMA and VTDMA measurements. It is noted that one additional functionalization of the SOA will not lead to significant increases in the overall O/C.

We probed for the existence of oligomeric species in the SOA products of the *m*-xylene photooxidation reaction system by flowing the SOA through a Dekati thermodenuder (set at 100°C) with a total residence time of 4 seconds prior to entering the HR-ToF AMS (Fig. 2.6). The average CO<sub>2</sub><sup>+</sup>/OA ratio without the thermodenuder increased from 8.2% to 9.0% and 10.3% when a thermal denuder operating at 50°C and 100°C was placed in front of the AMS. This result agrees with the fact that the more functionalized species are less volatile. When the thermal denuder was set to 150°C, the mass spectra of the thermally denuded aerosol dropped to background levels.

## 2.4 Conclusions

Simultaneous measurements of SOA volatility, hygroscopicity, density, and chemical composition were used to evaluate SOA aging within an environmental chamber. The measurements are consistent with SOA composition slightly increasing in functionalization over long periods of time. The aging was much stronger for photooxidation systems compared with the very stable  $\alpha$ -pinene dark ozonolysis system with hydroxyl scavenger. Even after 16 hours of aging, the O/C of the aerosol was lower than the AMS identified OOAI or OOAI fractions measured in Mexico City. The rate of

increase of O/C appears insufficient to obtain OOAI O/C even over a period of a couple of days. Little evidence was found for significant formation of high molecular weight SOA species. Further work, including multi-day simulations, may be necessary to produce SOA from aerosol precursors with sufficient O/C to match ambient observations within environmental chambers.

## 2.5 References

- Aiken, A. C., DeCarlo, P. F., Jimenez, J. L., 2007. Elemental analysis of organic species with electron ionization high-resolution mass spectrometry. *Analytical Chemistry* 79 (21), 8350–8358.
- Aiken, A.C., DeCarlo, P.F., Kroll, J.H., Worsnop, D.R., Huffman, J.A., Docherty, K., Ulbrich, I.M., Mohr, C., Kimmel, J.R., Sueper, D., Zhang, Q., Sun, Y., Trimborn, A., Northway, M., Ziemann, P.J., Canagaratna, M.R., Onasch, T.B., Alfarra, R., Prevot, A.S.H., Dommen, J., Duplissy, J., Metzger, A., Baltensperger, U., Jimenez, J.L., 2008. O/C and OM/OC Ratios of Primary, Secondary, and Ambient Organic Aerosols with High Resolution Time-of-Flight Aerosol Mass Spectrometry. *Environmental Science and Technology* 42, 4478-4485.
- An, W.J., Pathak, R.K., Lee, B.H., Pandis, S.N., 2007. Aerosol Volatility measurement using an improved thermodenuder: application to secondary organic aerosol. *Journal of Aerosol Science* 38, 305-314.
- Asad, A., Mmereki, B.T., Donaldson, D.J., 2004. Enhanced uptake of water by oxidatively processed oleic acid. *Atmospheric Chemistry and Physics* 4, 2083-2089.
- Bahreini, R., Keywood, M.D., Ng, N.L., Varutbangkul, V., Gao, S., et al. 2005. Measurements of secondary organic aerosol from oxidation of cycloalkenes, terpenes, and *m*-xylene using an aerodyne aerosol mass spectrometer. *Environment Science & Technology* 39, 5674-5688.
- Baltensperger, U., Kalberer, M., Dommen, J., Paulsen, D., Alfarra, M.R., Coe, H., Fisseha, R., Gascho, A., Gysel, M., Nyeki, S., et al., 2005. Secondary organic aerosols from anthropogenic and biogenic precursors. *Faraday Discussions* 130, 265–278.
- Broekhuizen, K.F., Thornberry, T., Kumar, P.P., Abbatt, J.P.D., 2004. Formation of cloud condensation nuclei by oxidative processing: unsaturated fatty acids. *Journal of Geophysical Research-Atmospheres* 109, doi:10.1029/2004JD005298.
- Carter, W.P.L., Cocker, D.R., Fitz, D.R., Malkina, I.L., Bumiller, K., Sauer, C.G., Pisano, J.T., Bufalino, C., Song, C., 2005. A new environmental chamber for evaluation of gas-phase chemical mechanisms and secondary aerosol formation. *Atmospheric Environment* 39, 7768-7788.
- Cocker, D. R., Clegg, S. L., Flagan, R. C., Seinfeld, J. H., 2001a. The effect of water on gas-particle partitioning of secondary organic aerosol. Part I: alpha-pinene/ozone system. *Atmospheric Environment* 35, 6049-6072.

- Cocker, D.R., Flagan, R.C., Seinfeld, J.H., 2001b. State-of-the-art facility for studying atmospheric aerosol chemistry. *Environmental Science and Technology* 35, 2594-2601.
- Davidson, C.I., Phalen, R.F., Solomon, P.A., 2005. Airborne Particulate Matter and Human Health: A Review. *Aerosol Science and Technology* 39, 737-749.
- DeCarlo, P.F., Kimmel, J.R., Trimborn, A., Northway, M.J., Jayne, J.T., Aiken, A.C., Gonin, M., Fuhrer, K., Horvath, T., Docherty, K., Worsnop, D.R., Jimenez, J.L., 2006. Field-Deployable, High-Resolution, Time-of-Flight Aerosol Mass Spectrometer. *Analytical Chemistry* 78, 8281-8289.
- Ehara, K., Hagwood, C., Coakley, K.J., 1996. Novel method to classify aerosol particles according to their mass-to-charge ratio-aerosol particle mass analyzer. *Journal of Aerosol Science* 27(2), 217-234.
- Eldering, A., Cass, G.R., 1996. Source-oriented model for air pollutant effects on visibility. *Journal of Geophysical Research-Atmospheres* 101, 19343-19369.
- Ellison, G.B., Tuck, A.F., Vaida, V., 1999. Atmospheric processing of organic aerosols. *Journal of Geophysical Research* 104, 11633-11641.
- Gao, S., Keywood, M., Ng, N.L., Surratt, J., Varutbangkul, V., Bahreini, R., Flagan, R.C., Seinfeld, J.H., 2004a. Lowmolecular-weight and oligomeric components in secondary organic aerosol from the ozonolysis of cycloalkenes and apinene. *Journal of Physical Chemistry A* 108, 10147-10164.
- Gao, S., Ng, N.L., Keywood, M., Varutbangkul, V., Bahreini, R., Nenes, A., He, J.W., Yoo, K.Y., Beauchamp, J.L., Hodyss, R.P., et al., 2004b. Particle phase acidity and oligomer formation in secondary organic aerosol. *Environmental Science and Technology* 38, 6582-6589.
- Gross, D.S., Galli, M.E., Kalberer, M., Prévôt, A.S.H., Dommen, J., Alfarra, M.R., Duplissy, J., Gaeggeler, K., Gascho, A., Metzger, A., et al., 2006. Real-time measurement of oligomeric species in secondary organic aerosol with the aerosol time-of-flight mass spectrometer. *Analytical Chemistry* 78, 2130-2137.
- Hearn, J.D., Lovett, A.J., Smith, G.D., 2005. Ozonolysis of oleic acid particles: evidence for a surface reaction and secondary reactions involving Criegee intermediates. *Physical Chemistry Chemical Physics* 7, 501-511.
- Iinuma, Y., Boge, O., Miao, Y., Sierau, B., Gnauk, T., Herrmann, H., 2005. Laboratory studies on secondary organic aerosol formation from terpenes. *Faraday Discussions* 130, 279-294.

Intergovernmental Panel on Climate Change (IPCC) Fourth Assessment Report: Climate Change 2007.

Jayne, J.T., Leard, D.C., Zhang, X., Davidovits, P., Smith, K.A., Kolb, C.E., Worsnop, D.R., 2000. Development of an Aerosol Mass Spectrometer for Size and Composition. *Analysis of Submicron Particles, Aerosol Science and Technology* 33, 49-70.

Jimenez, J.L., Jayne, J.T., Shi, Q., Kolb, C.E., Worsnop, D.R., Yourshaw, I., Seinfeld, J.H., Flagan, R.C., Zhang, X., Smith, K.A., Morris, J., Davidovits, P., 2003. Ambient Aerosol Sampling with an Aerosol Mass Spectrometer. *Journal of Geophysical Research - Atmospheres* 108(D7), 8425, doi:10.1029/2001JD001213.

Kalberer, M., Paulsen, D., Sax, M., Steinbacher, M., Dommen, J., Prévôt, A. S. H., Fisseha, R., Weingartner, E., Frankevich, V., Zenobi, R., Baltensperger, U., 2004. Identification of Polymers as Major Components of Atmospheric Organic Aerosols. *Science* 303, 1659-1662.

Kalberer, M., Sax, M., Samburova, V., 2006. Molecular size evolution of oligomers in organic aerosols collected in urban atmospheres and generated in a smog chamber. *Environmental Science and Technology* 40, 5917-5922.

Katrib, Y., Martin, S.T., Rudich, Y., Davidovits, P., Jayne, J.T., Worsnop, D.R., 2005. Density changes of aerosol particles as a result of chemical reaction. *Atmospheric Chemistry and Physics* 5, 275-291.

Kroll, J.H., Seinfeld, J.H., 2008. Chemistry of secondary organic aerosol: Formation and evolution of low-volatility organics in the atmosphere. *Atmospheric Environment* 42, 3593-3624.

Malloy, Q.G.J., Nakao, S., Qi, L., Austin, R., Stothers, C., Hagino, H., Cocker, D.R., 2009. *Aerosol Science and Technology* 43, 673-678.

Mmerekki, B.T., Donaldson, D.J., Gilman, J.B., Eliason, T.L., Vaida, V., 2004. Kinetics and products of the reaction of gas-phase ozone with anthracene adsorbed at the air-aqueous interface. *Atmospheric Environment* 38, 6091-6103.

Ng, N.L., Kroll, J.H., Keywood, M.D., Bahreini, R., Varutbangkul, V., Flagan, R.C., Seinfeld, J.H., Lee, A., Goldstein, A.H., 2006. Contribution of first- versus second-generation products to secondary organic aerosols formed in the oxidation of biogenic hydrocarbons. *Environmental Science and Technology* 40, 2283-2297.

- Philippin, S., Wiedensohler, A., Stratmann, F., 2004. Measurements of non-volatile fractions of pollution aerosols with an eight-tube volatility tandem differential mobility analyzer (VTDMA-8). *Journal of Aerosol Science* 35, 185-203.
- Pope, C.A., Dockery, D.W., 2006. Health effects of fine particulate air pollution: lines that connect, *Journal of the Air and Waste Management Association* 56, 709-742.
- Reynolds, J.C., Last, D.J., McGillen, M., Nijs, A., Horn, A.B., Percival, C., Carpernter, L.J., Lewis, A.C., 2006. Structural analysis of oligomeric molecules formed from the reaction products of oleic acid ozonolysis. *Environmental Science and Technology* 40, 6674-6681.
- Robinson, A.L., Donahue, N.M., Shrivastava, M.K., Weitkamp, E.A., Sage, A.M., Grieshop, A.P., Lane, T.E., Pierce, J.R., Pandis, S.N., 2007. *Science* 315, 1259-1262.
- Rudich, Y., 2003. Laboratory perspectives on the chemical transformations of organic matter in atmospheric particles. *Chemical Reviews* 103, 5097-5124.
- Rudich, Y., Donahue, N.M., Mentel, T.F., 2007. Aging of Organic Aerosol: Bridging the Gap between Laboratory and Field Studies. *The Annual Review of Physical Chemistry* 58, 321-352.
- Shilling, J.E., King, S.M., Mochida, M., Wornop, D.R., Martin, S.T., 2007. Mass Spectral evidence that small changes in composition caused by oxidative aging processes alter aerosol CCN properties. *The Journal of Physical Chemistry A* 111, 3358-3368.
- Song, C., Na, K.S., Cocker, D.R., 2005. Impact of the hydrocarbon to NO<sub>x</sub> ratio on secondary organic aerosol formation. *Environmental Science and Technology* 39, 3143-3149.
- Tolocka, M.P., Jang, M., Ginter, J.M., Cox, F.J., Kamens, R.M., Johnston, M.V., 2004. Formation of oligomers in secondary organic aerosol. *Environmental Science and Technology* 38, 1428-1434.
- Turpin, B.J., Huntzicker, J.J., 1995. Identification of secondary organic aerosol episodes and quantitation of primary and secondary organic aerosol concentrations during SCAQS. *Atmospheric Environment* 23, 3527-3544.
- Varutbangkul, V., Brechtel, F.J., Bahreini, R., Ng, N.L., Keywood, M.D., Kroll, J.H., Flagan, R.C., Seinfeld, J.H., Lee, A., Goldstein, A.H., 2006. Hygroscopicity of secondary organic aerosols formed by oxidation of cycloalkenes, monoterpenes,

- sesquiterpenes, and related compounds. *Atmospheric Chemistry and Physics* 6, 1121-1177.
- Virkkula, A., Van Dingenen, R., Raes, F., Hjorth, J., 1999. Hygroscopic properties of aerosol formed by oxidation of limonene,  $\alpha$ -pinene, and  $\beta$ -pinene. *Journal of Geophysical Research* 104, 3569-3579.
- Warren, B., Austin, R.L., Cocker, D.R., 2009. Temperature dependence of secondary organic aerosol. *Atmospheric Environment* 43, 3548-3555.
- Zhang, Q., Alfarra, M.R., Worsnop, D.R., Allan, J.D., Coe, H., Canagaratna, M.R., Jimenez, J.L., 2005. Deconvolution and quantification of hydrocarbon-like and oxygenated organic aerosols based on aerosol mass spectrometry. *Environment Science and Technology* 39, 4938-4952.
- Zhang, Q., Jimenez, J. L., Canagaratna, M. R., Allan, J. D., Coe, H., Ulbrich, I.M., Alfarra, M. R., Takami, A., Middlebrook, A.M., Sun, Y. L., Dzepina, K., Dunlea, E., Docherty, K., De-Carlo, P. F., Salcedo, D., Onasch, T., Jayne, J. T., Miyoshi, T., Shimojo, A., Hatakeyama, S., Takegawa, N., Kondo, Y., Schneider, J., Drewnick, F., Borrmann, S., Weimer, S., Demerjian, K., Williams, P., Bower, K., Bahreini, R., Cottrell, L., Griffin, R. J., Rautianinen, J., Sun, J. Y., Zhang, Y. M., Worsnop, D. R., 2007. Ubiquity and dominance of oxygenated species in organic aerosols in anthropogenically-influenced Northern Hemisphere midlatitudes, *Geophysical Research Letters* 34, L13801, doi:10.1029/2007GL029979.
- Ziemann, P.J., 2005. Aerosol products, mechanisms, and kinetics of heterogeneous reactions of ozone with oleic acid in pure and mixed particles. *Faraday Discussions* 130, 469-490.



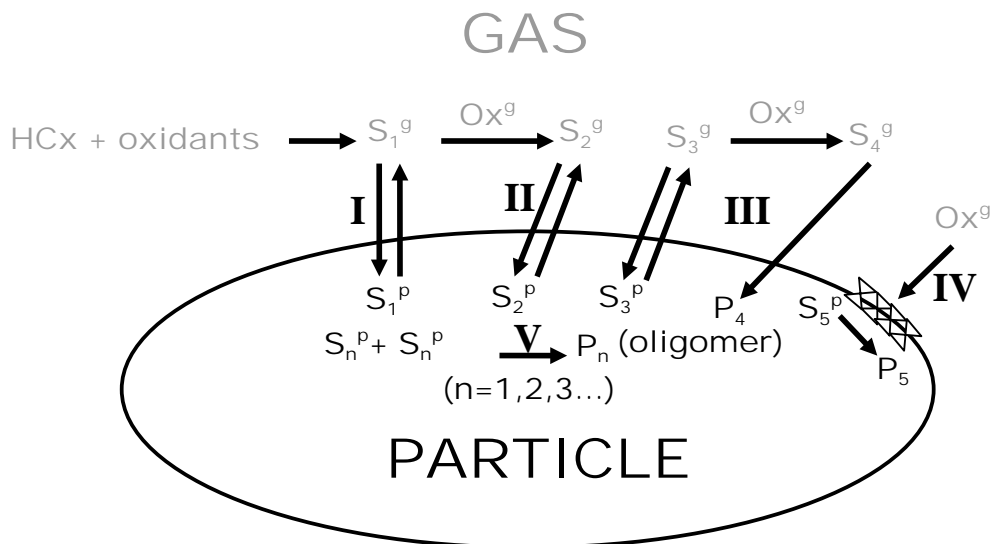


**Figure 2.1** Pathways of SOA formation and process, including gas-phase and particle-phase reactions. “S” stands for semi-volatile species in both phases; “P” for particle-phase low or nonvolatile species. Each reaction can possibly lead to changes in hygroscopicity, density, volatility, and oxygen content of aerosol.  $S_n$ ( $n=1,2,3\dots$ ) represents different products involved in the complex system. Note: The different numbers used at subscript just represent the different processes that could possibly occur in the system. They may be the same species.

run	compound	HC <sub>i</sub> <sup>a</sup>	M <sub>0</sub>	O <sub>3<i>i</i></sub>	NO <sub>x<i>i</i></sub>	CO <sub>i</sub>	Second	Experiment	RH	T
		(ppbV)	(μm <sup>3</sup> /cm <sup>3</sup> )	(ppbV)	(ppbV)	(ppmV)	oxidant/conc (ppbV)	Duration (mins)	(%)	(K)
898A	<i>m</i> -xylene	79.4	20.4	-	44.4	-	-	840	<0.5	300
904A	<i>α</i> -pinene <sup>b</sup>	50	71.9	309.1	-	73	-	252	<0.5	307
911A	<i>α</i> -pinene	100	246.0	316.2	-	104.7	-	978	<0.5	300
914A	<i>α</i> -pinene	100	398.6	342.4	-	-	NO/76.5	859	24.4	300
916A	<i>m</i> -xylene	162	36.5	-	19.7	-	-	858	<0.5	300
927A	<i>α</i> -pinene	100	144.1	-	19.3	-	-	577	<0.5	300
933A	<i>m</i> -xylene <sup>b</sup>	100	16.8	-	54.8	-	-	625	<0.5	300
934A	<i>m</i> -xylene	70b	9.0	-	43.6	-	-	699	<0.5	300
938A	<i>α</i> -pinene	100	278.9	329.3	-	104.3	-	431	<0.5	300
947A	<i>m</i> -xylene	108	21.2	-	16.3	-	-	859	<0.5	300
987A	<i>m</i> -xylene	500b	98.6	-	216.5	-	-	367	<0.5	300
1019A	<i>α</i> -pinene	100	127.1	-	18.0	-	-	526	<0.5	300
1020A	<i>m</i> -xylene	103	14.9	-	15.0	-	-	544	<0.5	300
1023A	<i>α</i> -pinene	100	-	305.4	-	79.1	-	510	<0.5	300

<sup>a</sup> i, initial conditions, <sup>b</sup> initial target concentration

**Table 2.1** Experimental conditions and results for the *α*-pinene and *m*-xylene oxidation systems

Note: the difference of PM formation for EPA898A and EPA934A is due to the latter experiment only running for 7 hours while the wall loss corrected PM volume is still increasing.

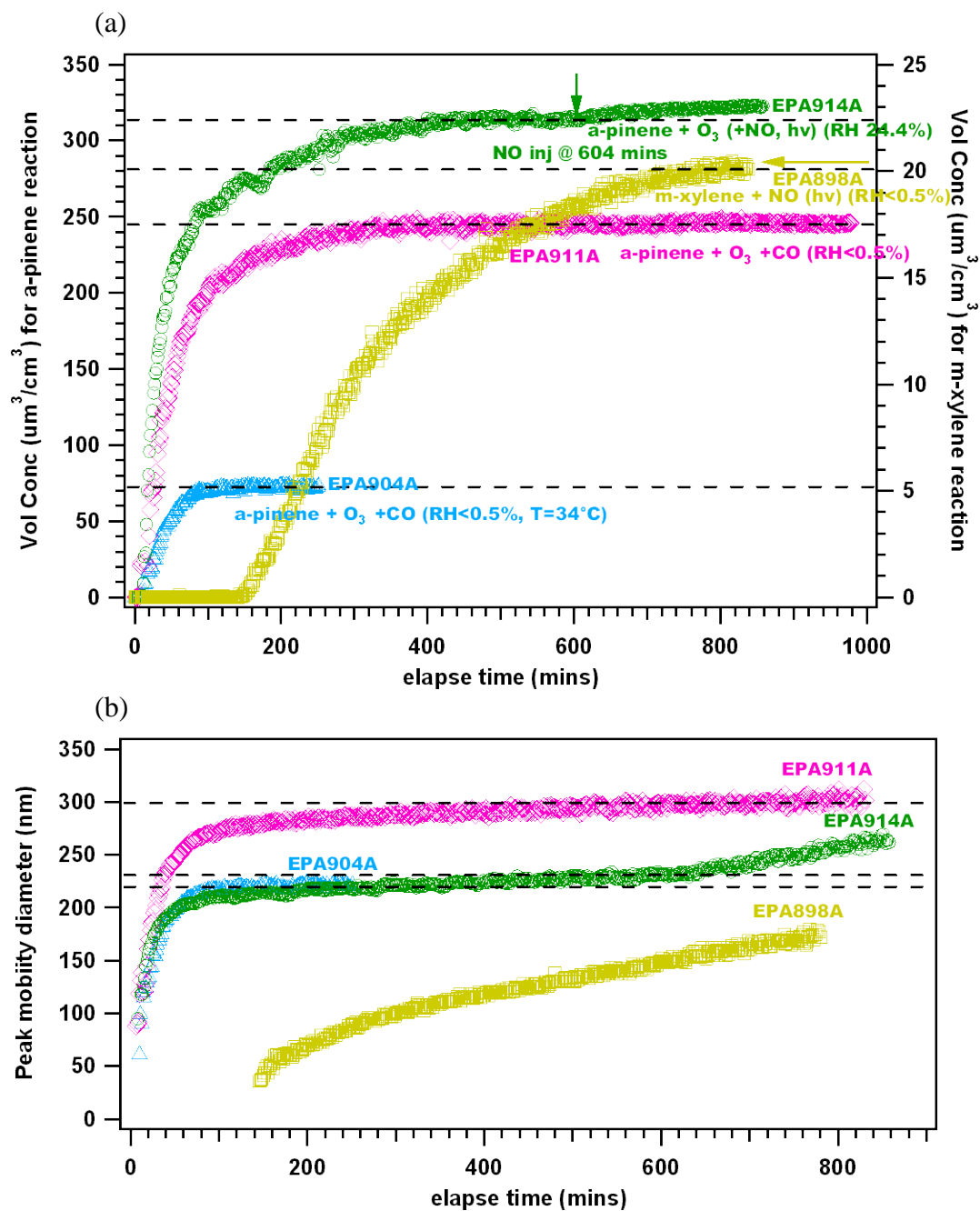


**Figure 2.2** Aerosol volume concentration (a) and peak mobility diameter evolution (b) for four experiments, one dry non-seeded ozonolysis, one humid non-seeded ozonolysis with later injection of NO, one dry non-seeded ozonolysis with initial condition ( $\alpha$ -pinene $\approx$ 50 ppb,  $\text{O}_3\approx$ 250-350 ppb, T=34C), and one dry photooxidation (*m*-xylene $\approx$ 79 ppb, NO $\approx$ 44 ppb). Dashed lines are shown to guide the eye.

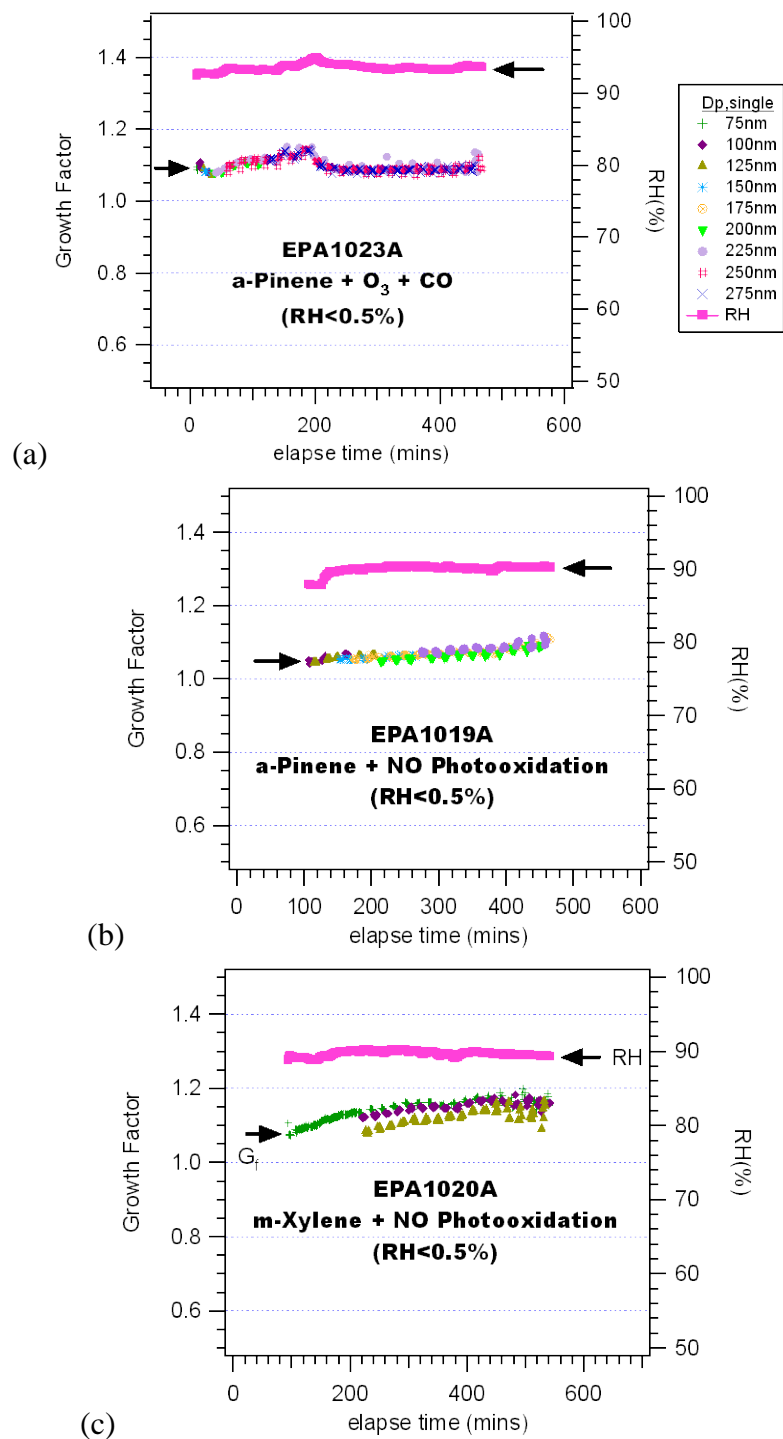


**Figure 2.3** The growth factor and the variations in RH in a typical operating scheme for (a)  $\alpha$ -pinene ozonolysis experiment, (b)  $\alpha$ -pinene photooxidation experiment and (c) *m*-xylene photooxidation experiment.

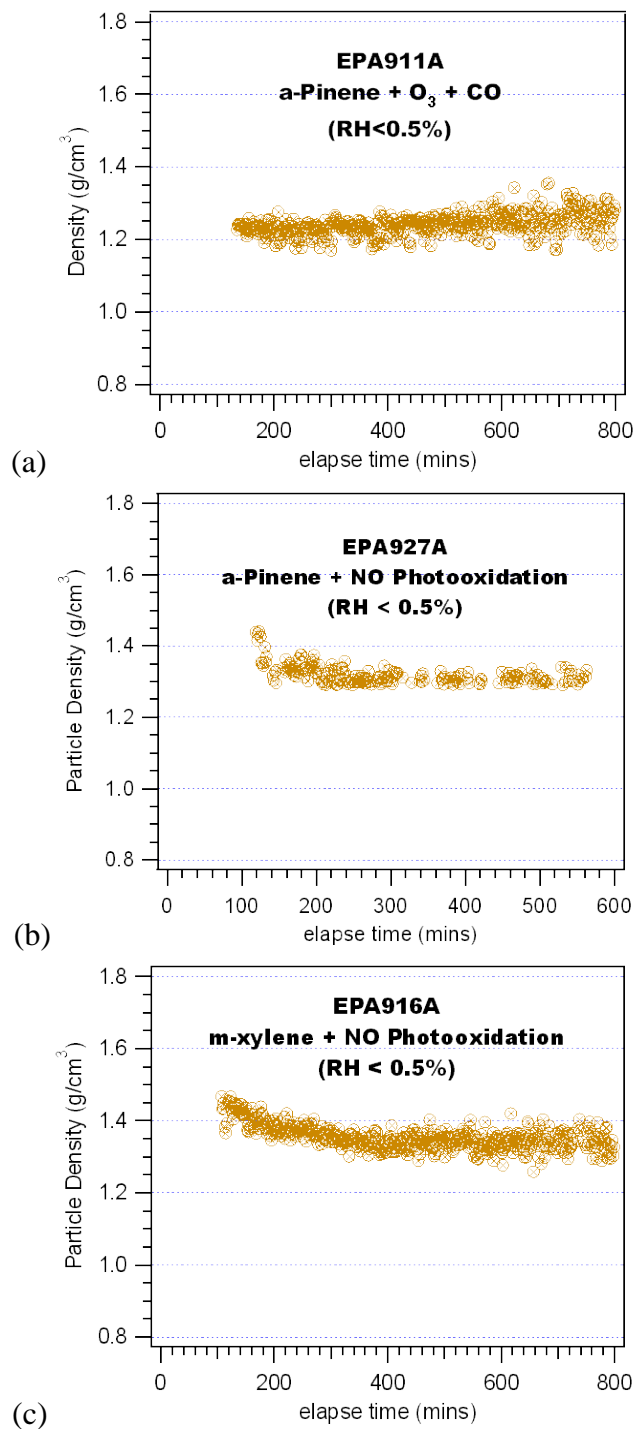


**Figure 2.4** The time evolution of particle density for three typical experiments: (a)  $\alpha$ -pinene ozonolysis with hydroxyl radical scavenger (b)  $\alpha$ -pinene photooxidation and (c) *m*-xylene photooxidation

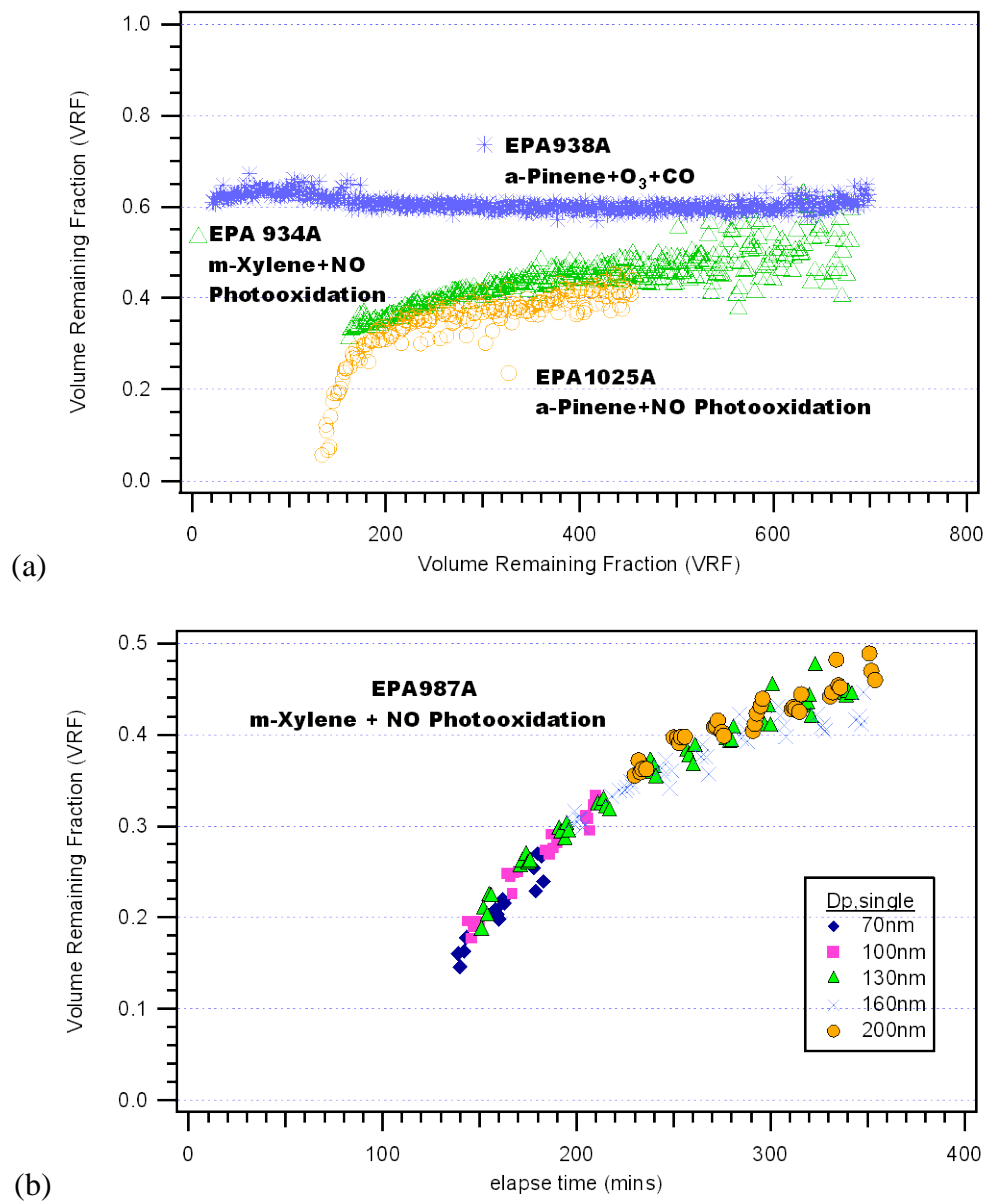


**Figure 2.5** The volume remaining fraction in typical operating schemes for: (a)  $\alpha$ -pinene ozonolysis experiment (dry),  $\alpha$ -pinene photooxidation experiment (dry) and *m*-xylene photooxidation experiment (dry) (b) an example of VRF variation on different selected single particle sizes.

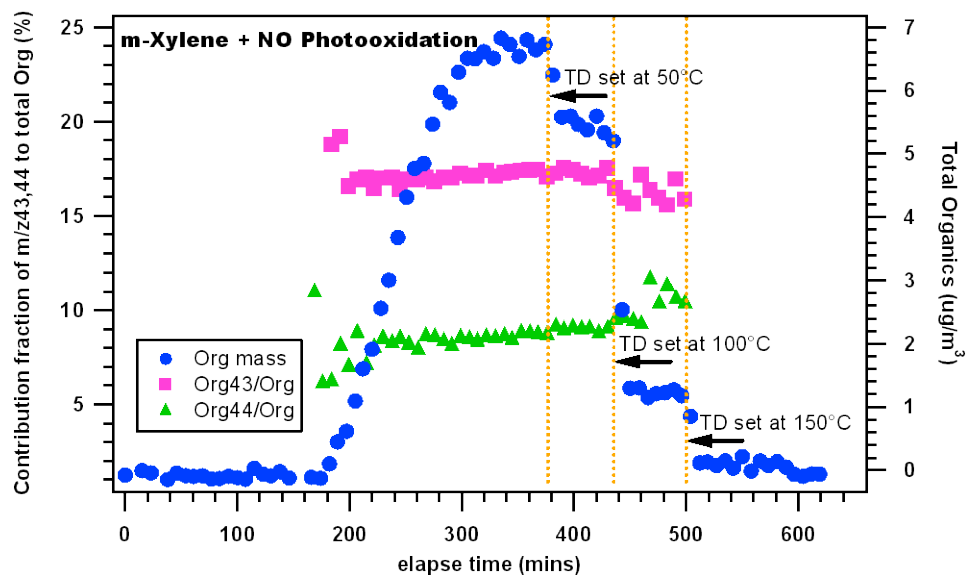


**Figure 2.6** The average ratio comparison for *m*-xylene photooxidation experiment (dry) without thermal denuder and with thermal denuder set at 50, 100 and 150°C

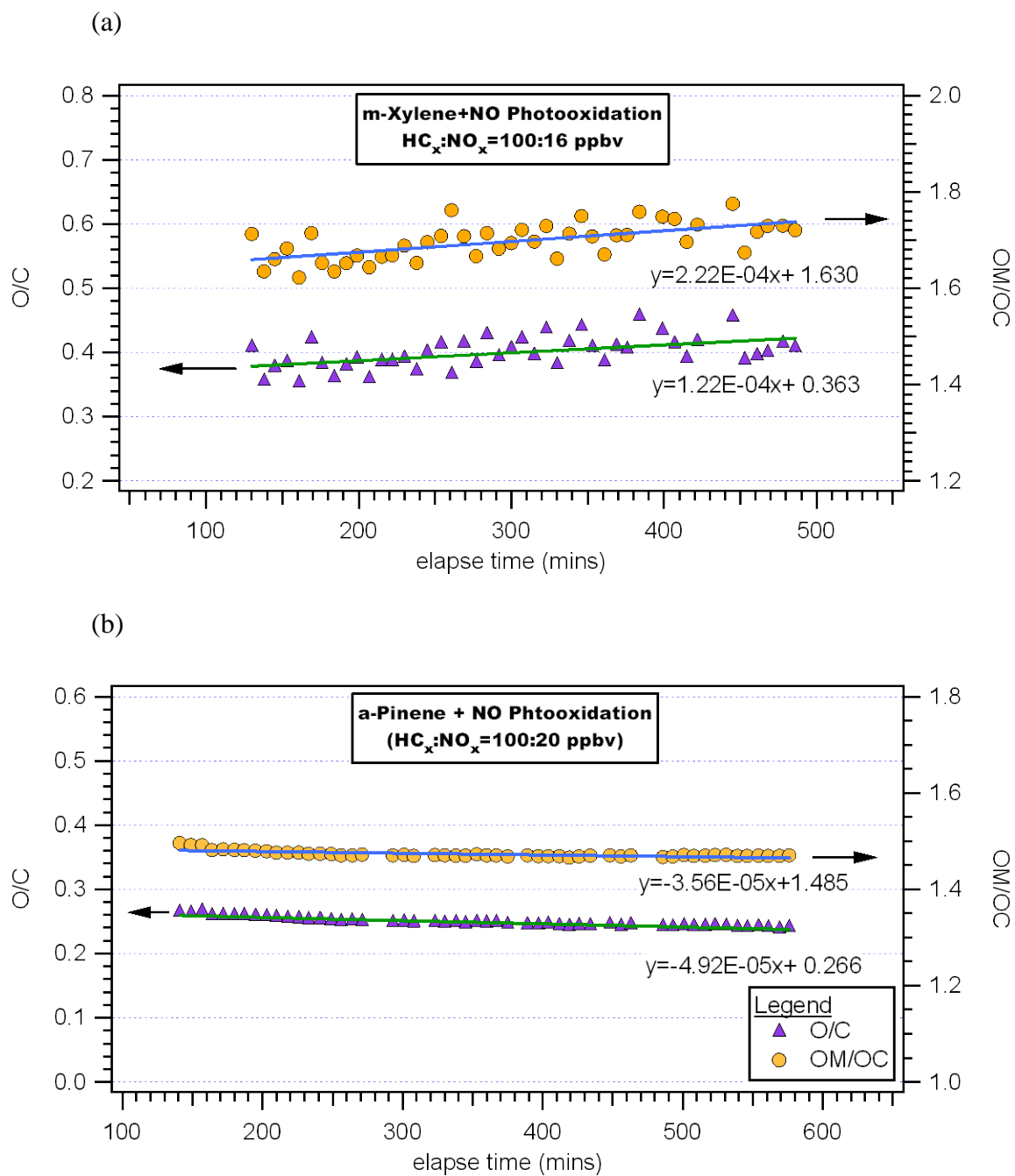


**Figure 2.7** Time series of average atomic O/C and OM/OC for experiments: (a) *m*-xylene photooxidation (dry) and (b)  $\alpha$ -pinene photooxidation (dry)



## Chapter 3

### 3.1 Introduction

Biogenic sources dominate the global emissions of volatile organic carbons (VOCs) in the atmosphere with estimated annual non-methane emissions of 491-1150 Tg carbon (Müller, 1992; Guenther et al., 1995). Approximately 11% of the biogenic VOCs are monoterpenes, for which the highest fraction is  $\alpha$ -pinene (25%) (Kanakidou et al., 2005). The ozonolysis of monoterpenes is reported to be one of the major contributors to secondary organic aerosol (SOA) (Griffin et al., 1999), with major SOA products of  $\alpha$ -pinene oxidation (e.g. pinoaldehyde, pinic and pinonic acids) observed in ambient aerosol (Yu et al., 1999; Cahill et al., 2006; Plewka et al., 2006). SOA is reported to account for a majority of organic aerosol in the atmosphere (Turpin, et al., 1995; Zhang et al., 2007) and contribute to climatic impacts, regional visibility reduction and potential health hazards (IPCC, 2007; Eldering and Cass, 1996; Davidson et al., 2005; Pope and Dockery, 2006).

Once formed, organic aerosol particles in the atmosphere may undergo further physical and chemical processing, thereby altering the physiochemical properties of aerosol, including hygroscopicity (Broekhuizen et al., 2004; Asad et al., 2004), density (Katrib et al., 2005; Bahreini et al., 2005), chemical composition (Mmereki et al., 2004), toxicity (Rudich et al., 2007), optical property (Rudich et al., 2007), and cloud condensation nuclei (CCN) activity (Shilling et al., 2007). Several pathways have been proposed for SOA aging processes: 1) heterogeneous reactive uptake of gas-phase

oxidants such as O<sub>3</sub>, OH and NO<sub>3</sub> by the condensed-phase molecules (Ellison et al., 1999); 2) further gas-phase oxidation of semi-volatile products that repartition between the gas and particle phase (Robinson et al., 2007); 3) organic semi-volatile monomers in the interior of SOA particles to form large molecular weight oligomeric compounds (Rudich, 2003; Ziemann, 2005); or 4) other heterogeneous processes leading to SOA formation (e.g., Kalberer et al., 2004, 2006; Tolocka et al., 2004; Baltensperger et al., 2005; Gao et al., 2004a,b; Gross et al., 2006).

Previous studies from our group demonstrate that there is only slight aging of SOA derived from  $\alpha$ -pinene and *m*-xylene photooxidation for up to the first 16 hours of irradiation. Chemical aging was not observed for SOA from dark  $\alpha$ -pinene ozonolysis with hydroxyl radical scavenger present (Qi et al., 2010). Therefore, the presence of trace amounts of oxidative radicals in the photooxidation systems is suspected to play an important role in chemical aging of SOA. The oxidative radicals may influence the aging processes via one or more of the four pathways described above during SOA formation.

Therefore, this chapter examines whether further functionalization of SOA from  $\alpha$ -pinene dark ozonolysis is enhanced by introduction of NO, H<sub>2</sub>O<sub>2</sub> or N<sub>2</sub>O<sub>5</sub> followed by photolysis. Typical experiments commence with  $\alpha$ -pinene dark ozonolysis with additional injections of NO/H<sub>2</sub>O<sub>2</sub>/N<sub>2</sub>O<sub>5</sub> and UV irradiation occurring only after SOA formation ceases. Chemical aging processes are discussed with respect to the changes in particle hygroscopicity and density as well as C:O:H ratios estimated from high resolution aerosol mass spectrometry.

## **3.2 Experimental Section**

### **3.2.1 Facility Overview**

Experiments are conducted in the UC Riverside/CE-CERT indoor environmental chamber, which is described in detail elsewhere (Carter et al., 2005). Dual 90m<sup>3</sup> Teflon reactors are suspended by a rigid steel framework in a temperature-controlled enclosure which is continuously flushed with purified air. The rigid framework slowly collapses the reactors during the experiments to minimize leaks and diffusion of contaminants into the reactors by maintaining a positive 0.03” H<sub>2</sub>O differential pressure between the reactors and enclosure. All experiments are conducted under dark conditions initially. Eighty 115 W Sylvania 350 black lights are used as light sources for irradiation with additional oxidant injections. A known volume of high purity liquid hydrocarbon precursor ( $\alpha$ -pinene: Sigma-Aldrich,  $\geq 99.0\%$ ) and 50 % wt hydrogen peroxide are injected through a heated glass injection manifold system and flushed into the chamber with pure N<sub>2</sub>. NO is introduced by flushing pure N<sub>2</sub> through a calibrated glass bulb filled to a predetermined partial pressure of pure NO. Lab synthesized nitrate radical is generated from N<sub>2</sub>O<sub>5</sub>, which was injected from a calibrated glass bulb filled to a predetermined partial pressure. The N<sub>2</sub>O<sub>5</sub> is heated and injected similar to NO. Ozone is injected using two Dalton ozone generators (Model Type: OZG-UV-01).

### **3.2.2 Particle and Gas Measurements**

Particle size distributions between 28 and 700 nm was monitored with scanning mobility particle sizers (SMPS) located inside the temperature controlled enclosure.

Particle sizing is validated with a suite of polystyrene latex spheres (PSL) (Duke Scientific Corp., Palo Alto, CA).

Real-time particle density is measured using an Aerosol Particle Mass Analyzer (APM) (Kanomax model 3600) in series with an SMPS. A custom Labview program determines mode diameter peak from a parallel SMPS and then actively configures the APM-SMPS to optimize instrument response. Density is acquired approximately every 75 s. Details of the instruments and theory are described elsewhere (Malloy et al., 2009; Ehara et al., 1996).

SOA hygroscopicity is continuously monitored with a custom-built Hygroscopic Tandem Differential Mobility Analyzer (HTDMA). The instrument follows the original design of Radar and McMurry with a configuration similar to that illustrated in Cocker et al. (2001). The particle diameter transmitted through the first SMPS was selected to match the peak size distribution measured by a parallel SMPS. Hygroscopic growth factor ( $G_f$ ) is reported as the ratio of the modal diameter of humidified aerosol (80.0%~85.0%±1.0%),  $D_{p,humidified}$ , to that of classified aerosol,  $D_{p,dry}$ ; i.e.,  $G_f = D_{p,humidified} / D_{p,dry}$ .  $D_{p,humidified}$  and  $D_{p,dry}$  are obtained from log-normal distributions fit to the TDMA size distribution output. The humidification system residence time is approximately 1 minute. HTDMA measurements are validated against lab-generated dry ammonium sulfate salt. The  $G_f$  is found to agree within 1.0% of theoretically calculated result using the Köhler model (Brechtel and Kreidenweis, 2000).

The evolution of particle elemental composition is tracked using an Aerodyne High Resolution Time-of-Flight Aerosol Mass Spectrometry (HR-ToF-AMS) operating

in the high resolution mode (deCarlo et al., 2006). The HR-ToF-AMS has been described in detail previously (deCarlo et al., 2006) and improves on mass resolution by using a custom high-resolution ToFMS (Tofwerk, Switzerland). More recently, a new elemental analysis (EA) technique was developed using HR-ToF-AMS sampling data (Aiken et al., 2007; 2008). The method is based on the property of electron ionization (EI) for molecules containing small atoms such as C, H, N, O and S that the sum of the ion signal intensities from all fragments is approximately proportional to the mass concentration of the original organic species. Thus, if the elemental composition of each fragment ion signal in a mass spectrum can be identified (as with HR mass spectra), the average composition of the ions can be calculated. For a complex spectrum from an unknown molecule or mixture, the best estimate of the composition can then be found by summing up the ion contributions across the entire mass spectrum, which is then represented as estimated ratios of oxygen-to-carbon (O/C), hydrogen-to-carbon (H/C), and nitrogen-to-carbon (N/C). Estimated atomic ratios are used to calculate Organic Matter (OM)/Organic Carbon (OC). In this study, the C:O:H ratio of the total aerosol was determined using the high resolution capabilities of the HR-ToF-AMS following the Peak Integration by Key Analysis (PIKA) and Analytical Procedure for Elemental Separation (APES) templates (DeCarlo et al., 2006, Aiken et al., 2008).

Decay of the parent hydrocarbon species was monitored with gas chromatography equipped with a flame ionization detector (GC-FID, Agilent 6890, Palo Alto, CA). A Thermal Environmental Instruments Model 42C was used to measure NO, NO<sub>y</sub> and (NO<sub>y</sub>

– NO) concentration. O<sub>3</sub> was monitored with a Dasibi Environmental Corp. Model 1003-AH O<sub>3</sub> analyzer.

### **3.2.3 Experiment Methodology**

A series of dark  $\alpha$ -pinene ozone reactions (Table 3.1) were conducted to evaluate the chemical aging of SOA. The experiments commenced by reaction of  $\alpha$ -pinene with ozone in identical, parallel reactors. After initial aerosol formation was complete, NO, H<sub>2</sub>O<sub>2</sub> or NO<sub>3</sub> was introduced to one reactor followed by UV irradiation of both reactors. Thus, changes in particle physical and chemical properties due to a second injection could be separated from photolysis effects. All experiments were conducted under dry conditions (RH<0.5%) condition in the absence of inorganic seed aerosol. All experiments were conducted until the volume of the reactor was exhausted.

## **3.3 Results**

### **3.3.1 $\alpha$ -Pinene Reaction with Ozone**

A series of  $\alpha$ -pinene/ozone experiments with and without hydroxyl radical scavenger were conducted to serve as a reference for work reported later. A plot of the wall-loss-corrected aerosol volume and aerosol electrical mobility diameter versus time for these experiments is displayed in Fig. 3.1. The final amount of aerosol formation from  $\alpha$ -pinene dark ozonolysis with CO remains constant around 414  $\mu\text{m}^3 \text{cm}^{-3}$  up to nine hours after the completion of the initial aerosol growth, which is not shown in the figure due to the difference in experiment duration from the other one. Without CO, the final

volume concentration arrives at  $415 \mu\text{m}^3 \text{cm}^{-3}$  ten hours after ozone was injected. The final electrical mobility diameters for the experiments with and without CO are 295 nm and 236 nm, respectively. On basis of aerosol volume production, the hydroxyl radical contribute one third of SOA formation according to SAPRC model estimation, i.e. two thirds of SOA volume concentration are attributable to ozone oxidation, and one third comes from hydroxyl radical reaction.

Measurement of SOA hydrophilicity provides indirect information about its chemical composition. Real-time hygroscopic  $G_f$  for  $\alpha$ -pinene ozonolysis (with and without hydroxyl radical scavenger) is presented in Fig. 3.2. The  $G_f$  of the aerosol remains constant ( $\sim 1.09$ ) at RH  $93.6\% \pm 0.4\%$  for the dry  $\alpha$ -pinene ozonolysis reaction (*with* CO) throughout the course of the experiment. However, the  $G_f$  continuously increases from 1.03 to 1.05 during ten hours of ozonolysis (*without* CO) at RH  $83.0\% \pm 0.5\%$  (differences in average  $G_f$  between the two experiments is easily attributed to differences in HTDMA RH). Increasing particle hydrophilicity is attributed to the presence of OH radical through either heterogeneous reactions or further gas-phase oxidation of semi-volatile products. It is noted that decreasing hydrophilicity would be observed through formation of large molecular weight oligomeric molecules.

### **3.3.2 $\alpha$ -Pinene Reaction with Ozone + Additional Reactants**

Based on the results from reference reactions of  $\alpha$ -pinene dark ozonolysis described in the previous section, the  $\cdot\text{OH}$  plays an important role in aerosol aging. Therefore, additional reactants were injected after the parent hydrocarbon was completely consumed and the wall-loss corrected volume concentration of the initial SOA production

from  $\alpha$ -pinene/ozone reactions plateaued. As a result, the  $\cdot\text{OH}$  or  $\cdot\text{NO}_3$  concentration was boosted to investigate the aging process of semi-volatile products present via gas-phase, surface or particle-phase reactions. For additional injection of NO only, black lights were turned on before the injection. In other cases, black lights were switched on after the additional reactants were injected. Additional reactants were only introduced into one side (referred as Side A) of the parallel reactors. The other side (referred as Side B) was used as a control for the effects of UV irradiation. Fig. 3.3 shows a representative temperature profile in Side B under dark and UV irradiation conditions. The temperature was maintained stable at  $297.6\pm 0.4$  K, preventing possible temperature influences on SOA volume concentration from the heat generated when the black lights were operated. A plot of the wall-loss corrected aerosol volume versus time for select experiments is displayed in Fig. 3.4.

Additional  $\text{H}_2\text{O}_2$  injection to  $\alpha$ -pinene/ozone (*without CO*) with UV irradiation yielded an increase of wall loss corrected volume of 6.7%. Additional NO injection with UV irradiation led to a volume increase of only 1.0%. The average volume increase for the NO control (UV lights only) led to an increase of 5.3%. These results indicate that UV irradiation alone can contribute to additional SOA formation from the  $\alpha$ -pinene dark (*with CO*) ozonolysis system. In the actinic region of UV lights, this reactive pathway is available to certain oxygenated organics, such as carbonyls, peroxides, and nitrates). Complex photochemical transformations are possible during the photolytic processes (Paulson et al., 2006), which may lead to the addition of functional groups. Finally,  $\cdot\text{OH}$  originating from the photolysis of nitrous acid (HONO) released from the Teflon film



(Carter et al., 2005) may contribute to the increase in volume. The reduced increase in aerosol electrical mobility diameter with additional NO injection in side A as referenced to side B is likely due to reaction of NO<sub>2</sub> with ·OH radical in the system generated by the dark reaction of O<sub>3</sub> with α-pinene resulting in a loss process of ·OH radical. Additional injection of NO<sub>3</sub> radical increased the wall loss corrected volume concentration by 5.9% before the black lights were turned on and continued growing with the lights on.

The evolution of aerosol hygroscopic G<sub>f</sub> with the additional reactant injection for α-pinene ozonolysis (without hydroxyl radical scavenger) is presented in Fig. 3.5. A transition in G<sub>f</sub> was observed after H<sub>2</sub>O<sub>2</sub> was injected and the black lights were turned on. The G<sub>f</sub> steadily increases from 1.04 to 1.11 at RH 82.6±0.5% by the end of the experiment, indicating an increase in the functionalization of the bulk SOA by hydroxyl radical. Combined with changes in volume concentration and size diameter for this system, it is speculated that the ·OH radical attacks the gas-phase product from the initial reaction of α-pinene/ozone producing more functionalized secondary product(s) that partition into the condensed phase. Similar trends were observed in the additional NO injection system with G<sub>f</sub> increasing from 1.03 to 1.09 (RH=81.7±0.6%). However, the G<sub>f</sub> remains constant (~1.04) at RH 79.9±0.6% with the additional injection of nitrate radical (Fig. 3.5c) even though the volume concentration shows an observable increase. This could be explained by the partitioning of new condensable species via gas-phase chemistry into the particle that are comparable in hygroscopic property as that of the products from α-pinene ozonolysis. As expected, an increasing G<sub>f</sub> was observed, similar to that observed for additional injection of NO, after the black lights were turned on.

Real time aerosol effective density for  $\alpha$ -pinene ozonolysis with additional injection of  $\text{H}_2\text{O}_2$  and  $\text{NO}$  is displayed in Fig. 3.6. Effective density remains constant ( $1.28 \text{ g/cm}^3$ ) for the dry  $\alpha$ -pinene ozonolysis reaction (*without*  $\text{CO}$ ) before the injection of a second reactant. A slight increase in SOA density is observed after the second reactant was introduced into the reactor with black lights on with the exception of nitrate radical additional injection. For the additional injection of nitrate radical, no change in particle density is observed.

Organic elemental analysis (EA) was applied to HR-ToF-AMS SOA data collected during select experiments. Time series of O/C ratio for  $\alpha$ -pinene ozonolysis with additional reactant injection are presented in Fig. 3.7. Values are not presented for aerosol mass loadings less than  $2.0 \mu\text{g m}^{-3}$  to reduce scatter due to noise at low mass loadings. An empirical formula of  $\text{C}_1\text{H}_{1.446\pm 0.010}\text{O}_{0.323\pm 0.008}$  was derived for SOA from  $\alpha$ -pinene ozonolysis without additional injection of reactants. After the compound injected, there is a measurable increase in O/C ratio (5.5%, 5.1% and 8.4% for  $\text{NO}$ ,  $\text{H}_2\text{O}_2$  and  $\text{N}_2\text{O}_5$ , respectively) compared to the ratio of control experiment within the same time duration in all three cases. This observation is consistent with the increasing organic functionalization of the suspended aerosol inferred from the HTDMA measurement except for nitrate radical.

### 3.4 Discussion

The ozone reaction with  $\alpha$ -pinene follows the “Criegee intermediate mechanism” of alkene ozonolysis (Atkinson and Arey, 2003). The initial step proceeds through

cycloaddition of O<sub>3</sub> to the –C=C– bond, forming a primary ozonide. The excited primary ozonide subsequently undergoes isomerization to yield chemically activated carbonyl oxides or Criegee intermediates. A large fraction of the carbonyl oxides are subject to prompt unimolecular reactions and collisional stabilization, leading to formation of ·OH, carbonyls, CO<sub>2</sub> and a variety of other products. Stabilized CIs may also undergo bimolecular reactions. Figure 3.8 illustrates the mechanistic diagram for the reactions of O<sub>3</sub> with α-pinene.

With the additional injection of H<sub>2</sub>O<sub>2</sub>, which is essentially NO<sub>x</sub>-free condition, some products are subsequently subject to further reactions forming more oxygenated compounds, e.g. pinonaldehyde. The possible reaction is displayed in Fig. 3.9.

With the additional injection of N<sub>2</sub>O<sub>5</sub> under dark condition, organic nitrate can be formed via heterogeneous reaction (Docherty and Ziemann, 2006) or RO<sub>2</sub> present will react with NO<sub>2</sub>, forming peroxyxynitrate via reaction (3-1) which increase the oxygen-content level, i.e. O/C ratio of the bulk SOA.



The time-series trace of m/z 30 including NO<sup>+</sup> (major fragment of nitrate containing compound) and CH<sub>2</sub>O<sup>+</sup> ions is plotted in Fig. 3.10. The NO<sup>+</sup> signal intensity increases as soon as the nitrate radical was injected, confirming the formation of organic nitrate. Both reactions can be occurring in terms of competitive RO<sub>2</sub> chemistry in the additional injection of NO reaction.

### 3.5 Conclusions

Previous studies demonstrate that hydroxyl radical plays a central role in the age process of chamber SOA (Qi et al., 2010). In this chapter, simultaneous measurements of SOA hygroscopicity, density, and chemical composition were made to evaluate the enhancement of SOA functionalization by the additional injection of NO, H<sub>2</sub>O<sub>2</sub>, and N<sub>2</sub>O<sub>5</sub> within an environmental chamber. Stable  $\alpha$ -pinene dark ozonolysis without hydroxyl radical scavenger was chosen as the studied system for convenience. We conclude that further aging of  $\alpha$ -pinene dark ozonolysis system via oxidation of first generation products is possible; distinct increases in hydrophilicity and oxygen content level are observed. In general, the condensable species formed from continuing oxidation are more hydrophilic and oxygenated. UV irradiation alone also has some effect on this specific system, which is likely due to the reaction of photosensitive carbonyls, peroxides, and nitrates along with OH derived from HONO emitted from the Teflon surface.

### 3.6 References

- Aiken, A. C., DeCarlo, P. F., Jimenez, J. L., 2007. Elemental analysis of organic species with electron ionization high-resolution mass spectrometry. *Analytical Chemistry* 79 (21), 8350–8358.
- Aiken, A.C., DeCarlo, P.F., Kroll, J.H., Worsnop, D.R., Huffman, J.A., Docherty, K., Ulbrich, I.M., Mohr, C., Kimmel, J.R., Sueper, D., Zhang, Q., Sun, Y., Trimborn, A., Northway, M., Ziemann, P.J., Canagaratna, M.R., Onasch, T.B., Alfarra, R., Prevot, A.S.H., Dommen, J., Duplissy, J., Metzger, A., Baltensperger, U., Jimenez, J.L., 2008. O/C and OM/OC Ratios of Primary, Secondary, and Ambient Organic Aerosols with High Resolution Time-of-Flight Aerosol Mass Spectrometry. *Environmental Science and Technology* 42, 4478-4485.
- Asad, A., Mmereki, B.T., Donaldson, D.J., 2004. Enhanced uptake of water by oxidatively processed oleic acid. *Atmos. Chem. and Phys.*, 4, 2083-2089.
- Atkinson, R., Arey, J., 2003. Atmospheric degradation of volatile organic compounds. *Chemistry Review* 103, 4605-4638.
- Bahreini, R., Keywood, M.D., Ng, N.L., Varutbangkul, V., Gao, S., et al., 2005. Measurements of secondary organic aerosol from oxidation of cycloalkenes, terpenes, and *m*-xylene using an aerodyne aerosol mass spectrometer. *Environ. Sci. & Technol.*, 39, 5674-5688.
- Baltensperger, U., Kalberer, M., Dommen, J., Paulsen, D., Alfarra, M.R., Coe, H., Fisseha, R., Gascho, A., Gysel, M., Nyeki, S., et al., 2005. Secondary organic aerosols from anthropogenic and biogenic precursors. *Faraday Discussions* 130, 265–278.
- Brechtel, F.J., and Kreidenweis, S.M., 2000. Predicting particle critical supersaturation from hygroscopic growth measurements in the humidified TDMA, Part I: Theory and sensitivity studies, *Journal of the Atmospheric Sciences*, 57, 1854–1871.
- Broekhuizen, K.F., Thornberry, T., Kumar, P.P., Abbatt, J.P.D., 2004. Formation of cloud condensation nuclei by oxidative processing: unsaturated fatty acids. *Journal of Geophysical Research-Atmospheres* 109, doi:10.1029/2004JD005298.
- Cahill, T. M., Seaman, V. Y., Charles, M. J., Holzinger, R., and Goldstein, A. H., 2006. Secondary organic aerosols formed from oxidation of biogenic volatile organic compounds in the Sierra Nevada Mountains of California, *J. Geophys. Res.-Atmos.*, 111, D16312, doi:16310.11029/12006JD007178.

- Carter, W.P.L., Cocker, D.R., Fitz, D.R., Malkina, I.L., Bumiller, K., Sauer, C.G., Pisano, J.T., Bufalino, C., Song, C., 2005. A new environmental chamber for evaluation of gas-phase chemical mechanisms and secondary aerosol formation. *Atmospheric Environment* 39, 7768-7788.
- Cocker, D.R., Flagan, R.C., Seinfeld, J.H., 2001. State-of-the-art facility for studying atmospheric aerosol chemistry. *Environmental Science and Technology* 35, 2594-2601.
- Davidson, C.I., Phalen, R.F., Solomon, P.A., 2005. Airborne Particulate Matter and Human Health: A Review. *Aerosol Sci. and Technol.*, 39, 737-749.
- DeCarlo, P.F., Kimmel, J.R., Trimborn, A., Northway, M.J., Jayne, J.T., Aiken, A.C., Gonin, M., Fuhrer, K., Horvath, T., Docherty, K., Worsnop, D.R., Jimenez, J.L., 2006. Field-Deployable, High-Resolution, Time-of-Flight Aerosol Mass Spectrometer. *Analytical Chemistry* 78, 8281-8289.
- Ehara, K., Hagwood, C., Coakley, K.J., 1996. Novel method to classify aerosol particles according to their mass-to-charge ratio-aerosol particle mass analyzer. *Journal of Aerosol Science* 27(2), 217-234.
- Eldering, A., Cass, G.R., 1996. Source-oriented model for air pollutant effects on visibility. *J. Geophys. Res.-Atmos.*, 101, 19343-19369.
- Ellison, G.B., Tuck, A.F., Vaida, V., 1999. Atmospheric processing of organic aerosols. *Journal of Geophysical Research* 104, 11633-11641.
- Gao, S., Keywood, M., Ng, N.L., Surratt, J., Varutbangkul, V., Bahreini, R., Flagan, R.C., Seinfeld, J.H., 2004a. Low molecular-weight and oligomeric components in secondary organic aerosol from the ozonolysis of cycloalkenes and apinene. *Journal of Physical Chemistry A* 108, 10147-10164.
- Gao, S., Ng, N.L., Keywood, M., Varutbangkul, V., Bahreini, R., Nenes, A., He, J.W., Yoo, K.Y., Beauchamp, J.L., Hodyss, R.P., et al., 2004b. Particle phase acidity and oligomer formation in secondary organic aerosol. *Environmental Science and Technology* 38, 6582-6589.
- Griffin, R. J., Cocker, D. R., Seinfeld, J. H., and Dabdub, D., 1999. Estimate of global atmospheric organic aerosol from oxidation of biogenic hydrocarbons, *Geophys. Res. Lett.*, 26, 2721–2724.
- Gross, D.S., Galli, M.E., Kalberer, M., Prévôt, A.S.H., Dommen, J., Alfarra, M.R., Duplissy, J., Gaeggeler, K., Gascho, A., Metzger, A., et al., 2006. Real-time

- measurement of oligomeric species in secondary organic aerosol with the aerosol time-of-flight mass spectrometer. *Analytical Chemistry* 78, 2130-2137.
- Guenther, A., Hewitt, C. N., Erickson, D., Fall, R., Geron, C., Graedel, T., Harley, P., Klinger, L., Lerdau, M., McKay, W. A., Pierce, T., Scholes, B., Steinbrecher, R., Tallamraju, R., Taylor, J., and Zimmerman, P., 1995. A Global-Model of Natural Volatile Organic-Compound Emissions, *J. Geophys. Res.-Atmos.*, 100, 8873–8892.
- Intergovernmental Panel on Climate Change (IPCC) Fourth Assessment Report: Climate Change 2007.
- Kalberer, M., Sax, M., Samburova, V., 2006. Molecular size evolution of oligomers in organic aerosols collected in urban atmospheres and generated in a smog chamber. *Environmental Science and Technology* 40, 5917-5922.
- Kanakidou, M., Seinfeld, J. H., Pandis, S. N., Barnes, I., Dentener, F. J., Facchini, M. C., Van Dingenen, R., Ervens, B., Nenes, A., Nielsen, C. J., Swietlicki, E., Putaud, J. P., Balkanski, Y., Fuzzi, S., Horth, J., Moortgat, G. K., Winterhalter, R., Myhre, C. E. L., Tsigaridis, K., Vignati, E., Stephanou, E. G., and Wilson, J., 2005. Organic aerosol and global climate modelling: a review, *Atmos. Chem. Phys.*, 5, 1053–1123.
- Katrib, Y., Martin, S.T., Rudich, Y., Davidovits, P., Jayne, J.T., Worsnop, D.R., 2005. Density changes of aerosol particles as a result of chemical reaction. *Atmos. Chem. and Phys.*, 5, 275-291.
- Malloy, Q.G.J., Nakao, S., Qi, L., Austin, R., Stothers, C., Hagino, H., Cocker, D.R., 2009. *Aerosol Science and Technology* 43, 673-678.
- Mmereki, B.T., Donaldson, D.J., Gilman, J.B., Eliason, T.L., Vaida, V., 2004. Kinetics and products of the reaction of gas-phase ozone with anthracene adsorbed at the air-aqueous interface. *Atmos. Environ.*, 38, 6091-6103.
- Müller, J. F., 1992. Geographical-Distribution and Seasonal-Variation of Surface Emissions and Deposition Velocities of Atmospheric Trace Gases, *J. Geophys. Res.-Atmos.*, 97, 3787–3804.
- Paulson, S.E., Liu, D.L., Orzechowska, G.E., Campos, L.M., Houk, K.N., 2006. Photolysis of heptanal. *Journal of Organic Chemistry* 71, 6403-6408.
- Plewka, A., Gnauk, T., Brüggemann, E., and Herrmann, H., 2006. Biogenic contributions to the chemical composition of airborne particles in a coniferous forest in Germany, *Atmos. Environ.*, 40, S103–S115.

- Qi, L., Nakao, S., Malloy, Q., Warren, B., Cocker, D., 2010. Can secondary organic aerosol formed in an atmospheric simulation chamber continuously age? *Atmospheric Environment*, in press.
- Robinson, A.L., Donahue, N.M., Shrivastava, M.K., Weitkamp, E.A., Sage, A.M., Grieshop, A.P., Lane, T.E., Pierce, J.R., Pandis, S.N., 2007. *Science* 315, 1259-1262.
- Rudich, Y., 2003. Laboratory perspectives on the chemical transformations of organic matter in atmospheric particles. *Chemical Reviews* 103, 5097-5124.
- Rudich, Y., Donahue, N.M., Mentel, T.F., 2007. Aging of Organic Aerosol: Bridging the Gap between Laboratory and Field Studies. *The Annual Review of Physical Chemistry* 58, 321-352.
- Shiling, J.E., King, S.M., Mochida, M., Wornop, D.R., Martin, S.T., 2007. Mass Spectral evidence that small changes in composition caused by oxidative aging processes alter aerosol CCN properties. *The Journal of Physical Chemistry A* 111, 3358-3368.
- Tolocka, M.P., Jang, M., Ginter, J.M., Cox, F.J., Kamens, R.M., Johnston, M.V., 2004. Formation of oligomers in secondary organic aerosol. *Environmental Science and Technology* 38, 1428-1434.
- Turpin, B.J., Huntzicker, J.J., 1995. Identification of secondary organic aerosol episodes and quantitation of primary and secondary organic aerosol concentrations during SCAQS. *Atmos. Environ.*, 23, 3527-3544.
- Yu, J. Z., Cocker, D. R., Griffin, R. J., Flagan, R. C., and Seinfeld, J. H., 1999. Gas-phase ozone oxidation of monoterpenes: Gaseous and particulate products, *J. Atmos. Chem.*, 34, 207–258.
- Zhang, D., Zhang, R., 2005. Ozonolysis of alpha-pinene and beta-pinene: kinetics and mechanism. *Journal of Chemical Physics* 122(11), 114308.
- Zhang, Q., Jimenez, J. L., Canagaratna, M. R., Allan, J. D., Coe, H., et al., 2007. Ubiquity and dominance of oxygenated species in organic aerosols in anthropogenically-influenced Northern Hemisphere midlatitudes, *Geophys. Res. Lett.*, 34, L13801, doi:10.1029/2007GL029979.
- Ziemann, P.J., 2005. Aerosol products, mechanisms, and kinetics of heterogeneous reactions of ozone with oleic acid in pure and mixed particles. *Faraday Discussions* 130, 469-490.



Docherty, K.S., Ziemann, P.J., 2006. Reaction of oleic acid particles with NO<sub>3</sub> radicals: Products, mechanism, and implications for radical-initiated organic aerosol oxidation. *Journal of Physical Chemistry A* 110 (10), 3567-3577.

run	compound	HC <sub>i</sub> <sup>a</sup>	M <sub>o</sub> <sup>b</sup>	O <sub>3,i</sub>	NO <sub>x,i</sub>	CO <sub>i</sub>	Second	Experiment	RH (%)	T (K)
		(ppbV)	( $\mu\text{m}^3/\text{cm}^3$ )	(ppbV)	(ppbV)	(ppmV)	oxidant/conc (ppbV)	Duration (mins)		
911A	$\alpha$ -pinene	100	415	316.2	-	104.7	-	978	<0.5	300
1023A	$\alpha$ -pinene	100	414	305.4	-	79.1	-	510	<0.5	300
1037A	$\alpha$ -pinene	80	273	358.1	-	-	NO/57.3	780	<0.5	300
1037B	$\alpha$ -pinene	80	304	322.6	-	-	-	780	<0.5	300
1038A	$\alpha$ -pinene	100	415	323.5	-	-	H <sub>2</sub> O <sub>2</sub> /2000 <sup>a</sup>	843	<0.5	300
1038B	$\alpha$ -pinene	100	425	318.7	-	-	-	843	<0.5	300
1074A	$\alpha$ -pinene	100	224	415.7	-	-	N <sub>2</sub> O <sub>5</sub> /20 <sup>a</sup>	605	<0.5	300

<sup>a</sup> target concentration

<sup>b</sup> M<sub>o</sub> is wall loss corrected volume concentration following method outlined in Carter et al. (2005).

**Table 3.1** Experimental conditions and results for the  $\alpha$ -pinene oxidation systems

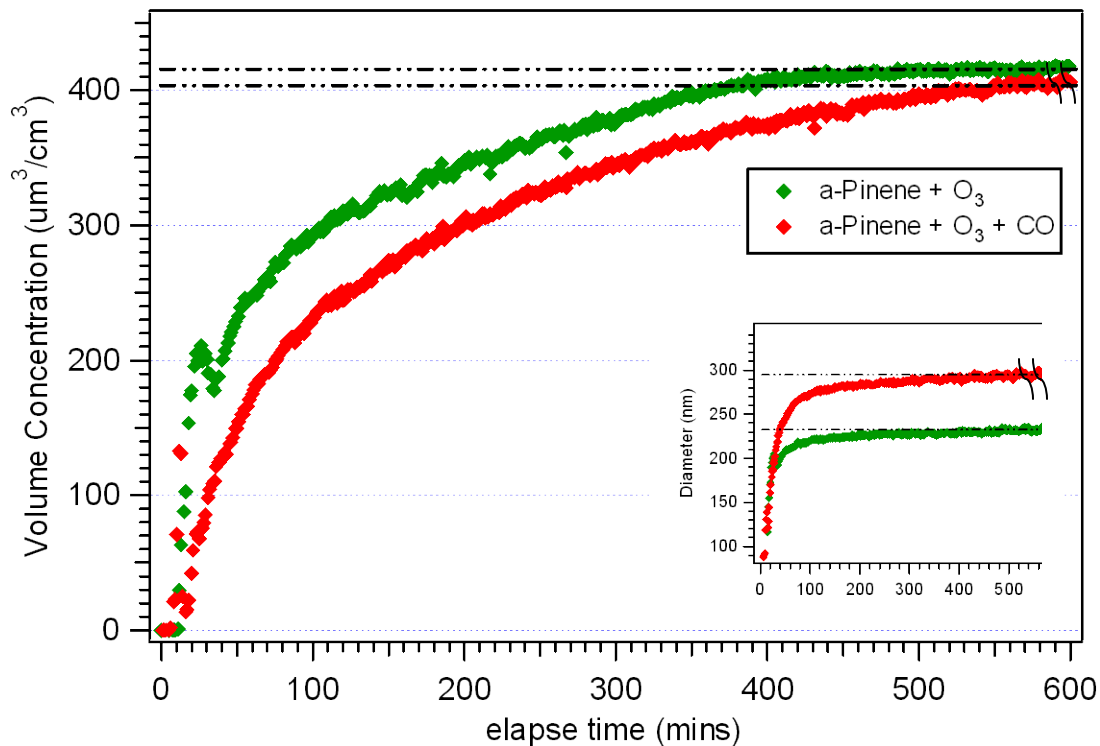


**Figure 3.1** Wall-loss corrected aerosol volume concentration and diameter for dry non-seeded ozonolysis with and without CO with initial condition ( $\alpha$ -pinene $\approx$ 100 ppb, O<sub>3</sub> $\approx$ 250-350 ppb, T=27°C). Dash lines are shown to guide the eye.

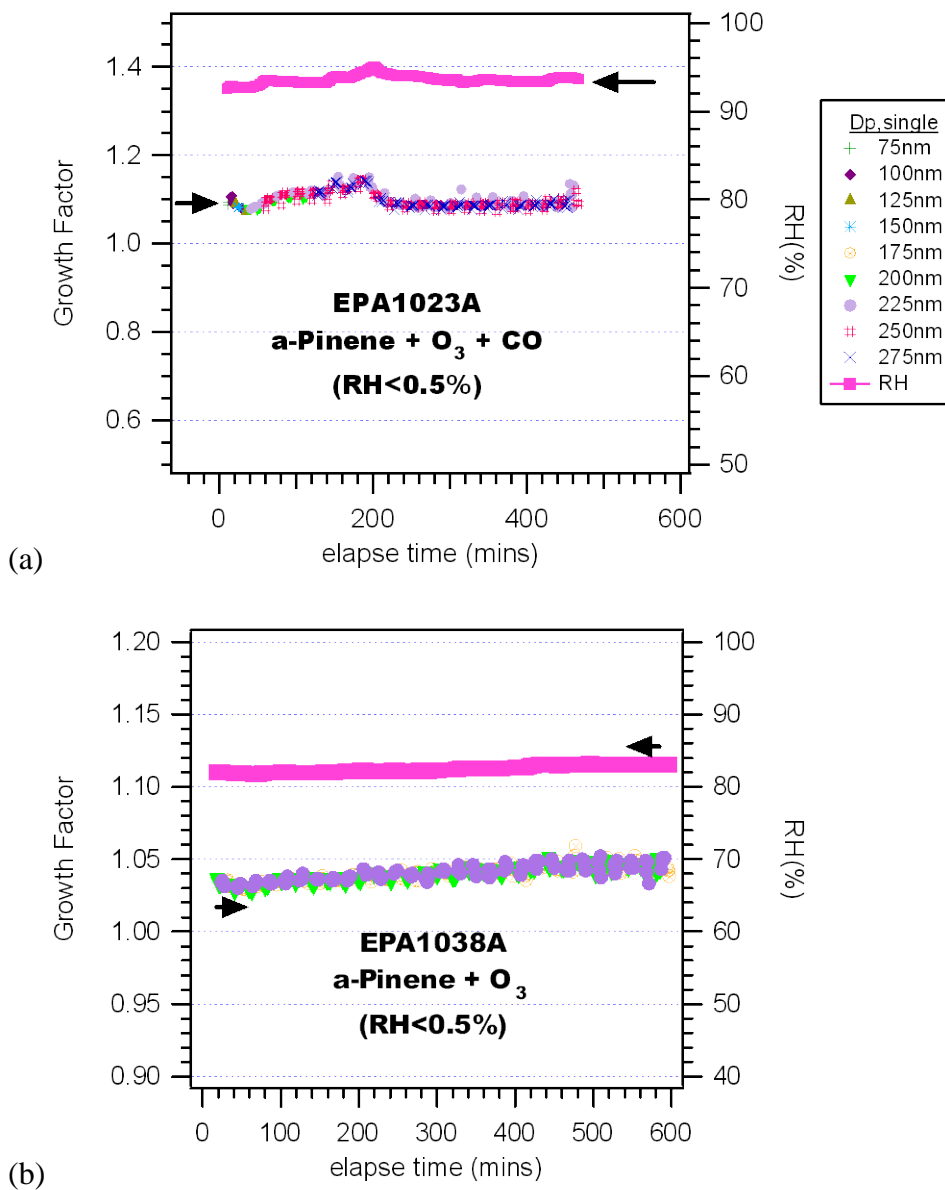


**Figure 3.2** The growth factor and the variations in RH in a typical operating scheme for (a)  $\alpha$ -pinene ozonolysis experiment with CO, (b)  $\alpha$ -pinene ozonolysis experiment without CO

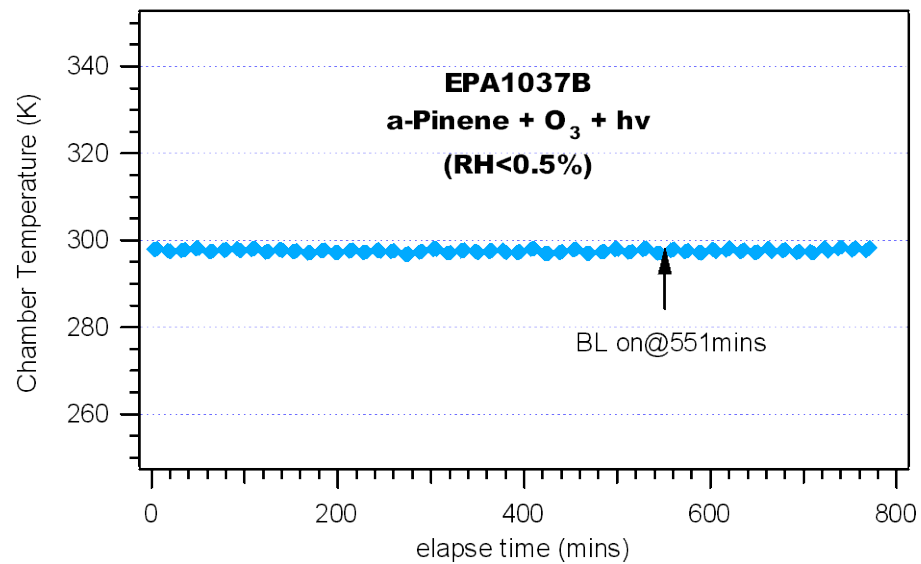


**Figure 3.3** A typical temperature profile inside the reactor over the course of the experiment

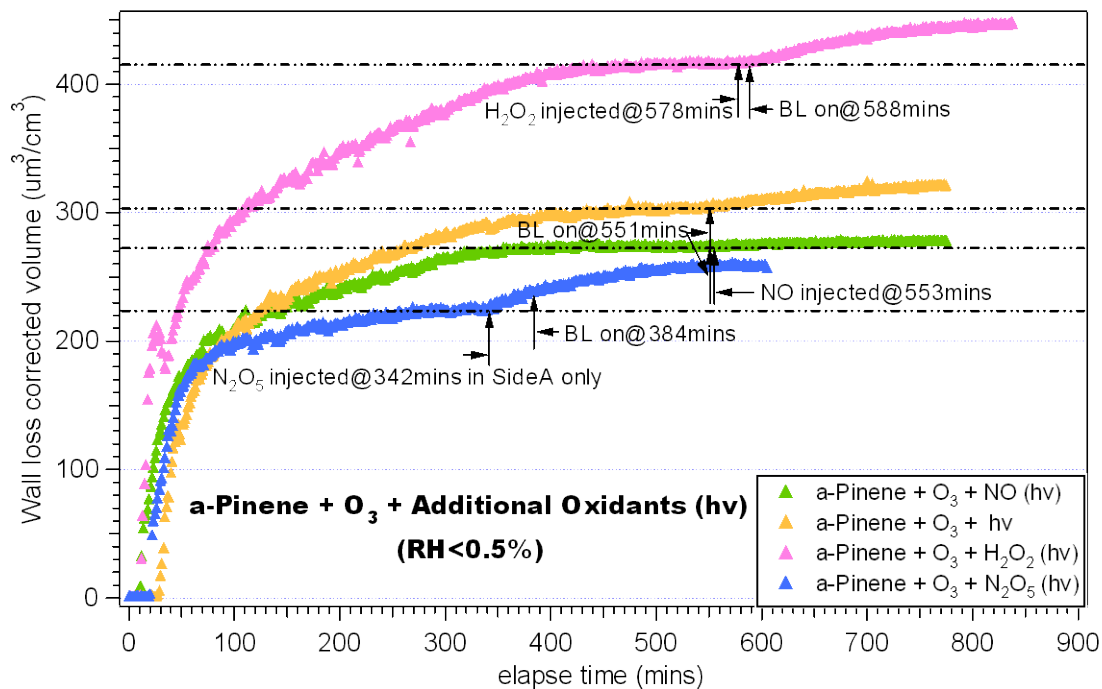
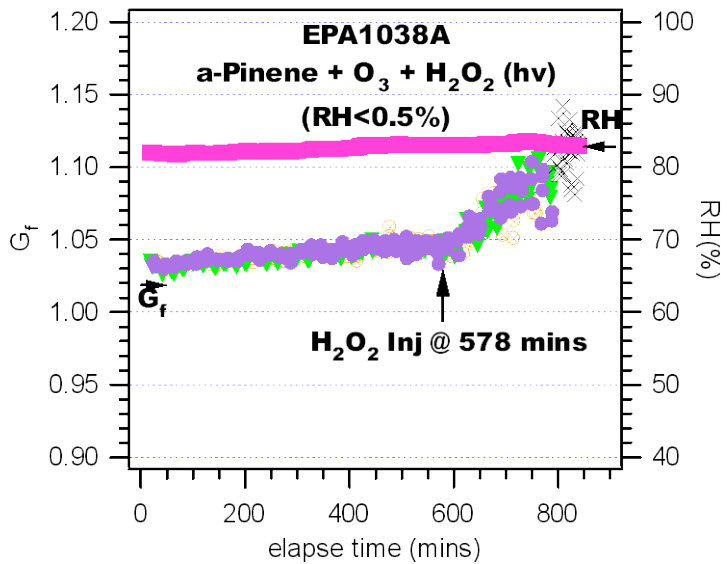
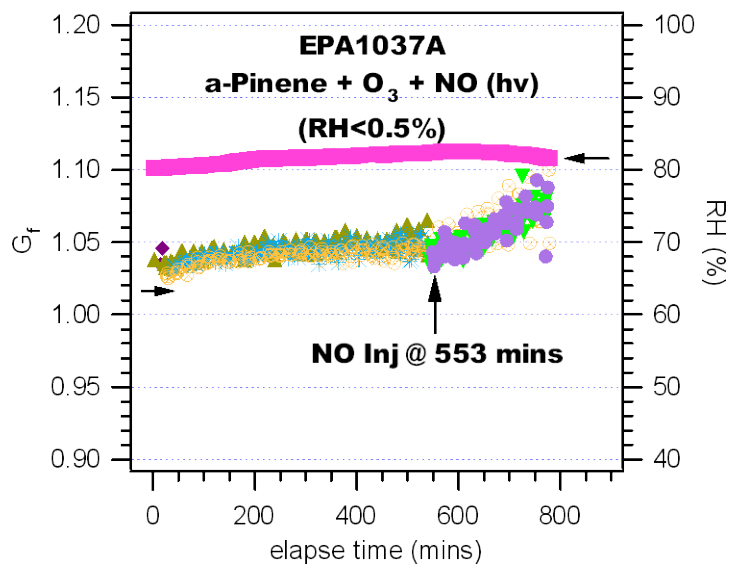


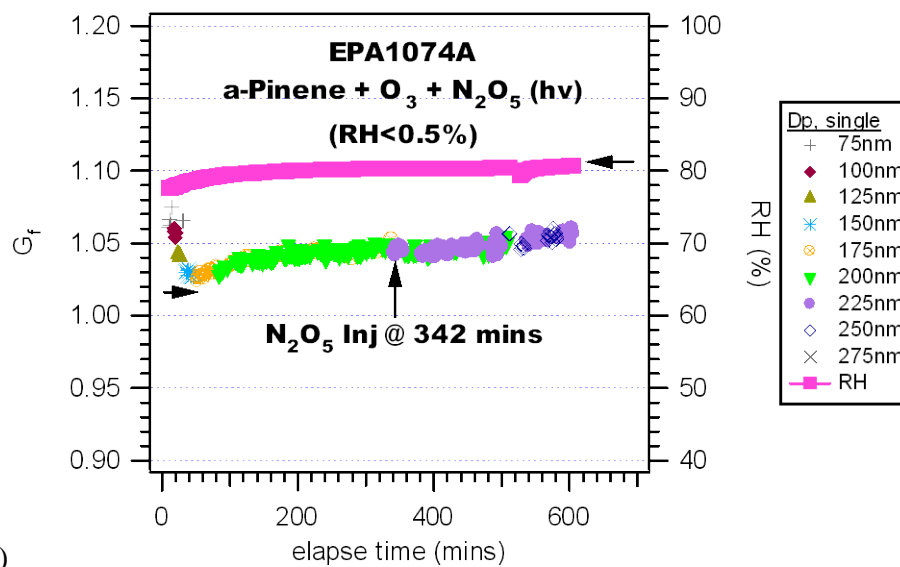
**Figure 3.4** Aerosol formation results for four experiments, light green: non-seeded ozonolysis with later injection of NO; light orange: non-seeded ozonolysis with later UV irradiation; light pink: non-seeded ozonolysis with later injection of H<sub>2</sub>O<sub>2</sub>; light blue: non-seeded ozonolysis with later injection of N<sub>2</sub>O<sub>5</sub>. Dashed lines are shown to guide the eye.



(a)



(b)



(c)

**Figure 3.5** The growth factor and the variations in RH in a typical operating scheme for (a)  $\alpha$ -pinene ozonolysis with additional  $H_2O_2$  injection, (b)  $\alpha$ -pinene ozonolysis with additional NO injection and (c)  $\alpha$ -pinene ozonolysis with additional  $N_2O_5$  injection



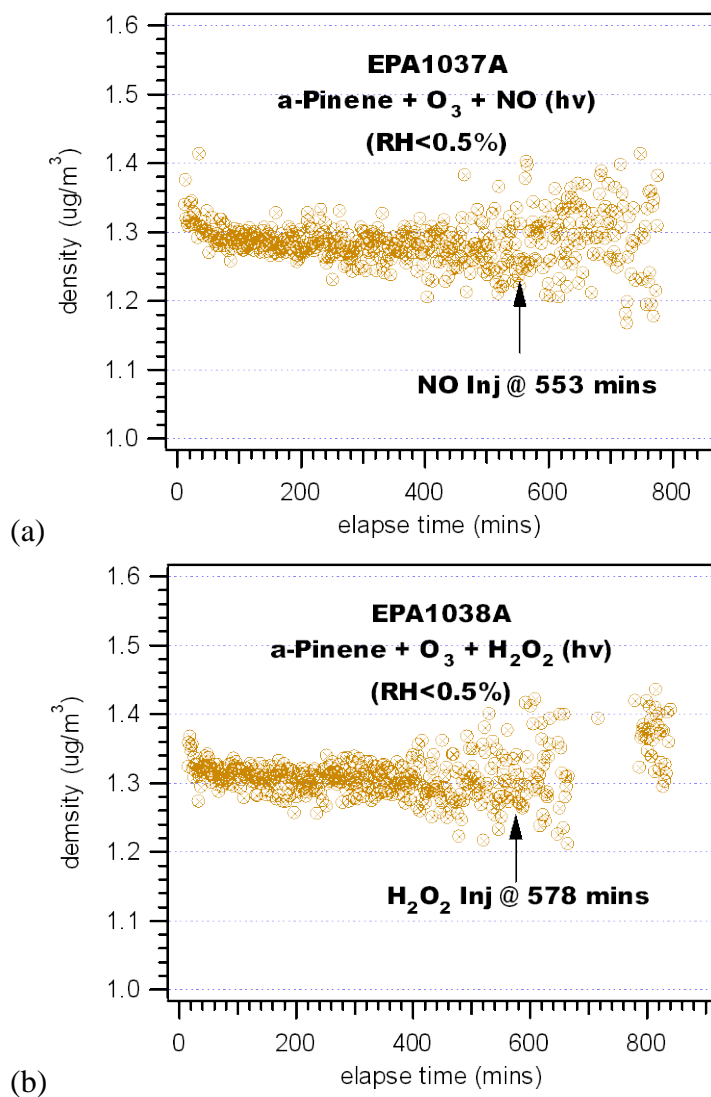
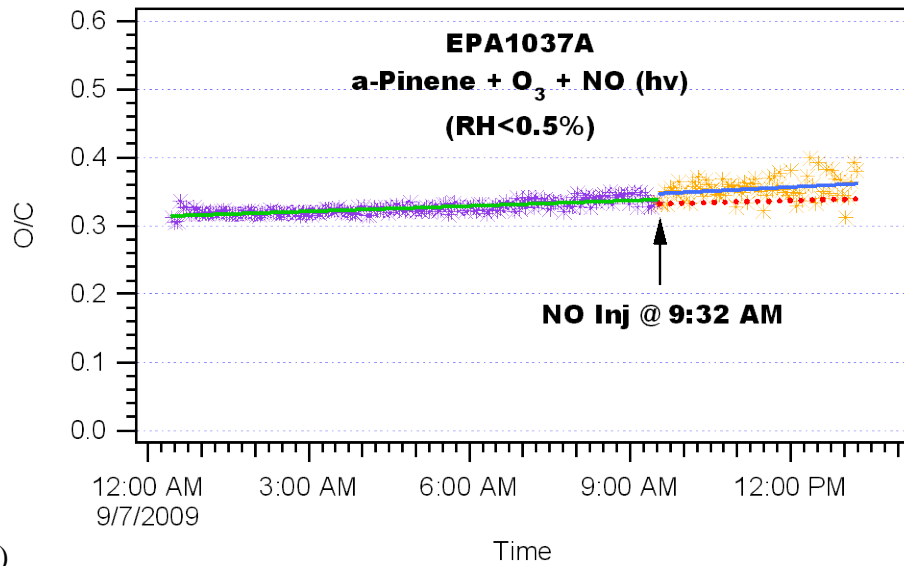
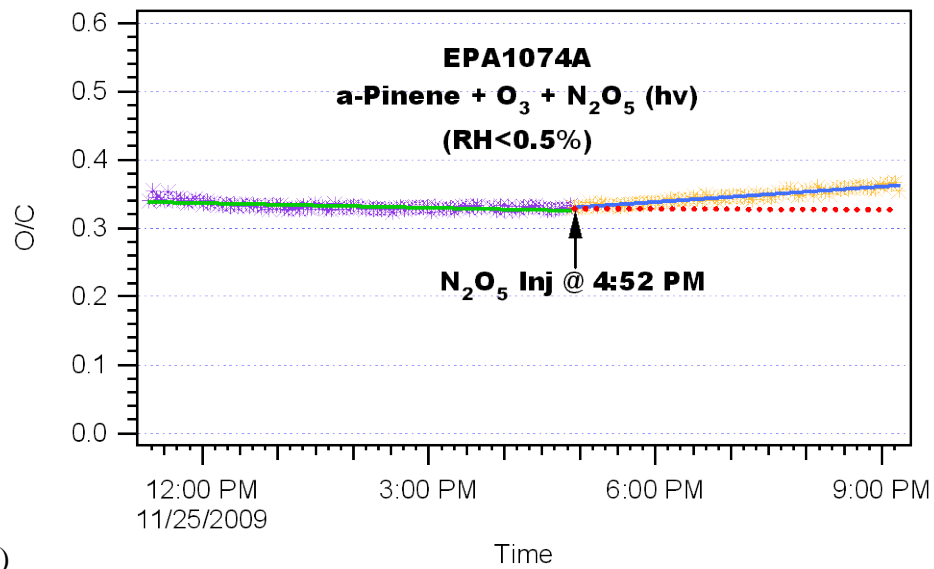


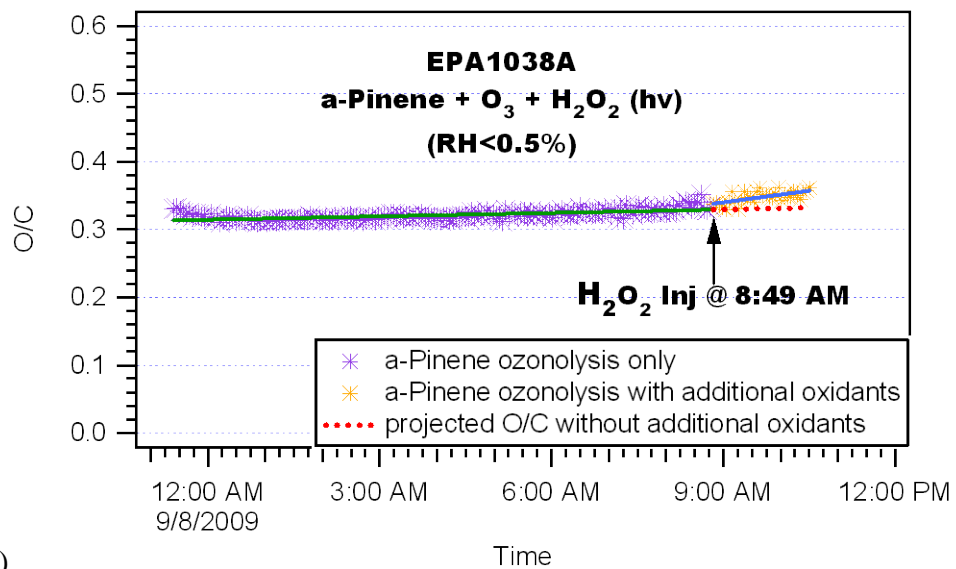
**Figure 3.6** The time evolution of particle density for two select experiments: (a)  $\alpha$ -pinene ozonolysis with additional NO injection (b)  $\alpha$ -pinene ozonolysis with additional H<sub>2</sub>O<sub>2</sub> injection



(a)



(b)



(c)

**Figure 3.7** Time series of average atomic O/C for  $\alpha$ -pinene/ozonolysis experiments with additional injection of: (a) NO; (b) N<sub>2</sub>O<sub>5</sub>; (c) H<sub>2</sub>O<sub>2</sub>

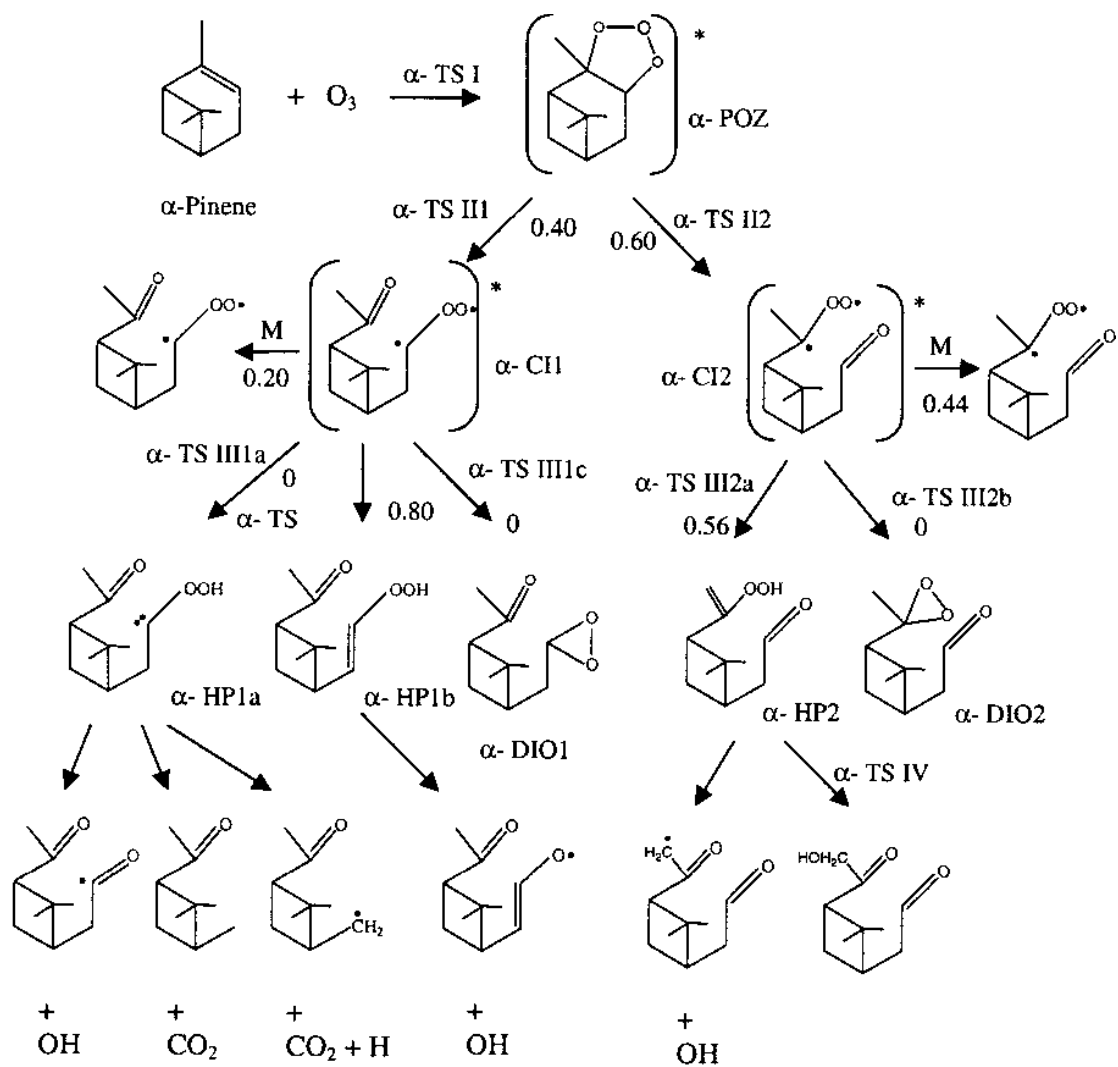


**Figure 3.8** Simplified mechanism of  $\alpha$ -pinene ozonolysis cited from Zhang and Zhang, 2005.

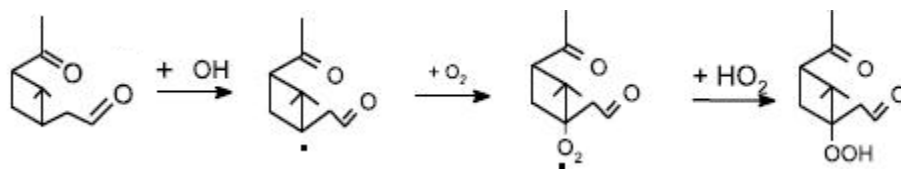


**Figure 3.9** Example of explicit mechanism of  $\cdot\text{OH}$  reaction with pinonaldehyde.

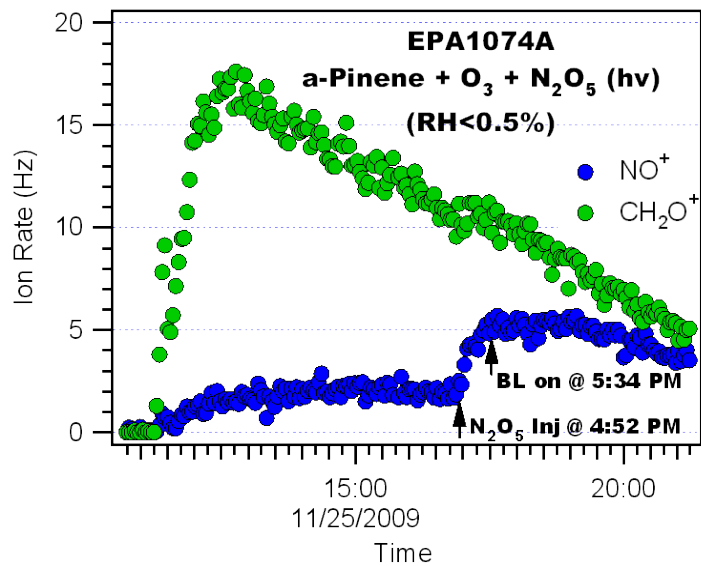


**Figure 3.10** A sample data set for time trace of  $\text{NO}^+$ , and  $\text{CH}_2\text{O}^+$  ions specifically in the additional injection of  $\text{N}_2\text{O}_5$  reaction

## Chapter 4

### 4.1. Introduction

SOA is organic aerosol formed from gas-phase oxidative processing of volatile organic compounds (VOCs) in the atmosphere (e.g., Kroll and Seinfeld, 2008). SOA comprises up to 80% of all ambient organic aerosol present (Turpin, et al., 1995; Zhang et al., 2007) and contributes to climatic impacts, regional visibility reduction and potential health hazards (IPCC, 2007; Eldering and Cass, 1996; Davidson et al., 2005; Pope and Dockery, 2006).

Due to the complexity of atmospheric organic compounds, indirect methods have been employed to estimate SOA formation. Pankow (1994a, b) and Odum et al. (1996) developed a thermodynamic method combined with an empirical model which has been widely used to analyze SOA formation within environmental chambers. Organic aerosol yield ( $Y$ ) is utilized to describe the SOA formation potential of a parent compound and is expressed as

$$Y = \sum_i Y_i = M_o \sum_i \frac{\alpha_i K_{om,i}}{1 + K_{om,i} M_o} \quad (4-1)$$

where  $M_o$  is the organic aerosol mass concentration ( $\mu\text{g m}^{-3}$ ),  $\alpha_i$  is the mass based stoichiometric coefficient and  $K_{om,i}$  is the gas-particle partitioning coefficient of compound  $i$ , respectively.  $K_{om,i}$  is then calculated as

$$K_{om,i} = \frac{RT}{MW_{om,i} \gamma_i p_{L,i}^o} \quad (4-2)$$

where  $R$  is the ideal gas constant,  $MW_{om,i}$  is the molecular weight of species  $i$ ,  $T$  is temperature, and  $\gamma_i$  and  $p_{L,i}^o$  are the activity coefficient and saturation liquid vapor

pressure, respectively, of compound *i*. These final two parameters are both functions of *T*. However, it is difficult to obtain the thermodynamic parameters for each individual specie to assess the extent to which the above equations can handle *T* dependence in an SOA forming system. Given the wide ranges of tropospheric temperatures, it is necessary to accurately predict temperature dependences when describing SOA formation. This work demonstrates the presence of thermally labile species that are not accounted for in current thermodynamic equilibrium models.

There has been considerable amount of work on aerosol yields from the ozonolysis of  $\alpha$ -pinene near room temperature (e.g., Hoffmann et al., 1997; Griffin et al., 1999; Cocker et al., 2001a; Berndt et al., 2003; Pathak et al., 2007a; Shilling et al., 2008), while studies covering more extended temperature ranges are very limited (Stainer et al., 2007; Pathak et al., 2007b) and work on aromatic hydrocarbons are even more rare (Takekawa et al., 2003). These earlier studies report SOA volume dependence per K ( $^{\circ}\text{C}$ ). Most recently, Warren et al. (2009a) explored the reversibility of SOA formation with temperature for the cyclohexene and  $\alpha$ -pinene ozonolysis systems and showed strong evidence that either gas-particle or particle-phase reaction are temperature dependent. This paper presents for the first-time a comprehensive investigation of temperature dependence for both physical and chemical properties of SOA produced in an environmental chamber.

## 4.2. Experimental Section

### 4.2.1 Facility Overview

Experiments were conducted in the UC Riverside/CE-CERT indoor environmental chamber, which is described in detail elsewhere (Carter et al., 2003). Dual 90m<sup>3</sup> Teflon reactors are suspended by a rigid steel framework in a temperature-controlled enclosure which is continuously flushed with purified air. The enclosure is temperature controlled within  $\pm 0.5$  K of the set point, with operational temperatures ranging from 273 K to 323 K. The rigid framework slowly collapses the reactors during the experiments to minimize leaks and diffusion of contaminants into the reactors by maintaining a positive 0.03" H<sub>2</sub>O differential pressure between the reactors and enclosure. 115 W Sylvania 350 black lights are used as light sources for all the experiments. Different numbers of light bulbs are used to match the NO<sub>2</sub> photolysis rate at different temperatures. A known volume of high purity liquid hydrocarbon precursor (*m*-xylene: Sigma-Aldrich,  $\geq 99.5\%$ ) is injected through a heated glass injection manifold system and flushed into the chamber with pure N<sub>2</sub>. NO<sub>2</sub> is introduced by flushing pure N<sub>2</sub> through a calibrated glass bulb filled to a predetermined partial pressure of pure NO<sub>2</sub>. For all experiments, after the non-wall loss corrected SOA volume started decay, the enclosure temperature was raised/lowered to another set point.

### 4.2.2 Light Intensity

The intensity of fluorescent blacklight lamps will decrease with decreasing room temperature. Furthermore, Warren et al. (2009b) recently reported that SOA formation



for aromatic systems is a strong function of NO<sub>2</sub> photolysis rate (denoted as  $k_1$ ). Therefore, it was essential that the NO<sub>2</sub> photolysis rate be maintained between experiments conducted at different temperatures. A series of  $k_1$  measurements (described in Carter et al., 2005) were performed varying temperature and number of lamps to ensure that a consistent  $k_1$  was achieved. In this study, a photolysis rate of 0.29 min<sup>-1</sup> was achieved for all experiments regardless of the system temperature.

#### **4.2.3 Particle and Gas Measurements**

Particle size distributions between 28 and 735 nm are monitored with scanning mobility particle sizers (SMPS) located inside a temperature controlled enclosure. Particle sizing was verified with a suite of polystyrene latex spheres (PSL) (Duke Scientific Corp., Palo Alto, CA).

Real-time particle density is measured using an Aerosol Particle Mass Analyzer (APM) (Kanomax model 3600) and SMPS in series. A custom Labview program determines mode diameter peak from a parallel SMPS and then actively configures the APM-SMPS to optimize instrument response. Density is acquired approximately every 75 s. Details of the instruments and theory are described elsewhere (Malloy et al., 2009; Ehara et al., 1996).

The hygroscopicity of chamber derived SOA is continuously monitored with a custom-built Hygroscopic Tandem Differential Mobility Analyzer (HTDMA). The instrument follows the original design of Radar and McMurry with the configuration similar to that illustrated in Cocker et al. (2001b). The particle diameter transmitted through the first SMPS was selected to match the peak size distribution measured by a

parallel SMPS. Hygroscopic growth factor is reported as the ratio of the modal diameter of humidified aerosol (85.0%~95.0%±1.0%),  $D_{p,\text{humidified}}$ , to that of classified aerosol,  $D_{p,\text{dry}}$ , i.e.,  $G_f = D_{p,\text{humidified}}/D_{p,\text{dry}}$ . Both size distributions are fitted to log-normal distributions to get  $D_{p,\text{humidified}}$  and  $D_{p,\text{dry}}$  for calculation. The residence time of the humidification system is approximately 1 minute. The HTDMA measurement is validated with lab-generated dry ammonium sulfate salt. The  $G_f$  is found to agree within 1.0% of theoretically calculated result using Köhler model at similar RH level (Brechtel and Kreidenweis, 2000). Parallel to the humidification system is a Dekati thermal denuder (TD) (model WAN 5912-4, Dekati Ltd., Finland) system with a 17s heating zone residence time (0.25 LPM flow rate) that can be alternatively operated to evaluate SOA volatility (VTDMA mode). The heating zone of the TD is set to 100°C. Volume remaining fraction (VRF) is then calculated as  $(D_{p,\text{after TD}}/D_{p,\text{before TD}})^3$ .

The evolution of particle elemental composition of aerosol particles is tracked using an Aerodyne High Resolution Time-of-Flight Aerosol Mass Spectrometry (HR-ToF-AMS) operating in the high resolution mode (deCarlo et al., 2006; Jimenez et al., 2003). The HR-ToF-AMS has been described in detail previously (deCarlo et al., 2006) and improves on mass resolution by using a custom high-resolution ToFMS (Tofwerk, Switzerland). More recently, a new elemental analysis (EA) technique was developed using HR-ToF-AMS sampling data (Aiken et al., 2007; 2008). The method is based on the property of electron ionization (EI) for molecules containing small atoms such as C, H, N, O and S that the sum of the ion signal intensities from all fragments is approximately proportional to the mass concentration of the original organic species.

Thus, if the elemental composition of each fragment ion signal in a mass spectrum can be identified (as with HR mass spectra), the average composition of the ions can be calculated. For a complex spectrum from an unknown molecule or mixture, the best estimate of the composition can then be found by summing up the ion contributions across the entire mass spectrum, which is then represented as estimated ratios of oxygen-to-carbon (O/C), hydrogen-to-carbon (H/C), and nitrogen-to-carbon (N/C). Estimated atomic ratios are used to calculate Organic Matter (OM)/Organic Carbon (OC). In this study, the C:O:H ratio of the total aerosol was determined using the high resolution capabilities of the HR-ToF-AMS following the Peak Integration by Key Analysis (PIKA) and Analytical Procedure for Elemental Separation (APES) templates (DeCarlo et al., 2006, Aiken et al., 2008). The sampling lines for APM, TDMA and AMS measurements were wrapped with insulation foam materials to prevent condensation/evaporation of semi-volatile components during sampling.

Decay of the parent hydrocarbon species is monitored with a gas chromatograph (GC-FID, Agilent 6890, Palo Alto, CA) equipped with a flame ionization detector. A Thermal Environmental Instruments Model 42C measured NO, NO<sub>y</sub> and (NO<sub>y</sub> – NO) concentration. O<sub>3</sub> is monitored with a Dasibi Environmental Corp. Model 1003-AH O<sub>3</sub> analyzer.

## 4.3. Results and Discussion

### 4.3.1 SOA production

A series of 6 *m*-xylene/NO<sub>x</sub> photooxidation isothermal experiments (listed in Table 4.1) were conducted under dry (RH<0.1%), non-seed conditions using the UCR/CE-CERT environmental chamber at three temperature set points (278 K, 300 K, 313 K). Temperature was then changed after 6-7h irradiation to evaluate the response of the SOA to temperature change. Initial *m*-xylene concentrations ranged from 107 ppb to 125 ppb, while NO<sub>2</sub> concentrations ranged from 14.8 ppb to 17.4 ppb. Fig. 4.1(a)-(c) displays the raw aerosol volume for all temperature conditions. The maximum raw volume are 23.5 μm<sup>3</sup> cm<sup>-3</sup>, 15.3 μm<sup>3</sup> cm<sup>-3</sup> and 9.9 μm<sup>3</sup> cm<sup>-3</sup> for 278 K, 300 K and 313 K, respectively. The enclosure was then heated or cooled to evaluate whether the SOA would obey gas-particle partitioning theory. For the experiment commencing at 278 K, the volume concentration dropped by 3.7 μm<sup>3</sup> cm<sup>-3</sup> when heated to 313 K. The decrease in the volume concentration is calculated as the difference between the projected non-wall loss corrected volume assuming the temperature was unchanged (278 K) and the actual measured volume concentration when heated to 313 K. For the room temperature (300 K) experiment, the volume concentration increased by 1.6 μm<sup>3</sup> cm<sup>-3</sup> when cooled to 278 K. For the 313 K run, it gained 1.7 μm<sup>3</sup> cm<sup>-3</sup> when the temperature was lowered to 278 K. These results show that this system is unable to partition between temperature set points, indicating the thermodynamic gas-particle partitioning theory alone cannot

explain the difference of SOA formation at the temperature set points for this specific system.

### 4.3.2 SOA density

The evolution of aerosol effective density and the temperature profile of the system over the course of the experiment are presented in Fig. 4.2. When the experiment starts at 278 K, the effective density stabilizes at 1.50-1.60 g cm<sup>-3</sup> with the initial nucleation species density as high as 1.90 g cm<sup>-3</sup>. When the system is heated from 278 K to 313 K, a transition point in SOA density is observed near 290-292 K, with the final density approaching ~1.35 g cm<sup>-3</sup> as the system approaches 313 K (Fig. 4.2a). The sudden drop in SOA density near 290-292 K suggests a dramatic change in particle-phase product distribution. However, when the experiment starts at 313 K, effective density remains constant at ~1.4 g cm<sup>-3</sup> (with slightly higher density at the onset of aerosol formation) even when the system was cooled to 278 K (Fig. 4.2b). The density of SOA formed at 300 K (1.4 g cm<sup>-3</sup>) is comparable to that formed at 313 K and does not change when either raising the temperature to 313 K or lowering the temperature to 278 K (Fig. 4.2c). These density trends are consistent with earlier work on *m*-xylene photooxidation by Malloy et al (2009) conducted at 300 K. The differences in density behavior at the temperature set points may be attributed to the formation of thermally labile aerosol component(s) that are produced at the lower reaction temperatures but break when the temperature increases to 290-292 K.

### 4.3.3 SOA hygroscopicity

Real-time hygroscopic growth factors for select experiments using HTDMA are shown in Fig. 4.3. When the experiment starts at 278 K, the hygroscopicity of *m*-xylene photooxidation aerosol shows a continuous increase of  $G_f$  (1.02-1.09 in Fig. 4.3a) at  $81.0 \pm 0.5\%$  RH, which is similar to previously observed phenomena at room temperature (e.g., Qi et al., 2010, Cocker et al., 2001c). When the system is heated from 278 K to 313 K, a transition point in SOA  $G_f$  is observed near 290-292 K, consistent with the transition point observed in the SOA density. The  $G_f$  then continues to slowly increase to 1.17 at 313 K. When the reaction starts at 313 K, the  $G_f$  is observed to increase from 1.05 to 1.15 over 7h irradiation at the same TDMA RH level. Similar to the density observations, no  $G_f$  transition point is observed as the system is cooled to 278 K from 313 K, nor is the  $G_f$  impacted by the decreasing temperature. Again, the  $G_f$  observations are consistent with the formation of thermally labile specie(s) at low chamber temperatures that break around 290 – 292 K.

### 4.3.4 SOA volatility

Measurement of SOA volatility can provide indirect information about its chemical composition (Philippin et al., 2003, Kalberer et al., 2004). The SOA VRF for *m*-xylene photooxidation experiments conducted at 278 K, 300 K, and 313 K are shown in Fig. 4.4(a)-(c). The VRF of the SOA after 4h UV irradiation is 14%, 29%, and 48% for the 278 K, 300 K, and 313 K systems, respectively. VRFs are observed to increase during the isothermal phase of the reaction for all three systems' T set points. Overall, the

volatility of SOA at different temperatures is 278 K > 300 K > 313 K, consistent with additional condensation of high vapor pressure semi-volatile species at the lower isothermal T set points. When reducing the temperatures of the 300 K and 313 K systems to 278 K, there is an immediate decrease in VRF observed for both systems, consistent with condensation of additional semi-volatile species as the system T lowers, which is easily re-evaporated at the 100°C TD set point. The VRFs decrease to 33% and 40% for 300 K and 313 K experiments, respectively, when the system temperatures arrive at 278 K. These VRFs remain higher than the projected VRF (~24%) for the low temperature system. For the 278 K experiment, the VRF slowly increases when the system starts heating up, and then shows a steeper increase when the system temperature approaches the 290-292 K threshold. The VRF time traces are consistent with the density and  $G_f$  observations for the 278 K experiment when heated past 290-292 K and are consistent with a thermally labile portion of the aerosol formed at the lowest T set point.

#### **4.3.5 SOA chemical composition**

As a result of both the extensive fragmentation caused by electron impact ionization and the thermal decomposition of molecules by the vaporizer, most of the signal intensity in the HR-ToF-AMS occurred below mass to charge ratio ( $m/z$ ) 100; parent molecular peaks were weak or unobserved. Therefore,  $m/z$  values of fragment ions were interpreted as tracers of the parent species and the change in contribution fraction of signal intensities could be attributed to evolution of aerosol species (e.g., change in signal intensity ratio of  $m/z$  44/43). For instance,  $m/z$  44 is commonly associated with fragments of oxo- and dicarboxylic acids ( $\text{CO}_2^+$ ) while  $m/z$  43 is a fragment normally associated

with oxidized organic molecules containing carbonyl groups ( $\text{C}_2\text{H}_3\text{O}^+$ ) (Alfarra et al., 2006). The average mass spectra of organics normalized to the total organic signal are displayed in Fig. 4.5. The same fragmentation table was used as that in Aiken et al. (2008). When the reaction starts at 278 K, the relative intensity of  $m/z$  44 ( $\text{CO}_2^+$ ) is 6.5% and then increases to 8.4% when the system temperature reaches 313 K. However, when the reaction starts at 313 K and then is cooled down to 278 K, the contribution fraction of  $\text{CO}_2^+$  ion is considerably higher and only changes from 10.0% to 9.7%. These results indicate that for this system the SOA produced at cold temperatures are less oxygenated than those produced at higher temperatures and that less oxygenated species are preferentially lost from the aerosol as the system is heated. The change in  $m/z$  44 relative intensity upon heating is attributed to evaporation of lighter-end semi-volatile species that may be less functionalized (oxygenated). The much higher  $m/z$  44 intensity for species in the 313 K isothermal experiment indicates that production of higher oxygen-containing compounds are favored at these higher temperatures. Similar phenomena were also observed in toluene/ $\text{NO}_x$  photooxidation reaction system (Hildebrandt et al., 2009). Furthermore, it is consistent with the other analytical techniques described in previous sections that the semi-volatile species formed at 313 K differ in composition from those formed at 278 K. Furthermore, the 278 K aerosol composition cannot be produced by condensation of semi-volatile species when cooling the system from 313 K system to 278 K. In other words, simple thermodynamic partitioning theory alone can not fully explain the data.



Organic elemental analysis (EA) was applied to HR-ToF-AMS SOA data collected from select experiments. Time series for O/C ratio for *m*-xylene photooxidation at cold temperature (278 K→313 K) and hot temperature (313 K→278 K) are presented in Fig. 4.6. Values are not presented for aerosol mass loadings less than 2.0  $\mu\text{g m}^{-3}$  to reduce scatter at low mass loadings. O/C values of  $0.40\pm 0.02$  were observed for the SOA from *m*-xylene photooxidation at 278 K. Overall, the O/C ratio remains stable for 6h while the system is maintained at 278 K and then slowly increases as the system temperature increases. There is an evident increase in O/C ratio when the system is heated to about 290-292 K as shown in the lower-right sub-figure. This observation is consistent with increasing organic functionalization of the suspended aerosol as the system crosses 290-292 K, which is also inferred above from the HTDMA, VTDMA and density measurements. O/C values of  $0.43\pm 0.03$  were observed for the SOA from *m*-xylene photooxidation at 313 K, and it slowly decreases as the system is cooled down, which can be attributed to a fraction of less oxidized compounds condensation.

#### **4.3.6 System Reversibility**

To further evaluate whether SOA formation was reversible, which would be expected from simple gas-particle partitioning theory, after non-wall-loss corrected SOA volume concentration started decaying, the enclosure temperature was raised to an alternate set point (300 K) and then returned to the original set point (278 K) with black lights off. The temperature cycling provides additional information about the SOA characteristics for *m*-xylene photooxidation. The volume concentration shown in Fig. 4.7

indicates that the SOA formed at 278 K loses about 20% of mass when heating up to 300 K and the aerosol volume does not restore to that formed at 278 K initially after cooling back to 278 K. This may be attributed to the thermally labile aerosol component that cannot form at higher temperature and breaks with a temperature increase.

The density was also operated during the temperature ramping experiment (278 K  $\rightarrow$  300 K  $\rightarrow$  278 K). As seen in Fig. 4.8, the initial density at 278 K was 2.2 g cm<sup>-3</sup>, and then dropped to around 1.6 g cm<sup>-3</sup>. After heating the density dramatically decreases to 1.35 g cm<sup>-3</sup> when passing the 290 K-292 K transitional point, similar to experiment 1046A, but remained the same when the temperature returned to 278 K, which is much lower than stabilized 1.6 g cm<sup>-3</sup> generated at 278 K. These results further indicate that the semi-volatile partitioning cannot explain the difference of the aerosol formed at 278 K.

#### **4.4 Conclusions**

Temperature has a clear and dramatic effect on the SOA formation not only in terms of particle volume but also chemical composition for the *m*-xylene photooxidation system. For the first time, strong evidence from perspectives of particle density, hygroscopicity, volatility and bulk elemental analysis is presented that the semi-volatile formation or particle-phase reactions are temperature dependent for this specific system. The results show that when the experiment commences at 313 K, and then is cooled down to 278 K, there are no significant changes in particle density, hygroscopicity, volatility, and chemical composition. However, aerosol formed at cold temperatures appears chemically and physically different than those formed at 300 K and 313 K. These observations indicate that traditional gas-particle partitioning theory alone cannot fully

explain *m*-xylene photooxidation system temperature dependence. A large transition in particle density, hygroscopicity, volatility and chemical composition was seen as the aerosol was warmed past 290-292 K. These observations are consistent with a thermally labile aerosol component.

This study indicates that it is insufficient to utilize enthalpy of vaporization or percent volume change per degree to predict SOA formation for differences in temperature with current models. The reason is apparently due to the fundamentally difference in physical and chemical properties of SOA formed at different temperatures. Further study is needed to identify the source and composition of the thermally labile species to allow for prediction of the SOA temperature dependence for this system. Therefore, the reaction mechanism can be improved accordingly. Other systems must be explored to identify the extent to which the phenomena observed for the *m*-xylene photooxidation experiment is present in other SOA systems.

## 4.5 References

- Aiken, A. C., DeCarlo, P. F., and Jimenez, J. L.: Elemental analysis of organic species with electron ionization high-resolution mass spectrometry, *Analytical Chemistry* 79 (21), 8350-8358, 2007.
- Aiken, A. C., DeCarlo, P. F., Kroll, J. H., Worsnop, D. R., Huffman, J. A., Docherty, K., Ulbrich, I. M., Mohr, C., Kimmel, J. R., Sueper, D., Zhang, Q., Sun, Y., Trimborn, A., Northway, M., Ziemann, P. J., Canagaratna, M. R., Onasch, T. B., Alfarra, R., Prevot, A. S. H., Dommen, J., Duplissy, J., Metzger, A., Baltensperger, U., and Jimenez, J. L.: O/C and OM/OC Ratios of Primary, Secondary, and Ambient Organic Aerosols with High Resolution Time-of-Flight Aerosol Mass Spectrometry, *Environmental Science and Technology* 42, 4478-4485, 2008.
- Alfarra, M. R., Paulsen, D., Gysel, M., Garforth, A. A., Dommen, J., Prevot, A. S. H., Worsnop, D. R., Baltensperger, U., and Coe, H.: A mass spectrometric study of secondary organic aerosols formed from the photooxidation of anthropogenic and biogenic precursors in a reaction chamber, *Atmos. Chem. Phys.* 6, 5279-5293, 2006.
- Berndt, T., Böge, O., and Stratmann, F.: Gas-phase ozonolysis of  $\alpha$ -pinene: gaseous products and particle formation, *Atmospheric Environment* 37, 3933-3945, 2003.
- Brechel F. J., and Kreidenweis S. M.: Predicting particle critical supersaturation from hygroscopic growth measurements in the humidified TDMA. part I: Theory and sensitivity studies, *Journal of the Atmospheric Sciences* 57, 1854-1871, 2000.
- Carter, W. P. L., Cocker, D. R., Fitz, D. R., Malkina, I. L., Bumiller, K., Sauer, C. G., Pisano, J. T., Bufalino, C., and Song, C.: A new environmental chamber for evaluation of gas-phase chemical mechanisms and secondary aerosol formation, *Atmospheric Environment* 39, 7768-7788, 2005.
- Cocker, D. R., Clegg, S. L., Flagan, R. C., and Seinfeld, J. H.: The effect of water on gas-particle partitioning of secondary organic aerosol. Part I:  $\alpha$ -pinene/ozone system, *Atmospheric Environment* 35, 6049-6072, 2001a.
- Cocker, D. R., Flagan, R. C., and Seinfeld, J. H.: State-of-the-art facility for studying atmospheric aerosol chemistry, *Environmental Science and Technology* 35, 2594-2601, 2001b.
- Cocker, D. R., Mader, B. T., Kalberer, M., Flagan, R. C., and Seinfeld, J. H.: The effect of water on gas-particle partitioning of secondary organic aerosol: II. m-xylene

- and 1,3,5-trimethylbenzene photooxidation systems, *Atmospheric Environment* 35, 6073-6085, 2001c.
- Davidson, C. I., Phalen, R. F., and Solomon, P. A.: Airborne Particulate Matter and Human Health: A Review, *Aerosol Science and Technology* 39, 737-749, 2005.
- DeCarlo, P. F., Kimmel, J. R., Trimborn, A., Northway, M. J., Jayne, J. T., Aiken, A. C., Gonin, M., Fuhrer, K., Horvath, T., Docherty, K., Worsnop, D. R., and Jimenez, J. L.: Field-Deployable, High-Resolution, Time-of-Flight Aerosol Mass Spectrometer, *Analytical Chemistry* 78, 8281-8289, 2006.
- Ehara, K., Hagwood, C., and Coakley, K. J.: Novel method to classify aerosol particles according to their mass-to-charge ratio-aerosol particle mass analyzer, *Journal of Aerosol Science* 27(2), 217-234, 1996.
- Eldering, A., Cass, G. R.: Source-oriented model for air pollutant effects on visibility, *Journal of Geophysical Research-Atmospheres* 101, 19343-19369, 1996.
- Griffin, R. J., Cocker, D. R., Flagan, R. C., and Seinfeld, J. H.: Organic aerosol formation from the oxidation of biogenic hydrocarbons, *Journal of Geophysical Research-Atmosphere* 104, 3555-3567, 1999.
- Hildebrandt, L., Donahue, N. M., and Pandis, S. N.: High formation of secondary organic aerosol from the photo-oxidation of toluene, *Atmos. Chem. Phys.* 9, 2973-2986, 2009.
- Hoffmann, T., Odum, J. R., Bowman, F., Collins, D., Klockow, D., Flagan, R. C., and Seinfeld, J. H.: Formation of organic aerosols from the oxidation of biogenic hydrocarbons, *Journal of Atmospheric Chemistry* 26, 189-222, 1997.
- Intergovernmental Panel on Climate Change (IPCC) Fourth Assessment Report: Climate Change 2007.
- Jimenez, J. L., Jayne, J. T., Shi, Q., Kolb, C. E., Worsnop, D. R., Yourshaw, I., Seinfeld, J. H., Flagan, R. C., Zhang, X., Smith, K. A., Morris, J., and Davidovits, P.: Ambient Aerosol Sampling with an Aerosol Mass Spectrometer, *Journal of Geophysical Research - Atmospheres* 108(D7), 8425, doi:10.1029/2001JD001213, 2003.
- Kalberer, M., Paulsen, D., Sax, M., Steinbacher, M., Dommen, J., Prévôt, A. S. H., Fisseha, R., Weingartner, E., Frankevich, V., Zenobi, R., and Baltensperger, U.: Identification of Polymers as Major Components of Atmospheric Organic Aerosols, *Science* 303, 1659-1662, 2004.

- Malloy, Q. G. J., Nakao, S., Qi, L., Austin, R., Stothers, C., Hagino, H., and Cocker, D. R.: Real-Time Aerosol Density Determination Utilizing a Modified Scanning Mobility Particle Sizer Aerosol Particle Mass Analyzer System, *Aerosol Science and Technology* 43, 673-678, 2009.
- Odum, J. R., Hoffmann, T., Bowman, F., Collins, D., Flagan, R. C., and Seinfeld, J. H.: Gas/particle partitioning and secondary organic aerosol yields, *Environmental Science & Technology* 30, 2580-2585, 1996.
- Pankow, J. F.: An absorption-model of gas-particle partitioning of organic compounds in the atmosphere, *Atmospheric Environment* 28, 185-188, 1994a.
- Pankow, J. F.: An absorption-model of the gas aerosol partitioning involved in the formation of secondary organic aerosol, *Atmospheric Environment* 28, 189-193, 1994b.
- Pathak, R. K., Presto, A. A., Lane, T. E., Stanier, C. O., Donahue, N. M., and Pandis, S. N.: Ozonolysis of  $\alpha$ -pinene: parameterization of secondary organic aerosol mass fraction, *Atmospheric Chemistry and Physics* 7, 3811-3821, 2007.
- Pathak, R. K., Stanier, C. O., Donahue, N. M., and Pandis, S. N.: Ozonolysis of  $\alpha$ -pinene at atmospherically relevant concentrations: temperature dependence of aerosol mass fractions (yields), *Journal of Geophysical Research-Atmospheres* 112, D03201, 2007.
- Philippin, S., Wiedensohler, A., and Stratmann, F.: Measurements of non-volatile fractions of pollution aerosols with an eight-tube volatility tandem differential mobility analyzer (VTDMA-8), *Journal of Aerosol Science* 35, 185-203, 2004.
- Pope, C. A., and Dockery, D. W.: Health effects of fine particulate air pollution: lines that connect, *Journal of the Air and Waste Management Association* 56, 709-742, 2006.
- Shilling, J. E., Chen, Q., King, S. M., Rosenoern, T., Kroll, J. H., Worsnop, D. R., McKinney, K. A., and Martin, S. T.: Particle mass yield in secondary organic aerosol formed by the dark ozonolysis of  $\alpha$ -pinene, *Atmospheric Chemistry and Physics* 8, 2073-2088, 2008.
- Stanier, C. O., Pathak, R. K., and Pandis, S. N.: Measurements of the volatility of aerosols from alpha-pinene ozonolysis, *Environmental Science & Technology* 41, 2756-2763, 2007.
- Takekawa, H., Minoura, H., and Yamazaki, S.: Temperature dependence of secondary organic aerosol formation by photo-oxidation of hydrocarbons, *Atmospheric Environment* 37, 3413-3424, 2003.

- Turpin, B. J., Huntzicker, J. J.: Identification of secondary organic aerosol episodes and quantitation of primary and secondary organic aerosol concentrations during SCAQS, *Atmospheric Environment* 23, 3527-3544, 1995.
- Warren, B., Austin, R. L., and Cocker, D. R.: Temperature dependence of secondary organic aerosol, *Atmospheric Environment* 43, 3548-3555, 2009a.
- Warren, B., Song, C., and Cocker, D. R.: Light intensity and light source influence on secondary organic aerosol formation for the m-xylene/NO<sub>x</sub> photooxidation system, *Environmental Science & Technology* 42, 5461-5466, 2009b.
- Zhang, Q., Jimenez, J. L., Canagaratna, M. R., Allan, J. D., Coe, H., Ulbrich, I., Alfarra, M. R., Takami, A., Middlebrook, A.M., Sun, Y. L., Dzepina, K., Dunlea, E., Docherty, K., De-Carlo, P. F., Salcedo, D., Onasch, T., Jayne, J. T., Miyoshi, T., Shimo, A., Hatakeyama, S., Takegawa, N., Kondo, Y., Schneider, J., Drewnick, F., Borrmann, S., Weimer, S., Demerjian, K., Williams, P., Bower, K., Bahreini, R., Cottrell, L., Griffin, R. J., Rautianinen, J., Sun, J. Y., Zhang, Y. M., and Worsnop, D. R.: Ubiquity and dominance of oxygenated species in organic aerosols in anthropogenically-influenced Northern Hemisphere midlatitudes, *Geophysical Research Letters* 34, L13801, doi:10.1029/2007GL029979, 2007.

Exp #	T <sub>0</sub> [K]	NO <sub>2,i</sub> [ppbV]	<i>m</i> -xylene <sub>i</sub> [μg m <sup>-3</sup> ]	Δ <i>m</i> -xylene [μg m <sup>-3</sup> ] <sup>a</sup>	Δ <i>M</i> <sub>o</sub> [μg m <sup>-3</sup> ] <sup>b</sup>	Temp Change	
						T <sub>2</sub> [k]	Δ <i>M</i> <sub>o</sub> [μg m <sup>-3</sup> ] <sup>c</sup>
1046A	278	15.7	544	223	13.3	313	↓3.7
1047A	313	15.0	475	322	-	278	-
1049A	300	14.8	465	310	11.0	313	↓2.9
1050A	300	17.4	491	332	11.6	278	↑1.6
1051A	313	16.4	483	330	7.4	278	↑1.7
1055A	278	15.6	604	279	15.3	313	↓3.4
1116A	278	18.8	413	188	23.4	-	-

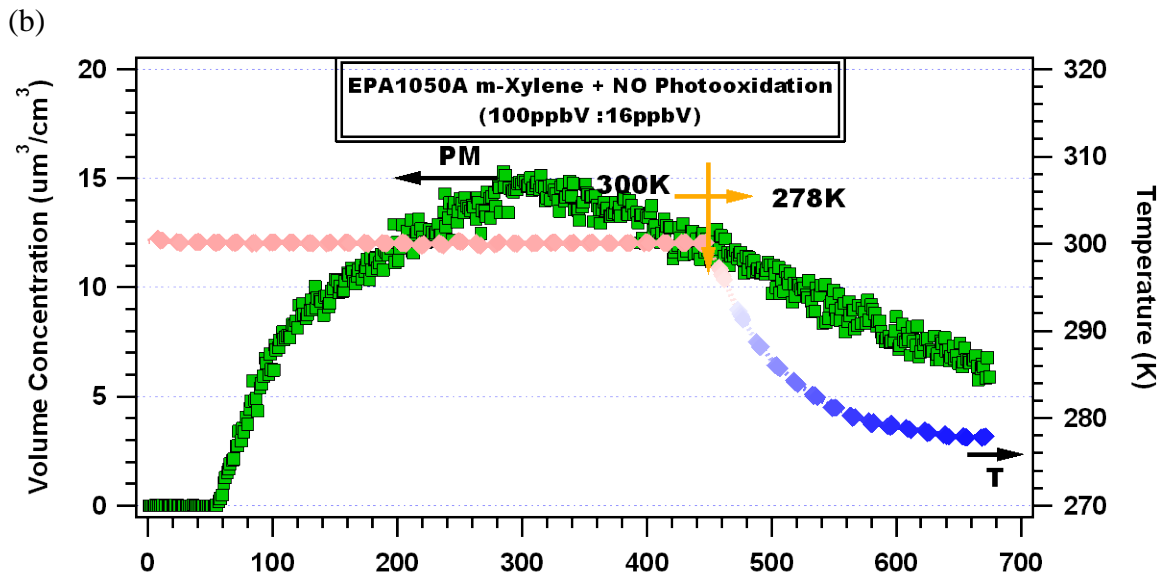
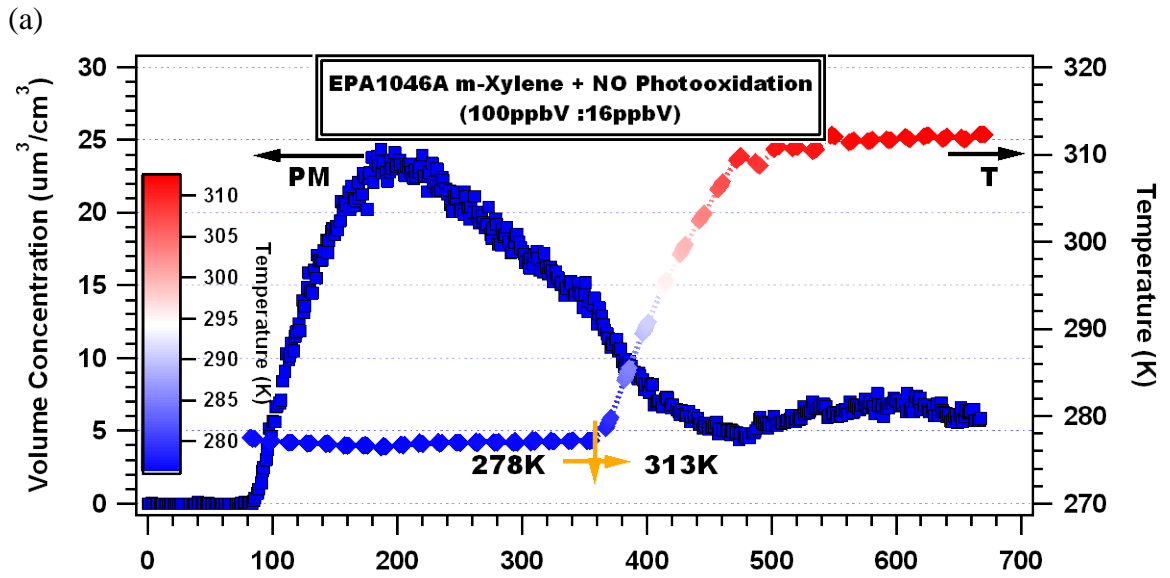
<sup>a</sup> this is the hydrocarbon consumed by the time when system temperature starts to change

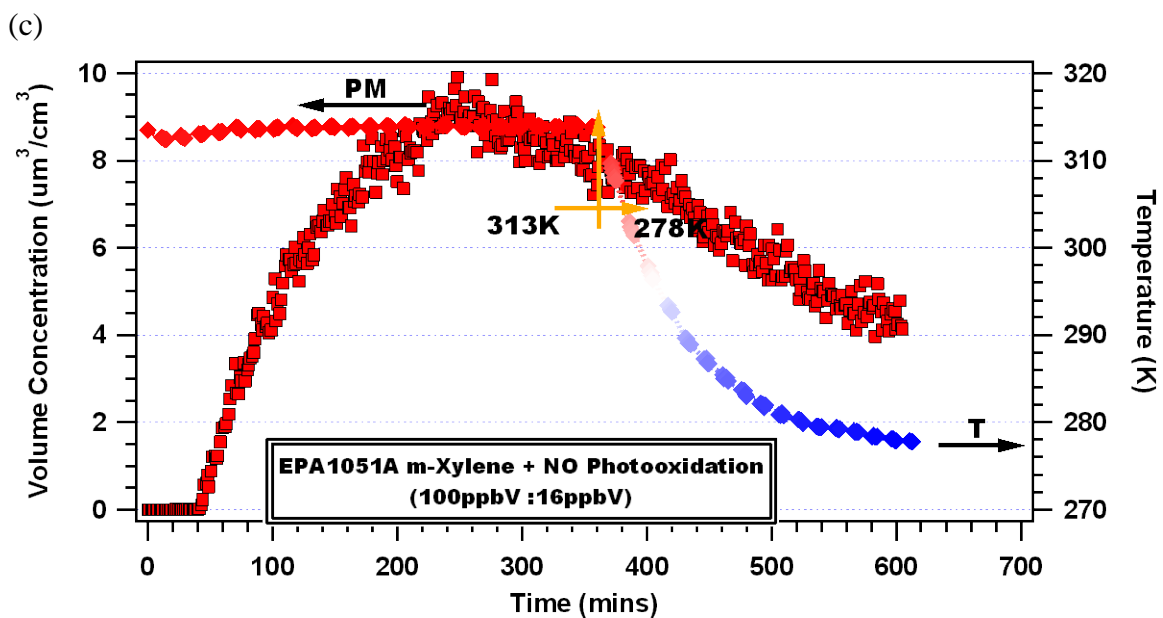
<sup>b</sup> non-wall-loss corrected PM volume concentration before system temperature changes (not the maximum volume concentration that the system achieved)

<sup>c</sup> particle mass condensed/evaporated when lowering/increasing the system temperature compared to the projected particle mass if the system remains at the initial temperature

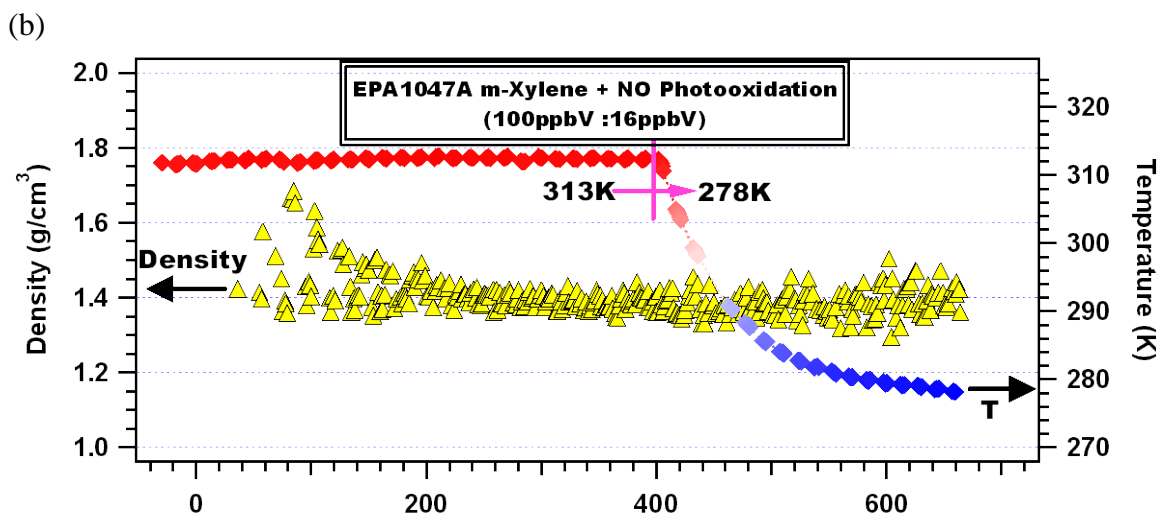
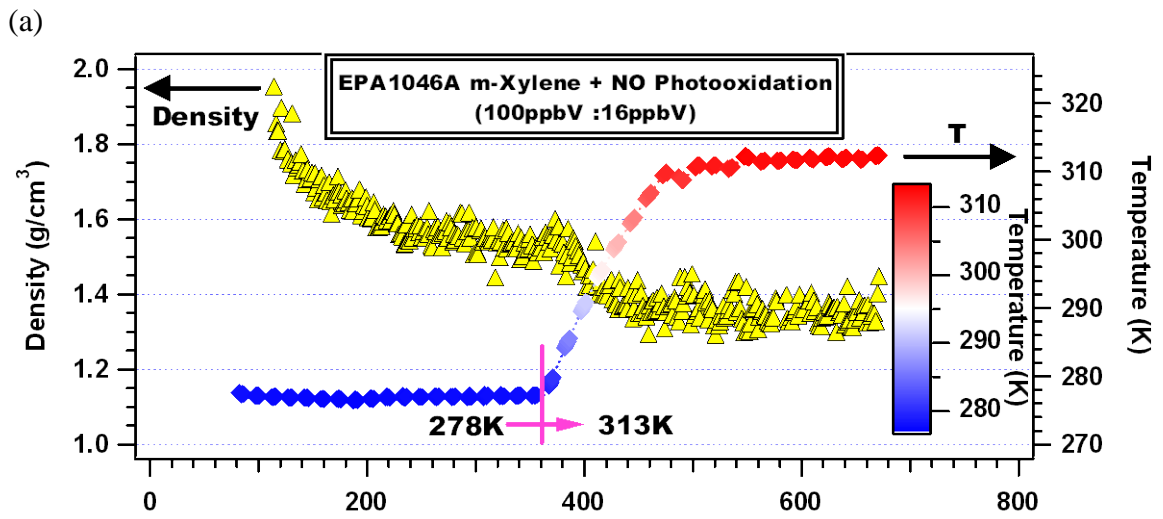
**Table 4.1** Experimental conditions and results summary for the *m*-xylene photooxidation reactions

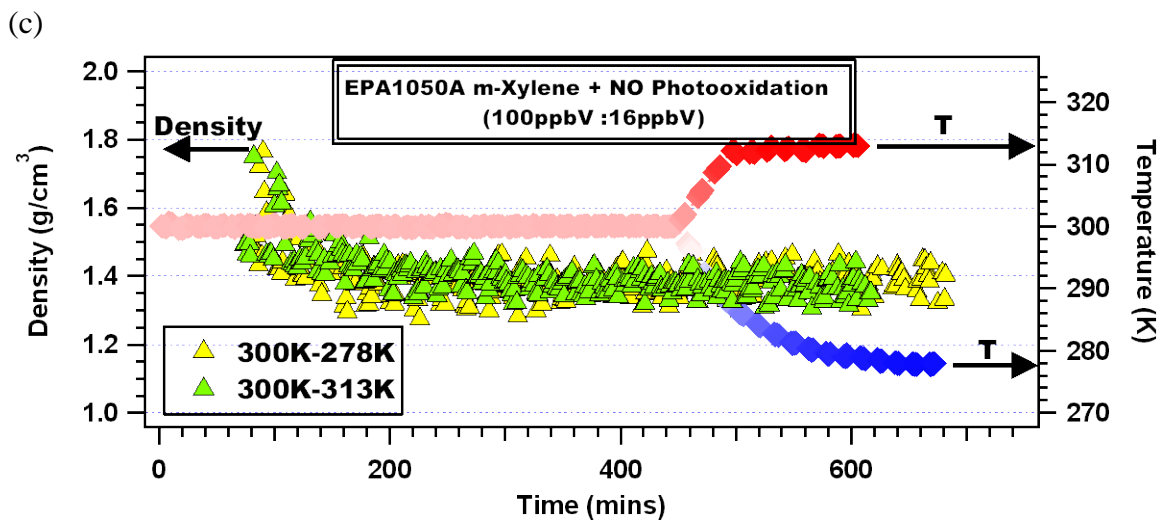




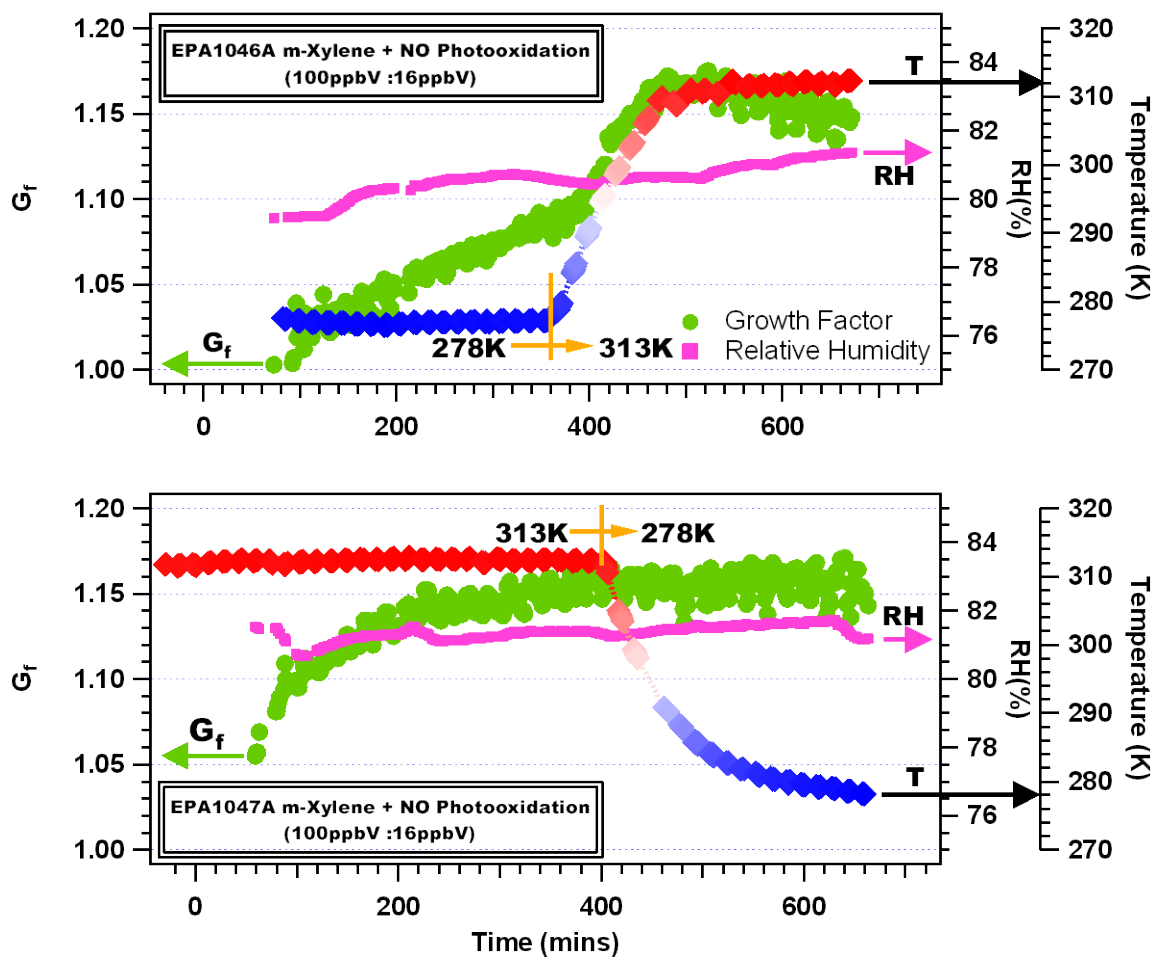


**Figure 4.1** Aerosol formation results for three selected temperature experiments; all three dry non-seeded photooxidation with initial target concentration (*m*-xylene $\approx$ 100 ppb,  $\text{NO}_2\approx$ 16 ppb). Blue squares represent the experiment starting at 278 K for 6h irradiation and then heated to 313 K; green squares represent the experiment starting at 300 K for 7.5h irradiation and then cooled to 278 K; red squares represent the experiment starting at 313 K for 6h irradiation and then cooled to 278 K.

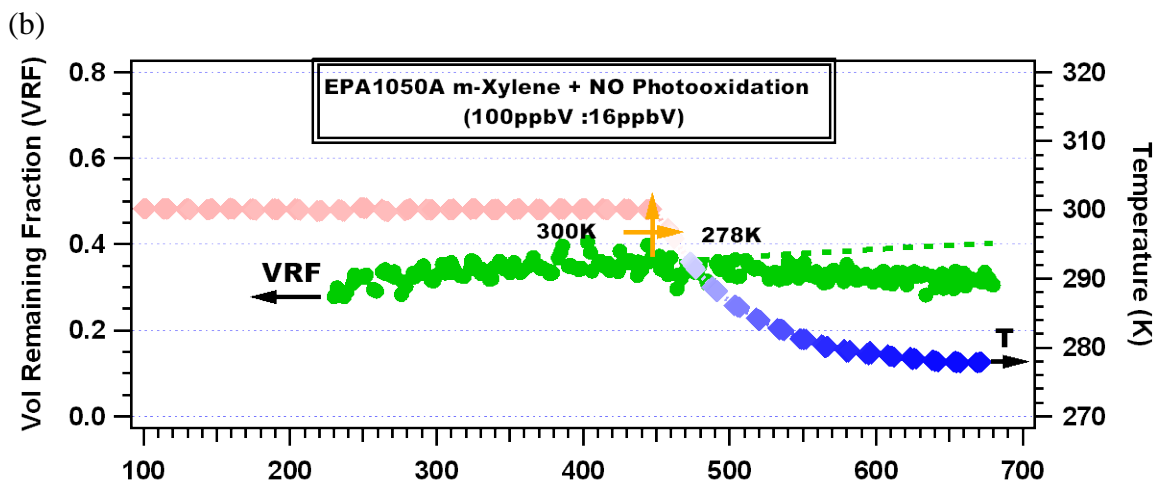
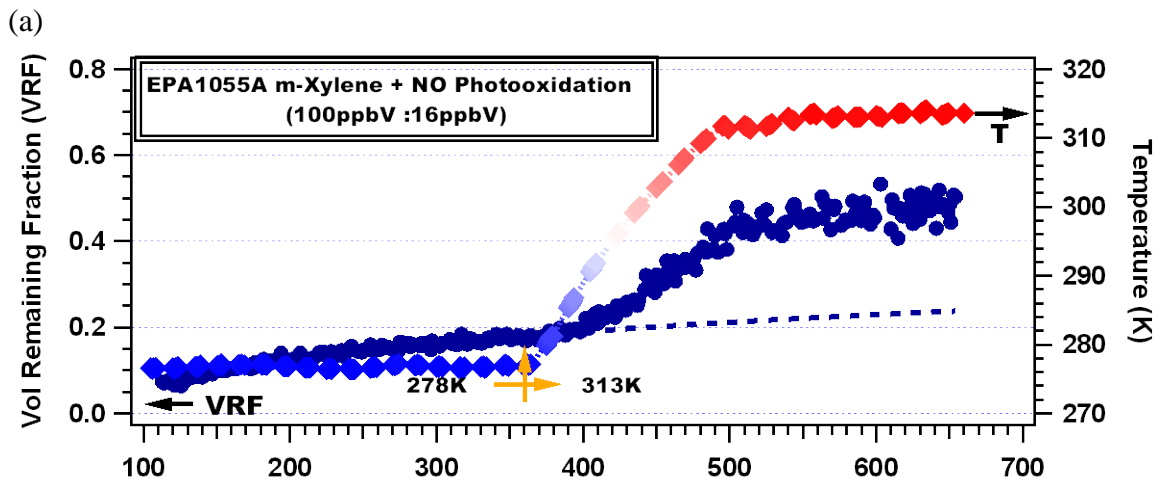




**Figure 4.2** The time evolution of particle density for four selected temperature experiments: initial concentrations *m*-xylene $\approx$ 100 ppb, NO<sub>2</sub> $\approx$ 16 ppb for (a)-(c); (a) 278 K $\rightarrow$ 313 K, (b) 313 K $\rightarrow$ 278 K, (c) 300 K $\rightarrow$ 278 K; 300 K $\rightarrow$ 313 K.



**Figure 4.3** Growth factor and RH for *m*-xylene photooxidation experiments at two different temperatures.



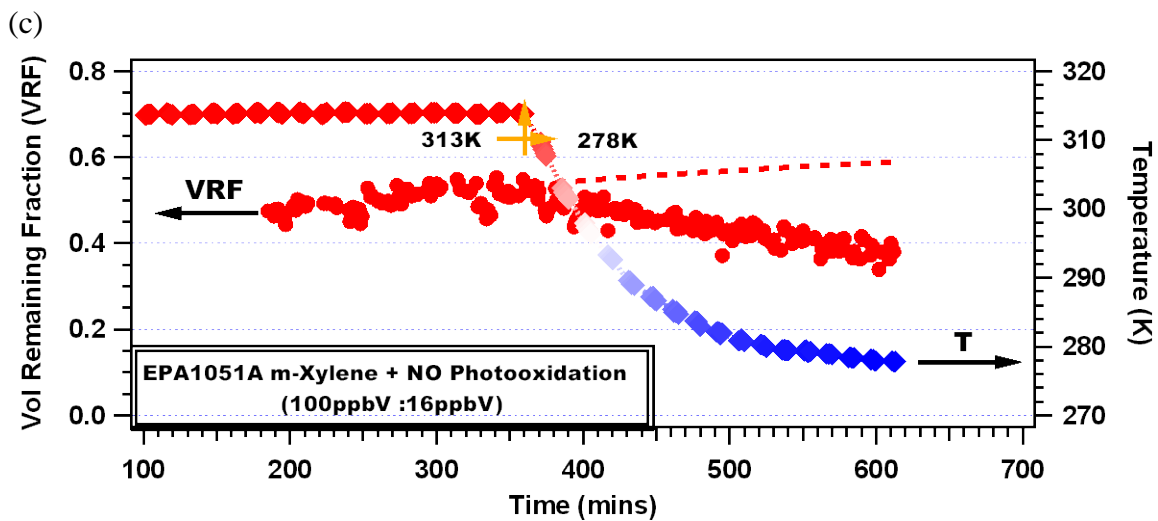


**Figure 4.4** The volume remaining fraction in typical operating schemes for *m*-xylene photooxidation experiment at three temperatures (a) 278 K  $\rightarrow$  313 K; (b) 300 K  $\rightarrow$  278 K; (c) 313 K  $\rightarrow$  278 K.

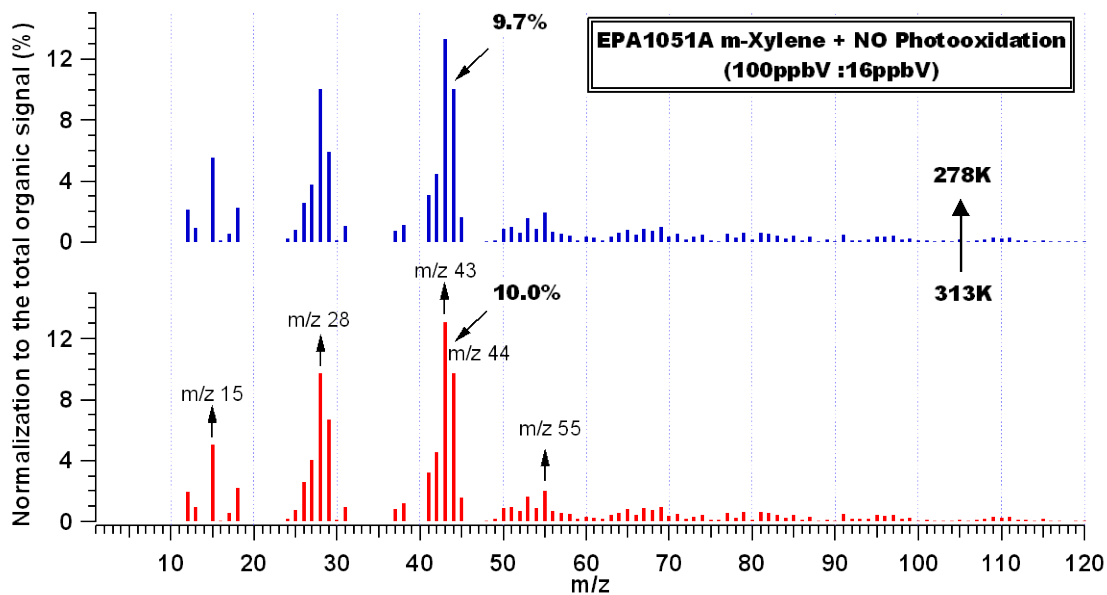
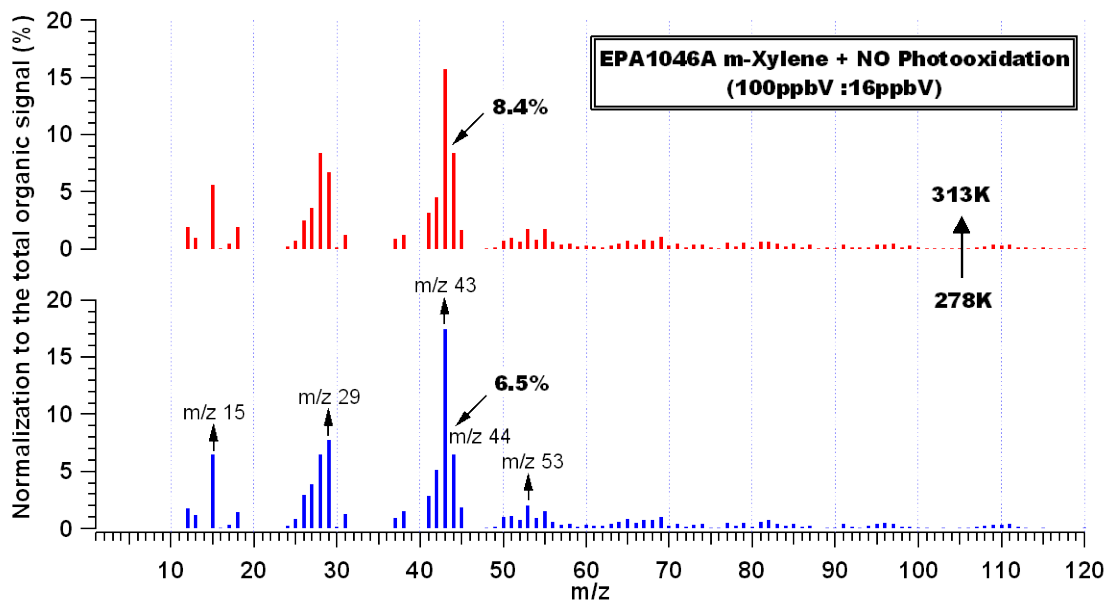


**Figure 4.5** The normalized average mass spectra of total organics for *m*-xylene photooxidation experiment at two temperatures (278 K, 313 K).



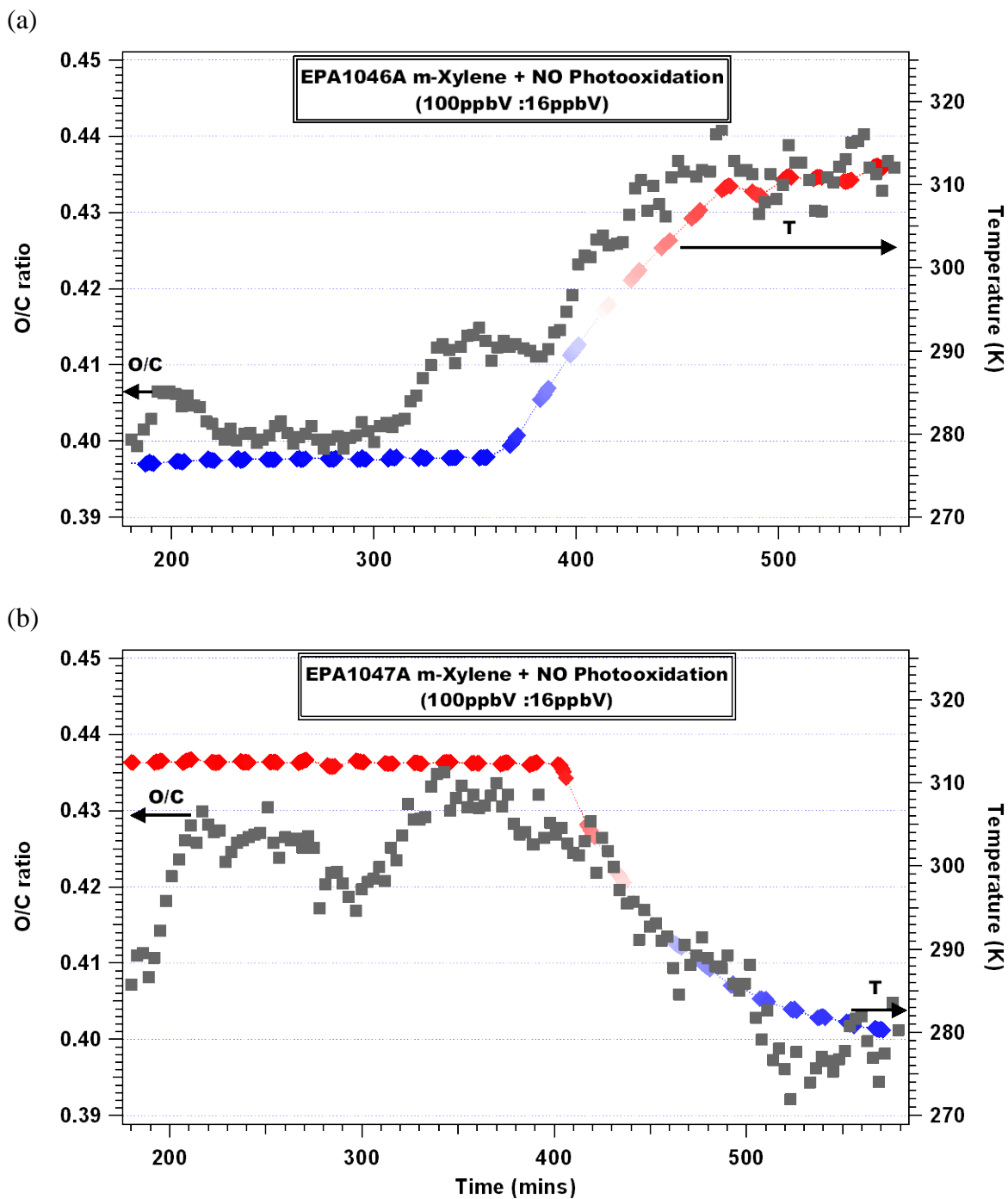


**Figure 4.6** The time series of O/C ratio for *m*-xylene photooxidation experiment at cold (a: 278 K→313 K) and hot temperature (b: 313 K→278 K). The grey square represents real-time O/C ratio.

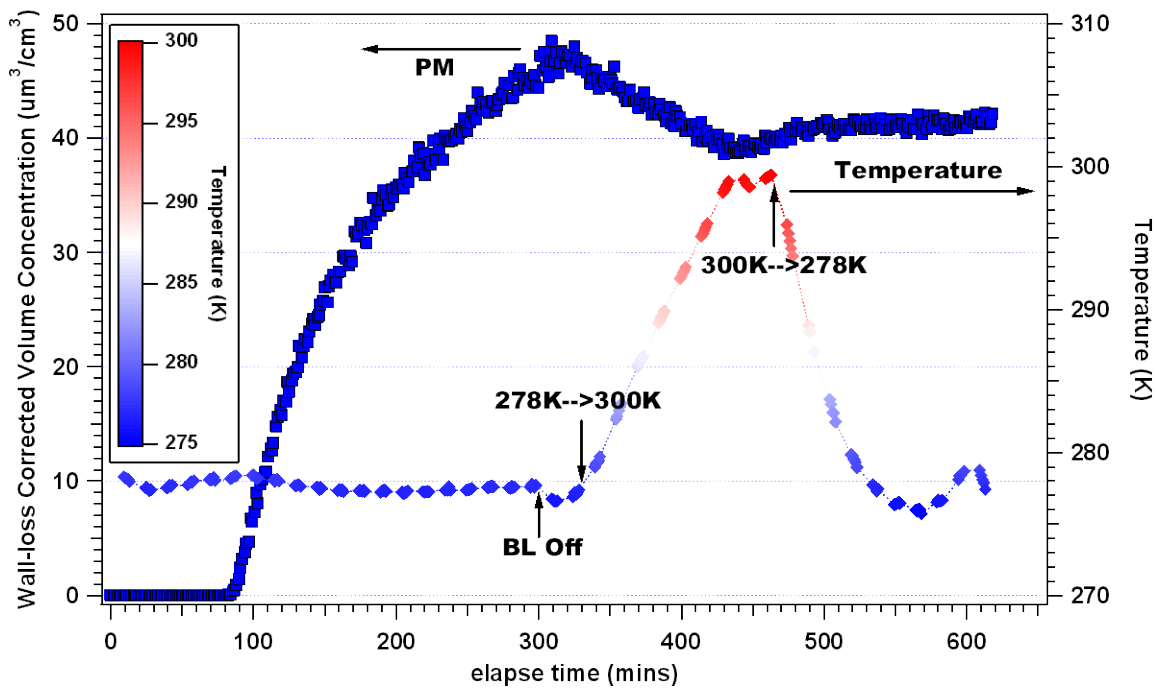


**Figure 4.7** Wall-loss corrected volume concentration for *m*-xylene photooxidation reaction (Targets: HC<sub>x</sub> : NO<sub>2</sub>=100 ppb:20 ppb)with temperature ramp from 278 K→300 K→278 K.

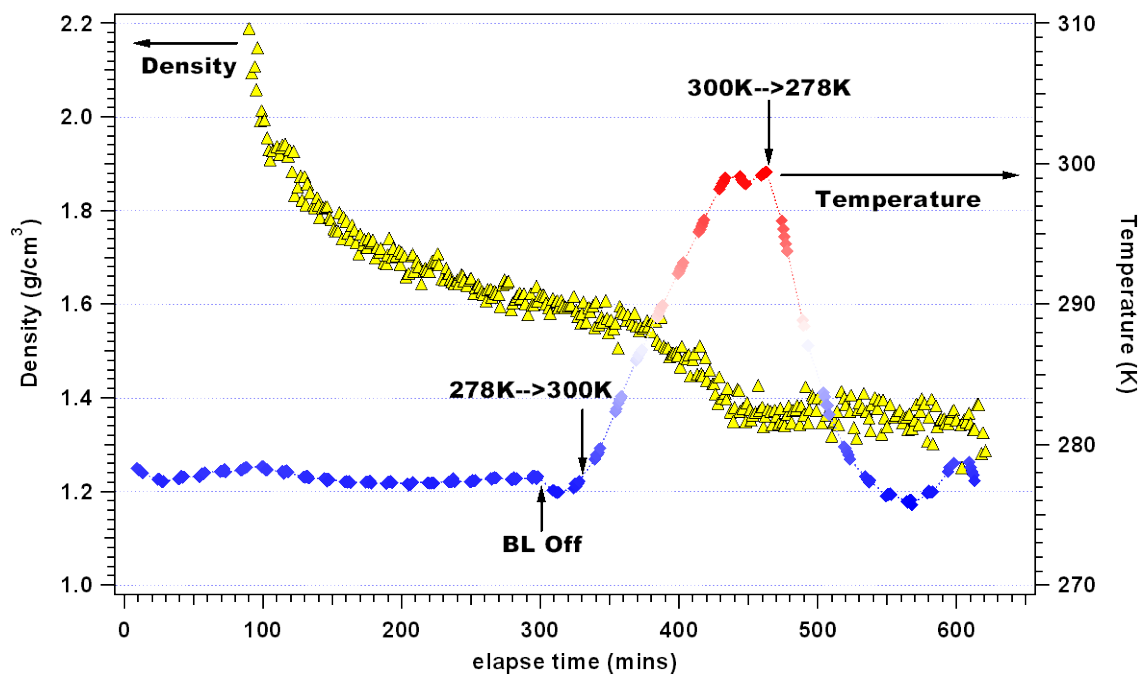


**Figure. 4.8** Particle density evolution for *m*-xylene photooxidation reaction (Targets: HC<sub>x</sub>:NO<sub>2</sub>=100 ppb:20 ppb) with temperature ramp from 278 K→300 K→278 K.

## Chapter 5

### 5.1 Introduction

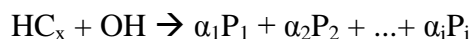
Secondary Organic Aerosol (SOA) refers to organic aerosol formed from gas-phase oxidative processing of volatile organic compounds (VOCs) in the atmosphere (e.g., Kroll and Seinfeld, 2008). SOA accounts for a majority of organic aerosol in the atmosphere. It comprises up to 80% of all organic aerosol present (Turpin, et al., 1995; Zhang et al., 2007) and contributes to climatic impacts, regional visibility reduction and potential health hazards (IPCC, 2007; Eldering and Cass, 1996; Davidson et al., 2005; Pope and Dockery, 2006).

The hydroxyl radical ( $\cdot\text{OH}$ ) initiates aromatic hydrocarbon oxidation often producing significant amounts of phenolic compounds (Atkinson, 1994). For example, a 25%-55% phenol yield is reported from  $\cdot\text{OH}$  oxidation of benzene (Atkinson et al., 1989; Bjergbakke et al., 1996; Berndt et al., 1999; Berndt and Böge 2001; Volkamer et al., 2002), while cresol isomers are identified to account for 15-42% of the products from  $\cdot\text{OH}$  oxidation of toluene (Atkinson et al., 1989; Klotz et al., 1998; Smith et al., 1998). Although initial oxidation of aromatics by  $\cdot\text{OH}$  are reasonably well understood, the continued oxidation of these products to form SOA remains poorly understood. A significant technical hurdle is the difficulty in identifying the majority of the aromatic SOA oxidation products.

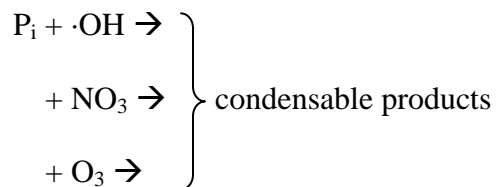
Song et al. (2005) described the relative importance of the hydroperoxy ( $\text{HO}_2$ ) reaction with organic peroxy ( $\text{RO}_2$ ) vs.  $\text{RO}_2$  reaction with  $\text{RO}_2$  routes with for the *m*-

xylene – NO<sub>x</sub> photooxidation system when evaluating SOA formation as a function of NO<sub>x</sub> concentration. Additionally, nitrophenol and nitrocresol products have been observed from phenol and o-cresol photooxidation, respectively (Grosjean, 1984, 1985; Atkinson et al., 1992). Additionally, small organic acid and aldehyde oxidation products such as pyruvic acid, acetaldehyde, nitro-aromatic products (Forstner et al., 1997), dicarbonyls and anhydrides (Arey et al., 2009) have been identified from the aromatic photooxidation reaction.

Aromatic photooxidation occurs through a multistep reaction pathway, initiated by ·OH oxidation, which may include one or more oxidants (O<sub>3</sub>, NO<sub>3</sub> or ·OH). This is simply expressed as:



where P<sub>1</sub> are condensable first generation products, P<sub>2</sub> are high-volatility products, and P<sub>i</sub> are intermediate products that continue to oxidize as:



A series of experiments focusing on *m*-xylene/NO<sub>x</sub> photooxidation using isotopically labeled (<sup>13</sup>C<sub>2</sub>) *m*-xylene and <sup>15</sup>NO coupled with mass spectroscopic analysis were performed in the UCR/CE-CERT environmental chamber to further elucidate the pathways for SOA formation from *m*-xylene oxidation.

## 5.2 Experimental Section

### 5.2.1 Facility Overview

Experiments were conducted in the UC Riverside/CE-CERT indoor environmental chamber, which is described in detail elsewhere (Carter et al., 2005). Dual 90 m<sup>3</sup> Teflon reactors are suspended by a rigid steel framework in a temperature-controlled enclosure which is continuously flushed with purified air. The enclosure was temperature controlled to  $300 \pm 0.5$  K for the experiments reported in this paper. The rigid framework slowly collapses the reactors during the experiments to minimize leaks and diffusion of contaminants into the reactors by maintaining a positive 0.03" H<sub>2</sub>O differential pressure between the reactors and enclosure. 115 W Sylvania 350 black lights were used as the light sources for these experiments. A known volume of high purity liquid hydrocarbon precursor (<sup>13</sup>C<sub>2</sub>) *m*-xylene: Sigma-Aldrich, 99% atom <sup>13</sup>C or (<sup>12</sup>C<sub>2</sub>) *m*-xylene: Sigma-Aldrich,  $\geq 99.5\%$ ) was injected through a heated glass injection manifold system and flushed into the chamber with pure N<sub>2</sub>. NO or <sup>15</sup>NO (Sigma-Aldrich, 98 atom % <sup>15</sup>N) was introduced by flushing pure N<sub>2</sub> through a calibrated glass bulb filled to a predetermined partial pressure of pure NO.

### 5.2.2 Particle and Gas Measurements

Particle size distributions between 28 and 735 nm are monitored with scanning mobility particle sizers (SMPS) located inside the temperature controlled enclosure. Particle sizing is verified with a suite of polystyrene latex spheres (PSL) (Duke Scientific Corp., Palo Alto, CA).

The evolution of particle elemental composition of aerosol particles is tracked using an Aerodyne High Resolution Time-of-Flight Aerosol Mass Spectrometry (HR-ToF-AMS) operating in high resolution mode (deCarlo et al., 2006). The HR-ToF-AMS has been described in detail previously (deCarlo et al., 2006) and improves on mass resolution by using a custom high-resolution ToFMS (Tofwerk, Switzerland). More recently, a new elemental analysis (EA) technique was developed using HR-ToF-AMS sampling data (Aiken et al., 2007; 2008). The method is based on the property of electron ionization (EI) for molecules containing small atoms such as C, H, N, O and S that the sum of the ion signal intensities from all fragments is approximately proportional to the mass concentration of the original organic species. Thus, if the elemental composition of each fragment ion signal in a mass spectrum can be identified (as with HR mass spectra), the average composition of the ions can be calculated. For a complex spectrum from an unknown molecule or mixture, the best estimate of the composition can then be found by summing up the ion contributions across the entire mass spectrum, which is then represented as estimated ratios of oxygen-to-carbon (O/C), hydrogen-to-carbon (H/C), and nitrogen-to-carbon (N/C). Estimated atomic ratios are used to calculate Organic Matter (OM)/Organic Carbon (OC). In this study, the fragment ions that contain  $^{12}\text{C}$  or  $^{13}\text{C}$ ,  $^{14}\text{N}$  or  $^{15}\text{N}$  of the aerosol was determined using the high resolution capabilities of the HR-ToF-AMS following the Peak Integration by Key Analysis (PIKA) template (deCarlo et al., 2006). Insulated sampling lines for APM, TDMA and AMS measurements prevented condensation/evaporation of semi-volatile components during sampling.

A gas chromatograph equipped with a flame ionization detector (GC-FID, Agilent 6890, Palo Alto, CA) monitors the parent hydrocarbon decay while a Proton Transfer Reaction Mass Spectrometer (PTR-MS, standard PTR-QMS series, Ionicon Analytik, Austria) monitored the concentrations of volatile and semi-volatile products in the gas phase with a proton affinity greater than that of water. Detailed description of working principles and applications of the PTR-MS is found in Lindinger et al. (1998). A Thermal Environmental Instruments Model 42C measured NO, NO<sub>y</sub> and (NO<sub>y</sub>-NO) concentration. A Dasibi Environmental Corp. Model 1003-AH monitored O<sub>3</sub>.

## 5.3 Results and Discussion

### 5.3.1 (<sup>13</sup>C<sub>2</sub>)*m*-xylene and (<sup>12</sup>C<sub>2</sub>)*m*-xylene Reaction Comparison

A series of experiments using isotopic (<sup>13</sup>C<sub>2</sub>)*m*-xylene or <sup>15</sup>NO were performed (Table 5.1) to evaluate our mechanistic understanding of SOA formation from aromatic hydrocarbons by tracking SOA formed with the methyl carbon (<sup>13</sup>C labeled) present relative to the ring carbon. Two nearly identical photooxidation experiments, one with 70 ppb of (<sup>13</sup>C<sub>2</sub>)*m*-xylene and one with 70 ppb (<sup>12</sup>C<sub>2</sub>)*m*-xylene, were conducted in the presence of 50 ppb of NO. The unit mass resolution (UMR) SOA spectrum from (<sup>13</sup>C<sub>2</sub>)*m*-xylene and (<sup>12</sup>C<sub>2</sub>)*m*-xylene SOA normalized by total organic signal is shown in Figure 5.1. The overall mass spectral pattern for *m/z* 10 to 90 (Figure 5.1 (a)) is similar for both isotopes with shifts of *m/z* ions attributed only to the presence of the <sup>13</sup>C present in the fragment (e.g. *m/z* 43 (C<sub>2</sub>H<sub>3</sub>O<sup>+</sup>) shifting to *m/z* 44 (<sup>13</sup>CCH<sub>3</sub>O<sup>+</sup>)). The mass spectral pattern from *m/z* 91 to 200 (Figure 5.1 (b)) is expected to include chemical information



associated with the ring. Apparent mass shifts of both +1 or +2 are observed in this range; e.g.,  $m/z$  95 from SOA derived from *m*-xylene photooxidation shifted to  $m/z$  96 for  $^{13}\text{C}$  labeled *m*-xylene. Similarly,  $m/z$  109, 121, 135 became  $m/z$  111, 123, 137, respectively indicating retention of the two  $^{13}\text{C}$  methyl groups in the SOA. Table 5.2 summarizes potential empirical formulas assignments for the most abundant ions in the aerosol for the isotopic reaction system. Possible reaction pathways are provided in Fig. 5.2 excerpted from Forstner et al. (1997). The identified ions in the SOA reflect the results of two major processes, H-atom abstraction by  $\cdot\text{OH}$  and  $\cdot\text{OH}$  addition to the ring. The latter reaction forms ring-retaining and ring-fragmentation products. As suggested in Fig. 5.2, the H-atom abstraction leads to the formation of *m*-tolualdehyde as intermediate product which is further oxidized to *m*-toluic acid ( $m/z$ 137, assigned as  $^{13}\text{C}_2\text{C}_6\text{H}_7\text{O}_2^+$ ). However, the major UMR mass fragments ions corresponding to this compound should also be present at  $m/z$  66, 92, 121. Although detected, these  $m/z$ 's are not significant. The  $\cdot\text{OH}$  addition pathway also yields ring-retaining and ring-fragmentation products. Ions detected at  $m/z$  123 and 125 proposed as  $^{13}\text{C}_2\text{C}_6\text{H}_9\text{O}^+$  and  $^{13}\text{C}_2\text{C}_6\text{H}_{11}\text{O}^+$ , respectively, may be produced via this pathway. Some of the smaller (lower  $m/z$ ) ions are then attributed to further fragmentation by electron ionization of these two compounds (loss of  $-\text{CH}_2$  or  $^{-13}\text{CH}_2$  groups). Arey et al. (2009) report that dicarbonyl products account for up to 52% of total gas-phase products in the *m*-xylene photooxidation system via further ring-opening and oxidation steps after the initial  $\cdot\text{OH}$  addition reaction. Ions at  $m/z$  43, 44, 55 associated with  $\text{C}_2\text{H}_3\text{O}^+$ ,  $\text{CO}_2^+$  and  $\text{C}_3\text{H}_3\text{O}^+$  contributed significantly to total organic signals. She speculates that these ions are potential fragments from dicarbonyl compounds. The

precursor hydrocarbon and partial gas-phase products was measured using online PTR-MS. The instrument successfully detects ( $^{13}\text{C}_2$ )*m*-xylene (at  $m/z$  109) and ( $^{12}\text{C}_2$ )*m*-xylene (at  $m/z$  107) and proves to be useful for identification of shift in mass charge ratio due to the isotopic carbon. Figure 5.3 showed time evolution of the mass spectra presumably assigned to acetaldehyde, formic acid, glyoxal, acetic acid, methyl-glyoxal and dicarbonyls. The volatile organic carbon products are expected to form via ring cleavage and further oxidation after the initial  $\cdot\text{OH}$  attached to the ring. The reaction pathways to form those gas-phase products are depicted in Fig. 5.4. And then the major compounds from isotopic and regular reactions as shown in Fig. 5.3 are used to validate the proposed mechanism. Comparing the isotope with the regular *m*-xylene reaction, three fourths of acetaldehyde formed in the regular system shifted by +1 and is identified as  $^{13}\text{CH}_3\text{CHO}$ . Formic acid, acetic acid and glyoxal maintain similar levels within these two systems and no shift in  $m/z$  is observed. Others  $m/z$ 's including  $m/z$  72, 98, 112 detected as  $m/z$  73, 99, 113, 114 from the regular ( $^{12}\text{C}_2$ )*m*-xylene photooxidation, exhibit shifts by +1 owing to the retention of  $^{13}\text{C}$ , while the evolution trend does indicate a slight difference between the potential assignment compounds at these  $m/z$ 's.

### 5.3.2 $^{15}\text{NO}$ and $^{14}\text{NO}$ Reaction Comparison

Experiments using isotopic  $^{15}\text{NO}$  and  $^{14}\text{NO}$  reaction with ( $^{12}\text{C}_2$ )*m*-xylene were performed to evaluate the importance of the  $\text{NO}_2$  adduct reaction after initial OH abstraction from the aromatic compound (Table 5.1, EPA931A and EPA932A). These two experiments were similar with initial concentrations of 80 ppb ( $^{12}\text{C}_2$ )*m*-xylene/50 ppb  $^{15}\text{NO}$  and 70 ppb ( $^{12}\text{C}_2$ )*m*-xylene/50 ppb  $^{14}\text{NO}$ , respectively. The HR-ToF-AMS UMR

organic mass spectrum, normalized with total organics, is presented in Fig. 5.5. The HR mass spectra for both NO and  $^{15}\text{NO}$  experiments were inspected from  $m/z$  10 to  $m/z$  150. The signals beyond  $m/z$  150 are below the noise level. Overall, there were no mass fragment shift except for those attributed to nitrate ions, indicating that none of the non-nitrate associated fragments contained both carbon and nitrogen. Therefore, we focus the rest of our investigation on  $m/z$  30, 46 and 63 (and corresponding +1  $m/z$  peaks for  $^{15}\text{NO}$  experiments).

High resolution mass spectra for nitrate signal were analyzed with the capability of Peak Integration by Key Analysis (PIKA) template (deCarlo et al., 2006; Aiken et al., 2008). The top two figures in Fig. 5.6 display  $m/z$  30 and 46 from  $(^{12}\text{C}_2)m\text{-xylene}/^{14}\text{NO}$  reaction, of which the major ion identifies as  $\text{NO}^+$  and  $\text{NO}_2^+$ . Similarly, the bottom two figures illustrate  $m/z$  31 and 47 from from  $(^{12}\text{C}_2)m\text{-xylene}/^{15}\text{NO}$  reaction, of which the major ion is  $^{15}\text{NO}^+$  and  $^{15}\text{NO}_2^+$ , respectively. Shown in Fig. 5.6 is the simplified mechanism of forming nitrogen-containing ring-retaining products, which give the nitrate fragments. The  $\cdot\text{OH}$  abstraction followed by the  $\text{NO}_2$  adduct to form the nitrophenol species is favored under extremely high levels of  $\text{NO}_x$ . In current study, the photooxidation reaction carried out initially at 100 ppb level of hydrocarbon and <100 ppb level of NO. Under these conditions, the reaction of aromatic-OH adduct with  $\text{NO}_2$  is not expected to be significant. Two typical experiments with  $\text{HC}_x$ : NO ratios of 6.25 and 1.4, respectively as low and high  $\text{NO}_x$  concentration conditions were selected to estimate the organic nitrate contribution to the total organics (Fig. 5.7). The principle described above with high resolution resolved peaks was applied to calculate the nitrate mass,

which excludes the interference ions assigned to nitrate when using the UMR mass spectra. The fraction was higher during nucleation and decreased during the condensational growth period for both experiments. The observation is consistent with density observations (described in the previous chapters) that the higher density at the onset of particle formation may be attributed to production of organic nitrates. That the organic nitrate signal only accounts for 5%-10% of total organic signal evidenced the insignificance of organic nitrate in this aromatic-NO<sub>x</sub> photooxidation reaction system.

## 5.4 Conclusions

This work evaluated the potential reaction pathways and organic nitrate contribution from selected *m*-xylene/NO photooxidation system by comparing aerosol products formed from regular (<sup>12</sup>C<sub>2</sub>)*m*-xylene and <sup>14</sup>NO and isotopic (<sup>13</sup>C<sub>2</sub>)*m*-xylene and <sup>15</sup>NO reactions. UMR mass spectra indicate the formations of ring-containing products via oxidation of methyl group or OH direct adduct on the ring. Fragment ions of ring open and oxidation products are detected in the particle phase and shifted using (<sup>13</sup>C<sub>2</sub>)*m*-xylene with HR-ToF-AMS. Some major products are also identified in the gas phase with PTR-MS and shifted with isotopic *m*-xylene, which proves the rationality of proposed reaction mechanism. Organic nitrate fragments are observed in the system but contribute less than 10% of total organic mass. With isotopic <sup>15</sup>NO, we confirm that no product ions contain –C–N– bond other than the nitrate compounds bonds of –NO and –NO<sub>2</sub>.

## 5.5 References

- Aiken, A. C., DeCarlo, P. F., Jimenez, J. L., 2007. Elemental analysis of organic species with electron ionization high-resolution mass spectrometry. *Analytical Chemistry* 79 (21), 8350–8358.
- Aiken, A.C., DeCarlo, P.F., Kroll, J.H., Worsnop, D.R., Huffman, J.A., Docherty, K., Ulbrich, I.M., Mohr, C., Kimmel, J.R., Sueper, D., Zhang, Q., Sun, Y., Trimborn, A., Northway, M., Ziemann, P.J., Canagaratna, M.R., Onasch, T.B., Alfarra, R., Prevot, A.S.H., Dommen, J., Duplissy, J., Metzger, A., Baltensperger, U., Jimenez, J.L., 2008. O/C and OM/OC Ratios of Primary, Secondary, and Ambient Organic Aerosols with High Resolution Time-of-Flight Aerosol Mass Spectrometry. *Environmental Science and Technology* 42, 4478-4485.
- Arey, J., Obermeyer, G., Aschmann, S., Cusick, R., Atkinson, R., 2009. Dicarbonyl products of the OH radical-initiated reaction of a series of aromatic hydrocarbons. *Environmental Science and Technology* 43, 683-689.
- Atkinson, R. Gas-phase tropospheric chemistry of organic compounds. *Journal of Physical and Chemical Reference Data* 1994, Monograph (2), 1-216.
- Atkinson, R. Kinetics and mechanisms of the gas-phase reactions of the hydroxyl radical with organic compounds. *Journal of Physical and Chemical Reference Data* 1989, Monograph (1), 1-246.
- Atkinson, R., Aschmann, S.M., Arey, J., 1992. Reactions of OH and NO<sub>3</sub> radicals with phenol, cresols, and 2- nitrophenol at 296±2K. *Environmental Science and Technology* 26, 1397-1403.
- Berndt, T., Böge, O., 2001. Gas-phase reaction of OH radicals with benzene: products and mechanism. *Physical Chemistry Chemical Physics* 3, 4946-4959.
- Berndt, T., Böge, O., Herrmann, H., 1999. On the formation of benzene oxide/oxepin in the gas-phase reaction of OH radicals with benzene. *Chemical Physics Letters* 314, 435-442.
- Bjergbakke, E., Sillesen, A., Pagsberg, P., 1996. UV spectrum and kinetics of hydroxycyclohexadienyl radicals. *Journal of Physical Chemistry* 100, 5729-5736.
- Carter, W.P.L., Cocker, D.R., Fitz, D.R., Malkina, I.L., Bumiller, K., Sauer, C.G., Pisano, J.T., Bufalino, C., Song, C., 2005. A new environmental chamber for evaluation of gas-phase chemical mechanisms and secondary aerosol formation. *Atmospheric Environment* 39, 7768-7788.

- Davidson, C.I., Phalen, R.F., Solomon, P.A., 2005. Airborne Particulate Matter and Human Health: A Review. *Aerosol Science and Technology* 39, 737-749.
- DeCarlo, P.F., Kimmel, J.R., Trimborn, A., Northway, M.J., Jayne, J.T., Aiken, A.C., Gonin, M., Fuhrer, K., Horvath, T., Docherty, K., Worsnop, D.R., Jimenez, J.L., 2006. Field-Deployable, High-Resolution, Time-of-Flight Aerosol Mass Spectrometer. *Analytical Chemistry* 78, 8281-8289.
- Eldering, A., Cass, G.R.: Source-oriented model for air pollutant effects on visibility. *J. Geophys. Res.-Atmos.*, 101, 19343-19369, 1996.
- Forstner, H.J.L., Flagan, R.C., Seinfeld, J.H., 1997. Secondary organic aerosol from the photooxidation of aromatic hydrocarbons: molecular composition. *Environmental Science and Technology* 31, 1345-1358.
- Grosjean, D., 1984. Atmospheric reactions of o-cresol: gas phase and aerosol products. *Atmospheric Environment* 18, 1641-1652.
- Grosjean, D., 1985. Reactions of o-cresol and nitrocresol with NO<sub>x</sub> in sunlight and with ozone-nitrogen dioxide mixtures in the dark. *Environmental Science and Technology* 19, 968-974.
- Intergovernmental Panel on Climate Change (IPCC) Fourth Assessment Report: Climate Change 2007.
- Klotz, B., Sørensen, S., Barnes, I., Becker, K.H., Etzkorn, T., Volkamer, R., Platt, U., Wirtz, K., Martín-Reviejo, M., 1998. Atmospheric oxidation of toluene in a large volume outdoor photoreactor: in situ determination of ring-retaining product yields. *Journal of Physical Chemistry A* 102, 10289-10299.
- Kroll, J.H., Seinfeld, J.H., 2008. Chemistry of secondary organic aerosol: Formation and evolution of low-volatility organics in the atmosphere. *Atmospheric Environment* 42, 3593-3624.
- Lindinger, W., Hansel, A., Jordan, A., 1998. On-line monitoring of volatile organic compound at pptv levels by means of Proton-Transfer Reaction Mass Spectrometry (PTR-MS) medical applications, food control and environmental research. *International Journal of Mass Spectrometry and Ion Processes* 173(3), 191-241.
- Pope, C.A., Dockery, D.W., 2006. Health effects of fine particulate air pollution: lines that connect, *Journal of the Air and Waste Management Association* 56, 709-742.

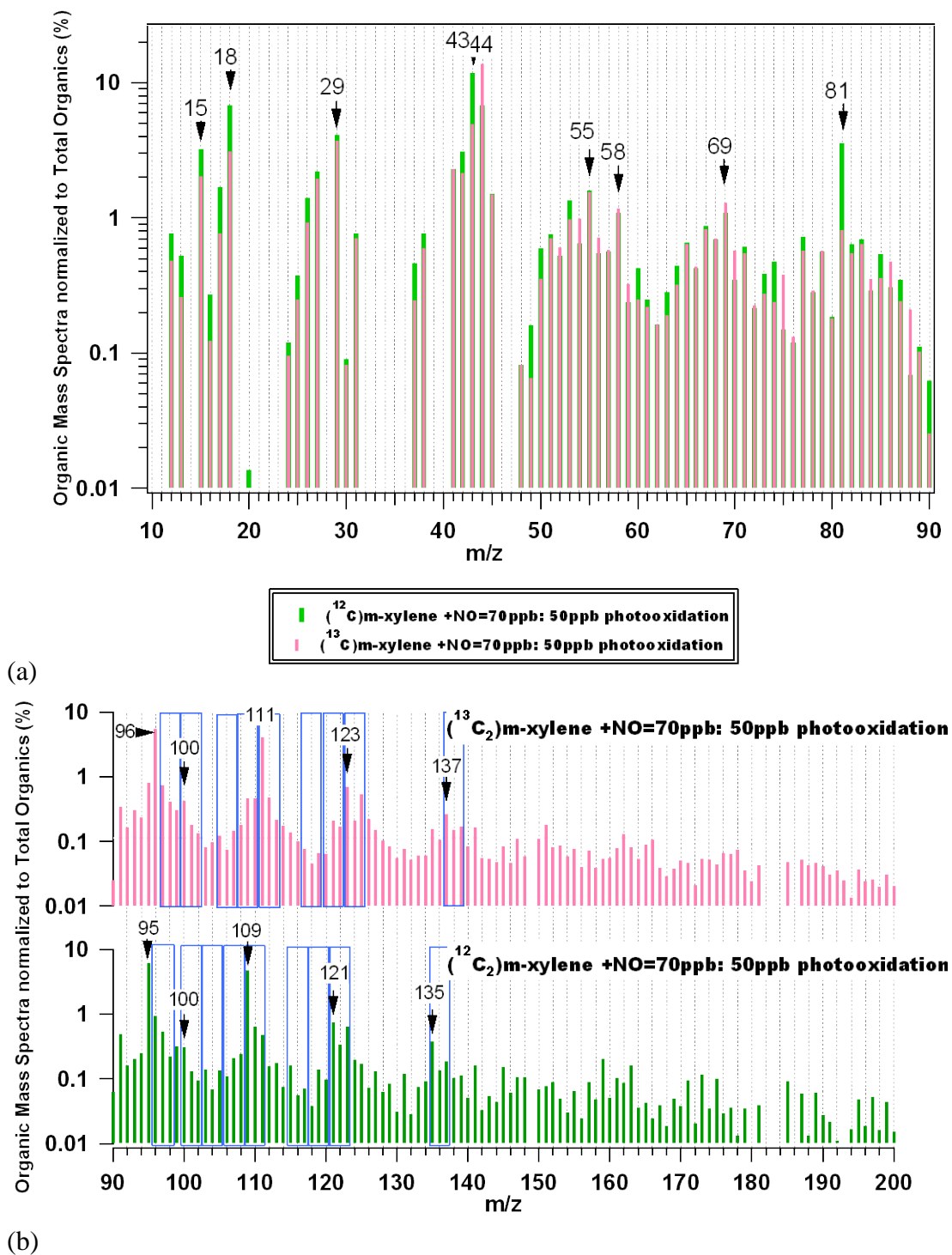
- Smith, D.F., McIver, C.D., Kleindienst, T.E., 1998. Primary product distribution from the reaction of hydroxyl radicals with toluene at ppb NO<sub>x</sub> mixing ratios. *Journal of Atmospheric Chemistry* 30, 209-228.
- Song, C., Na, K.S., Cocker, D.R., 2005. Impact of the hydrocarbon to NO<sub>x</sub> ratio on secondary organic aerosol formation. *Environmental Science and Technology* 39, 3143–3149.
- Turpin, B.J., Huntzicker, J.J.: Identification of secondary organic aerosol episodes and quantitation of primary and secondary organic aerosol concentrations during SCAQS. *Atmos. Environ.*, 23, 3527-3544, 1995.
- Volkamer, R., Klotz, B., Barnes, I., Imamura, T., Wirtz, K., Washida, N., Becker, K.H., Platt, U., 2002. OH-initiated oxidation of benzene: I. phenol formation under atmospheric conditions. *Physical Chemistry Chemical Physics* 4, 1598-1610.
- Zhang, Q., Jimenez, J. L., Canagaratna, M. R., Allan, J. D., Coe, H., Ulbrich, I., Alfarra, M. R., Takami, A., Middlebrook, A.M., Sun, Y. L., Dzepina, K., Dunlea, E., Docherty, K., De-Carlo, P. F., Salcedo, D., Onasch, T., Jayne, J. T., Miyoshi, T., Shimo, A., Hatakeyama, S., Takegawa, N., Kondo, Y., Schneider, J., Drewnick, F., Borrmann, S., Weimer, S., Demerjian, K., Williams, P., Bower, K., Bahreini, R., Cottrell, L., Griffin, R. J., Rautianinen, J., Sun, J. Y., Zhang, Y. M., Worsnop, D. R.: Ubiquity and dominance of oxygenated species in organic aerosols in anthropogenically-influenced Northern Hemisphere midlatitudes, *Geophys. Res. Lett.*, 34, L13801, doi:10.1029/2007GL029979, 2007.

<b>run</b>	<b>compound</b>	<b>HC<sub>i</sub><sup>a</sup></b> <b>(ppbV)</b>	<b>M<sub>0</sub><sup>b</sup></b> <b>(μm<sup>3</sup>/cm<sup>3</sup>)</b>	<b>NO<sub>x,i</sub></b> <b>(ppbV)</b>	<b>RH</b> <b>(%)</b>	<b>T</b> <b>(K)</b>
EPA928	( <sup>13</sup> C <sub>2</sub> ) <i>m</i> -xylene/NO	80.5	10.0	9.9	<0.5	300
EPA929	( <sup>13</sup> C <sub>2</sub> ) <i>m</i> -xylene/NO	85.2	16.3	43.8	<0.5	300
EPA931	( <sup>12</sup> C <sub>2</sub> ) <i>m</i> -xylene/NO	75.4	10.6	43.6	<0.5	300
EPA932	( <sup>12</sup> C <sub>2</sub> ) <i>m</i> -xylene/ <sup>15</sup> NO	86.2	13.2	50.0 <sup>c</sup>	<0.5	300

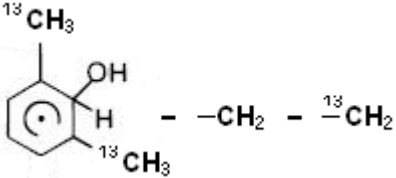
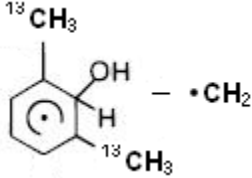
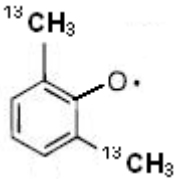
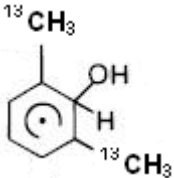
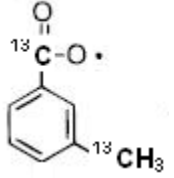
- a. Initial hydrocarbon concentration
- b. M<sub>0</sub> is wall loss corrected volume concentration following method outlined in Carter et al. (2005).
- c. Target concentration

**Table 5.1** Experimental conditions and results for the *m*-xylene photooxidation systems





**Figure 5.1** UMR mass spectrum comparison for (a)  $(^{13}\text{C}_2)\text{m-xylene}/\text{NO}$  and (b)  $(^{12}\text{C}_2)\text{m-xylene}/\text{NO}$  (initial targets: 70 ppb *m-xylene* + 50 ppb NO).

Peak	Formula	Possible Structure*
43.017/43.053	$C_2H_3O^+ / C_3H_7^+$	
43.991/44.023	$CO_2^+ / ^{13}CCH_3O^+$	
55.017/55.057	$C_3H_3O^+ / C_4H_7^+$	
58.042	$C_3H_6O^+$	
69.031/69.071	$C_4H_5O^+ / C_5H_9^+$	
81.037/81.069	$C_5H_5O^+ / ^{13}CC_5H_8^+$	
96.057	$^{13}CC_5H_7O^+$	
111.08	$^{13}C_2C_5H_9O^+$	
123.08	$^{13}C_2C_6H_9O^+$	
125.1	$^{13}C_2C_6H_{11}O^+$	
137.06	$^{13}C_2C_6H_7O_2^+$	

**Table 5.2** List of major ion peaks observed for the reaction of ( $^{13}C_2$ )*m*-xylene/NO in the smog chamber and their potential assignments

Note: \* the OH radical can add to different position, therefore, product isomers may co-exist in the system.

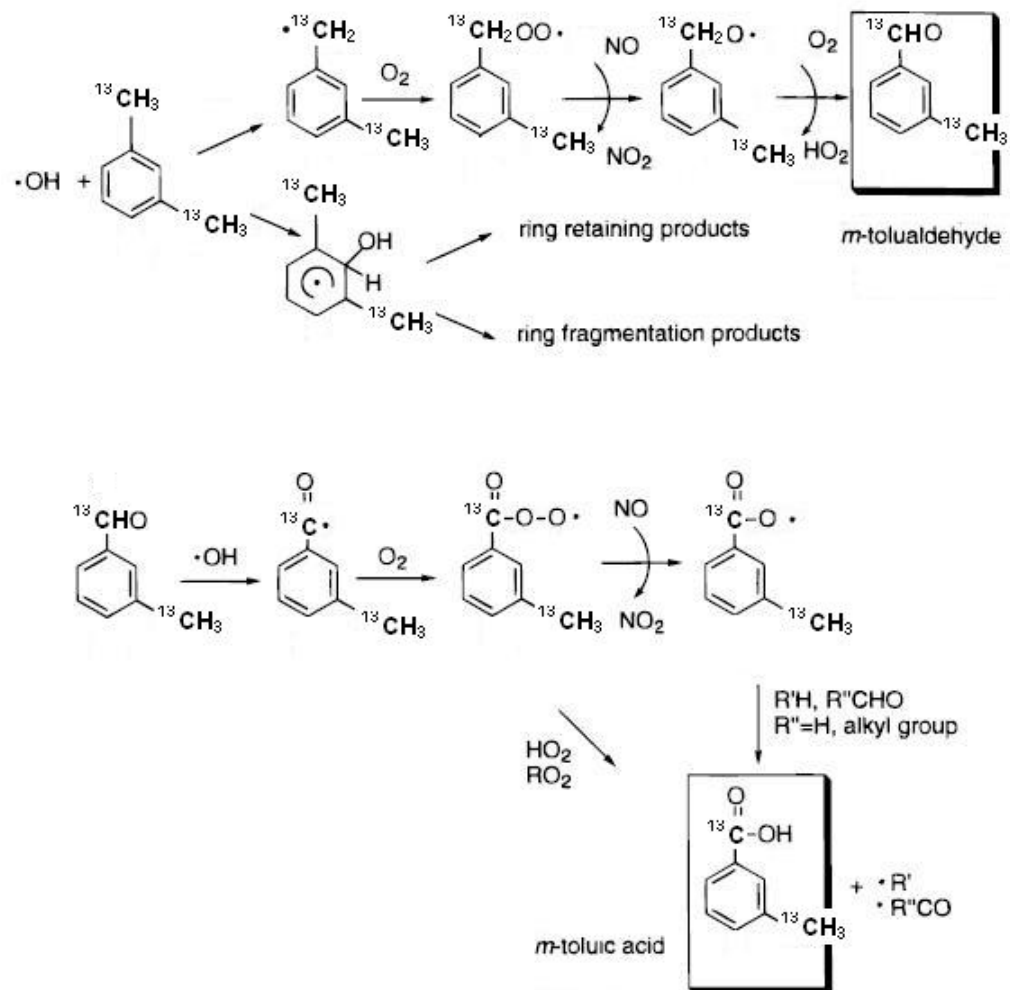


**Figure 5.2**  $(^{13}\text{C}_2)\text{-}m\text{-xylene-OH}$  initial reaction split and details of abstraction path. Modified based on Forster et al., (1997).

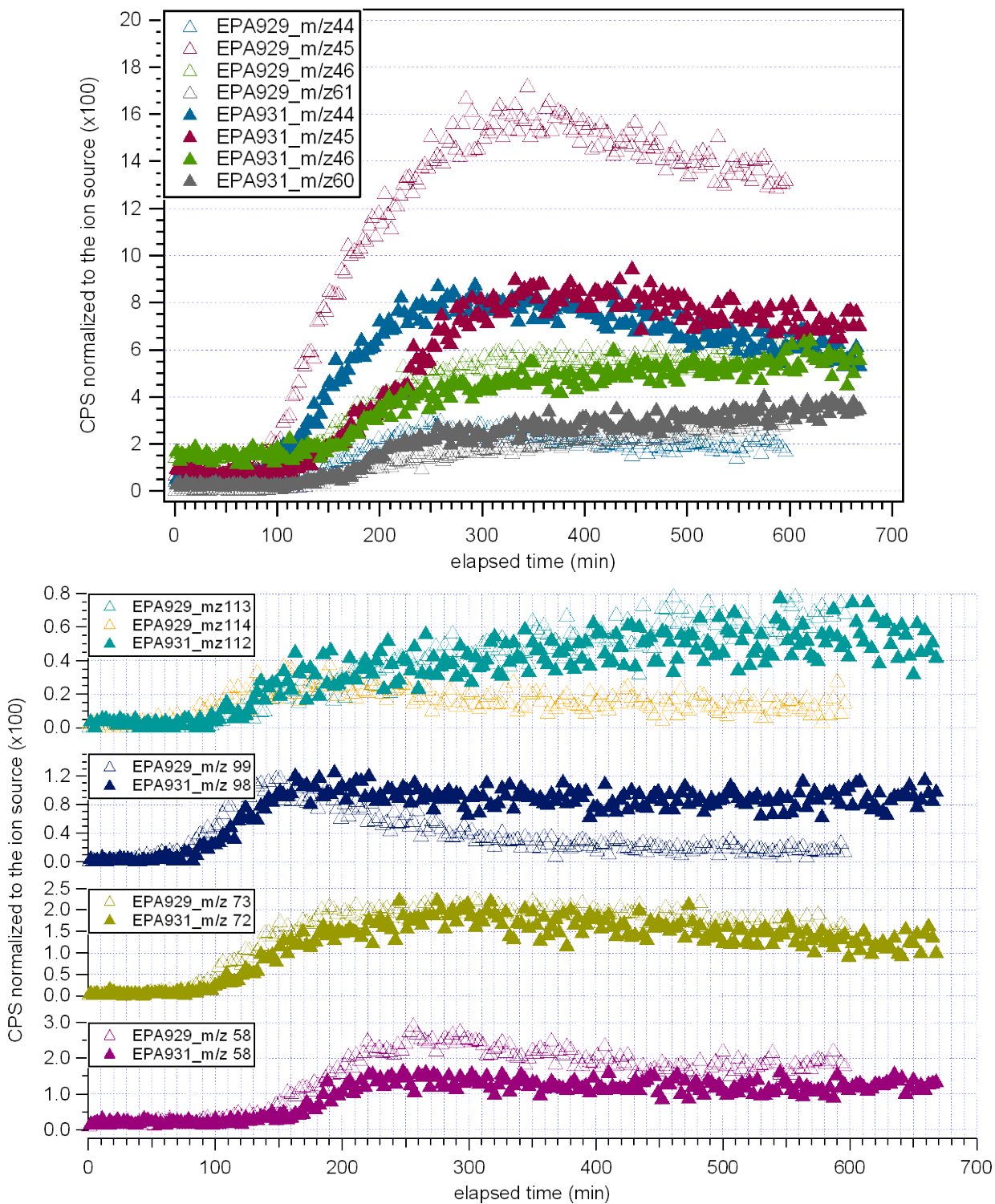


**Figure 5.3** Real time measurements of major gas-phase products from PTR-MS

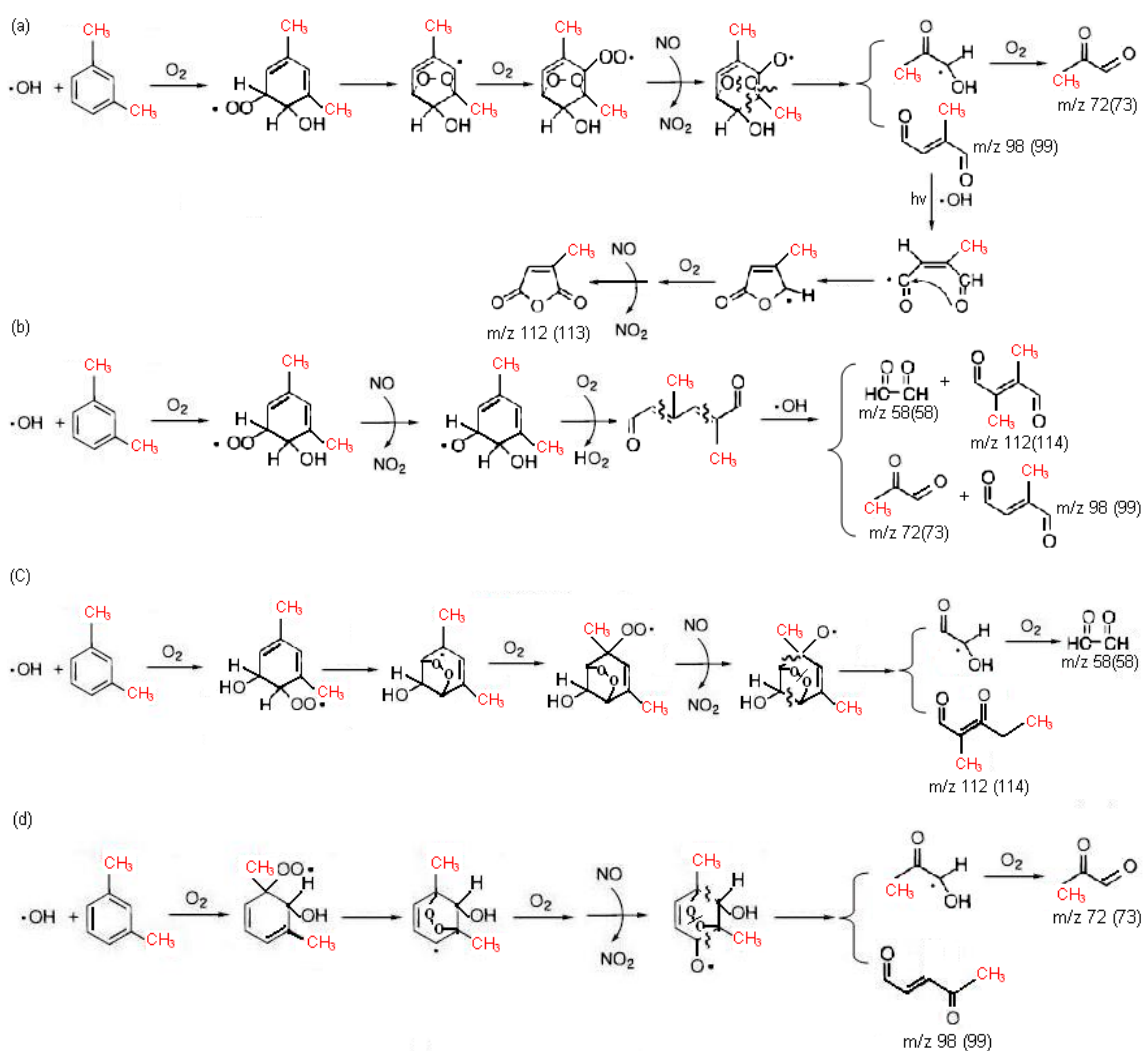


**Figure 5.4** Mechanism of *m*-xylene-OH reaction leading to the major gas-phase products  
 Note: the red methyl group indicates where the isotopic  $^{13}\text{C}$  is. *m/z* below the compound is the mass charge ratio for regular ( $^{12}\text{C}_2$ )*m*-xylene reaction and in the bracket is the ratio for isotopic ( $^{13}\text{C}_2$ ) *m*-xylene reaction.

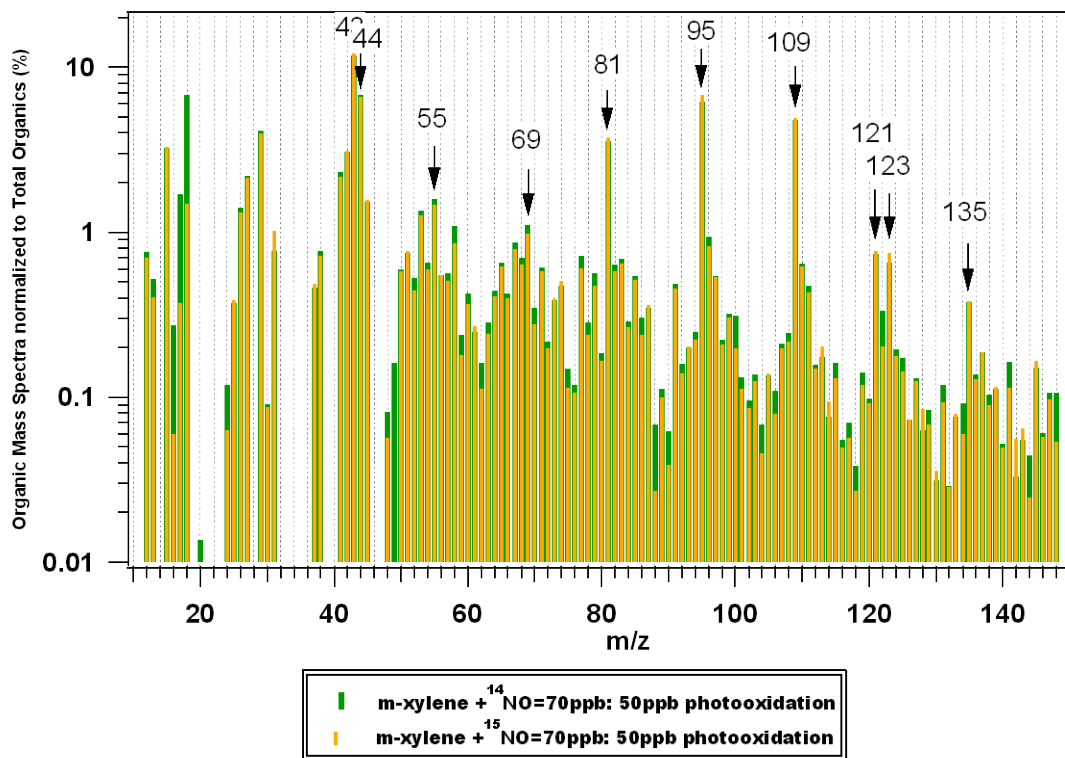


**Figure 5.5** UMR mass spectrum comparison for (<sup>12</sup>C<sub>2</sub>)m-xylene /<sup>14</sup>NO and (<sup>12</sup>C<sub>2</sub>)m-xylene /<sup>15</sup>NO photooxidation reactions

Note: No UMR <sup>14</sup>N nitrate signal: m/z 30, 46, 63 shown; m/z 31, 47, 64 corresponding to <sup>15</sup>NO is shown.

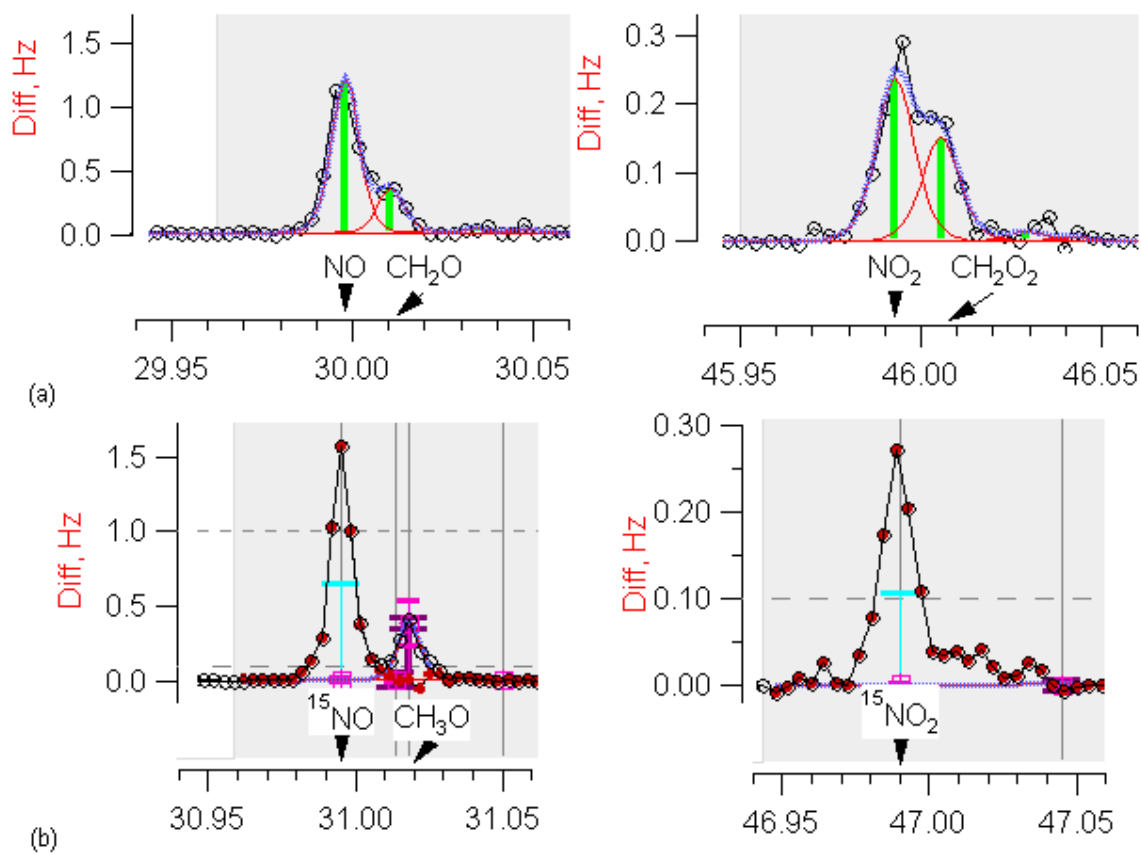


**Figure 5.6** Example of high resolution spectra of (a)  $m/z$  30 and 46 for  $(^{12}\text{C}_2)m$ -xylene  $/^{14}\text{NO}$  and (b)  $m/z$  31 and 47 for  $(^{12}\text{C}_2)m$ -xylene  $/^{15}\text{NO}$  photooxidation reactions, specifically.

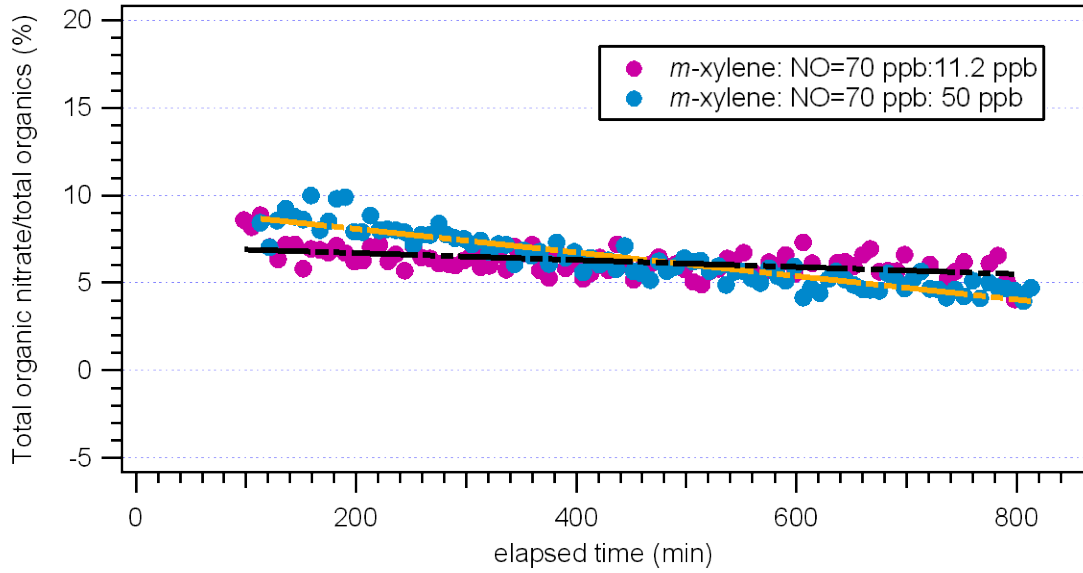


**Figure 5.7** Contribution of organic nitrate to total organics for high and low HC<sub>x</sub>: NO cases. Dash lines are fit with linearity.



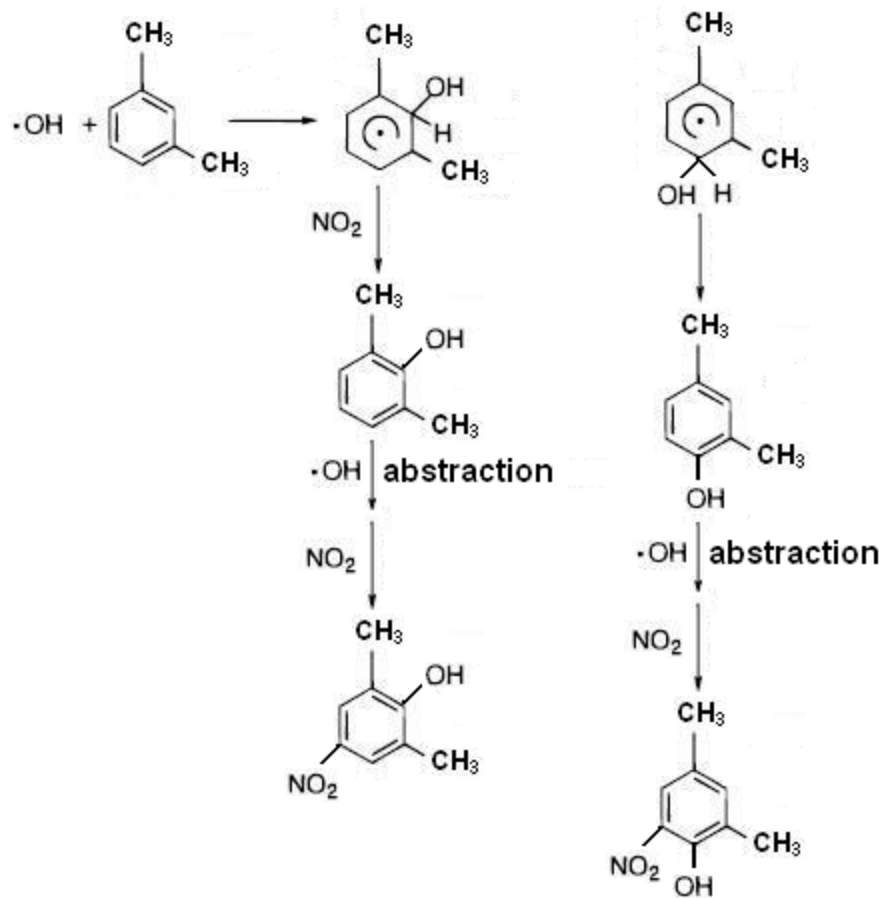


**Figure 5.8** Reaction of  $\text{NO}_2$  resulting from *m*-xylene-OH reaction leading to observed organic nitrate

## **Chapter 6**

### **6.1 Introduction**

Biomass combustion emissions contribute significantly to aerosol species in the atmosphere (Crutzen and Andrea, 1990). Particle emissions mainly arise from natural fires, prescribed burns, and residential wood combustion, which affect climatic impacts, regional visibility reduction and potential health hazards (Naeher et al., 2007, Watson, 2002). Although biomass burning emission in the United States is reported to account for only ~5% of annual average emissions (van der Werf et al., 2006), they play a significant role in urban and regional air quality (McMeeking et al., 2006; Park et al., 2006, 2007; Robinson et al., 2006). Park et al. (2007) estimated that biomass burning contributed about 50% of the annual mean total particulate carbon concentration within the U.S., and that summer wildfires drove the greatest variability in observed total particulate carbon. In addition, wood smoke emissions from wildfires and prescribed burns are responsible for occasional severe episodes of air pollution (Fraser and Lakshmanan, 2000; Phuleria et al., 2005). Prescribed burns are carried out to protect manmade structures, residential communities and the natural pattern of an ecological system. With the frequency and magnitude of wildfires increasing in some regions, it is expected that the demand for prescribed burns will increase in vulnerable regions, resulting in enhanced impacts from biomass burns (Spracklen et al., 2007; Haines et al., 2001).

Models require information input including burned area, fuel loading inventories and fuel-based emission factors (EFs) to estimate fire emissions and their impacts.

Emission factors are defined as the mass of a chemical species emitted to the mass of fuel burned (e.g. Schultz et al., 2008; Wiedinmyer et al., 2006). EFs have been extensively measured in the laboratory and field in the past 40 years, however, there remains a significant uncertainty and variability in estimates from different geographic regions (Schultz et al., 2008; Wiedinmyer et al., 2006). Andrea and Merlet (2001) compiled EF for three ecosystem types: savanna and grassland, tropical forests and extratropical forests based on a full literature review. However, the recommended values did not necessarily reflect the specific fuel types and combustion conditions. Battye and Battye (2002) also summarized previous work on EF that has been applied to field studies, primary emissions from fires in forest regions in the northwestern US and Alaska, as well as chaparral fires in southeastern US (Cofer et al., 1988a, 1988b; Friedli et al., 2001; Hays et al., 2002; Muhle et al., 2007; Yokelson et al., 1999). While field studies have the advantage of measuring emissions from real fires, controlled laboratory studies are used to fill in informational gaps in burn time, space and combustion phase. Some laboratory studies of biomass fuel burns have been published (Chakrabarty et al., 2006; Chen et al., 2006, 2007; Hays et al., 2002), but measurements of emission from individual chaparral or southwestern US plant species are very rare (McMeeking et al., 2009).

This project aimed to provide the EF of PM<sub>2.5</sub> and gaseous pollutants for southwestern biomass fuels. The study took place at the U.S. Forest Service's Fire Sciences Laboratory at Missoula, Montana. We deployed a comprehensive set of measurements that include both gas-phase and speciated particle-phase emissions. More specifically, for biomass burning smoke aerosol, real-time particle size distribution,

number and volume concentrations, total surface area, and elemental composition are measured simultaneously with filter and other substrate sampling for offline analysis. This chapter herein focuses on the chemical composition analysis using high-resolution time-of-flight aerosol mass spectrometer (HR ToF-AMS). The elemental ratios (organic matter/organic carbon (OM/OC), oxygen/carbon (O/C), hydrogen/carbon (H/C), nitrogen/carbon (N/C)), mass spectra, and levoglucosan analysis for nine plant species during flaming and smoldering phases are presented.

## **6.2 Experimental Section**

### **6.2.1 Fuel selection and treatment**

Fuel characterization and fuel bed configuration are very important parameters to determine particle emissions. In this study, a total of 49 burns, consisting of 9 different types of plant species representative of this ecosystem (Table 6.1), were burned individually. Chamise (*Adenostoma fasciculatum*) is an evergreen shrub and the leaves are shiny with flammable oils especially in warmer weather. California sagebrush, of the *Asteraceae* family, is a shrub that grows in coastal sage scrub, coastal strand, chaparral, and dry foothill communities. Coastal sage scrub is a low scrubland community (or soft chaparral) characterized by low-growing aromatic, and drought-deciduous shrubs adapted to the semi-arid Mediterranean climate of the coastal lowlands. Maritime chaparral is dominated by woody shrubs such as Manzanita and found only in areas with a predominance of summer fog. Oak savanna is a type of savanna, or lightly-forested grassland, with oaks as the dominant tree species. California oak woodland is a plant

community found throughout the California chaparral and woodlands eco-region of California and northwestern Baja California. The dominant trees are oaks, interspersed with other broadleaf and coniferous trees, with an understory of grasses, herbs, geophytes, and California native plants. Mesquite is a leguminous plant of the *Prosopis* genus which is an extremely hardy, drought-tolerant plant. Ceanothus is a genus of about 50-60 species of shrubs or small trees in the buckthorn family *Rhamnaceae*. The majority of the species are evergreen, but the handful of species adapted to cold winters is deciduous. Ceanothus species are easily identified by their unique leaf-vein structure shared by all plants within this genus. Manzanita is a common name for many species of the genus *Arctostaphylos*. They are evergreen shrubs or small trees present in the chaparral biome of western North America. They are characterized by smooth, orange or red bark and stiff, twisting branches. Samples of chamise and ceanothus were collected from Ft. Hunter-Liggett (CA), about 400 km northwest of Los Angeles. Samples of Manzanita, California sage, coastal sage and maritime chaparral were collected from Vandenberg Air Force Base (CA), about 250 km northwest of Los Angeles. Samples of oak savanna, oak woodland and mesquite were collected from Ft. Huachuca (AZ), about 900 km southeast of Los Angeles. These fuels represent chaparral and oak woodland from southwestern U.S. They often grow so densely that it is all but impenetrable to large animals and humans. This, and its generally arid condition, makes it notoriously prone to wildfires. Clinton et al. (2006) estimated that ~ 80% of the fuels consumed by major wildfires in southern California in 2003 were attributable to shrubs and duffs. Bulk characteristics of the fuel beds are listed in Table 6.2. Average moisture content (oven-

dry mass basis, ASTM D4442-07) of the fuel beds at the time of burning ranged from 4 to 33%, similar to fuel moisture in dead fuels. The initial oven-dry mass in the fuel beds ranged from about 670 to 4630 g. Bulk density of the fuel beds ranged from 5.8 to 14 kg/m<sup>3</sup> and the packing ratio (defined as the ratio of fuel bulk density to fuel density) ranged from 0.010 to 0.024. These packing ratios for the southwestern fuels are similar to those reported for laboratory fire spread experiments (Weise et al., 2005), but 1 to 2 orders of magnitude larger than packing ratios observed in the field. 18 out of 49 fuel beds (chamise, ceanothus, manzanita, and California sagebrush) were ignited using a propane torch with the aid of small amount of isopropyl alcohol. The rest of the burns were initiated with only the propane torch. The fuel arrangement for burning significantly affected fuel consumption. The fuel beds were arranged horizontally (Fig. 6.1b) with up to 90% of fuel consumption percentage except for ceanothus. We attempted to arrange the chamise/scrub oak fuels vertically as found in nature (Fig. 6.1a), but the fire did not spread well resulting in an average consumption of 30 % for this fuel type.

### **6.2.2 Facility and combustion**

All the experiments were conducted in the combustion laboratory at the U.S. Forest Service's Fire Science Laboratory (FSL), Missoula, MT, (schematic displayed in Fig. 6.2). Detailed descriptions can be found elsewhere (Yokelson et al., 1996). The main combustion room measures 12.5m x 12.5m x 22m in height. The stack is located at the room center 2.1m above the ground and extends through the ceiling. The combustion exhaust is vented via a 3.6 m diameter hood attached to a 1.6 m diameter stack. Sampling ports that position near the center of the exhaust flow and pass through the walls of the

stack are located about 16.5 m above the floor. The instruments were deployed on a platform surrounding the stack at about the same height as the sampling ports. The lab is slightly pressurized with pre-conditioned outside air to precisely control temperature, and relative humidity. The air velocity in the chimney was set to 1.5 m/s or 3 m/s by controlling the exhaust fan speed to maintain proper entrainment of fresh air.

### 6.2.3 Real-time particle measurements

A dilution sampler was used to cool the sample prior to injection into the online instrumentation. In brief, an isokinetic sampling probe was inserted in the stack center. The sample flow was then diluted using a partial flow dilution system with a single venturi (Agrawal et al., 2008). A 13.5:1 ratio was determined using CO as a tracer. Dilution house air was treated with silica gel→charcoal denuder→HEPA in series. The diluted aerosol flow then passed through a PM<sub>10</sub> impactor to remove large particles present before distributing the sample flow to the HR-ToF-AMS and other online particle measurement instrumentation. Figure 6.3 depicts the schematic flow chart of sampling system in detail. This chapter here only presents the results of elemental composition of organic particle species from HR ToF-AMS for each individual fuel. The instrument operated in the high resolution mode and has been described in detail previously (DeCarlo et al., 2006) and improves on mass resolution by using a custom high-resolution ToFMS (Tofwerk, Switzerland). More recently, a new elemental analysis (EA) technique was developed using HR-ToF-AMS sampling data (Aiken et al., 2007; 2008). The method is based on the property of electron ionization (EI) for molecules containing small atoms such as C, H, N, O and S that the sum of the ion signal intensities from all

fragments is approximately proportional to the mass concentration of the original organic species. Thus, if the elemental composition of each fragment ion signal in a mass spectrum can be identified (as with HR mass spectra), the average composition of the ions can be calculated. For a complex spectrum from an unknown molecule or mixture, the best estimate of the composition can then be found by summing up the ion contributions across the entire mass spectrum, which is then represented as estimated ratios of O/C, H/C, and N/C. Estimated atomic ratios are used to calculate OM/OC. In this study, the C:O:H ratio of the total aerosol was determined using the high resolution capabilities of the HR-ToF-AMS following the Peak Integration by Key Analysis (PIKA) and Analytical Procedure for Elemental Separation (APES) templates (DeCarlo et al., 2006, Aiken et al., 2008).

#### 6.2.4 Real-time gas measurement

Fire integrated modified combustion efficiency (MCE) has been widely used in previous studies to describe combustion conditions. MCE is defined as the molar ratio of the emitted CO and CO<sub>2</sub> (Ward and Radke, 1993) and calculated as below,

$$MCE = \frac{[\Delta CO_2]}{[\Delta CO_2] + [\Delta CO]} \quad (6-1)$$

where  $[\Delta CO_2]$  and  $[\Delta CO]$  are the excess molar mixing ratios of CO<sub>2</sub> and CO. For stack smoke, MCE was calculated for each burn by dividing the total mass of CO<sub>2</sub> emitted by the net mass of CO<sub>2</sub> plus CO emitted. Ward and Radke (1993) classified combustion conditions into three phases based on MCE i.e., flaming when MCE > 0.97; mixed state when 0.85 < MCE < 0.97; smoldering when 0.75 < MCE < 0.85. Real-time



CO and CO<sub>2</sub> measurements were made using an Open-Path Fourier Transform Infrared (OP-FTIR) spectrometer.

## **6.3 Results**

### **6.3.1 Modified combustion efficiency**

We attempted to segregate the mode of combustion during each burn using instantaneous MCE value and other indicator while some other studies report combustion conditions by using integrated or averaged MCE over the entire burn. Accordingly, the combustion process was segregated into three phases, i.e. flaming, mixed and smoldering. Fire-integrated mean MCE values for selected burns covering all 9 vegetation ranged from approximately 0.980-1.014, 0.871-0.912, and 0.817-0.900 with standard deviation from 0.008-0.049, 0.026-0.049, and 0.008-0.036 for flaming, mixed and smoldering periods, respectively. The MCE results are displayed in Fig. 6.4. The fuel moisture content is below 15% except for oak woodland. However, we do not observe a dependence of MCE on fuel moisture as reported in other study (Mcmeeking et al., 2009) for the fuel moisture content less than 15%. Regards to the medium level of fuel moisture, the oak woodland appears to have the lowest MCE during flaming phase and highest MCE during the mixed and smoldering phases.

### **6.3.2 Mass spectra of different southwest fuel types**

Figure 6.5 shows the average unit mass resolution (UMR) mass spectra of organics, nitrate, sulfate, ammonia and chloride throughout flaming, mixed and

smoldering phases of burn for the nine southwestern biomass fuels. One burning experiment was selected for each type of fuel and each m/z was normalized to the total organic mass.

Since the majority of particle mass are emitted during flaming and mixed phases, the mass spectra pattern of relative intensity under these particular combustion conditions more closely represents the results of the entire burn. Generally, the hydrocarbon fragment ions  $C_nH_{2n-1}^+$  such as  $C_3H_5^+$  at m/z 41,  $C_4H_7^+$  at m/z 55 and  $C_5H_9^+$  at m/z 69 and  $C_nH_{2n+1}^+$  such as  $C_2H_5^+$  at m/z 29,  $C_3H_7^+$  at m/z 43,  $C_4H_9^+$  at m/z 57 significantly dominate the m/z patterns for all fuels. The observations are consistent with those Weimer et al. (2008) reported for the European forest and residential wood types using quadruple-AMS (Q-AMS). However, differences in the characteristics varied by fuel type. In summary, the mass spectra of particle emissions is characterized by the fragment m/z 44 ( $CO_2^+$ ) predominant possibly owing to decarboxylation of oxo- and dicarboxylic acids (Alfarra et al., 2006) for the coastal sage, California sage, oak savanna and Manzanita. The reason could be that when there are still a lot of biopolymers such as cellulose and lignin available indicated by the hydrocarbon fragments while more readily oxidized organics are found simultaneously due to the easy and fast combustion properties of these fuels. In addition, Andrea and Merlet (2001) stated that the flaming phase can exhibit strong variation depending on different internal parameters such as moisture. There is significant contribution of chloride emission during the flaming phase for all the fuels with the exception of oak woodland. Maritime chaparral and California sage scrub have the highest fractions. When the fire goes to mixed phase, dramatic

decrease in chloride emission was observed in Ceanothus and Chamise compared to the other six fuels. For sulfate emission, maritime chaparral, California sage scrub, chamise, Manzanita, mesquite, oak woodland have higher contribution fractions than coastal sage brush, Ceanothus, and oak savanna. During the mixed phase, only Manzanita and California sage scrub have decent amount of sulfate emitted, indicating the majority of sulfur containing compound in the other fuels burned rapidly and emitted instantaneously as the fire lid. The emissions of nitrate and ammonia seem to occur and maintain relatively the same level in both phases for most of the fuels. When the fire goes to smoldering phase, organics become dominant while all the inorganic species fade significantly.

The relative contributions of  $m/z$  29, 43, 44, 60 and 73 to the total organic mass were shown in Table 8.3 to evidently reveal the chemical composition of all fuel types. No substantial difference is seen for all the fuel types with an exception of higher  $m/z$  44 and lower  $m/z$  29 fractions for Manzanita case. A highest and lowest contribution of levoglucosan reflected by  $m/z$  60 and 73 were observed for oak savanna and sage species, respectively. More details will be discussed in later section. Additionally, the mass spectra from all biomass fuel types do not hint to a specific mass spectral signature that can be used exclusively for a specific species assignment.

### **6.3.3 Bulk chemical composition**

Elemental carbon (EC) and OC emission factor from many biomass fuels has been extensively characterized earlier (Hays et al., 2005; Mazzoleni et al., 2007; Habib et al., 2008; Mcmeeking et al., 2009) as bulk chemical analysis of carbonaceous aerosol.

This work reports new measurements of bulk chemical composition of organic carbonaceous species using HR-ToF-AMS. As a result of both the extensive fragmentation caused by electron impact ionization and the thermal decomposition of molecules by the vaporizer, most of the signal intensity in the HR-ToF-AMS occurred below mass to charge ratio ( $m/z$ ) 100; parent molecular peaks were weak or unobserved. Therefore, the EA was conveniently applied to the data set of collected samples and interpreted as bulk chemical composition. To the author's best knowledge, this is the first time that real time elemental ratios and empirical formula derived with respect to MCE have been reported.

Figure 6.6 shows an example of time evolution of O/C, H/C, N/C and OM/OC during flaming, mixed and smoldering phases from Chamise burn. Similar analyses are made to the other fuels as well. The average elemental ratios for each fuel during flaming, mixed and smoldering are then derived and displayed in Fig. 6.7. The O/C ratio during flaming periods ranged from 0.200-0.476 with standard deviation of 0.051-0.090. The H/C ratio ranged from 1.435-1.764 with standard deviation of 0.068-0.108. The N/C ratio ranged from 0.026-0.325 with standard deviation of 0.005-0.165. Similarly, the mean O/C, H/C and N/C are 0.170-0.432, 1.484-1.713 and 0.024-0.377 for mixed phase. And the ratios during the smoldering phase are found to be 0.155-0.372, 1.493-1.749 and 0.070-0.519. Note that the MCE of oak savanna remained high during the entire burn; there is no obvious smoldering phase for that fuel species. The empirical formulas of organic carbonaceous aerosol derived from EA from each fuel during different combustion phase were summarized in Table 6.4. In general, the O/C and H/C ratios are

close for the flaming, mixed and smoldering phases, while N/C ratio varies to much higher extent with bigger uncertainty. The possible reason can be attributed to the distinct behavior that nitrogen element participates in the combustion process under different conditions. Overall, the Rangeland ecosystem group including California sage brush and California sage scrub show the highest oxygen content level. The Chaparral ecosystem group which contains ceanothus, chamise and Manzanita has lower O/C during the flaming phase while higher oxygen content level during the mixed phase compared to the Coastal plain ecosystem including oak savanna and oak woodland.

#### **6.3.4 Comparison of organic mass based on organic carbon using two methodologies**

A correction factor is conventionally used to compute the total organic mass concentration, accounting for associated O, H, N, and other elements from measured C mass concentrations attributable to OC. The most common method is to use a thermal-optical carbon analyzer (Sunset Laboratories, Forest Grove, OR) and NIOSH method 5040 to determine the organic/elemental carbon collected on a Quartz media. The concentrations of individual elements and water-soluble ions are analyzed by energy dispersion X-ray fluorescence (XRF) and ion chromatography (IC), respectively. The results for this analysis can be found in a separate paper by Ehsan et al. (manuscript in preparation, 2010). Thus  $PM_{2.5}$  mass emissions can be reconstructed by summing all identified aerosol species, which is expressed as:

$$reconstructed\ PM_{2.5} = \sum (ionic\ species) + EC + OC \times multiplier\ factor + metals$$

(6-2)

A rational multiplier factor is normally applied and the reconstructed  $PM_{2.5}$  mass concentration can then be compared with the gravimetric mass concentration collected on pre-baked Teflon filter measured by electronic scale directly to check the mass enclosure. Reid et al. (2005) recommended OM/OC factor of 1.4-1.8 for biomass burning aerosol using the same analytical technique.

With the development of HR ToF-AMS and analytical templates, real time OM/OC now can be calculated from the estimated atomic ratios described in previous section. The theoretical details can be found elsewhere (Aiken et al., 2008, 2009). Therefore, the more realistic emission characteristics are captured compared to the offline analysis. Figure 6.8 displayed the OM/OC results from the AMS online method (offline analyses were not completed at the time of publication).

### **6.3.5 Levoglucosan analysis**

Levoglucosan (1,6-anhydro- $\beta$ -D-glucopyranose), a cellulose combustion product, has been reported as a biomass burning tracer (Simoneit et al., 1999, 2002) due to its high resistance to degradation in the ambient atmosphere (Fraser and Lakshmanan, 2000). Some of the levoglucosan is consumed in various reactions during combustion; nevertheless, it is emitted in large quantities and results in the particle-phase of smoke. Levoglucosan is source-specific to any fuel type that contains cellulose; therefore, it can be used as a specific tracer for the particulate emissions from biomass burning. Increasing effort has been put into levoglucosan quantification methodology development in recent years, which are roughly quantified using either gas chromatography (GC) or liquid

chromatography. But these conventional methods require long preparation of samples, expensive cost and derivatization treatment in some cases.

More recently, advanced instrumentation has been developed among which the HR-ToF-AMS addresses the most extensive application. The HR-ToF-AMS has been described in detail previously (deCarlo et al., 2006) and improves on mass resolution by using a custom high-resolution ToFMS (Tofwerk, Switzerland). Alfarrá et al. (2007) have recently identified specific marker fragments for wood-burning particle emissions using a quadrupole-AMS (Q-AMS). Results showed that the contribution of mass fragments 60, 73 and 137 to the total organic mass were enhanced during evening periods relative to morning periods and were therefore suggested to be marker fragments for wood-burning particle emissions.

With the capability of high-resolution module, the ion fragment identification can be improved even more than the UMR mass spectra. The molecular structure of levoglucosan can be depicted as Fig. 6.9. The cleavage of the molecule by EI ionization gives the major fragmented ions of  $C_2H_4O_2^+$  at  $m/z$  60 and  $C_3H_5O_2^+$  at  $m/z$  73. However,  $m/z$  73 is observed to contain two fragmented ions, i.e.  $C_3H_5O_2^+$  and  $C_3H_7NO^+$  as shown in Fig. 6.10 for some fuel types. Therefore, it is not accurate to use UMR  $m/z$  73 as marker fragment for biomass burns as opposed to  $C_3H_5O_2^+$  ion. And thus the time evolution of  $C_2H_4O_2^+$  and  $C_3H_5O_2^+$  vs. total organics throughout flaming, mixed and smoldering phases is illustrated in Fig. 6.11 to manifest the variation of levoglucosan content at different phases of biomass burning. The contour plot starts with flaming period labeled with dark color and then goes to lighter color as the fire approaches to

smoldering phase. Overall, the  $C_2H_4O_2^+$  follows a linear relationship with total organics except for oak savanna. Ceanothus has the highest levoglucosan contribution fraction followed by oak woodland, Chamise and maritime chaparral. Oak savanna, Manzanita and mesquite have intermediate levels while California sage and coastal sage have the lowest content of levoglucosan in emitted particulate. Similar phenomena were also observed for the evolution of  $C_3H_5O_2^+$  ion. The overall contribution of  $C_2H_4O_2^+$  +  $C_3H_5O_2^+$  as indicative of levoglucosan to the total organic mass ranges from 0.75%-2.46%. A correlation curve between  $C_2H_4O_2^+$  and  $C_3H_5O_2^+$  is plotted in Fig. 6.12. Generally, they follow the linear relationship well with  $C_3H_5O_2^+$  universally lower than  $C_2H_4O_2^+$ .

## 6.4 Conclusions

This chapter characterizes real-time organic particle elemental analysis using HR-ToF-AMS from the laboratory scale biomass burns for a variety of southwestern US fuels. The evolution of OM/OC, H/C, O/C and N/C from fire ignition to extinction was measured to capture the transient and integrated chemical composition of the non-refractory portion of bulk particles. Time averaged elemental ratios were segregated into three combustion modes: flaming, mixed and smoldering which are classified based on the MCE values. In general, the particle concentrations were highest during flaming phase and then gradually decreased during mixed and smoldering phase. For each fuel, the hydrogen fragment ions dominate the UMR mass spectra and no specific fragments exhibit that can be assigned to an intrinsic type of species. High resolution of m/z 60 and 73 supposedly designated to levoglucosan has been resolved for biomass marker



validation. The results imply that using  $C_2H_4O_2^+ + C_3H_5O_2^+$  to estimate the contribution of levoglucosan in the future may be more sufficient.

Our investigation showed that by using the HR ToF-AMS one can refer to real time chemical information under different burning conditions (flaming, mixed and smoldering). The nitrogen containing fraction gives the most fluctuation for some vegetations, which could possibly be attributed to the different elemental abundance of the plant species or the uncertainty of elemental analysis method applied to the data sets. For the future, therefore, further investigations are needed to relate the chemical characteristics of particle emissions with the biofuel elemental properties.

## 6.5 References

- Agrawal, H., Malloy, Q., Welch, W., Miller, W., Cocker, D.R.III, 2008. In-use gaseous and particulate matter emissions from a modern ocean going container vessel. *Atmos. Environ.* 42 (21), 5504-5510.
- Aiken, A. C., DeCarlo, P. F., Jimenez, J. L., 2007, Elemental analysis of organic species with electron ionization high-resolution mass spectrometry. *Analytical Chemistry* 79 (21), 8350–8358.
- Aiken, A.C., DeCarlo, P.F., Kroll, J.H., Worsnop, D.R., Huffman, J.A., Docherty, K., Ulbrich, I.M., Mohr, C., Kimmel, J.R., Sueper, D., Zhang, Q., Sun, Y., Trimborn, A., Northway, M., Ziemann, P.J., Canagaratna, M.R., Onasch, T.B., Alfarra, R., Prevot, A.S.H., Dommen, J., Duplissy, J., Metzger, A., Baltensperger, U., Jimenez, J.L., 2008, O/C and OM/OC Ratios of Primary, Secondary, and Ambient Organic Aerosols with High Resolution Time-of-Flight Aerosol Mass Spectrometry. *Environmental Science and Technology* 42, 4478-4485.
- Alfarra, M. R., D. Paulsen, M. Gysel, A. A. Garforth, J. Dommen, A. S. H. Prévôt, D. R. Worsnop, U. Baltensperger, and H. Coe, 2006. A mass spectrometric study of secondary organic aerosols formed from the photooxidation of anthropogenic and biogenic precursors in a reaction chamber, *Atmos. Chem. Phys.*, 6, 5279– 5293.
- Alfarra, M. R., A. S. H. Prévôt, S. Szidat, J. Sandradewi, S. Weimer, V. Lanz, D. Schreiber, M. Mohr, and U. Baltensperger, 2007. Identification of the mass spectral signature of organic aerosols from wood burning emissions, *Environ. Sci. Technol.*, 41, 5770 – 5777, doi:10.1021/es062289b.
- Andreae, M. O., and Merlet, P., 2001, Emission of trace gases and aerosols from biomass burning, *Global Biogeochem. Cycles*, 15(4), 955–966, doi:10.1029/2000GB001382.
- Battye, W., and Battye, R., 2002, *Development of Emissions Inventory Methods for Wildland Fire*, 91 pp., U.S. Environ. Prot. Agency, Chapel Hill, N. C.
- Chakrabarty, R. K., Moosmüller, H., Garro, M. A., Arnott, W. P., Walker, J., Susott, R. A., Babbitt, R. E., Wold, C. E., Lincoln, E. N. and Hao, W. M., 2006, Emissions from the laboratory combustion of wildland fuels: Particle morphology and size, *J. Geophys. Res.*, 111, D07204, doi:10.1029/2005JD006659.
- Chen, L. W. A., Moosmüller, H., Arnott, W. P., Chow, J. C. and Watson, J. G., 2006, Particle emissions from laboratory combustion of wildland fuels: In situ optical

- and mass measurements, *Geophys. Res. Lett.*, 33, L04803, doi:10.1029/2005GL024838.
- Chen, L. W. A., Moosmüller, H., Arnott, W. P., Chow, J. C., Watson, J. G., Susott, R. A., Babbitt, R. E., Wold, C. E., Lincoln, E. N. and Hao, W. M., 2007, Emissions from laboratory combustion of wildland fuels: Emission factors and source profiles, *Environ. Sci. Technol.*, 41(12), 4317–4325, doi:10.1021/es062364i.
- Clinton, N. E., Gong, P. and Scott, K., 2006, Quantification of pollutants emitted from very large wildland fires in southern California, USA, *Atmos. Environ.*, 40(20), 3686–3695, doi:10.1016/j.atmosenv.2006.02.016.
- Cofer, W. R., Levine, J. S., Riggan, P. J., Sebacher, D. I., Winstead, E. L., Shaw, E. F., Brass, J. A. and Ambrosia, V. G., 1988a, Trace gas emissions from a mid-latitude prescribed chaparral fire, *J. Geophys. Res.*, 93(D2), 1653–1658, doi:10.1029/JD093iD02p01653.
- Cofer, W. R., Levine, J. S., Sebacher, D. I., Winstead, E. L., Riggan, P. J., Brass, J. A. and Ambrosia, V. G., 1988b, Particulate-emissions from a mid-latitude prescribed chaparral fire, *J. Geophys. Res.*, 93(D5), 5207–5212, doi:10.1029/JD093iD05p05207.
- Crutzen, P. J., and Andreae, M. O., 1990, Biomass burning in the tropics-Impact on atmospheric chemistry and biogeochemical cycles, *Science*, 250 (4988), 1669–1678, doi:10.1126/science.250.4988.1669.
- DeCarlo, P.F., Kimmel, J.R., Trimborn, A., Northway, M.J., Jayne, J.T., Aiken, A.C., Gonin, M., Fuhrer, K., Horvath, T., Docherty, K., Worsnop, D.R., Jimenez, J.L., 2006, Field-Deployable, High-Resolution, Time-of-Flight Aerosol Mass Spectrometer. *Analytical Chemistry* 78, 8281-8289.
- Fraser, M. P., Lakshmanan, K., 2000, Using levoglucosan as a molecular marker for the long-range transport of biomass combustion aerosols. *Environ. Sci. Technol.* 34 (21), 4560-4564.
- Friedli, H. R., Atlas, E., Stroud, V. R., Giovanni, L., Campos, T. and Radke, L. F., 2001, Volatile organic trace gases emitted from North American wildfires, *Global Biogeochem. Cycles*, 15(2), 435 – 452, doi:10.1029/2000GB001328.
- Habib, G., Venkataraman, C., Bond, T. and Schauer, J., 2008. Chemical, microphysical and optical properties of primary particles from the combustion of biomass fuels. *Environ. Sci. Technol.* 42, 8829-8834.

- Haines, T. K., Busby, R. L. and Cleaves, D. A., 2001, Prescribed burning in the south: Trends, purpose, and barriers, *South. J. App. For.*, 25(4), 149 – 153.
- Hays, M. D., Geron, C. D., Linna, K. J., Smith, N. D., and Schauer, J. J., 2002, Speciation of gas-phase and fine particle emissions from burning of foliar fuels, *Environ. Sci. Technol.*, 36(11), 2281– 2295, doi:10.1021/es0111683.
- Mazzoleni, L. R., B. Zielinska, and H. Mossmueller, 2007. Emissions of levoglucosan, methoxy phenols, and organic acids from prescribed burns, laboratory combustion of wildland fuels, and residential wood combustion, *Environ. Sci. Technol.*, 41, 2115– 2122, doi:10.1021/es061702c.
- McMeeking, G. R., et al. (2009), Emissions of trace gases and aerosols during the open combustion of biomass in the laboratory, *J. Geophys. Res.*, 114, D19210, doi:10.1029/2009JD011836.
- McMeeking, G. R., et al., 2006, Smoke-impacted regional haze in California during the summer of 2002, *Agric. For. Meteorol.*, 137(1–2), 25–42, doi:10.1016/j.agrformet.2006.01.011.
- Muhle, J., Lueker, T. J., Su, Y., Miller, B. R., Prather, K. A. and Weiss, R. F., 2007, Trace gas and particulate emissions from the 2003 southern California wildfires, *J. Geophys. Res.*, 112, D03307, doi:10.1029/2006JD007350.
- Naeher, L. P., Brauer, M., Lipsett, M., Zelikoff, J. T., Simpson, C. D., Koenig, J. Q., and Smith, K. R., 2007, Woodsmoke health effects: A review, *Inhal. Toxicol.*, 19(1), 67– 106, doi:10.1080/08958370600985875.
- Park, R. J., Jacob D. J., and Logan, J. A., 2007, Fire and biofuel contributions to annual mean aerosol mass concentrations in the United States, *Atmos. Environ.*, 41(35), 7389 – 7400, doi:10.1016/j.atmosenv.2007. 05.061.
- Park, R. J., Jacob D. J., Kumar, N., and Yantosca, R. M., 2006, Regional visibility statistics in the United States: Natural and transboundary pollution influences, and implications for the Regional Haze Rule, *Atmos. Environ.*, 40(28), 5405–5423, doi:10.1016/j.atmosenv.2006.04.059.
- Phuleria, H. C., Fine, P. M., Zhu, Y. F., Sioutas, C., 2005, Air quality impacts of the October 2003 Southern California wildfires. *J. Geophys. Res.* 110, D07S20, doi: 10.1029/2004JD004626.
- Reid, J. S., R. Koppmann, T. F. Eck, and D. P. Eleuterio, 2005. A review of biomass burning emissions part II: Intensive physical properties of biomass burning particles, *Atmos. Chem. Phys.*, 5, 799–825.

- Robinson, A. L., Subramanian, R., Donahue, N. M., Bernardo-Bricker, A. and Rogge, W. F., 2006, Source apportionment of molecular markers and organic aerosol. 2. Biomass smoke, *Environ. Sci. Technol.*, 40(24), 7811–7819, doi:10.1021/es060782h.
- Simoneit, B. R. T., 2002. Biomass burning – A review of organic tracers for smoke from incomplete combustion, *Appl. Chem.*, 17, 129–162.
- Simoneit, B. R. T., J. J. Schauer, C. G. Nolte, D. R. Oros, V. O. Elias, M. P. Fraser, W. F. Rogge, and G. R. Cass, 1999. Levoglucosan, a tracer for cellulose in biomass burning and atmospheric particles, *Atmos. Environ.*, 33, 173-182, doi:10.1016/S1352-2310(98)00145-9.
- Spracklen, D. V., Logan, J. A., Mickley, L. J., Park, R. J., Yevich, R., Westerling, A. L. and Jaffe, D. A., 2007, Wildfires drive interannual variability of organic carbon aerosol in the western U.S. in summer, *Geophys. Res. Lett.*, 34, L16816, doi:10.1029/2007GL030037.
- van der Werf, G. R., Randerson, J. T., Giglio, L., Collatz, G. J., Kasibhatla, P. S., and Arellano, A. F., 2006, Interannual variability in global biomass burning emissions from 1997 to 2004, *Atmos. Chem. Phys.*, 6, 3423 – 3441.
- Ward, D. E., and L. F. Radke (1993), Emission measurements from vegetation fires: A comparative evaluation of methods and results, in *Fire in the Environment: The Ecological, Atmospheric, and Climatic Importance of Vegetation Fires*, edited by P. J. Crutzen and J.-G. Goldammer, pp. 53–76, John Wiley, Chichester, U. K.
- Watson, J. G., 2002, Visibility: Science and regulation, *J. Air Waste Manage. Assoc.*, 52(6), 628–713.
- Weimer, S., Alfarra, M.R., Schreiber, D., Mohr, M., Prévôt, A.S., Baltensperger, U., 2008. Organic aerosol mass spectral signatures from wood-burning emissions: influence of burning conditions and wood type. *Journal of Geophysical Research* 113, D10303, doi: 10.1029/2007JD009309.
- Weise, D. R., Zhou, X. Y., Sun, L. L. and Mahalingam, S., 2005, Fire spread in chaparral - 'go or no-go?', *Int J Wildland Fire*, 14, 99-106.
- Yokelson, R. J., Goode, J. G., Ward, D. E., Susott, R. A., Babbitt, R. E., Wade, D. D., Bertschi, I., Griffith, D. W. T. and Hao, W. M., 1999, Emissions of formaldehyde, acetic acid, methanol, and other trace gases from biomass fires in North Carolina measured by airborne Fourier transform infrared spectroscopy, *J. Geophys. Res.*, 104(D23), 30,109– 30,125, doi:10.1029/1999JD900817.

Yokelson, R. J., Griffith, D. W. T. and Ward, D. E., 1996, Open-path Fourier transform infrared studies of large-scale laboratory biomass fires, *J. Geophys. Res.*, 101(D15), 21,067– 21,080, doi:10.1029/96JD01800.

<b>Fuel Type</b>	<b>Plant Species</b>
Chamise	<i>Adenostoma fasciculatum</i> , <i>Quercus berberidifolia</i>
Ceanothus	<i>Ceanothus leucodermis</i>
Maritime chaparral	<i>Ceanothus impressus</i> var. <i>impressus</i> , <i>C. cuneatus</i> var. <i>fascicularis</i> , <i>Salvia mellifera</i>
Coastal sage scrub	<i>Salvia mellifera</i> , <i>Ericameria ericoides</i> , <i>Artemisia californica</i>
California sagebrush	<i>Artemisia californica</i> , <i>Ericameria ericoides</i>
Manzanita	<i>Arctostaphylos rudis</i> , <i>Arctostaphylos purissima</i>
Oak savanna	<i>Quercus emoryi</i> , <i>Eragrostis lehmanniana</i>
Oak woodland	<i>Quercus emoryi</i> , <i>Arctostaphylos pungens</i>
Masticated mesquite	<i>Prosopis velutina</i> , <i>Baccharis sarothroides</i>

**Table 6.1** Plant species that used as southwestern biomass fuels in this study

<b>Fuel Type</b>	<b># of Burns</b>	<b>Moisture content (%)</b>	<b>Fuel bed mass (g)</b>	<b>Bulk density (kg/m<sup>3</sup>)</b>	<b>Packing ratio</b>	<b>Mass consumption (%)</b>
Chamise	6	11.9	2079	8.6	0.015	38
Ceanothus	6	10.2	2007	5.8	0.01	54
Maritime chaparral	5	11.2	2871	7.5	0.013	95
Coastal sage scrub	5	9.3	2299	6.0	0.01	95
California sagebrush	6	9.0	2460	6.4	0.011	93
Manzanita	6	12.6	2906	7.6	0.013	94
Oak savanna	5	14.3	2788	7.3	0.012	91
Oak woodland	5	32.8	2054	5.3	0.009	95
Masticated mesquite	5	4.3	1831	14.3	0.024	92

**Table 6.2** Fuel bed properties for the 9 plant species



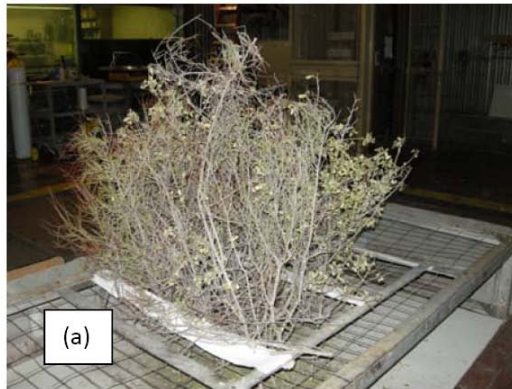


**Figure 6.1** Two pictures showing fuel and fuel bed before fire

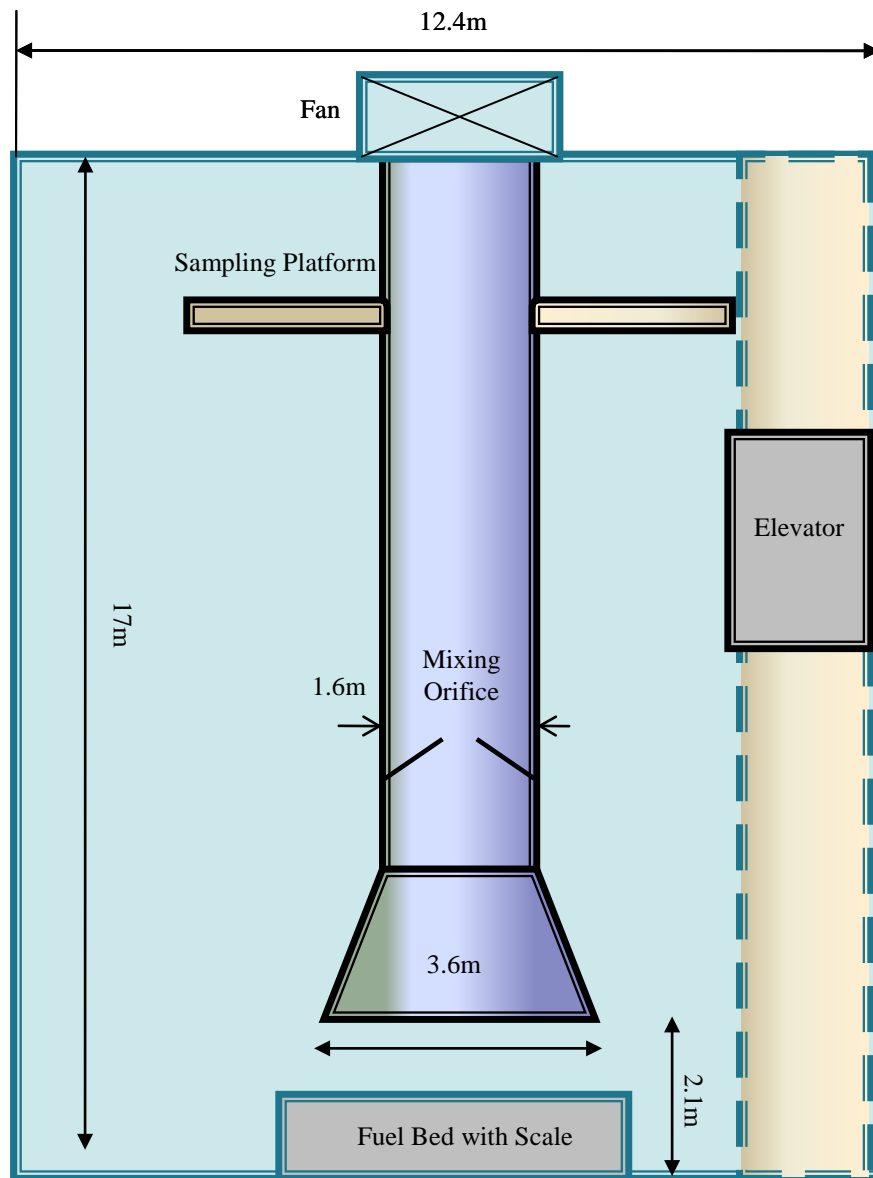


**Figure 6.2** Schematic of the US Forest Service Science Laboratory combustion facility at Missoula, MT.

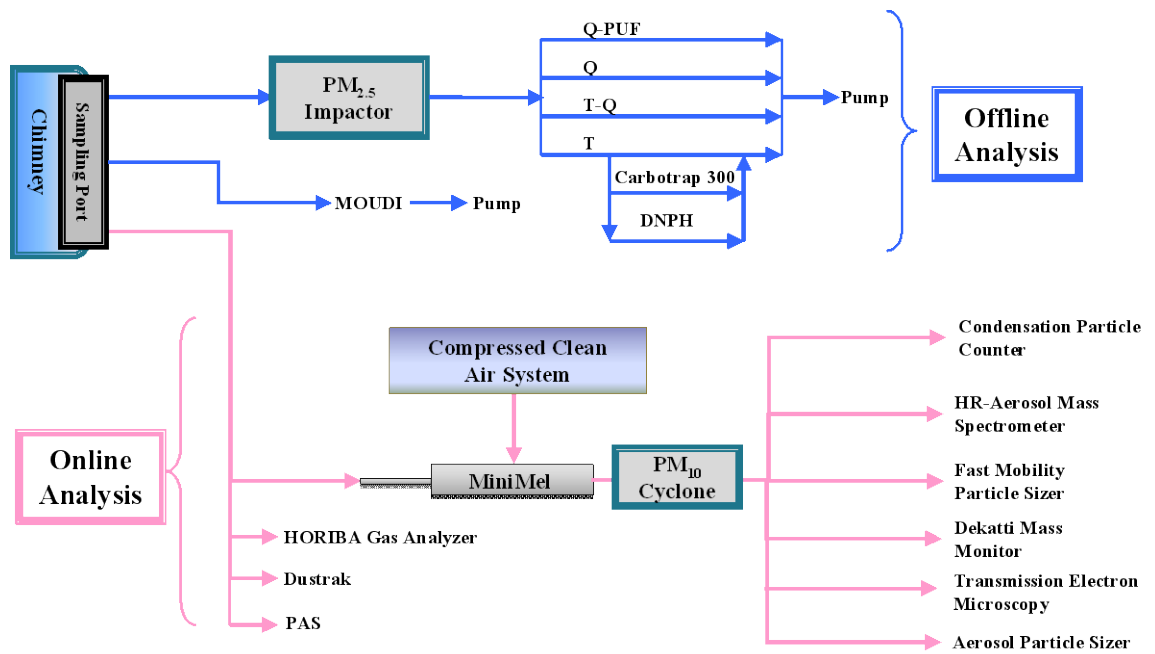


**Figure 6.3** Schematic of online and offline sampling system

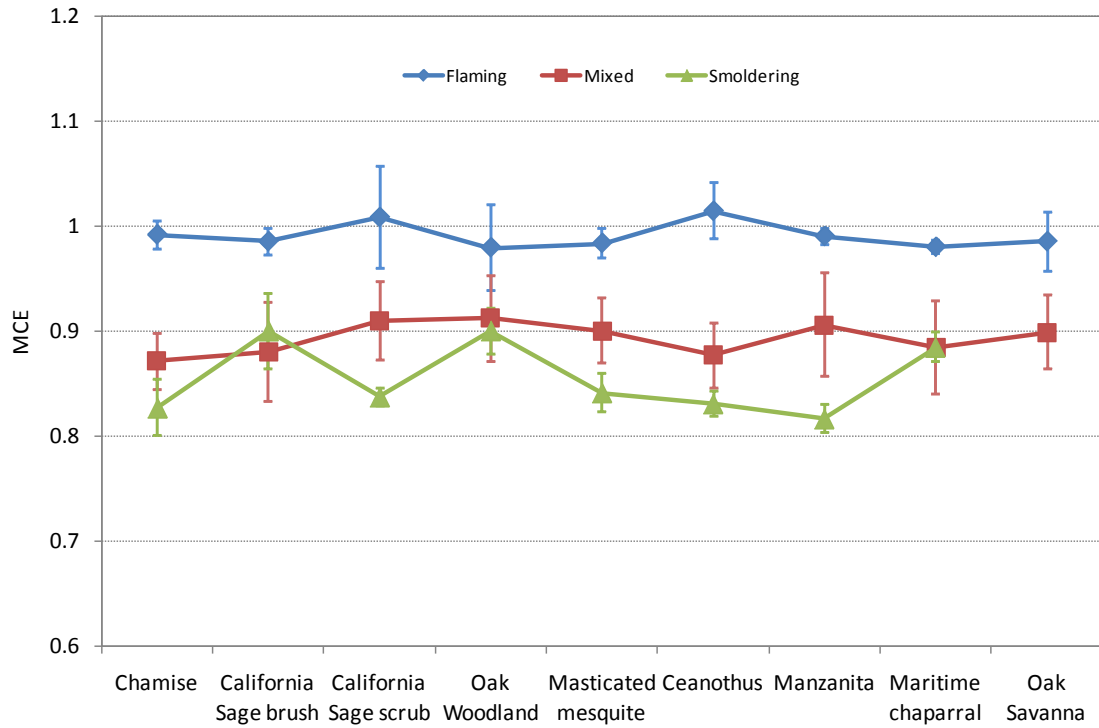


**Figure 6.4** Averaged MCE for 9 fuel species during flaming, mixed and smoldering phases

(a)

Fuel Type	m/z29/org (%)	m/z43/org (%)	m/z44/org (%)	m/z60/org (%)	m/z73/org (%)
chamise	3.62	6.07	9.30	0.72	0.69
CA sage	1.79	2.91	6.47	0.44	0.27
Coastal sage	4.47	3.35	9.19	0.77	0.40
Oak savanna	2.27	4.60	5.58	0.76	0.31
Oak woodland	3.72	4.12	8.93	0.90	0.61
mesquite	3.19	4.10	5.97	0.60	0.51
ceanothus	4.33	7.06	5.76	0.93	0.77
Manzanita	3.63	5.00	11.51	0.98	0.80
Maritime chaparral	1.90	3.15	5.21	0.54	1.11

(b)

Fuel Type	m/z29/org (%)	m/z43/org (%)	m/z44/org (%)	m/z60/org (%)	m/z73/org (%)
chamise	4.87	5.48	4.10	1.24	0.94
CA sage	2.67	3.66	6.14	0.55	0.53
Coastal sage	2.49	4.12	9.34	0.89	0.58
Oak savanna	4.27	3.51	4.09	1.50	1.30
Oak woodland	3.89	4.24	2.88	1.22	0.66
mesquite	4.04	4.58	4.61	1.03	0.77
ceanothus	5.96	4.76	2.72	1.43	1.30
Manzanita	3.71	4.37	14.68	0.36	0.36
Maritime chaparral	3.90	5.07	1.84	1.12	0.66

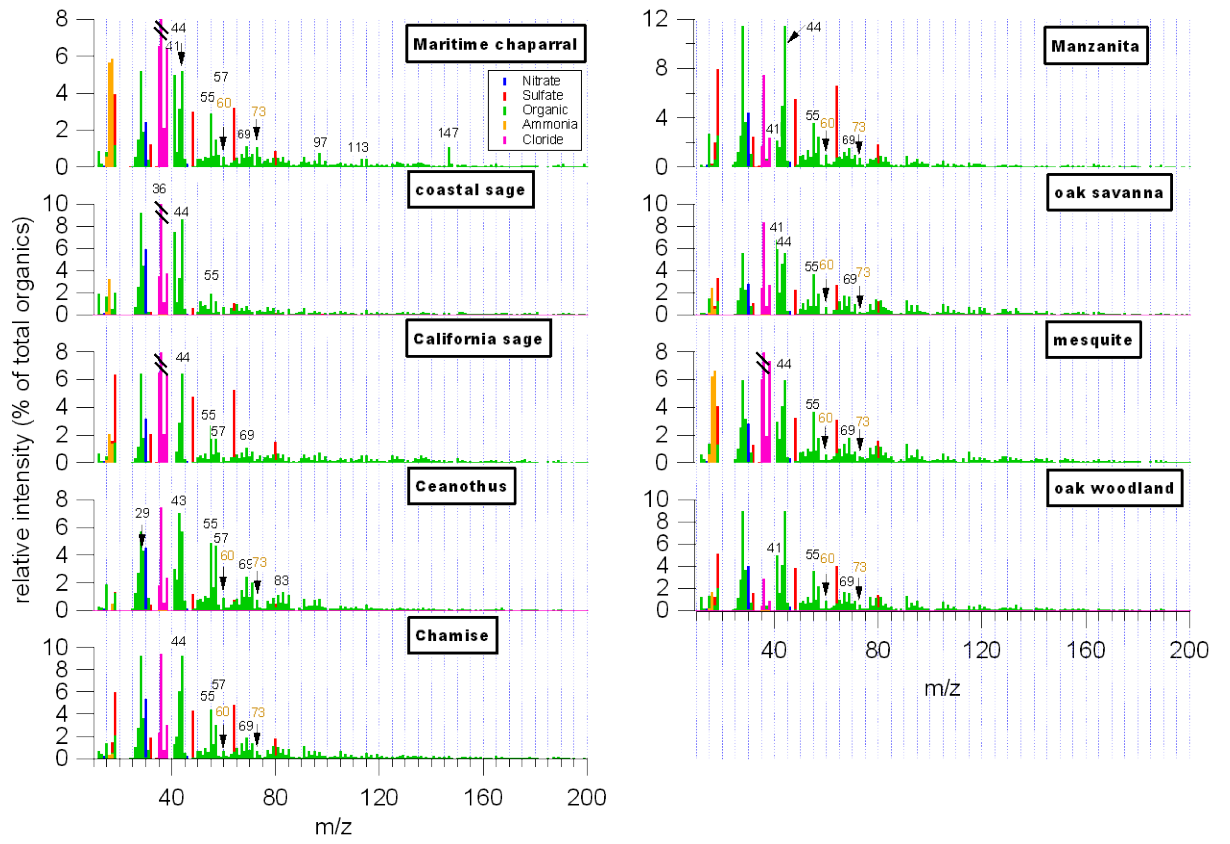
(c)

Fuel Type	m/z29/org (%)	m/z43/org (%)	m/z44/org (%)	m/z60/org (%)	m/z73/org (%)
chamise	4.72	5.45	2.25	1.23	0.92
CA sage	0	6.35	6.90	1.28	0.94
Coastal sage	4.58	5.83	0	1.13	1.12
Oak savanna <sup>a</sup>	NA	NA	NA	NA	NA
Oak woodland	3.31	5.09	1.44	1.10	0.76
mesquite	7.89	3.78	4.20	0.09	0.22
ceanothus	6.18	0.81	2.38	0.73	0.18
Manzanita	2.67	3.50	17.15	0.75	0.71
Maritime chaparral	2.87	5.57	1.41	0.68	0.49

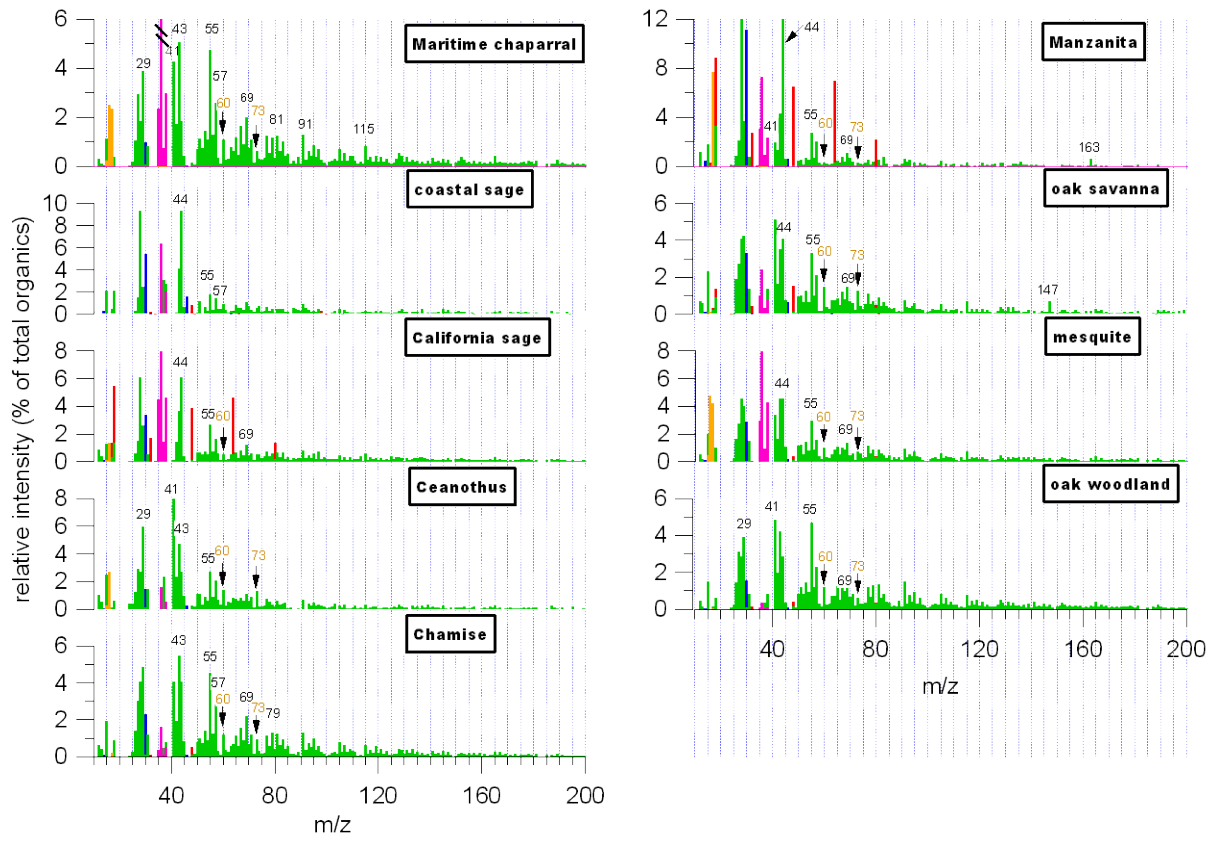
Note: a. no obvious smoldering phase observed for this fuel

**Table 6.3** Ratios of m/z 29, 43, 44, 60 and 73 for all nine fuels (a) flaming; (b) mixed; (c) smoldering

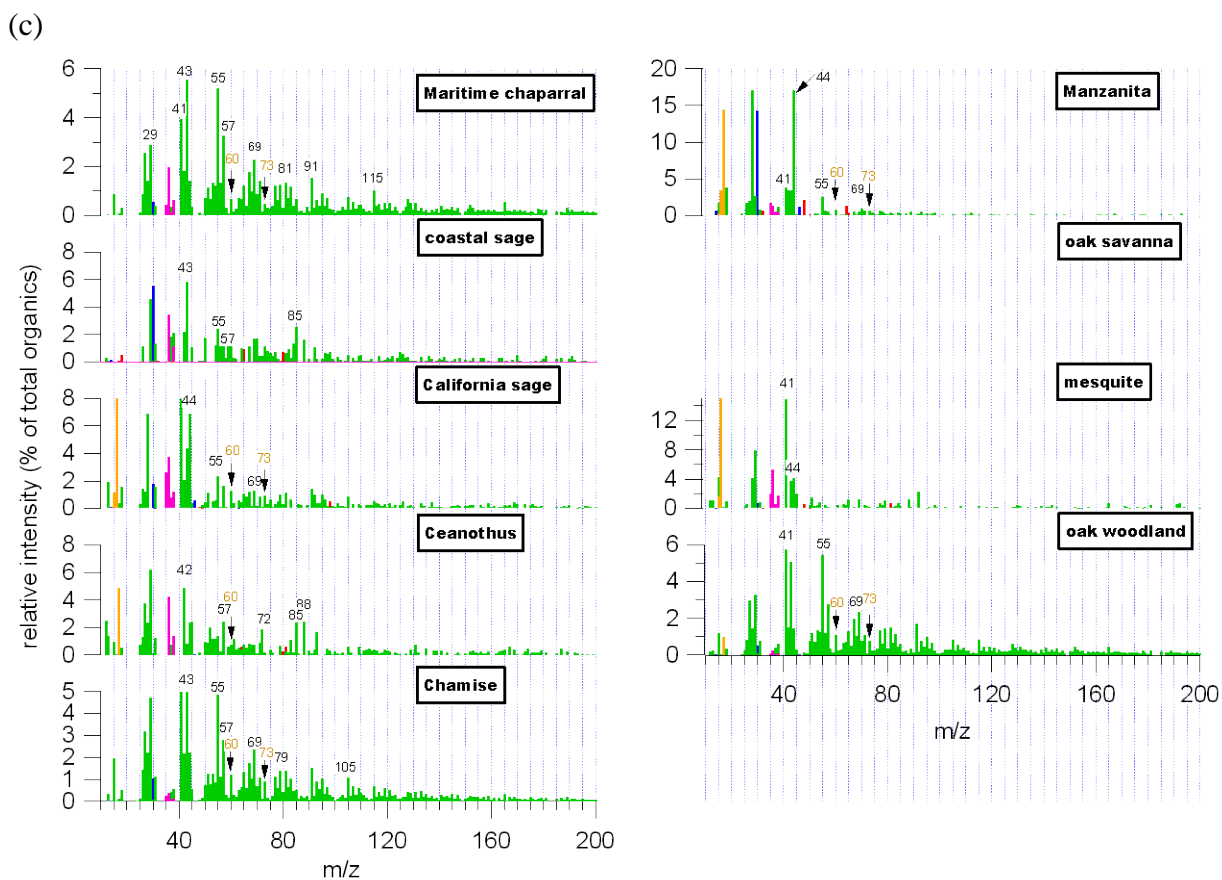
(a)



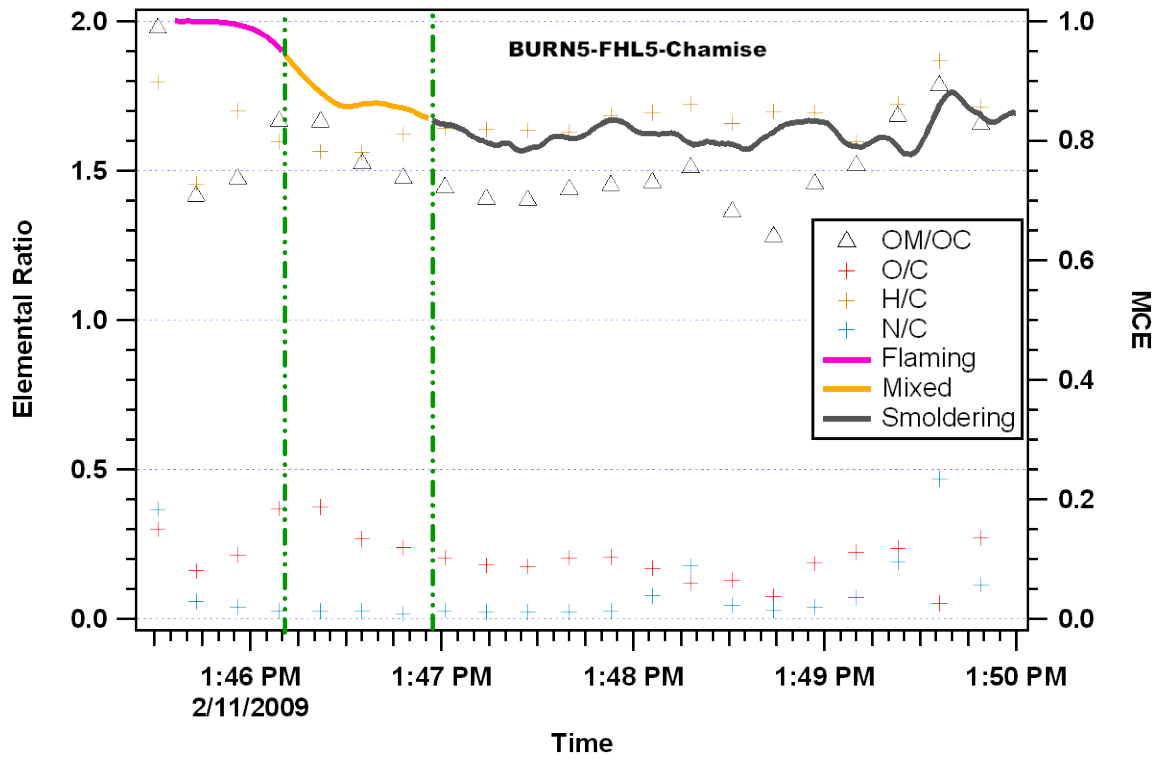
(b)



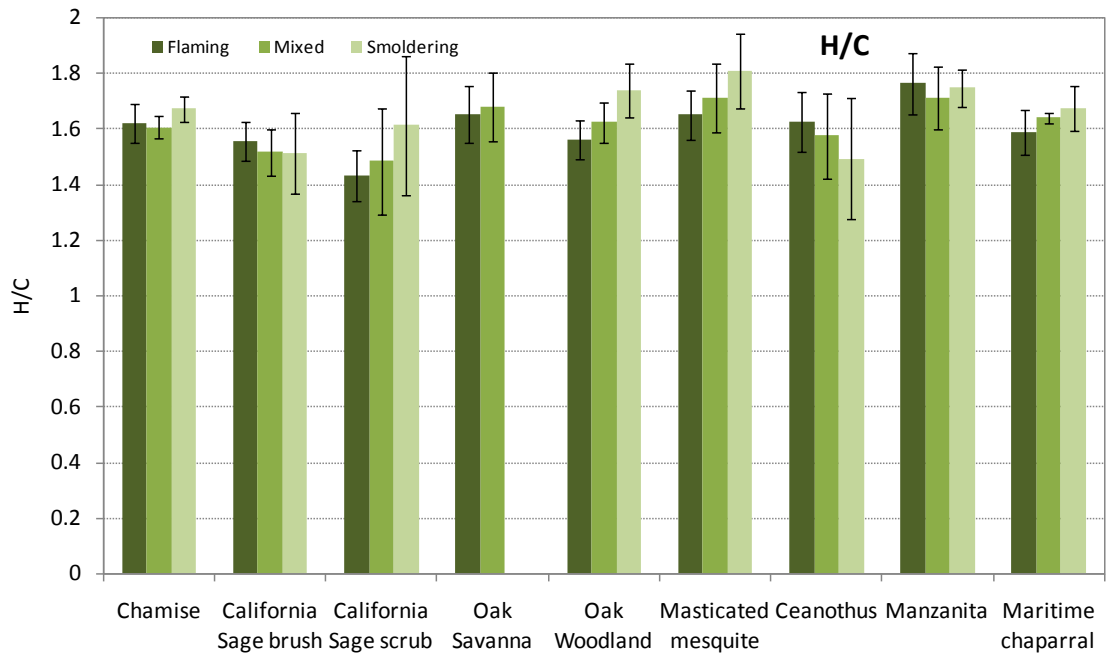
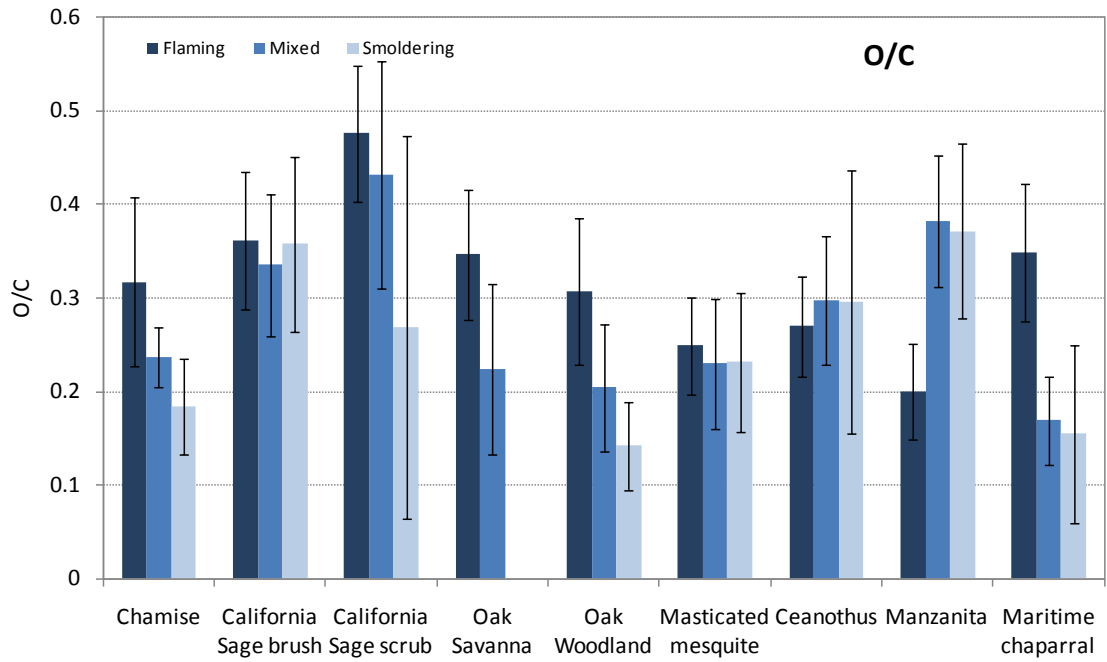




**Figure 6.5** Averaged normalized mass spectra for (a) flaming, (b) mixed and (c) smoldering phases of measured particle components from the combustion of different southwestern biomass fuels.



**Figure 6.6** The elemental ratio evolution of particles at different phases from Chamise burning. Note: all the markers correspond to the primary y-axis; all the lines correspond to the secondary y-axis.



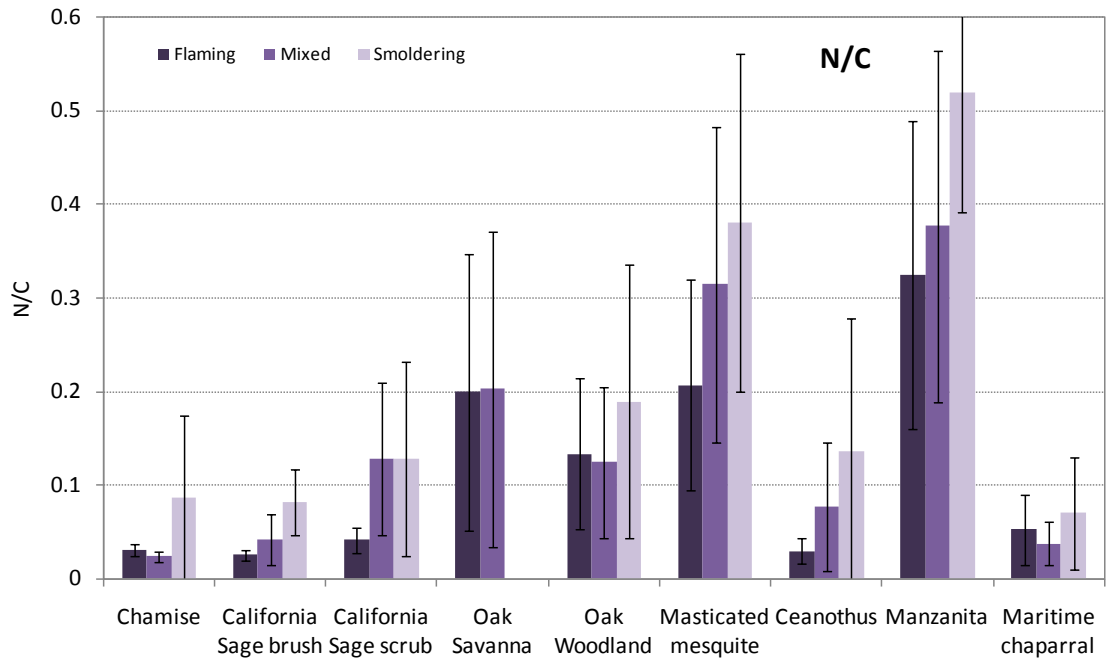
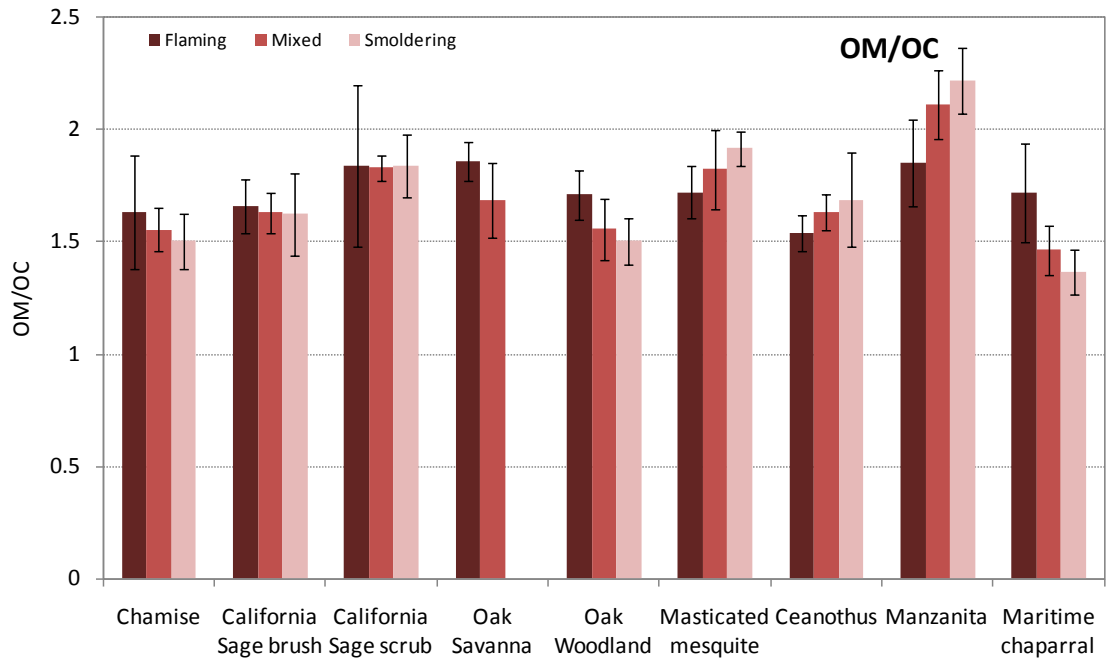


**Figure 6.7** Averaged elemental ratios of organic carbonaceous aerosol from the combustion of different biomass fuels

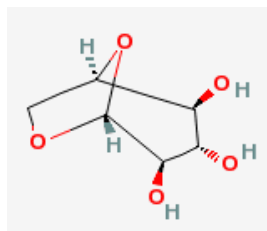
Fuel type	Empirical Formula		
	Flaming	Mixed	Smoldering
Chamise	$C_1H_{1.62\pm 0.07}O_{0.32\pm 0.09}N_{0.03\pm 0.01}$	$C_1H_{1.61\pm 0.04}O_{0.24\pm 0.03}N_{0.02\pm 0.01}$	$C_1H_{1.67\pm 0.04}O_{0.18\pm 0.05}N_{0.09\pm 0.09}$
California Sage brush	$C_1H_{1.56\pm 0.07}O_{0.36\pm 0.07}N_{0.03\pm 0.01}$	$C_1H_{1.52\pm 0.08}O_{0.34\pm 0.08}N_{0.04\pm 0.03}$	$C_1H_{1.51\pm 0.15}O_{0.36\pm 0.09}N_{0.08\pm 0.04}$
California Sage scrub	$C_1H_{1.43\pm 0.09}O_{0.48\pm 0.07}N_{0.04\pm 0.01}$	$C_1H_{1.48\pm 0.19}O_{0.43\pm 0.12}N_{0.13\pm 0.08}$	$C_1H_{1.61\pm 0.25}O_{0.27\pm 0.20}N_{0.13\pm 0.10}$
Oak Savanna	$C_1H_{1.65\pm 0.10}O_{0.35\pm 0.07}N_{0.20\pm 0.15}$	$C_1H_{1.68\pm 0.12}O_{0.22\pm 0.09}N_{0.20\pm 0.17}$	NA <sup>a</sup>
Oak Woodland	$C_1H_{1.56\pm 0.07}O_{0.31\pm 0.08}N_{0.13\pm 0.08}$	$C_1H_{1.62\pm 0.07}O_{0.20\pm 0.07}N_{0.12\pm 0.08}$	$C_1H_{1.74\pm 0.09}O_{0.14\pm 0.05}N_{0.19\pm 0.15}$
Masticated mesquite	$C_1H_{1.65\pm 0.09}O_{0.25\pm 0.05}N_{0.21\pm 0.11}$	$C_1H_{1.71\pm 0.12}O_{0.23\pm 0.07}N_{0.31\pm 0.17}$	$C_1H_{1.81\pm 0.14}O_{0.23\pm 0.07}N_{0.38\pm 0.18}$
Ceanothus	$C_1H_{1.62\pm 0.11}O_{0.27\pm 0.05}N_{0.03\pm 0.01}$	$C_1H_{1.58\pm 0.15}O_{0.30\pm 0.07}N_{0.08\pm 0.07}$	$C_1H_{1.49\pm 0.22}O_{0.30\pm 0.14}N_{0.14\pm 0.14}$
Manzanita	$C_1H_{1.76\pm 0.11}O_{0.20\pm 0.05}N_{0.32\pm 0.16}$	$C_1H_{1.71\pm 0.11}O_{0.38\pm 0.07}N_{0.38\pm 0.19}$	$C_1H_{1.75\pm 0.07}O_{0.37\pm 0.09}N_{0.52\pm 0.13}$
Maritime chaparral	$C_1H_{1.59\pm 0.08}O_{0.35\pm 0.07}N_{0.05\pm 0.04}$	$C_1H_{1.64\pm 0.02}O_{0.17\pm 0.05}N_{0.04\pm 0.02}$	$C_1H_{1.68\pm 0.08}O_{0.15\pm 0.10}N_{0.07\pm 0.06}$

Note: a. no obvious smoldering phase observed for this fuel

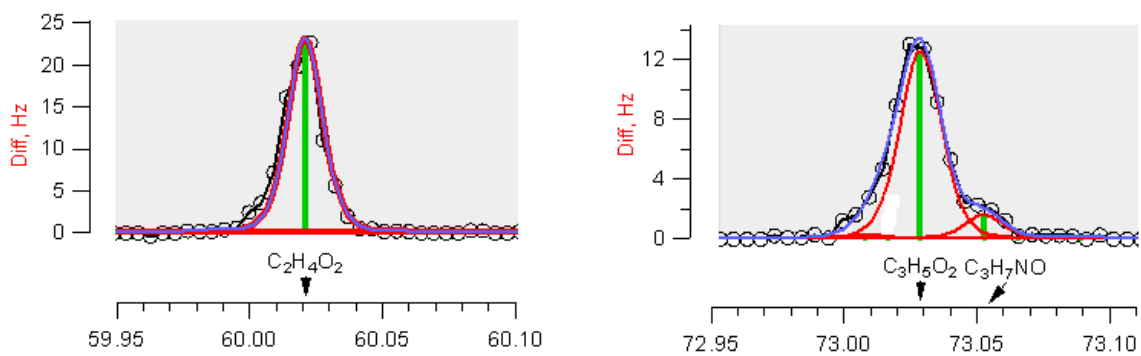
**Table 6.4** Empirical formula for nine biomass fuels during flaming, mixed and smoldering phases



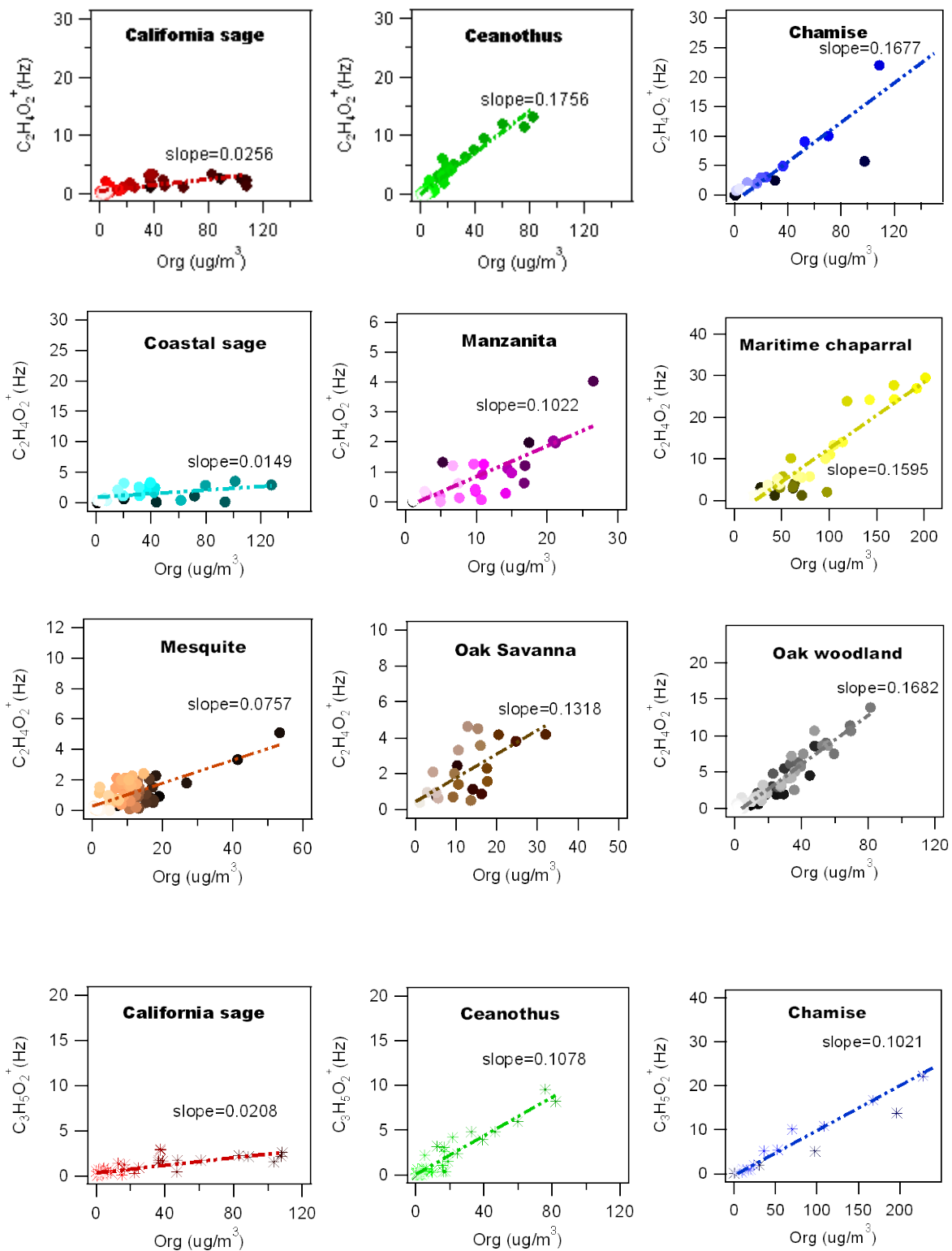
**Figure 6.8** Averaged OM/OC from the combustion of different biomass fuels



**Figure 6.9** Molecular structure of levoglucosan



**Figure 6.10** Peaks resolved for m/z 60 and 73 from Chamise burning





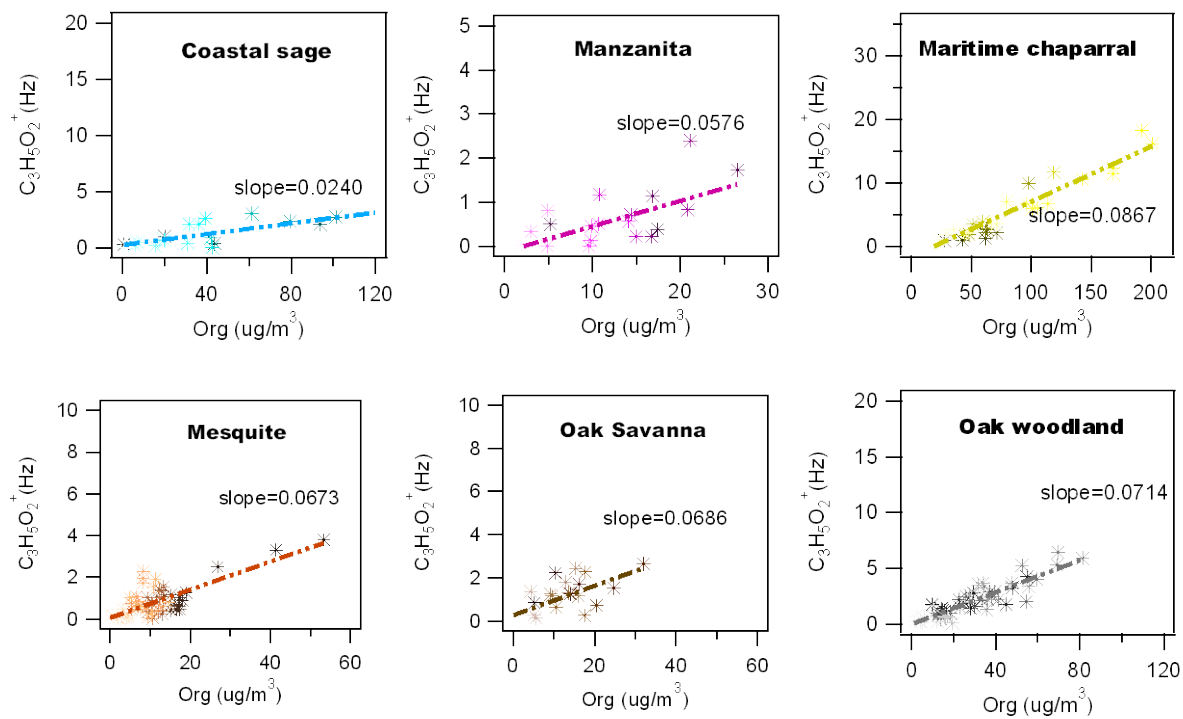


**Figure 6.11** Time evolution of  $\text{C}_2\text{H}_4\text{O}_2^+$  and  $\text{C}_3\text{H}_5\text{O}_2^+$  ions vs. total organics of aerosol emissions for nine southwestern biomass fuels

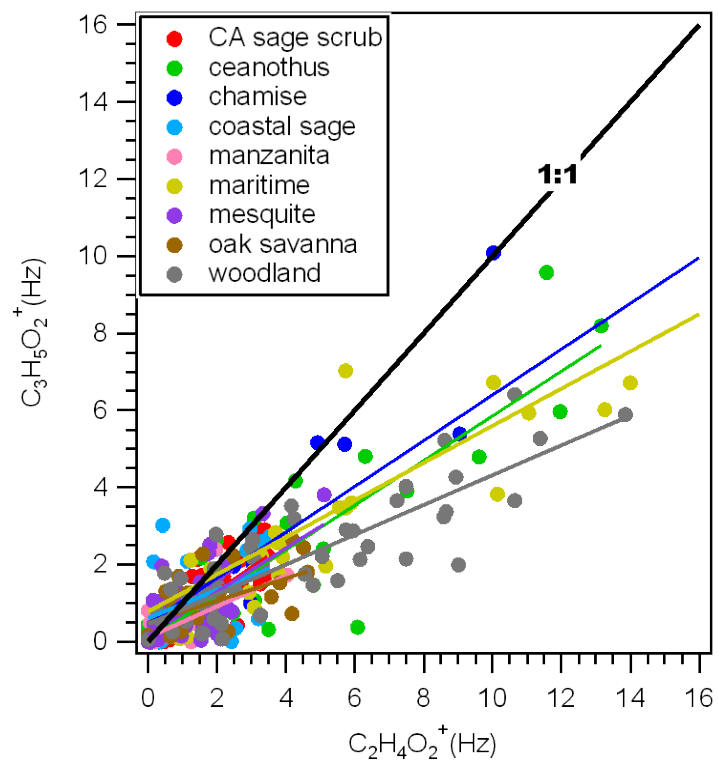


**Figure 6.12** The relationship between  $C_2H_4O_2^+$  and  $C_3H_5O_2^+$  fragment ions

## Chapter 7

### 7. Conclusions

The overall objective of this study was to improve our understanding of SOA aging processes formed from aromatic and mono-terpene hydrocarbons, and further our knowledge of influence of temperature on SOA formation. This was achieved through a number of environmental chamber experiments operating under varying conditions through use of complementary mass spectrometry techniques. Additionally, we implemented a technique for measuring primary organic aerosol from southwestern biomass burns that will be used in future experiments to investigate the aging processes of wood smoke within an atmospheric simulation chamber.

Chapter 2 details the experimental evidence that demonstrated aging of SOA for select photooxidation reaction systems through simultaneous measurement of SOA volatility, hygroscopicity, density, and chemical composition. The aging was much stronger for photooxidation systems compared with the very stable  $\alpha$ -pinene dark ozonolysis system with hydroxyl scavenger. Even after 16 hours of aging, the O/C of the aerosol was lower than the AMS identified OOAI or OOAI fractions measured in Mexico City. The rate of increase of O/C appears insufficient to obtain OOAI O/C even over a period of a couple of days. Little evidence was found for significant formation of high molecular weight SOA species.

Chapter 3 describes a series of atmospheric chamber studies performed in order to extend the knowledge of the effects of hydroxyl and nitrate radicals on the SOA aging

process from ozonolysis of  $\alpha$ -pinene gained from the chapter 2. We found that that further aging of  $\alpha$ -pinene dark ozonolysis system via oxidation of first generation products is possible; distinct increases in hydrophilicity, and oxygen content level were observed. However, the reaction rates are slow and thus slight volume gain is obtained from the additional reaction, which probably contributed to the gas-phase reaction mainly. UV irradiation alone also has some effect on this specific system, which is likely due to the reaction of photosensitive carbonyls, peroxides, and nitrates or HONO emitted from the Teflon wall. These results confirm that the hydroxyl radical plays a crucial role in SOA aging.

Chapter 4 focuses on the influence of temperature on SOA for *m*-xylene/NO<sub>x</sub> photooxidation system. The results show that when the experiment commences at 313 K, and then is cooled down to 278 K, there are no significant changes in particle density, hygroscopicity, volatility, and chemical composition. However, aerosol formed at cold temperatures appears chemically and physically different than those formed at 300 K and 313 K. A large transition in particle density, hygroscopicity, volatility and chemical composition was seen as the aerosol was warmed past 290-292 K. These observations are consistent with a thermally labile aerosol component. Additionally, after SOA formation completion at 278 K, the temperature was raised to a different set-point (300 K) and then returned to 278 K to evaluate the system reversibility. It turned out that neither the aerosol volume nor the particle density was able to restore to those formed at 278 K initially, which confirms the hypothesis of presence of thermally labile components.

Chapter 5 explores the potential reaction mechanism from selected *m*-xylene/NO<sub>x</sub> photooxidation system by comparing the mass spectra of gas- and particle-phase products from regular (<sup>12</sup>C<sub>2</sub>)*m*-xylene and <sup>14</sup>NO and isotopic (<sup>13</sup>C<sub>2</sub>)*m*-xylene and <sup>15</sup>NO reactions. UMR mass spectra indicate the formations of ring-containing products via oxidation of methyl group or OH direct adduct on the ring and following ring-open oxidation fragmented products. However, the ratio of <sup>13</sup>C/<sup>12</sup>C analysis for the bulk particle-phase products cannot be explained by current published mechanisms and estimates of potential yields of the products expected for these reaction pathways. More efforts are still needed to digest this information combined with other bulk chemical properties, such as O/C, H/C. Organic nitrate fragments are observed in the system but contribute 5-10% of total organic mass. With isotopic <sup>15</sup>NO, we confirm that no product ions contain –C–N– bond other than the nitrate compounds bonds of –NO and –NO<sub>2</sub>.

Chapter 6 describes the application of our HR-ToF-AMS for non-refractory organic aerosol measurement of PM<sub>2.5</sub> from nine southwest biomass burns. The evolution of OM/OC, H/C, O/C and N/C from fire ignition to extinction was measured to capture the transient and integrated chemical composition of the non-refractory portion of bulk particles. For each fuel, the hydrogen fragment ions dominate the UMR mass spectra with no specific fragment ions attributable to an individual ecological combination. The results imply that C<sub>2</sub>H<sub>4</sub>O<sub>2</sub><sup>+</sup> (m/z 60.021) plus C<sub>3</sub>H<sub>5</sub>O<sub>2</sub><sup>+</sup> (m/z 73.029) are more sufficient to estimate the contribution of levoglucosan. The levoglucosan content in the organic particle ranged from 0.74% for coastal sage to 1.93% for chamise.

## **APPENDICES**

## **Appendix A**

### **Secondary Organic Aerosol Formation from Primary Aliphatic Amines with NO<sub>3</sub> Radical**

Reference: Malloy, Q. G.J., Qi, L., Warren, B., Cocker, D.R.III, Erupe, M.E., and Silva, P.J., 2009. *Atmospheric Chemistry and Physics*, 9 (6), 2051-2060.

## 1 Introduction

Amines are found to be emitted into the atmosphere by a variety of anthropogenic and biogenic sources including automobile emissions, waste treatment facilities, and agricultural animal operations (Westerholm et al., 1993, Manahan 1990, Schade and Crutzen 1995). Amine emission rates from dairy operations have been estimated to range from 0.2 to 11 lbs per head of cattle per year (Bailey et al., 2005). Additionally, Mosier et al. (1973) has identified cattle feedlots as a major source of methylamine, ethylamine, propylamine, and butylamine as well as other amine compounds.

Removal routes for amines from the atmosphere include reactions with either nitric or sulfuric acid to form the corresponding nitrate salts or oxidation by OH, O<sub>3</sub>, and NO<sub>3</sub> (Seinfeld and Pandis 1998, Finlayson-Pitts and Pitts 2000, Silva et al., 2008). Little work has been performed on the NO<sub>3</sub> initiated oxidation of amines however; it is thought to be similar to the OH route and therefore proceed by four possible reaction pathways. The predominant pathway (Fig. A.1) is through abstraction of the alpha hydrogen, which forms the alkoxy radical after addition of molecular oxygen and NO to NO<sub>2</sub> conversion or RO<sub>2</sub>-RO<sub>2</sub> in the absence of NO. The alkoxy radical then proceeds to form an amide. The second route proceeds by loss of an alkyl group from the nitrogen, followed by formation of nitramine, nitrosamine, or imines. Imines' are then believed to undergo reactions leading to formation of aldehyde products. It is possible for these oxidation products to have a low enough vapor pressure to condense onto existing particles or form new particles by nucleating, creating secondary organic aerosol (SOA). Once in the



aerosol, they can undergo further reactions forming multifunctional species (Pitts et al., 1978).

The presence of organic nitrogen in the particle phase has been reported as far back as the early 1970's when Novakov et al. (1972) found nitrogen with oxidation states similar to that of organic nitrogen compounds in aerosol collected in Pasadena, California. More recently, studies have reported the presence of amine like compounds in ambient particles in both urban and rural settings (Murphy and Thomson 1997, Angelino et al., 2001, Tan et al., 2002, Glagolenko and Phares 2004, Beddows et al., 2004). Furthermore, amine like compounds have also been reported in fog water and rain drops obtained in the central valley of California by Zhang and Anastasio (2003). In addition to these studies, recent work by Barsanti et al. and Smith et al. have correlated new particle events with elevated amine concentrations. These researchers suggest that amine compounds participate in these nucleation events, possibly acting as cloud condensation nuclei (Barsanti et al., 2008, Smith et al., 2008)

Recent work has attempted to shed light on the processes that lead to the presence of amines in the aerosol-phase through mass spectrometry studies of aerosol generated in smog chambers. These studies have shown that most particles generated from amines are in the form of alkyl nitrate salts (Angelino et al., 2001). The exception to this has been tertiary amines, where Murphy et al. (2007) determined secondary organic aerosol formation mass yields of 5-23% (Murphy et al., 2007). More recently, Silva et al. (2008) observed increases in amine ions from nighttime ambient aerosol sampling (Silva et al., 2008). He estimated that amine containing particles account for 0.5-6  $\mu\text{g}/\text{m}^3$  of the

ultrafine aerosol in Logan, Utah. Subsequently, laboratory investigations of trimethylamine (TMA) with  $\text{NO}_3$  revealed the presence of highly oxidized large molecular weight ions indicating that  $\text{NO}_3$  can play a significant role in the nighttime chemistry of TMA with estimated gas-to-particle conversions of 65%. Therefore, this paper investigates secondary particle formation from other commonly emitted primary amines.

## 2 Experimental

All experiments were conducted at the UCR/CE-CERT Environmental Chamber, which has been described in detail elsewhere (Carter et al., 2005). In short, this facility consists of two  $90 \text{ m}^3$  Teflon reactors attached to a rigid collapsible frame, which are maintained at a slight positive pressure to minimize diffusion of any contaminate into the reactors. The reactors are located in a temperature controlled room, which is continually flushed with pure air. Connected to the reactors are a suite of instrumentation including an Aerodyne high resolution time of flight mass spectrometer (HR-ToF-AMS), and two scanning mobility particle spectrometers (SMPS), built in house, capable of sizing particles from 28-730nm (Wang and Flagan 1990). Particle number and volume were wall loss corrected using the method of Bowman et al. (1997), additionally, particle mass loadings were calculated assuming a unit density (Bowman et al., 1997). Ports into the chamber enable introduction of compounds of interest as well as monitoring of  $\text{NO}_x$  using a Thermal Environmental Instruments model 42C chemiluminescent analyzer and  $\text{O}_3$  by a Dasibi Environmental Corp 1003-AH. Initial concentrations of  $\text{NO}_x$  and  $\text{O}_3$  were below the detection limits of our analyzers (50 ppt and 2 ppb, respectively) for each

experiment performed. PTRMS measurements of the parent amine were also attempted; however, no measureable ion signals were detected for the parent amine compounds.

Amines (Sigma Aldrich, purity  $\geq 99\%$ ) were introduced into a dark chamber by injecting a known volume of liquid amine into a small glass injection manifold or by introducing a known volume of the gas phase amine into a calibrated bulb based on calculated partial pressures. Pure nitrogen was then passed over the liquid or through the bulb, flushing the amine into the reactors. Table A.1 lists the experimental conditions of all experiments conducted. 350-400 ppb of ozone was introduced by passing 35 psi of pure air through two UV ozone generators only after the mass concentration of particles formed from initial injection of the parent amine had reached a steady state ( $\sim 2$  hrs).  $\text{NO}_x$  was added to the reactors as NO using a calibrated bulb approximately 2 hrs after ozone addition, when aerosol mass concentrations had once again reached a steady value. Total aerosol yields (Y) were determined using the aerosol yield equation as defined by Odum et al. with slight modification.

$$Y = \frac{\Delta M}{\Delta ROG} \quad \text{Eq 1.}$$

where  $\Delta M$  ( $\mu\text{g}/\text{m}^3$ ) is the total aerosol mass concentration produced for a given amount of reactive organic gas reacted ( $\Delta ROG$ ,  $\mu\text{g}/\text{m}^3$ ) (Odum et al., 1996). This definition differs from the more traditional form of the yield equation in that it accounts for the fact that all aerosol produced might not be organic in nature

Sampling of aerosol for off-line analysis was performed by drawing air for 3 hours at 25 LPM from the reactors through a stainless steel sampling port located just

below the chamber onto pre-baked quartz fiber filters (Pall Life Sciences Laboratory). Filters were then extracted by sonication for 30 min with 5 ml of HPLC grade water (Fisher Scientific Optima Grade). During the sonication period, the extracts were kept cold to minimize liquid phase reactions and losses due to volatilization. Extracts were then filtered through a 1  $\mu\text{m}$  pore size syringe filter (Whatman) to remove any quartz fibers and concentrated to 1 ml under a stream of pure nitrogen before analysis.

### **2.1 High Pressure Liquid Chromatograph – Time Of Flight Mass Spectrometer (HPLC-TOF)**

The HPLC-TOF (Agilent Technologies, model 6210) was operated in positive ionization mode with an atmospheric pressure chemical ionization source with a gas temperature of 300 °C, vaporizer temperature of 250 °C, corona current of 4  $\mu\text{A}$ , drying gas flow of 5  $\text{L min}^{-1}$  and a nebulizer pressure of 40 psig. Ultra pure nitrogen was used as the carrier gas. Samples were injected using a flow injection process with HPLC grade water along with two mass reference compounds to ensure a mass accuracy of 5 ppm or greater. No acidic modifier was used in the mobile phase to prevent acid-base reactions during analysis. Analytical standards for identified products were not commercial available.

### **2.2 High Resolution Time of Flight Aerosol Mass Spectrometer (AMS)**

Details of this instrument and data analysis methods have been explained in detail by DeCarlo et al. (DeCarlo et al., 2006). In brief, the instrument samples through an aerodynamic lens into a time-of-flight chamber; particles between 50-600 nm are transmitted with 100% efficiency. In the time-of-flight chamber particles are accelerated

until impacting on to a tungsten heater maintained at 600 °C, at which point the non-refractory aerosol vaporizes and is subjected to electron impact ionization at 70 eV.

Ions are guided using a series of lenses to the orthogonal extractor, where they are pulsed into the time-of-flight chamber approximately every 13  $\mu$ s. Depending on the mode of operation ions are either reflected towards a micro-channel plate (MCP) detector following a standard reflectron time-of-flight configuration (V-mode), or ions leaving the reflector are directed first to a hard mirror then back towards the reflector then finally to the MCP (W-mode), more than doubling the path length of V-mode operation and increasing m/z resolution.

### **3 Results and Discussion**

#### **3.1 Methylamine**

Particle formation was observed immediately after injection of methylamine into the clean reactors (Fig. A.2). These particles result from the formation of methylammonium nitrate produced by reaction of methylamine with trace amounts of  $\text{NO}_x$  present in the chamber (see Section 4.1 for discussion of this salt formation). Addition of ozone had no effect on the particle number or volume. However, a rapid increase in particle number and volume was observed after addition of  $\text{NO}_3$  (as  $\text{O}_3 + \text{NO}_x$ ) to the chamber; ultimately producing  $< 2 \mu\text{g}/\text{m}^3$  of aerosol after wall loss correction. Assuming total consumption of methylamine, an aerosol mass yield of 1.6% was determined using equation 1.

Particle composition (Fig. A.3) measured by the AMS in W-mode after addition of  $\text{NO}_x$  to the system clearly shows the fragments of m/z 30 ( $\text{CH}_4\text{N}^+$ ), m/z 41 ( $\text{C}_3\text{H}_5^+$ ), m/z 42 ( $\text{C}_2\text{H}_4\text{N}^+$ ), and a small signal from ion m/z 46 ( $\text{NO}_2^+$ ). Proposed structures of

these ions are shown in Figure A.4. Off-line filter analysis was not performed due to the lack of mass formed during this experiment.

### 3.2 Ethylamine

Particle formation is seen immediately after injection of ethylamine to the reactors (Fig. A.5). These particles are from aminium nitrate salt formed from reactions between the amine and trace amounts of  $\text{NO}_x$  in the chamber, similar to the methylamine system. Addition of ozone to the system had no measureable effect on particle number or mass. However, in contrast to methylamine, particle formation increased at a rapid rate once  $\text{NO}_3$  was introduced to the chamber (as  $\text{O}_3 + \text{NO}$ ), ultimately producing  $\sim 80 \mu\text{g}/\text{m}^3$  (mass yield  $\sim 44\%$ ).

The mass spectrum as detected by the AMS (Fig. A.6) shows the  $m/z$  fragments appear similar to that of methylamine despite the dramatic differences in aerosol formed, with the exception of the appearance of  $m/z$  44 ( $\text{C}_2\text{H}_6\text{N}^+$ ). W-mode data indicates the appearance of a high mass fragments at  $m/z$  59.035 and 100.06, which can be attributed to  $\text{C}_2\text{H}_5\text{NO}^+$  and  $\text{C}_4\text{H}_8\text{N}_2\text{O}^+$  respectively and which might account for the differences in aerosol formation between the methylamine system and this system.

Filter analysis (Fig. A.6) indicates the presence of ions at  $m/z$ 's of 88.07605 and 90.09154 which have been identified as a hydroxyl containing imine ( $\text{C}_4\text{H}_{10}\text{NO}^+$ ) and the stable carbinolamine ( $\text{C}_4\text{H}_{12}\text{NO}^+$ ), respectively. Figure A.7 lists the major ions and proposed structure associated with them. Water was used as the sole extraction solvent to efficiently remove nitrate salts from the filter, which were originally thought to dominate the aerosol phase species by their formation through acid-base chemistry. Clearly this

was not the case; therefore, the possibility exists that hydrophobic compounds remained on the filter during extraction that were not detected by HPLC-TOF analysis.

### 3.3 Propylamine

Similar to the two previously studied amines, an initial nucleation burst of aminium nitrate salt was apparent immediately after injection of the amine followed by the rapid decay in particle number and volume (Fig. A.8). A second rapid burst of particle formation was observed after addition of  $\text{NO}_3$  (as  $\text{O}_3 + \text{NO}_x$ ) to the chamber; similar to the initial burst it was followed by decay of the particle volume indicating possible formation and evaporation of salts. However, the particle mass loading eventually stabilized around  $53 \mu\text{g}/\text{m}^3$  (yield of 22%). Very little  $\text{NO}^+$  or  $\text{NO}_2^+$  signal was apparent in the high resolution HR-ToF-AMS data, indicating that a large portion of the condensable species formed by the addition of  $\text{NO}_x$  to the chamber were not nitrate salts.

The spectrum obtained by the AMS (Fig. A.9) is markedly different from that of methylamine and ethylamine showing prominent mass fragments upwards of  $m/z$  146. Using the W-mode of the AMS, these fragments can be attributed to 100.07 ( $\text{C}_5\text{H}_{10}\text{NO}^+$ ), 100.11 ( $\text{C}_6\text{H}_{14}\text{N}^+$ ), 114.09 ( $\text{C}_6\text{H}_{12}\text{NO}^+$ ), 128.11 ( $\text{C}_6\text{H}_{12}\text{N}_2\text{O}^+$ ), and 146.08 ( $\text{C}_6\text{H}_{12}\text{NO}_3^+$ ). The appearance of these heavy molecular weight ions, some with no oxygen present, indicates the formation of nitrogen carbon bonds.

Mass spectra, normalized to the most abundant ion, obtained from the HPLC-TOF (Fig. A.9) indicate several important ions. The 74.06088 peak can be attributed to the amide of propylamine. Also indicated in the HPLC-TOF spectra is the presence of ions with masses 88.07601, 90.09061, 102.08960, and 114.09111. These four ions have been

identified as imines containing a hydroxyl group ( $88.07601\text{-C}_4\text{H}_{10}\text{NO}^+$ ) and ( $102.08960\text{-C}_5\text{H}_{12}\text{NO}^+$ ), a stable carbinolamine ( $90.09061\text{-C}_4\text{H}_{12}\text{NO}^+$ ), and an imine containing a carbonyl group ( $114.0911\text{-C}_6\text{H}_{12}\text{NO}^+$ ). Figure A.10 shows the major ions detected and their corresponding structure.

### 3.4 Butylamine

Not unlike the three previously examined amines, a large initial nucleation burst of aminium nitrate salt was observed after injection of butylamine into the chamber followed by a rapid decay in particle number. Addition of ozone resulted in no obvious change in particle number or mass (Fig. A.11). Only after addition of  $\text{NO}_3$  (as  $\text{O}_3 + \text{NO}$ ) did we observe a rapid increase in particle mass and number, ultimately producing  $130 \mu\text{g}/\text{m}^3$  (yield of 44%).

Spectra from the AMS (Fig. A.12) indicate high mass fragments much like the propylamine/ $\text{NO}_3$  system. Employing the W-mode of the AMS we were able to identify these ions as  $100.07$  ( $\text{C}_5\text{H}_{10}\text{NO}^+$ ),  $128.10$  ( $\text{C}_7\text{H}_{14}\text{NO}^+$ ),  $142.12$  ( $\text{C}_8\text{H}_{16}\text{NO}^+$ ),  $156.12$  ( $\text{C}_8\text{H}_{16}\text{N}_2\text{O}^+$ )  $158.11$  ( $\text{C}_8\text{H}_{16}\text{NO}_2^+$ ), and  $174.11$  ( $\text{C}_8\text{H}_{16}\text{NO}_3^+$ ).

Figure A.12 also shows the spectrum obtained from a filter sample. Again, many significant ions are observed in this spectrum including  $102.09151$  ( $\text{C}_5\text{H}_{12}\text{NO}^+$ ),  $142.12229$  ( $\text{C}_8\text{H}_{16}\text{NO}^+$ ),  $158.11767$  ( $\text{C}_8\text{H}_{16}\text{NO}_2^+$ ), and  $174.11122$  ( $\text{C}_8\text{H}_{16}\text{NO}_3^+$ ). Masses  $74.09705$  ( $\text{C}_4\text{H}_{12}\text{N}^+$ ) and  $88.07614$  ( $\text{C}_4\text{H}_{10}\text{NO}^+$ ) represent the parent amine and amide formed during oxidation, while the ion appearing at  $142.12229$  corresponds to the formation of an imine product. Ions at 158 and 174 show among the highest degree of oxidation of any peaks observed, requiring the presence of 2 and 3 oxygen atoms



respectively. Identification of a structure of these two peaks is difficult due to multiple possible empirical formulas. Major ions and their associated structures are shown in figure A.13.

#### **4 Mass Spectrum Interpretation**

Two general trends are observed in the AMS and HPLC-TOF spectra: first, the formation of imines which contain a hydroxyl group (mass 88.07605 for ethylamine, mass 114.0911 for propylamine, and mass 142.12229 for butylamine); second, the presence of imines containing a carbonyl group (100.06 for ethylamine, 128.11 for propylamine, and 156.12 for butylamine). These peaks show extremely large carbon to oxygen ratios, allowing us to discount aldol condensation reactions as a route leading to their formation.

Furthermore, the observance of an amide peak in only those systems which formed aerosol (Fig. A.14) indicates that it plays a major role in the aerosol formation process. This is further supported from the high resolution HPLC-TOFMS, where the presence of the amide peak was confirmed for propylamine and butylamine (the ethylamine amide mass is below the  $m/z$  capabilities of the HPLC-TOF). This observation is explained by examination of bond dissociation enthalpies (BDE) of the hydrogen attached to the alpha carbon of aliphatic amines (Lalevee et al., 2002). Lalevee noticed a decrease in energy as the alkyl chain increased in carbon number, thus indicating why methylamine, with a carbon-hydrogen BDE of 92.4 kcal/mol was unable to oxidize to formamide, while ethyl, propyl, and butylamine with lower carbon-hydrogen BDE's were able to undergo hydrogen abstraction by  $\text{NO}_3$ .

Finally, the observation of carbinolamines in ethyl, propyl, and butylamine systems suggests that the route of aerosol formation must include this class of compounds as an intermediate or product. The presence of carbinolamine compounds is not wholly unexpected as they are the intermediate compounds to imine formation via reactions between carbonyl compounds and primary or secondary amines. These compounds have been observed as intermediates in other carbonyl-amine reactions and have been shown to have a slow reverse reaction, remaining stable in solution for up to 24 hrs. (Cheung et al., 2005, Cocivera et al., 1976, Pedersen et al., 1999).

#### **4.1 Salt Formation and Nitros/Nitramines**

The particles formed immediately following injection of the amines followed the same trend of a rapid decrease in number concentration before eventually reaching an equilibrium concentration and is consistent with the particles achieving a gas-particle equilibrium. This same observation was made by Murphy et al. for a similar system who attributed it to the volatilization of Triethylammonium nitrate while undergoing gas-particle partitioning (Murphy et al., 2007). In all cases, with the exception of methylamine, the mass of particles formed during these events accounted for less than 4 % of the total mass formed by the end of the experiment. In addition, W-mode AMS data indicates the presence of strong  $\text{NO}^+$  and  $\text{NO}_2^+$  ions during this initial particle formation. The presence of strong  $\text{NO}^+$  and  $\text{NO}_2^+$  signals is a indication of aminium nitrate salt formation commonly observed for acid-base reactions involving amines (Murphy et al., 2007; Figure A.4, panel B in Silva et al.). However, we can exclude the corresponding aminium salts as a significant portion of the aerosol formed in the later portion of our experiments,

after addition of  $\text{NO}_3$ , due to the small contribution of  $\text{NO}^+$  and  $\text{NO}_2^+$  to the total aerosol signal (Fig.A.15) during this period. Therefore, the complete lack of  $\text{NO}^+$  signal and relatively small intensity of  $\text{NO}_2^+$  signal during the later part of our experiments indicates that most of the secondary aerosol formed after addition of  $\text{NO}_3$  were not aminium nitrate salts and therefore must organic in nature.

Due to the extremely high vapor pressures associated with nitroamines and nitrosamines, their existence in the aerosol is highly unlikely. As evidence for this, the vapor pressure of N-nitros-butanamine and N-nitro-butanamine were calculated to be 24.3 and 1.4 torr respectively, using the group contribution method of Myrdal and Yalkowsky (Myrdal and Yalkowsky 1997). These two compounds were chosen because they are the highest molecular weight nitros/nitroamine compounds conceivably formed in our systems, and represent the most extreme cases. Additionally, the presence of nitroamines and nitrosamines can be excluded due to the absence of the expected strong molecular ions signal (Bulusu et al 1970, Rainey et al. 1978). Other ions expected from the formation of these types of compounds would be a strong  $\text{NO}^+$  ion associated with nitrosamines and  $\text{NO}_2^+$  ions from nitroamines, neither of which were observed in significant amounts in AMS spectra as stated earlier. While the possible decomposition of these compounds cannot be definitively ruled out, due to their high vapor pressures, it is highly unlikely they are capable of being present in the aerosol in appreciable amounts.

## **5 Proposed Aerosol Formation Mechanism**

We propose a reaction sequence (Fig. A.16) similar to that of formation of a Schiff base. Mass spectral evidence of amide formation, coupled with the observation of

the carbinolamine intermediate and imine product in only those systems that formed aerosol gives support to this proposed mechanism. In this reaction, the amine (compound I in figure A.16) reacts with the nitrate radical, losing a hydrogen attached to the alpha carbon leading to formation of a peroxy radical. This peroxy radical, in the absence of NO, can undergo RO<sub>2</sub>-RO<sub>2</sub> self reactions yielding 2 amide molecules (compound II) and molecular oxygen. Alternatively, amide products may be generated by reactions between RO<sub>2</sub> and NO<sub>3</sub> leading to NO<sub>2</sub> and O<sub>2</sub> byproducts. Subsequent reactions between the amide molecule and the parent amine proceeds by a nucleophilic attack by the parent amine on an amide, followed by a 1,3-hydrogen transfer forming a stable carbinolamine intermediate (compound III). Compounds II and III have been confirmed by mass spectral analysis as present in our aerosol in all three aerosol forming systems. The hydroxyl group of the carbinolamine will then undergo protonation followed by dehydration resulting in formation of an iminium ion (compound IV). Loss of the hydrogen from the positively charged nitrogen ultimately leads to formation of an imine (compound V). The imine product (compound V) has also been observed in all three aerosol forming systems by means of online and offline mass spectra techniques.

Imine formation has been observed on particle surfaces, and is known to be promoted in slightly acidic conditions (pH 4-5) (Haddrell and Agnes 2004, Zahardis et al., 2008, Jencks 1959). However, without structural information, the assignments of mass spectrum ions remain tentative and can only be extended to empirical formula confirmation. Therefore, other reaction mechanisms cannot be completely ruled out.

To confirm the particle formation resulted from oxidation by  $\text{NO}_3$ , additional experiments under dark conditions with only the parent amine and  $\text{N}_2\text{O}_5$  present. These results indicated no significant mass formation until injection of  $\text{N}_2\text{O}_5$ , which subsequently resulted in a rapid burst of particle number and volume, identical to the experimental results shown above.

## **6 Implications**

The data presented here indicates that under nighttime conditions, in locations with sufficiently high nitrate radical concentrations, reactions of primary amines with the nitrate radical can be of great importance to new particle formation. We observe that the formation of organic aerosol from reactions between primary amines and  $\text{NO}_3$  is sufficiently fast to be competitive with the acid-base reactions leading to aminium nitrate salts production. This was supported by online and offline mass spectrometry which showed organic aerosol formation dominating the aerosol mass spectra. Aerosol mass yields for the four amines studied were estimated to be < 2% for methylamine, 23% for propylamine, while ethylamine and butylamine had yields of ~ 44%.

The presence of amide products in all three aerosol forming systems indicate that the C-H bond strengths for ethyl, propyl, and butylamine were sufficiently weak to be abstracted by  $\text{NO}_3$ , while methylamine oxidation by nitrate did not produce observable amide products. Observation of carbinolamine and imine products demonstrated that the oxidation of primary aliphatic amines proceeds by a Schiff base reaction mechanism, ultimately leading to imine formation. This implies that secondary oxidation chemistry plays a key role in the new particle formation processes from amines. Furthermore, these

experiments suggest that further research into the reaction kinetics of nitrate and amines is needed, as there is no data in the current literature providing kinetic measurements. As such, aerosol formation from amines may be greatly under predicted by current air quality models and more research is needed in order to understand the complex interactions of amines and  $\text{NO}_3$  in the lower troposphere.

## References

- Angelino, S., Suess, D. T., Prather, K. A.: Formation of aerosol particles from reactions of secondary and tertiary alkylamines: Characterization by aerosol time-of-flight mass spectrometry, *Environmental Science & Technology*, 35, 3130-3138, 2001
- Bailey, D., Cativiela, J. P., Descary, B., Grantz, D., Hamilton, K. D., Martin, P. E., Meyer, D., Mullinax, D., Simunovic, C. A., Sweet, J., Warner, D., Watson, J., "Dairy Emissions Factors for Volatile Organic Compounds",
- Barsanti, K. C., McMurry, P. H., Smith, J. N.: The Potential Contribution of Organic Salts to new Particle Growth, *Atmospheric Chemistry and Physics Discussions*, 8, 20723-20748, 2008
- Beddows, D. C. S., Donovan, R. J., Harrison, R. M., Heal, M. R., Kinnersley, R. P., King, M. D., Nicholson, D. H., Thompson, K. C.: Correlations in the chemical composition of rural background atmospheric aerosol in the UK determined in real time using time-of-flight mass spectrometry, *Journal of Environmental Monitoring*, 6, 124-133, 2004
- Bowman, F. M., Odum, J. R., Seinfeld, J. H., Pandis, S. N.: Mathematical model for gas-particle partitioning of secondary organic aerosols, *Atmospheric Environment*, 31, 3921-3931, 1997
- Carter, W. P. L., Cocker, D. R., Fitz, D. R., Malkina, I. L., Bumiller, K., Sauer, C. G., Pisano, J. T., Bufalino, C., Song, C.: A new environmental chamber for evaluation of gas-phase chemical mechanisms and secondary aerosol formation, *Atmospheric Environment*, 39, 7768-7788, 2005
- Cheung, A., Struble, E., He, J. Y., Yang, C., Wang, E., Thurston, D. E., Liu, P.: Direct liquid chromatography determination of the reactive imine SJG-136 (NSC 694501), *Journal of Chromatography B-Analytical Technologies in the Biomedical and Life Sciences*, 822, 10-20, 2005
- Cocivera, M., Fyfe, C. A., Effio, A., Vaish, S. P., Chen, H. E.: Flow Nuclear Magnetic-Resonance Study of Dehydration of Tetrahedral Intermediate Resulting from Addition of Hydroxylamine to Acetaldehyde, *Journal of the American Chemical Society*, 98, 1573-1578, 1976
- DeCarlo, P. F., Kimmel, J. R., Trimborn, A., Northway, M. J., Jayne, J. T., Aiken, A. C., Gonin, M., Fuhrer, K., Horvath, T., Docherty, K. S., Worsnop, D. R., Jimenez, J. L.: Field-deployable, high-resolution, time-of-flight aerosol mass spectrometer, *Analytical Chemistry*, 78, 8281-8289, 2006

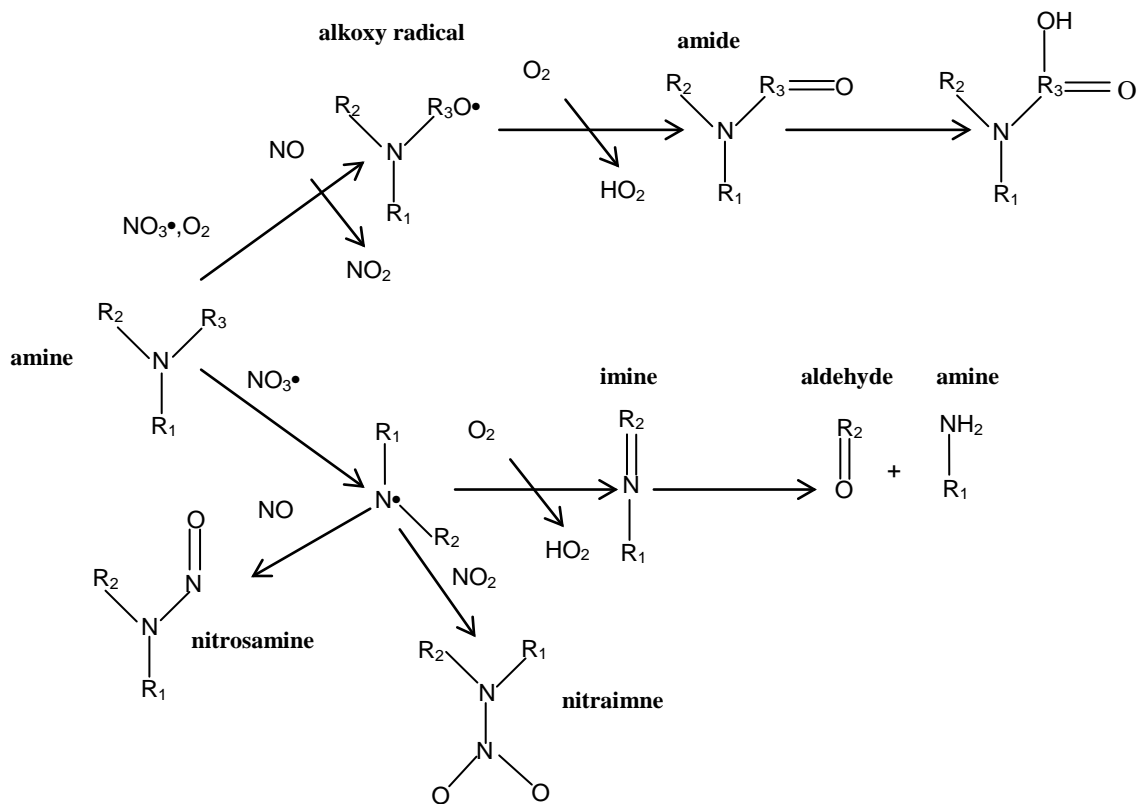
- Finlayson-Pitts, B., Pitts, J. N.: Chemistry of the Upper and Lower Atmosphere. Academic Press, 2000
- Glagolenko, S., Phares, D. J.: Single-particle analysis of ultrafine aerosol in College Station, Texas, Journal of Geophysical Research-Atmospheres, 109, 2004
- Haddrell, A. E., Agnes, G. R.: A class of heterogeneous/multiphase organic reactions studied on droplets/particles levitated in a laboratory environment: aldehyde plus 1,8-diaminonaphthalene equals imine, Atmospheric Environment, 38, 545-556, 2004
- Jencks, W. P.: Studies on the Mechanism of Oxime and Semicarbazone Formation, Journal of the American Chemical Society, 81, 475-481, 1959
- Lalevee, J., Allonas, X., Fouassier, J. P.: N-H and alpha(C-H) bond dissociation enthalpies of aliphatic amines, Journal of the American Chemical Society, 124, 9613-9621, 2002
- Manahan, S. E.: Environmental Chemistry. 4<sup>th</sup>; Lewis, 1990
- Murphy, D. M., Thomson, D. S.: Chemical composition of single aerosol particles at Idaho Hill: Positive ion measurements, Journal of Geophysical Research-Atmospheres, 102, 6341-6352, 1997
- Murphy, S. M., Sorooshian, A., Kroll, J. H., Ng, N. L., Chhabra, P., Tong, C., Surratt, J. D., Knipping, E., Flagan, R. C., Seinfeld, J. H.: Secondary aerosol formation from atmospheric reactions of aliphatic amines, Atmospheric Chemistry and Physics, 7, 2313-2337, 2007
- Myrdal, P. B., Yalkowsky, S. H.: Estimating pure component vapor pressures of complex organic molecules, Industrial & Engineering Chemistry Research, 36, 2494-2499, 1997
- Odum, J. R., Hoffmann, T., Bowman, F., Collins, D., Flagan, R. C., Seinfeld, J. H.: Gas/particle partitioning and secondary organic aerosol yields, Environmental Science & Technology, 30, 2580-2585, 1996
- Pedersen, E. J., Urbansky, E. T., Marinas, B. J., Margerum, D. W.: Formation of cyanogen chloride from the reaction of monochloramine with formaldehyde, Environmental Science & Technology, 33, 4239-4249, 1999
- Pitts, J. N., Grosjean, D., Vancauwenberghe, K., Schmid, J. P., Fitz, D. R.: Photo-Oxidation of Aliphatic-Amines under Simulated Atmospheric Conditions -



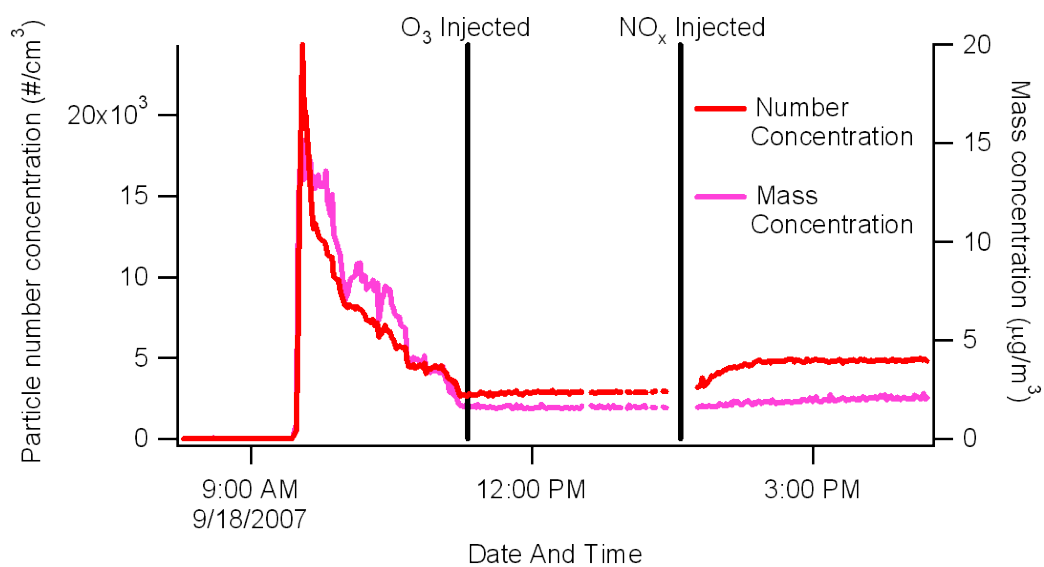
- Formation of Nitrosamines, Nitramines, Amides, and Photo-Chemical Oxidant, *Environmental Science & Technology*, 12, 946-953, 1978
- Schade, G. W., Crutzen, P. J.: Emission of Aliphatic-Amines from Animal Husbandry and Their Reactions - Potential Source of N<sub>2</sub>O and HCN, *Journal of Atmospheric Chemistry*, 22, 319-346, 1995
- Seinfeld, J. H., Pandis, S. N.: *Atmospheric Chemistry and Physics: From Air pollution to Climate Change*. John Wiley and Sons, Inc., 1998
- Silva, P., Erupe, M., Malloy, Q. G. J., Li, Q., Warren, B., Price, D., Elias, J., Cocker, D. R.: Trimethylamine as Precursor to Secondary Organic Aerosol Formation via Nitrate Radical Reaction in the Atmosphere, *Environmental Science & Technology*, Accepted, 2008
- Smith, J. N., Dunn, M. J., VanReken, T. M., Iida, K., Stolzenberg, M. R., McMurry, P. H., Huey, L. G.: Chemical Composition of Atmospheric Nanoparticles Formed from Nucleation in Tecamac, Mexico: Evidence for an Important Role of Organic Species in Nanoparticle Growth, *Geophys. Res. Lett.*, 35,
- Tan, P. V., Evans, G. J., Tsai, J., Owega, S., Fila, M. S., Malpica, O.: On-line analysis of urban particulate matter focusing on elevated wintertime aerosol concentrations, *Environmental Science & Technology*, 36, 3512-3518, 2002
- Wang, S. C., Flagan, R. C.: Scanning Electrical Mobility Spectrometer, *Aerosol Science and Technology*, 13, 230-240, 1990
- Westerholm, R., Li, H., Almen, J.: Estimation of Aliphatic Amine Emissions in Automobile Exhausts, *Chemosphere*, 27, 1381-1384, 1993
- Zahardis, J., Geddes, S., Petrucci, G. A.: The ozonolysis of primary aliphatic amines in fine particles, *Atmospheric Chemistry and Physics*, 8, 1181-1194, 2008

**Table A.1** List of Experiments Performed and Concentrations of reactants

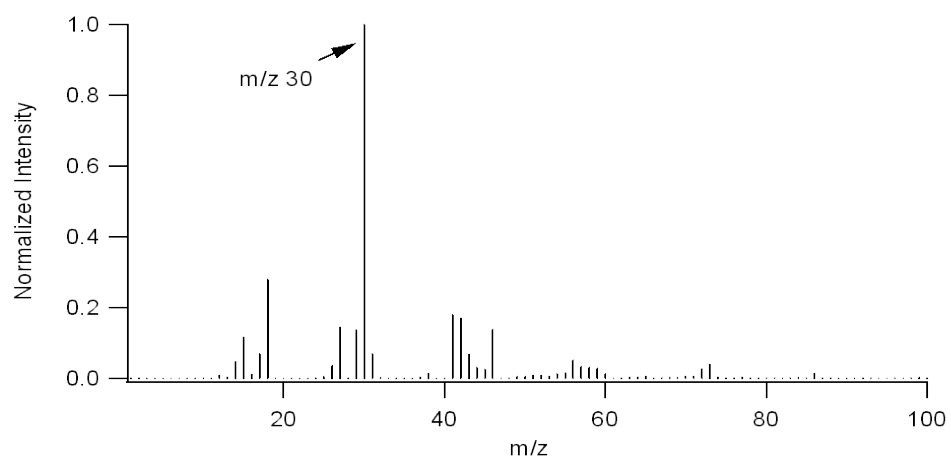
Experiment	Amine	Estimated Initial Amine Concentration (ppb)	Ozone Concentration (ppb)	NO <sub>x</sub> Concentration (ppb)
831	Butylamine	100	352	39
833	Propylamine	100	328	61
834	Methylamine	100	350	34
842	Ethylamine	100	400	25



**Figure A.1** Proposed reaction scheme of amine oxidation adapted from Schade et al., 1995 to show oxidation by  $\text{NO}_3$ .

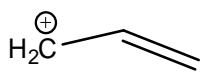


**Figure A.2** Wall loss corrected aerosol mass and number evolution for methylamine/ $\text{NO}_3^\bullet$  reaction showing little organic aerosol formation after addition of  $\text{NO}_x$ .



**Figure A.3** Background subtracted AMS spectrum normalized to m/z 30 from the methylamine/  $\text{NO}_3^-$  system showing no mass fragments other than those of the parent amine.

HR-ToF-AMS ions

30.035	
41.037	
42.035	

**Figure A.4** Proposed structures of AMS ions for Methylamine/NO<sub>3</sub> system.

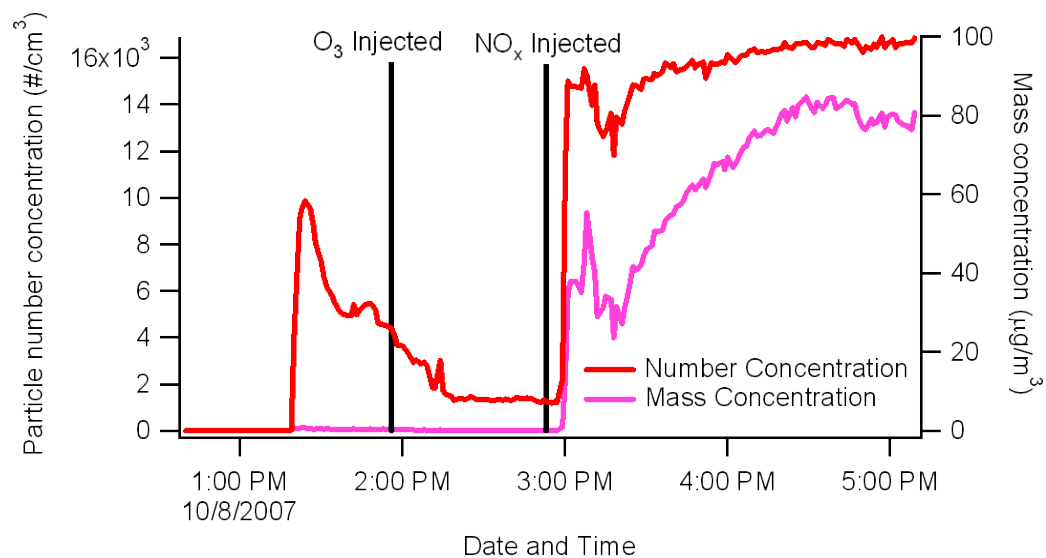


**Figure A.5** Wall loss corrected aerosol mass and number evolution for ethylamine/NO<sub>3</sub><sup>•</sup> reaction indicating a rapid and large increase in organic aerosol formation after addition of NO<sub>x</sub>.

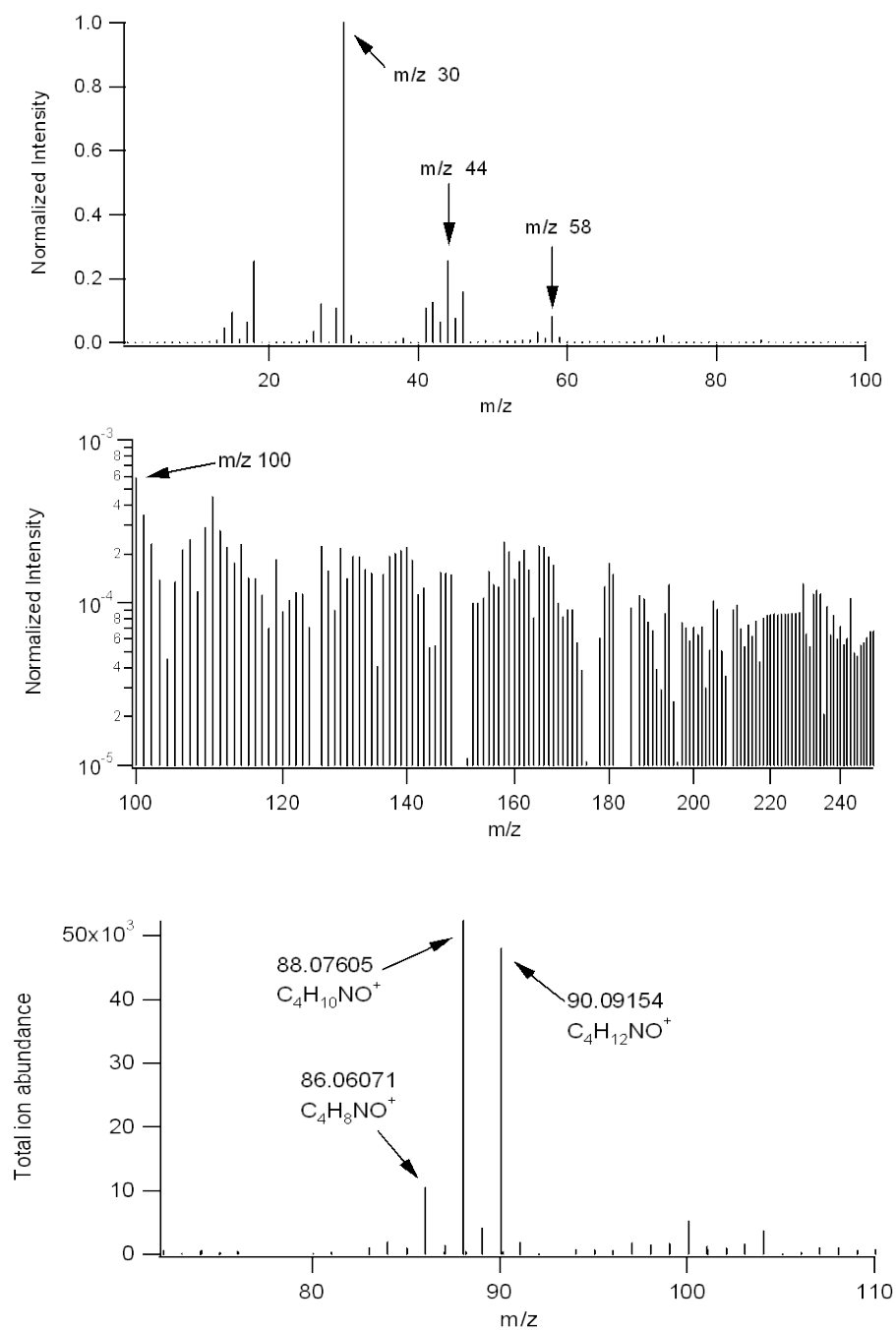
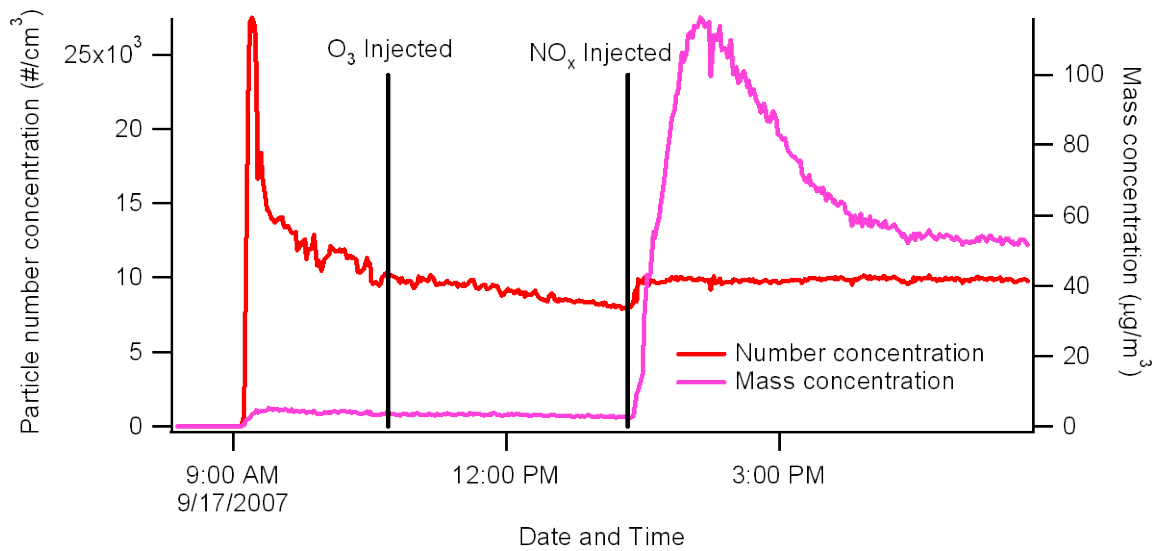


**Figure A.6** Frames 1 and 2: AMS mass spectra normalized to m/z 30 of the ethylamine/ $\text{NO}_3^\bullet$  system indicating the important peaks. Frame 3: HPLC-TOF filter spectrum of ethylamine/ $\text{NO}_3^\bullet$  indicating formation of imines and their stable intermediates.

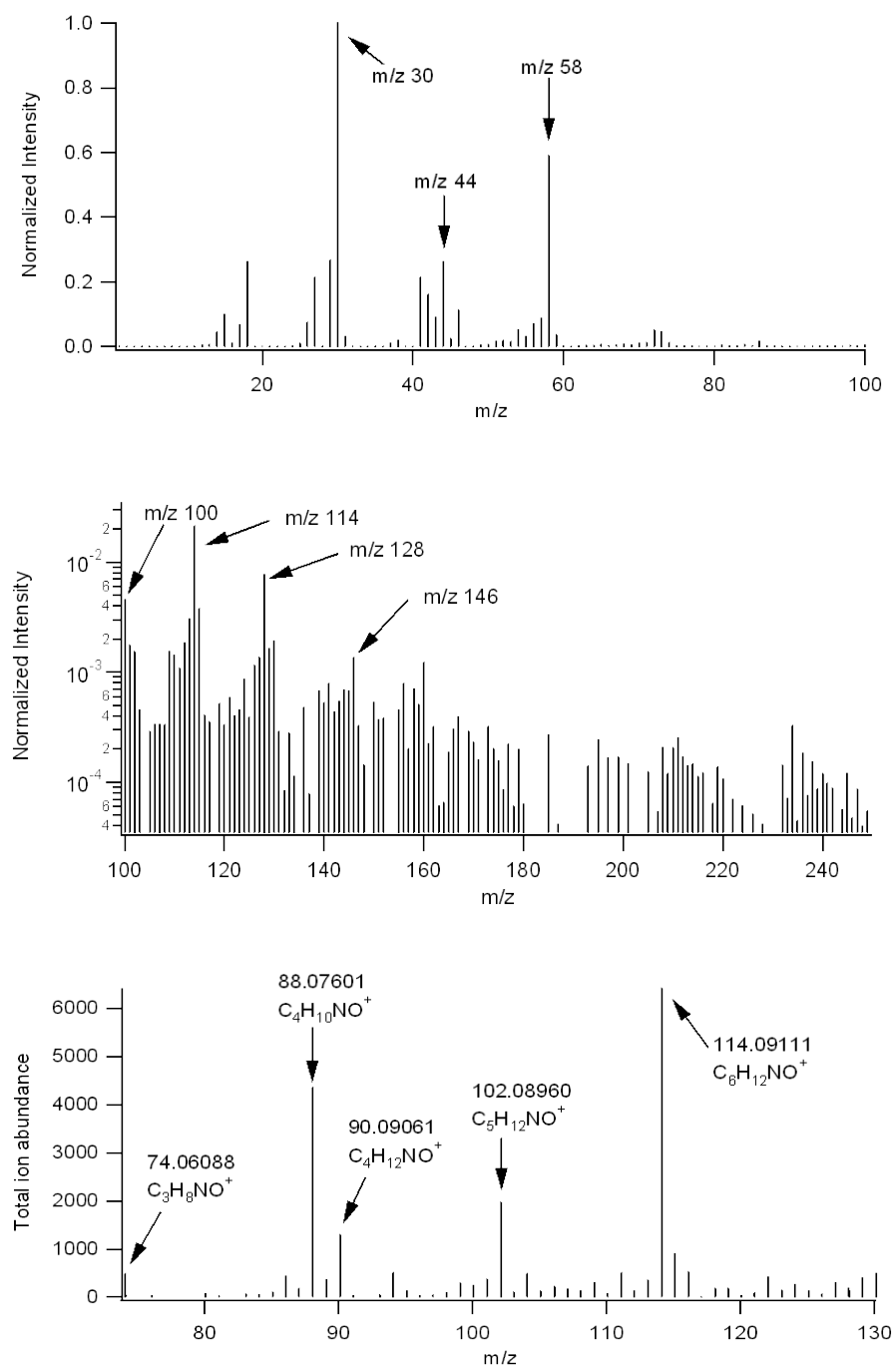


HR-ToF-AMS ions		HPLC-TOF ions	
	30.036		86.06071
	44.052		88.07605
	58.066		
	59.035		90.09154
	100.06		

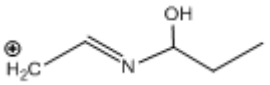
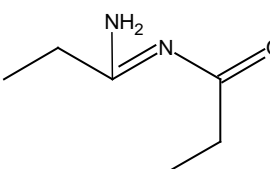
**Figure A.7** Proposed structure of AMS and LC-MS ions for Ethylamine/ $\text{NO}_3$  system



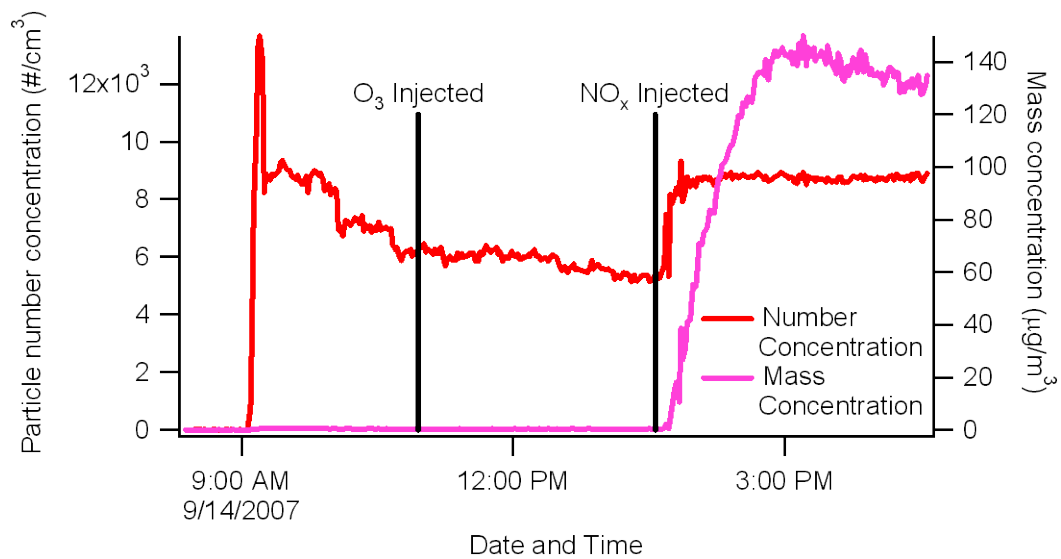
**Figure A.8** Wall loss corrected aerosol mass and number evolution for propylamine/ $\text{NO}_3$  reaction indicating a rapid and large increase in aerosol formation after addition of  $\text{NO}_x$  followed by a rapid loss of a portion of this aerosol.



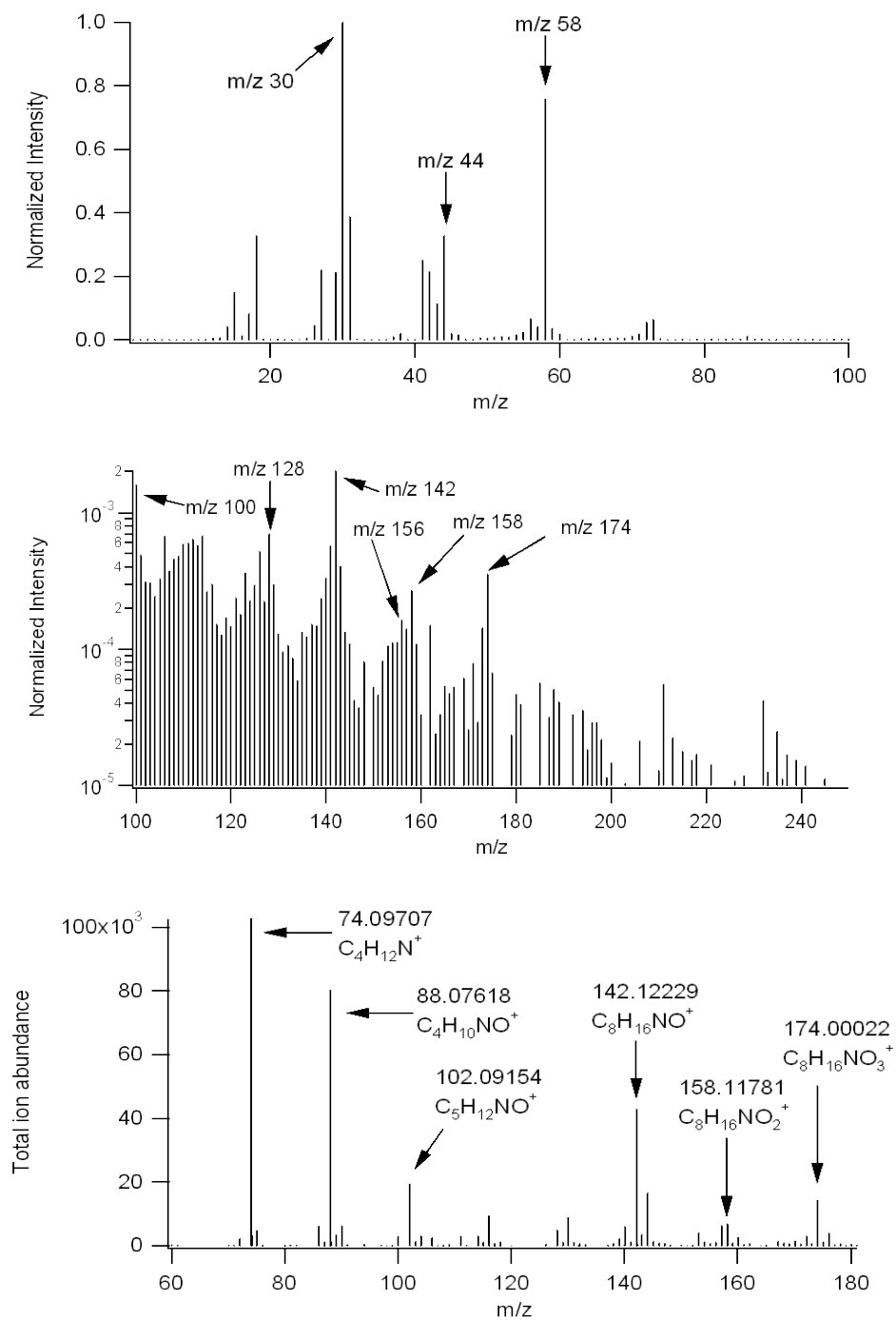
**Figure A.9** Frames 1 and 2: AMS spectrum (normalized to m/z 30) of the propylamine/ $NO_3^\bullet$  system indicating presence of high mass fragments spaced 14 mass units apart. Frame 3: HPLC-TOF filter spectrum showing imine products and stable intermediates.

HR-ToF-AMS ions	HPLC-TOF ions
	100.07
	100.11
	114.09
	128.11
	146.08
	74.06088
	88.07601
	90.09061
	102.08960
	114.09111

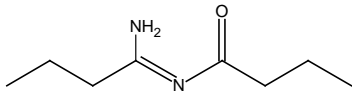
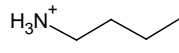
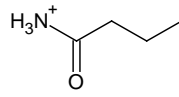
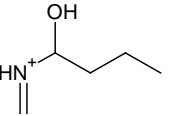
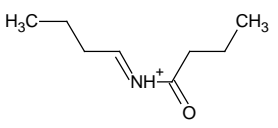
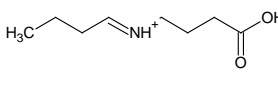
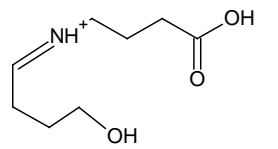
**Figure A.10** Proposed structures of AMS and LC-MS ions for Propylamine/ $\text{NO}_3$  system.



**Figure A.11** Wall loss corrected aerosol mass and number evolution for butylamine/ $\text{NO}_3^\bullet$  reaction indicating a rapid and large increase in organic aerosol formation after addition of  $\text{NO}_x$ .



**Figure A.12** Frames 1 and 2: AMS spectra normalized to largest peak (m/z 30) from butylamine/NO<sub>3</sub><sup>+</sup> system showing the formation of imines some with high degrees of oxidation. Frame 3. HPLC-TOF filter spectrum confirming presence of amide products.

HR-ToF-AMS ions		HPLC-TOF ions	
	100.07		74.09705
	128.10		88.07614
	142.12		102.09151
	156.12		142.12229
	158.11		158.11767
	174.11		174.11122

**Figure A.13** Proposed structures of the AMS and LC-MS ions for Butylamine/ $\text{NO}_3$  system.

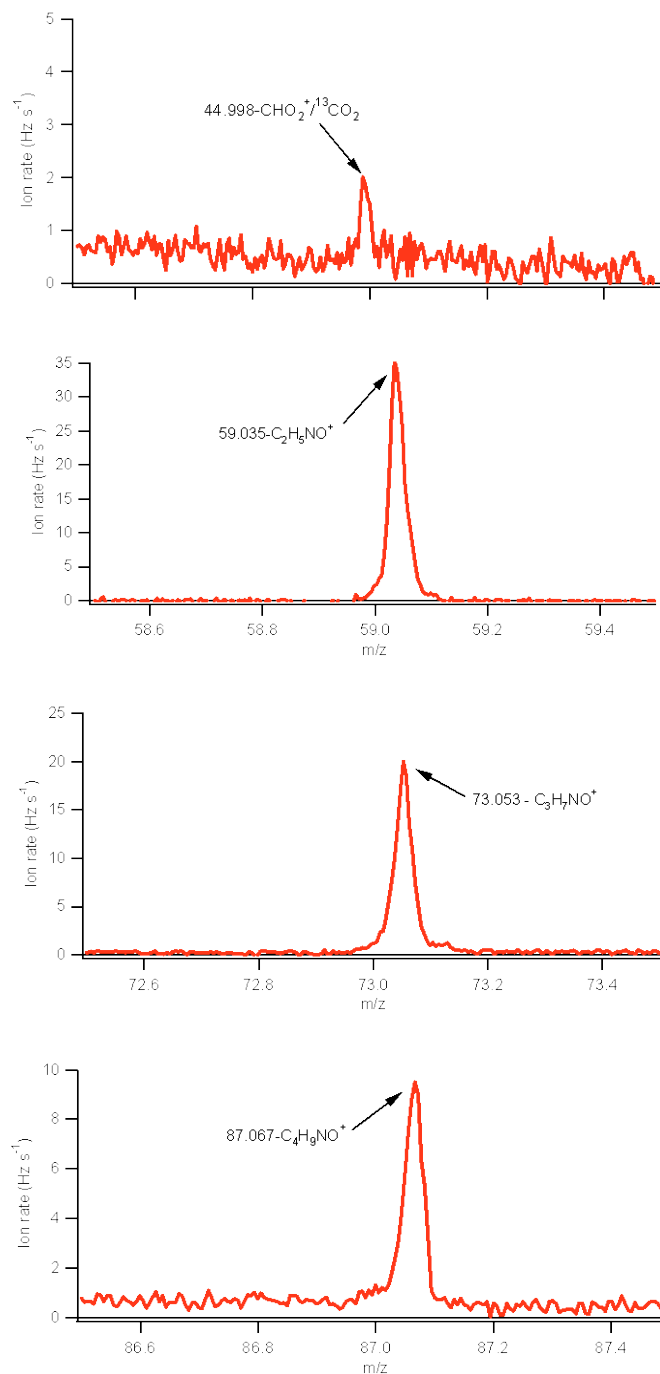


**Figure A.14** Background subtracted W-mode spectrums of (from top to bottom) methylamine, ethylamine, propylamine, and butylamine systems indicating amide peaks are only present in the aerosol forming systems.



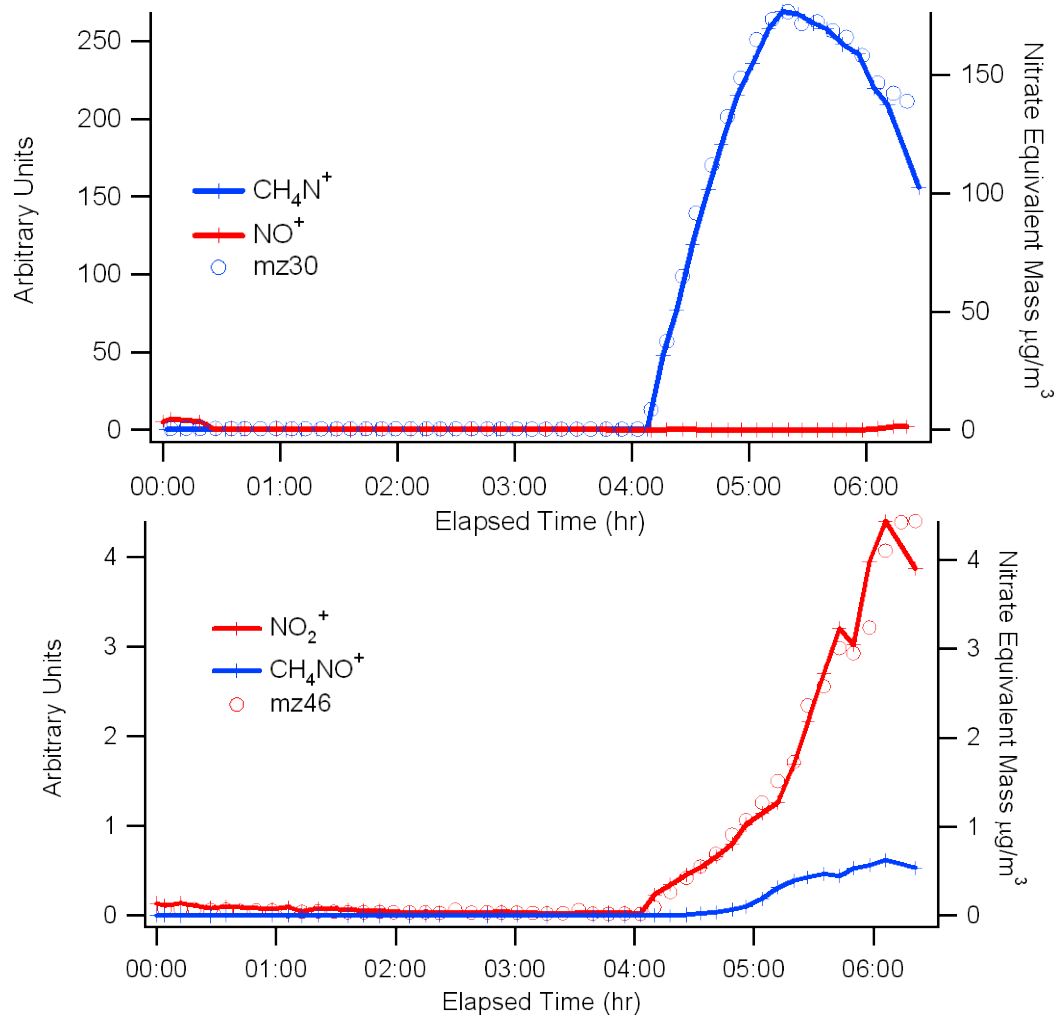


**Figure A.15** Time traces of  $m/z$  30 ions (upper frame) and  $m/z$  46 ions (lower frame) plotted on the left Y-axis along with total mass formation of the respective ions (open circles), plotted on the right Y-axis for butylamine/ $\text{NO}_3$ . The absence of  $\text{NO}^+$  and small amounts of  $\text{NO}_2^+$  give further indication that aerosol formed was mostly organic in nature.

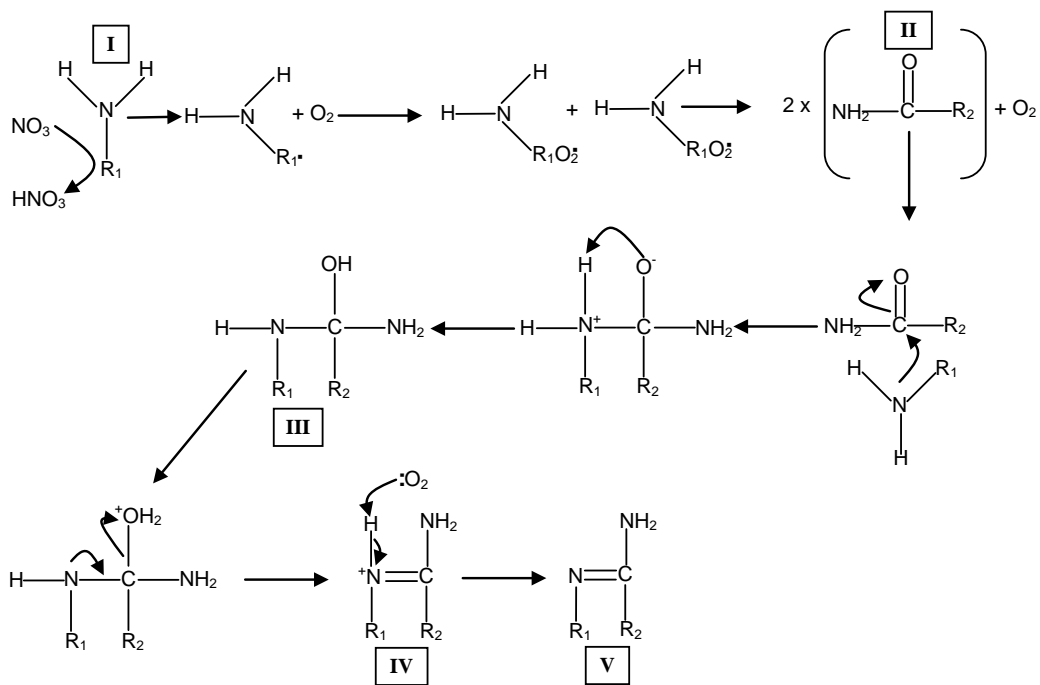


**Figure A.16** Schematic of imine formation from a primary amine.  $\text{R}_1$  equals  $\text{CH}_3$  for methylamine,  $\text{C}_2\text{H}_5$  for ethylamine,  $\text{C}_3\text{H}_7$  for propylamine, etc.  $\text{R}_2$  equals  $\text{R}_1\text{-CH}_2$  (i.e. H for methylamine,  $\text{CH}_3$  for ethylamine,  $\text{C}_2\text{H}_5$  for propylamine, etc.).

## **Appendix B**

### **Trimethylamine as precursor to secondary organic aerosol formation via nitrate radical reaction in the atmosphere**

Reference: Silva, P., Erupe, M., Malloy, Q. G. J., Qi, L., Warren, B., Price, D., Elias, J., and Cocker, D. R.III, 2008. Trimethylamine as Precursor to Secondary Organic Aerosol Formation via Nitrate Radical Reaction in the Atmosphere, *Environmental Science & Technology* 42 (13), 4689-4696.

## Introduction

Numerous studies have shown that significant concentrations of amines are present near agricultural facilities such as dairies and feedlots. Research during the 1970s qualitatively examined the presence of amines from such sources, showing a number of simple primary, secondary, and tertiary amines and indicating that amines make up to 10% of total gas-phase nitrogen (Luebs et al. 1973, Mosier et al. 1973). Recent studies have reported quantitative data, showing that amines are present at ppb levels near agricultural operations. Schade and Crutzen (1995) estimated a global input of 0.15 Tg N annually to the atmosphere from animal husbandry, with trimethylamine present in the highest concentration. Rabaud *et al.* (2003) detected numerous amines in the air at a dairy with concentrations up to 560  $\mu\text{g}/\text{m}^3$  (187 ppb) for butylamine. Other estimates from regulatory agencies show possibly higher emission factors for amines, up to 12 lb hd-yr<sup>-1</sup> (Bailey 2005).

The major reactions of aliphatic amines in the gas-phase are believed to be with atmospheric oxidants such as OH and O<sub>3</sub>. Atkinson (1989) reported rate constants for the reaction of OH ( $k_{OH}$ ) with various alkyl amines on the order of 2-9  $\times 10^{-11}$  cm<sup>3</sup> molecule<sup>-1</sup> s<sup>-1</sup>. This leads to atmospheric lifetimes on the order of ~3-13 hours assuming an OH concentration of 1 $\times 10^{-6}$  molecules cm<sup>-3</sup>. Rate constants for gas-phase reactions between amines and ozone were reported by Tuazon *et al.* (1994). Relatively rapid reactions with ozone were observed for the secondary and tertiary amines. Reactions with other atmospheric gases have not been reported.

During the 1970s, studies into amine chemistry focused on production of nitrosamines. Nitrosamines are carcinogens in animals and the reaction was of concern for potential health impacts. It was shown (Pitts et al. 1978, Tuazon et al. 1978) that under photochemical oxidation conditions, amines react with nitrous acid to form nitrosamines. Since HONO forms readily from NO<sub>2</sub> in the presence of water, the reaction proceeds if amines are present. However, nitrosamines rapidly undergo photolysis (Tuazon et al. 1984) in the atmosphere yielding back the amine and NO.

Sporadic reports of particulate amines have appeared for several decades. The earliest work was performed by Novakov and co-workers (Novakov et al. 1972, Dod et al. 1984, Appel et al. 1985) who conducted a series of particle studies using X-ray photoelectron spectroscopy. Data indicated the presence of a non-ammonium reduced form of nitrogen in particles and suggested that ammonium measurements using water-based extraction methods may suffer from positive artifacts due to hydrolysis of amines. Later studies suggested that amino acids accounted for the reduced form of nitrogen (Milne et al. 1993). However, other reports (Gorzelska et al. 1990, Gorzelska et al. 1992) indicated the presence of amines in precipitation droplets. Recently, Murphy *et al.* (2007) performed chamber reactions looking at particulates from amines and reported that primary and secondary amines produce salts but that tertiary amines produce non-salt secondary organic aerosol in yields of ~5-23% via reactions with OH and ozone.

In the last 10 years, a number of studies using single particle laser desorption/ionization-mass spectrometry (SPLDI-MS) have indicated the presence of amines at many different sites. Murphy and Thomson (Murphy et al. 1997) were the first

to report that single particle mass spectra acquired at Idaho Hill showed evidence of fragment ions of amines. Since then many other groups utilizing laser mass spectrometry have reported similar findings. Angelino *et al.* (2001) reported signals of amine components in up to 80% of particles in Riverside, California. The amines exhibited a strong diurnal pattern correlating with wind direction, interpreted as indicating fresh emissions. Outdoor smog chamber experiments performed during the study confirmed that alkyl amines can react with ambient concentrations of gases to form condensed-phased products. Other studies by Tan *et al.* (2002) at an urban site in Toronto, Ontario, Glagolenko and Phares (2004) in College Station, Texas, and Beddows *et al.* (2004) at a rural site in Scotland have observed amine fragmentation patterns in single particle mass spectra. None of these SPLDI-MS studies have addressed the issue of quantifying the signals to determine mass concentrations of the amines. However SPLDI-MS methods are known to suffer from significant matrix-effects that make quantitative analysis difficult (Morrical *et al.* 1998, Gross *et al.* 2000).

Quantitative studies of particulate amines are rare. Zhang and Anastasio (2003) discussed the concentrations of free and combined amino compounds in particles and fogwater at Davis, California. Fine particles were enriched in protein-related amino compounds while fogwater contained more non-protein related compounds (e.g. methylamine). Zhang and Anastasio (2003) also showed that organic nitrogen compounds react with ozone in fogwater to form inorganic ions. Makela *et al.* (2001) reported that amines may play a role in particle nucleation events. The presence of

dimethylammonium in particles (the protonated cation of dimethylamine) was the major difference between particle nucleation events and non-events in a forest in Finland.

Despite the mounting anecdotal evidence that amines are present in the particulate phase, no attempt at systematic identification and quantification of amine contributions to ambient particulate matter has been described. Here we present evidence from ambient studies in Utah that amines can be a significant component of ambient particles. Data from smog chamber experiments suggests that the reaction of trimethylamine with nitrate radical is a process for producing secondary organic aerosol.

### **Ambient Data from Utah**

Over the last several years, an Aerodyne quadrupole aerosol mass spectrometer (Q-AMS) has sampled fine particles in Logan, Utah (Silva et al. 2007). As previously reported, Logan experiences wintertime inversions with average surface temperatures of -10 °C leading to acute PM<sub>2.5</sub> episodes (Malek et al. 2006). For example, during January and February 2004, PM<sub>2.5</sub> concentrations in Logan reached values of 130-140 µg/m<sup>3</sup>. The major constituent of fine particles in Logan as measured by both off-line methods and the Q-AMS is ammonium nitrate, making up 50-80% of the particle mass loading. Another 15-25% of the mass is normally made up of organic matter (OM).

The Q-AMS can differentiate between different types of OM as described by Zhang *et al.* (2005). The Q-AMS detects hydrocarbon-like organic aerosols (HOA) and oxygenated organic aerosols (OOA) similar to other locations where Q-AMS instruments have sampled. However the Q-AMS in Logan often detects organic aerosol that does not fit the fragmentation patterns of either HOA or OOA. The mass spectrum at these times is

dominated by even-number mass fragments correlating with the pattern  $(C_nH_{2n+2}N)^+$ . This is the set of peaks often observed by the SPLDI-MS techniques and includes  $m/z$  58, 86, and 100 which strongly indicate presence of amines (McLafferty 1993). The presence of even number peaks is evidence of an odd number of nitrogen's. This signature was observed during the strong winter inversions of 2004, but as one contributor to the overall particle mass spectral signal. During 2005, this signature was the dominant organic aerosol observed in the mass spectra acquired from two locations in the valley. The "amine" contribution was larger in raw ion counts (Hz) than either the HOA or OOA fractions.

However, the 2005 data indicate that amine-related ions can show different temporal profiles. Figure B.1 shows profiles obtained from four different ion peaks representing the amine series:  $m/z$  58, 86, 100, and 114. The profiles indicate two distinct sources and/or chemical processes. Mass-to-charge peaks 58 and 114 are highly correlated ( $r^2=0.783$ ) and show a series of gradual, but continuous buildups in ion counts during mild inversion conditions. Mass-to-charge ions 86 and 100 also are well correlated ( $r^2=0.836$ ), however with time trends showing short, transient spikes in ion counts. The two sets of peaks are poorly correlated with each other ( $m/z$  58:100 gives  $r^2=0.093$ ;  $m/z$  86:114 gives  $r^2=0.008$ ). Figure B.2 shows hourly mean, median, and range of data for the combined amine mass concentration for 16-28 February. A diurnal profile is observed with mass loadings reaching peak concentrations during the middle of the night while decreasing during the day. The diurnal profile is largely due to amine peaks associated with  $m/z$  58 from Figure B.1. This behavior is also observed for other components in the



data set (sulfate in particular). This behavior could signify diurnal boundary layer changes, temperature effects shifting gas-particle partitioning, chemical processes involving nocturnal reactions, or some combination. Measurements by the State of Utah using a filter dynamics measurement system (FDMS, Thermo R&P) showed overnight increases of PM<sub>2.5</sub> of 5-20  $\mu\text{g}/\text{m}^3$  during nighttime periods. According to Q-AMS concentration measurements, amines may make up  $\sim 20\%$  of this total, not accounting for the different size fraction ( $\sim\text{PM}_1$ ) detected by the AMS.

## **Experimental**

Laboratory experiments were conducted in an effort to identify possible aerosol phase products. All experiments were conducted at the UCR/CE-CERT Environmental Chamber, which has been described in detail elsewhere (Carter et al. 2005). In short, this facility consists of two 90m<sup>3</sup> Teflon reactors attached to a rigid collapsible frame, which are maintained at a slight positive pressure to minimize diffusion of any contaminate into the reactors. The reactors are located in a temperature controlled room, which is continually flushed with pure air. Connected to the reactors are a suite of instrumentation including an Aerodyne high resolution time of flight mass spectrometer (HR-ToF-AMS), and two scanning mobility particle spectrometers (SMPS), built in house, capable of sizing particles from 28–730 nm (Wang and Flagan 1990). Particle number and volume were wall loss corrected using the method of Bowman *et al.* (1997), additionally, particle mass loadings were calculated assuming a unit density. Ports into the chamber enable introduction of compounds of interest as well as monitoring of NO<sub>x</sub> using a Thermal Environmental Instruments model 42C chemiluminescent analyzer and O<sub>3</sub> by a Dasibi

Environmental Corp 1003-AH. Initial concentrations of NO<sub>x</sub> and O<sub>3</sub> were below the detection limits of our analyzers (50 ppt and 2 ppb, respectively) for each experiment performed. Trimethylamine amine (25 wt. % in water Sigma-Aldrich) was introduced into a dark chamber by injecting a known volume of liquid amine into a small glass injection manifold, pure nitrogen was then passed over the liquid flushing the amine into the reactors. NO<sub>x</sub> was introduced into the chambers by filling a calibrated bulb to the desired partial pressure then flushed into the chamber by pure nitrogen. 350–450 ppb of ozone was introduced by passing 35 psi of pure air through two UV ozone generators NO<sub>x</sub> was added to the reactors as NO using a calibrated bulb. Nitric acid (HNO<sub>3</sub>) was added to the reactors by passing pure nitrogen gas over a known volume of liquid HNO<sub>3</sub>, while dinitrogen pentoxide (N<sub>2</sub>O<sub>5</sub>) was added to the chamber in the same manner as NO. Table B.1 lists the experimental conditions of all experiments conducted. Total aerosol yields (Y) were determined using the aerosol yield equation as defined by Odum *et al.* (1996) with slight modification.

$$Y = \frac{\Delta M}{\Delta HC} \quad (1)$$

where  $\Delta M$  ( $\mu\text{g}/\text{m}^3$ ) is the total aerosol mass concentration produced (organic and inorganic) for a given amount of reactive organic gas reacted ( $\Delta\text{ROG}$ ,  $\mu\text{g}/\text{m}^3$ ). Because of uncertainties in the TMA measurement technique, all yields were calculated based on estimated injection concentrations and total consumption of the hydrocarbon.

Sampling of aerosol for off-line analysis was performed by drawing air for 3 hr. at 25 LPM from the reactors through a stainless steel sampling port located just below the chamber onto pre-baked quartz fiber filters (Pall Life Sciences Laboratory). Filters were

then extracted by sonication for 30 min. with 5 ml. of HPLC grade water (Fisher Scientific Optima Grade). During the sonication period, the extracts were kept cold to minimize liquid phase reactions and losses due to volatilization. Extracts were then filtered through

### **Results from Laboratory Experiments**

Wall-loss corrected temporal profiles obtained using the SMPS for several of these systems are displayed in Figure B.3. Gray trendlines show the reaction of TMA with O<sub>3</sub> followed by NO<sub>x</sub> (circles) and NO<sub>x</sub> followed by O<sub>3</sub> (diamonds). For the first reaction, interaction of TMA (~100 ppb) and ozone (measured at 427 ppb) resulted in some particle formation. Particle mass loading leveled off at ~11 µg/m<sup>3</sup> in the SMPS data after 1 hour. Nitric oxide was injected later at a concentration of ~35 ppb. A larger rise in particle concentration was detected reaching 85 µg/m<sup>3</sup>. In contrast, the reaction of TMA (~100 ppb) and nitric oxide (46.7 ppb) showed no particle formation observed on either the SMPS or Q-AMS. Approximately 30 minutes later, ozone was injected into the chamber at a measured mixing ratio of 333 ppb. Rapid particle formation was observed on both the SMPS and Q-AMS instruments. The SMPS measured a peak volume concentration of 179.6 µg/m<sup>3</sup>.

Figure B.4a shows the mass spectrum obtained using the Q-AMS from the reaction of trimethylamine and the O<sub>3</sub>/NO<sub>x</sub> system. The highest intensity peaks observed are *m/z* 30 (NO<sup>+</sup>/CH<sub>4</sub>N<sup>+</sup>), 44 (CO<sub>2</sub><sup>+</sup>), and 58 (C<sub>3</sub>H<sub>8</sub>N<sup>+</sup>), consistent with the major peaks expected from trimethylamine and nitrate ion. The spectrum also shows that reaction products produce fragment ions at masses much larger than the parent ion for TMA.

(molecular weight 59) The largest ion observed is  $m/z$  207, but others include  $m/z$  97, 104, 141, 146, 159, 161, 175, and 191. This indicates the formation of molecular species significantly larger than the parent TMA. The Q-AMS spectrum appears consistent with the data reported by Murphy *et al.* (2007) in their experiments.

To assess the impact of acid-base reaction contributions, we ran a chamber reaction with a direct interaction between TMA and nitric acid. Figure B.3 shows the SMPS time trend of the experiment (dark gray triangles). At the beginning of the experiment, 100 ppb of TMA was injected into the chamber. Approximately 20 minutes later, NO was added to the chamber to remove ozone. Measured concentration of NO was 54 ppb. No particle formation was observed. Approximately 5 minutes later, nitric acid was injected directly to the chamber at an estimated mixing ratio of 93 ppb. Particle formation was observed, leveling off at  $\sim 50 \mu\text{g}/\text{m}^3$  after 150 minutes.

The average mass spectrum from the particles formed during this reaction is shown in Figure B.4b. The spectrum is very simple, showing only fragments from nitrate ( $m/z$  30, 46) and trimethylamine ( $m/z$  30, 42, 58, and 59). This is not surprising since the simple acid-base reaction should result in an amine-nitrate salt. This implies that the higher mass peaks shown in Figure B.4a are from chemical interactions other than simple acid-base production of organic aerosol. After concentrations leveled off, ozone was added to the chamber at a measured concentration of 357 ppb. Particulate mass concentration increased more, leveling off at  $\sim 140 \mu\text{g}/\text{m}^3$ . After interaction with ozone, the mass spectrum from the reaction resembled the spectrum displayed in Figure B.4a again, the TMA/O<sub>3</sub>/NO<sub>x</sub> reaction system.

Because the TMA/HNO<sub>3</sub> reaction product cannot account for the higher mass spectral peaks observed in the TMA/O<sub>3</sub>/NO<sub>x</sub> reaction system and the observed kinetics was slower, we hypothesized that the interaction of O<sub>3</sub> and NO<sub>2</sub> in the previous experiment could form nitrate radical which could be a potential player in the reaction system. The interaction of TMA and NO<sub>3</sub> was directly studied. Figure B.3 shows the SMPS time trend (black squares). TMA was injected into the chamber at 100 ppb. Approximately 1 hour later 100 ppb of dinitrogen pentoxide was injected through a heated line into the chamber. Through the heated inlet, N<sub>2</sub>O<sub>5</sub> should have converted immediately to NO<sub>2</sub> and NO<sub>3</sub>. Particle formation was nearly instantaneous. Over 100 μg/m<sup>3</sup> were detected using the SMPS 7 minutes later. The concentration leveled off at ~160 μg/m<sup>3</sup>. The Q-AMS spectrum of the particles is shown in Figure B.4c. The reaction of TMA and NO<sub>3</sub> produces a mass spectrum very similar to Figure B.4a, indicating that nitrate radical may be significant for starting the formation of particulate matter from amine precursors. Nitrate radical as the major reactant is consistent with the observation in Logan that amine-related Q-AMS peaks are dominant during nocturnal hours, however confirmation that the smog-chamber products are the same as ambient ones cannot be made because the signal at the high-mass peaks observed here are below detection limits in ambient samples where amine concentrations are much lower.

Interpretation of the mass spectra obtained in Figures B.4a and B.4c could plausibly be consistent with either a typical oxidation involving RO<sub>2</sub> radicals or the addition of NO<sub>2</sub> and/or NO<sub>3</sub> groups onto an amine backbone. To further elucidate the fragment ions detected, we performed several isotope-labeled experiments with

deuterated trimethylamine (TMA-d9) and  $^{15}\text{N}$ -labeled nitric oxide ( $^{15}\text{NO}$ ). Figure B.5a and 5b show product mass spectra obtained from the reaction of TMA-d9 (98 atom % D) with  $\text{O}_3/\text{NO}_x$  and TMA with  $\text{O}_3/^{15}\text{NO}_x$  (98.5 atom %  $^{15}\text{N}$ ) respectively. In Figure B.5a, a clear difference of major ion peaks is shown from the normal TMA. For example  $m/z$  58 is the major fragment ion for TMA through loss of one proton ( $\text{C}_3\text{H}_8\text{N}^+$ ), and the analogous ion  $m/z$  66 ( $\text{C}_3\text{D}_8\text{N}^+$ ) is observed for the TMA-d9 spectrum. Similarly, a number of other ion shifts are observed in the spectrum. Major ion peaks at  $m/z$  74, 88, 104, and 191 appear to shift to  $m/z$  78, 94, 110, and 202 respectively. In contrast, Figure B.5b obtained from the reaction of TMA/ $\text{O}_3/^{15}\text{NO}_x$  shows the same high-mass ion peaks as observed for the reaction with TMA/ $\text{O}_3/\text{NO}_x$ . This indicates that addition of  $\text{NO}_2$  or  $\text{NO}_3$  groups is not a major contributor to the high mass peaks, though it cannot rule out contribution to other ions present in the spectrum.

Definitive identification of all the ion peaks in the spectrum was not possible using the Q-AMS. However, the HR-ToF-AMS has higher resolving power to identify most peaks present in the spectra. Figure B.6 shows high resolution spectra of peaks detected in the TMA/ $\text{O}_3/\text{NO}_x$  reaction at  $m/z$  30, 46, 104, and 191 using the HR-ToF-AMS. Of note is the observation that  $m/z$  30 is not due to the  $\text{NO}^+$  ion which would have an exact mass of 29.998 Da. This ion is not observed while two peaks at 30.009 and 30.036 are. These ions are due to ( $\text{CH}_2\text{O}^+$ ) and ( $\text{CH}_4\text{N}^+$ ) respectively. This observation further indicates that the formation of amine-nitrate acid-base salts is not a major particle-formation mechanism under the conditions here because nitrate salts yield both  $\text{NO}^+$  and  $\text{NO}_2^+$  as major fragments. The peak at nominal  $m/z$  46 does show significant signal due to

$\text{NO}_2^+$ (45.993), in addition to signal at 46.030( $\text{CH}_4\text{NO}^+$ ). This indicates that fragmentation may include the presence of nitro-groups on an organic backbone. Definitive identification of higher mass ions detected in the spectrum include  $m/z$  74 ( $\text{C}_2\text{H}_4\text{NO}_2^+$ ), 88 ( $\text{C}_3\text{H}_6\text{NO}_2^+$ ), 104 ( $\text{C}_3\text{H}_6\text{NO}_3^+$ ), and 191( $\text{C}_6\text{H}_{11}\text{N}_2\text{O}_5^+$ ). A complete list of the high mass ions and proposed identification based on high resolution spectra is included in Table B.2.

To obtain added information on the chemical composition of particles formed in the TMA/ $\text{O}_3$ / $\text{NO}_x$  reaction, particles were collected on a Teflon filter for off-line chemical analysis. Particles were extracted in water and analyzed using high-resolution atmospheric pressure chemical ionization (APCI) mass spectrometry. Ions were observed up to  $\sim 800$   $m/z$ , a very high molecular weight considering the starting compound (TMA) has a molar mass of only 59 Da. A repeating series of ions separated by 103 amu was observed. This sequence is identified by mass defect and indicates the loss of  $\text{C}_3\text{H}_5\text{NO}_3$ . This repeating unit contains one proton less than the ion observed in the AMS spectra at  $m/z$  104, and perhaps indicates formation of an oligimer or macromolecule during the smog chamber reaction. This unit is composed of TMA with three oxygens attached, and again indicates secondary oxidation chemistry providing the major mechanism for the aerosol formation process. These ions cannot be observed in the Q-AMS because the mass range is only up to 300 amu, and probably would not be observed even on the HR-ToF-AMS because of the much harder ionization source (EI). ESI mass spectrum is included in Figure B.7. Observed rates indicate that the reaction between TMA and  $\text{NO}_3$  displayed fast kinetics. Although we could not monitor the rate from the precursor gases,

a lower boundary for the gas-reaction kinetics can be estimated by assuming that all the  $\text{N}_2\text{O}_5$  was converted to  $\text{NO}_3$  and that all of the  $\text{NO}_3$  was consumed. Using second order reaction kinetics and using the time between initial injection of  $\text{NO}_3$  and peak concentration of particulates, the estimated lower boundary of the rate constant was  $4.4 \times 10^{-16} \text{ cm}^3/\text{molec}/\text{s}$ . If the amount of  $\text{NO}_3$  consumed was less than 100%, then the rate constant is even higher. The overall aerosol yield determined by equation 1 was 65% for the TMA/ $\text{N}_2\text{O}_5$  reaction and 37% for the TMA/ $\text{O}_3/\text{NO}_x$  system, assuming unit density.

The data here suggest that secondary organic aerosol production from amines may be important in areas where nitrate radical mixing ratios are high enough to contribute to oxidative chemistry. While amines also react with ozone, it is the combination of ozone and nitrogen oxides that creates greater amounts of secondary organic aerosol. Salts can be formed from the combination of amines and nitric acid, however the reaction appears relatively slow and does not account for high mass fragments observed in the mass spectra. Nitrate radical reacts rapidly with trimethylamine.

These experiments imply that further research is needed into the reaction chemistry of amines with oxidants, especially nitrate radical for which no kinetics measurements have been reported in the literature. In the Cache Valley, Utah, the mixing ratios and sources of gas-phase amines are not known. However, given the high ammonia concentrations encountered, it is anticipated that livestock facilities are likely significant sources of amines. While not definitive, smog chamber experiments indicate that secondary oxidation chemistry may dominate over acid-base chemistry as a source of particles from amine precursors. This indicates that the response factor for amines in



ambient data sets from Utah maybe closer to that of neutral amines such as trimethylamine-n-oxide rather than the amine-salts. However, another analytical technique such as a chromatographic method will probably be needed to confirm the implication to amine mass concentration in ambient data.

## References

- Angelino, S., Suess, D. T. and Prather, K. A. (2001). Formation of aerosol particles from reactions of secondary and tertiary alkylamines: Characterization by aerosol time-of-flight mass spectrometry. *Environ. Sci. Technol.* 35(15):3130-3138.
- Appel, B. R., Tokiwa, Y., Hsu, J., Kothny, E. L. and Hahn, E. (1985). Visibility as Related to Atmospheric Aerosol Constituents. *Atmos. Environ.* 19(9):1525-1534.
- Atkinson, R., Baulch, D. L., Cox, R. A., Hampson, R. F., Kerr, J. A. and Troe, J. (1989). Evaluated Kinetic and Photochemical Data for Atmospheric Chemistry .3. Iupac Subcommittee on Gas Kinetic Data Evaluation for Atmospheric Chemistry. *J. Phys. Chem. Ref. Data* 18(2):881-1097.
- Bailey, D., Cativiela, J. P., Descary, B., Grantz, D., Hamilton, K. D., Martin, P. E., Meyer, D., Mullinax, D., Simunovic, C. A., Sweet, J., Warner, D., and Watson, J. (2005). Dairy Emissions Factors for Volatile Organic Compounds, *San Joaquin Valley Air Pollution Control District, Fresno, CA,*.
- Beddows, D. C. S., Donovan, R. J., Harrison, R. M., Heal, M. R., Kinnersley, R. P., King, M. D., Nicholson, D. H. and Thompson, K. C. (2004). Correlations in the chemical composition of rural background atmospheric aerosol in the UK determined in real time using time-of-flight mass spectrometry. *J. Environ. Monitor.* 6(2):124-133.
- Bowman, F. M., Odum, J. R., Seinfeld, J. H. and Pandis, S. N. (1997). Mathematical model for gas-particle partitioning of secondary organic aerosols. *Atmos. Environ.* 31(23):3921-3931.
- Carter, W. P. L., Cocker, D. R., Fitz, D. R., Malkina, I. L., Bumiller, K., Sauer, C. G., Pisano, J. T., Bufalino, C. and Song, C. (2005). A new environmental chamber for evaluation of gas-phase chemical mechanisms and secondary aerosol formation. *Atmos. Environ.* 39(40):7768-7788.
- Dod, R. L., Gundel, L. A., Benner, W. H. and Novakov, T. (1984). Non-Ammonium Reduced Nitrogen Species in Atmospheric Aerosol-Particles. *Science of the Total Environment* 36(JUN):277-282.
- Glagolenko, S. and Phares, D. J. (2004). Single-particle analysis of ultrafine aerosol in College Station, Texas. *J. Geophys. Res. [Atms.]* 109(D18205)
- Gorzelska, K. and Galloway, J. N. (1990). Amine Nitrogen in the Atmospheric Environment over the North Atlantic Ocean. *Global Biogeochem. Cycles* 4(3):309-334.

- Gorzelska, K., Galloway, J. N., Watterson, K. and Keene, W. C. (1992). Water-Soluble Primary Amine Compounds in Rural Continental Precipitation. *Atmos. Environ.* 26(6):1005-1018.
- Gross, D. S., Galli, M. E., Silva, P. J. and Prather, K. A. (2000). Relative sensitivity factors for alkali metal and ammonium cations in single particle aerosol time-of-flight mass spectra. *Anal. Chem.* 72(2):416-422.
- Luebs, R. E., Laag, A. E. and Davis, K. R. (1973). Ammonia and Related Gases Emanating from a Large Dairy Area. *California Agriculture* 27(2):10-12.
- Makela, J. M., Yli-Koivisto, S., Hiltunen, V., Seidl, W., Swietlicki, E., Teinila, K., Sillanpaa, M., Koponen, I. K., Paatero, J., Rosman, K. and Hameri, K. (2001). Chemical composition of aerosol during particle formation events in boreal forest. *Tellus B* 53(4)
- Malek, E., Davis, T., Martin, R. S. and Silva, P. J. (2006). Meteorological and environmental aspects of one of the worst national air pollution episodes (January, 2004) in Logan, Cache Valley, Utah, USA. *Atmos. Res.* 79(2):108-122.
- McLafferty, F. W.; Turecek, F. (1993) *Interpretation of Mass Spectra*, 4th ed.; University Science Books, Sausalito, California.
- Milne, P. J. and Zika, R. G. (1993). Amino-Acid Nitrogen in Atmospheric Aerosols - Occurrence, Sources and Photochemical Modification. *J. Atmos. Chem.* 16(4):361-398.
- Morrison, B. D., Ferguson, D. P. and Prather, K. A. (1998). Coupling two-step laser desorption/ionization with aerosol time-of-flight mass spectrometry for the analysis of individual organic particles. *J. Am. Soc. Mass Spectrom.* 9(10):1068-1073.
- Mosier, A. R., Andre, C. E. and Viets, F. G. (1973). Identification of Aliphatic-Amines Volatilized from Cattle Feedyard. *Environ. Sci. Technol.* 7(7):642-644.
- Murphy, D. M. and Thomson, D. S. (1997). Chemical composition of single aerosol particles at Idaho Hill: Positive ion measurements. *J. Geophys. Res. [Atms.]* 102(D5):6341-6352.
- Murphy, S. M., Sorooshian, A., Kroll, J. H., Ng, N. L., Chhabra, P., Tong, C., Surratt, J. D., Knipping, E., Flagan, R. C. and Seinfeld, J. H. (2007). Secondary aerosol formation from atmospheric reactions of aliphatic amines. *Atmos. Chem. Phys.* 7(9):2313-2337.

- Novakov, T., Otvos, J. W., Mueller, P. K. and Alcocer, A. E. (1972). Chemical Composition of Pasadena Aerosol by Particle-Size and Time of Day .3. Chemical States of Nitrogen and Sulfur by Photoelectron Spectroscopy. *J. Colloid Interf. Sci.* 39(1):225-234.
- Odum, J. R., Hoffmann, T., Bowman, F., Collins, D., Flagan, R. C. and Seinfeld, J. H. (1996). Gas/particle partitioning and secondary organic aerosol yields. *Environ. Sci. Technol.* 30(8):2580-2585.
- Pitts, J. N., Grosjean, D., Vancauwenberghe, K., Schmid, J. P. and Fitz, D. R. (1978). Photo-Oxidation of Aliphatic-Amines under Simulated Atmospheric Conditions - Formation of Nitrosamines, Nitramines, Amides, and Photo-Chemical Oxidant. *Environ. Sci. Technol.* 12(8):946-953.
- Rabaud, N. E., Ebeler, S. E., Ashbaugh, L. L. and Flocchini, R. G. (2003). Characterization and quantification of odorous and non-odorous volatile organic compounds near a commercial dairy in California. *Atmos. Environ.* 37(7):933-940.
- Schade, G. W. and Crutzen, P. J. (1995). Emission of Aliphatic-Amines from Animal Husbandry and Their Reactions - Potential Source of N<sub>2</sub>O and HCN. *J. Atmos. Chem.* 22(3):319-346.
- Silva, P. J., Vawdrey, E. L., Corbett, M. and Erupe, M. (2007). Fine particle concentrations and composition during wintertime inversions in Logan, Utah, USA. *Atmos. Environ.* 41(26):5410-5422.
- Tan, P. V., Evans, G. J., Tsai, J., Owega, S., Fila, M. S. and Malpica, O. (2002). On-line analysis of urban particulate matter focusing on elevated wintertime aerosol concentrations. *Environ. Sci. Technol.* 36(16):3512-3518.
- Tuazon, E. C. (1994). Kinetics and Products of the Gas-Phase Reactions of O<sub>3</sub> with Amines and Related Compounds. *Res. Chem. Inter.* 20(3-5):303-320.
- Tuazon, E. C., Carter, W. P. L., Atkinson, R., Winer, A. M. and Pitts, J. N. (1984). Atmospheric Reactions of N-Nitrosodimethylamine and Dimethylnitramine. *Environ. Sci. Technol.* 18(1):49-54.
- Tuazon, E. C., Winer, A. M., Graham, R. A., Schmid, J. P. and Pitts, J. N. (1978). Fourier-Transform Infrared Detection of Nitramines in Irradiated Amine-Nox Systems. *Environ. Sci. Technol.* 12(8):954-958.
- Wang, S. C. and Flagan, R. C. (1990). Scanning Electrical Mobility Spectrometer. *Aerosol Sci. Tech.* 13(2):230-240.

- Zhang, Q. and Anastasio, C. (2003). Conversion of fogwater and aerosol organic nitrogen to ammonium, nitrate, and NO<sub>x</sub> during exposure to simulated sunlight and ozone. *Environ. Sci. Technol.* 37(16):3522-3530.
- Zhang, Q. and Anastasio, C. (2003). Free and combined amino compounds in atmospheric fine particles (PM<sub>2.5</sub>) and fog waters from Northern California. *Atmos. Environ.* 37(16):2247-2258.
- Zhang, Q., Worsnop, D. R., Canagaratna, M. R. and Jimenez, J. L. (2005). Hydrocarbon-like and oxygenated organic aerosols in Pittsburgh: insights into sources and processes of organic aerosols. *Atmos. Chem. Phys.* 5:3289-3311.

**Table B.1** List of experimental conditions for reactions

Experiment number	Trimethylamine (ppb)	O <sub>3</sub> (ppb)	NO <sub>x</sub> (ppb)	HNO <sub>3</sub> (ppb)	N <sub>2</sub> O <sub>5</sub> (ppb)
1	100	330	35	-	-
2	100	330	47	-	-
3	100	360	54	95	-
4	100	-	-	-	100
5 <sup>a</sup>	100	380	48	-	-
6 <sup>b</sup>	100	370	45	-	-

a-TMA-d9 injected, b-<sup>15</sup>N injected

**Table B.2** List of major ion peaks observed for the reaction of trimethylamine in the smog chamber and their potential assignments

<b>Peak</b>	<b>Formula</b>
30.036 / 30.062	$\text{CH}_4\text{N}^+ / \text{CH}_2\text{O}^+$
43.982 (small) / 44.052	$\text{CO}_2^+ / \text{C}_2\text{H}_6\text{N}^+$
45.993	$\text{NO}_2^+$
58.066	$\text{C}_3\text{H}_8\text{N}^+$
73.02	$\text{C}_2\text{H}_2\text{NO}_2^+$
74.02	$\text{C}_2\text{H}_4\text{NO}_2^+$
88.04	$\text{C}_3\text{H}_6\text{NO}_2^+$
104.04	$\text{C}_3\text{H}_6\text{NO}_3^+$
191.07	$\text{C}_6\text{H}_{11}\text{N}_2\text{O}_5^+$
207.06	$\text{C}_6\text{H}_{11}\text{N}_2\text{O}_6^+$

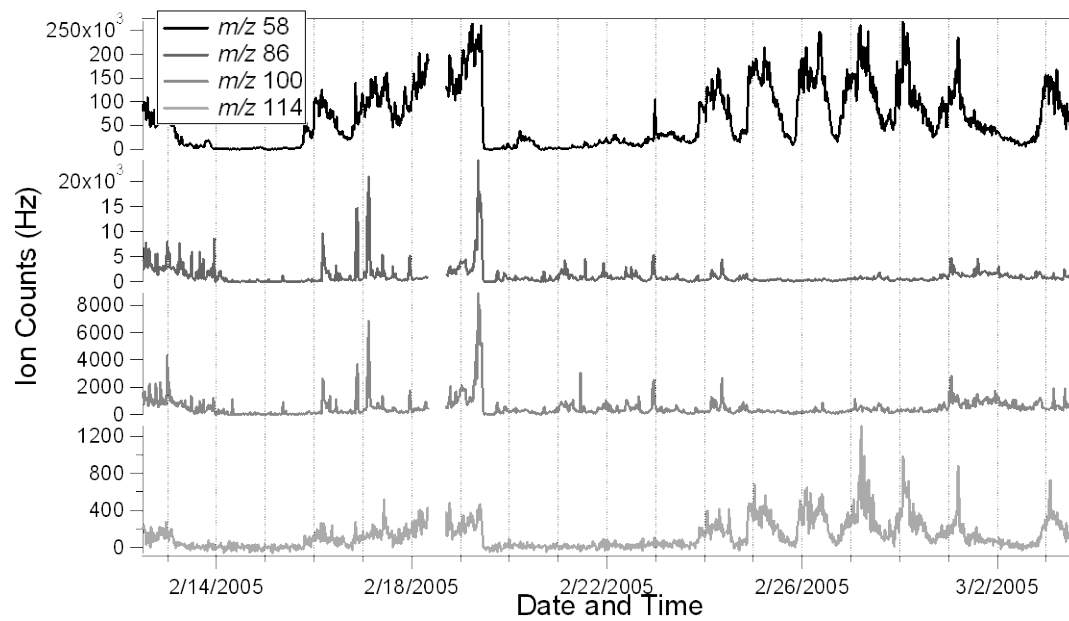


**Figure B.1** Temporal profiles of individual mass-to-charge ions associated with amines measured in downtown Logan during February, 2005.



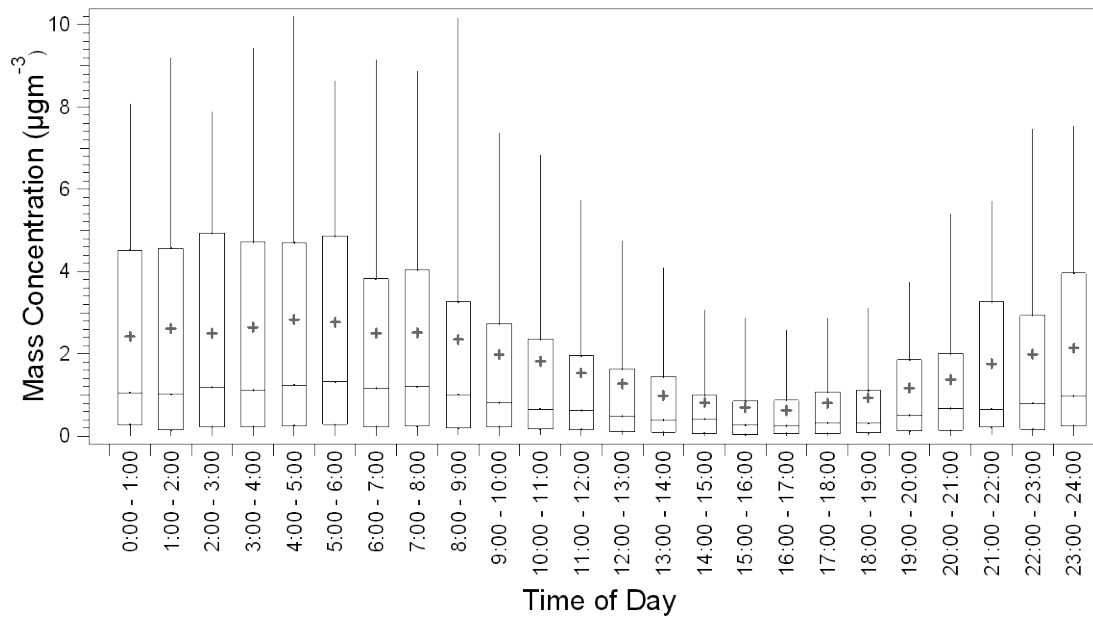


**Figure B.2** Diurnal profile of amine-related peaks measured in downtown Logan during February, 2005. Crosses represent median values; bars represent 0-100 percentile value

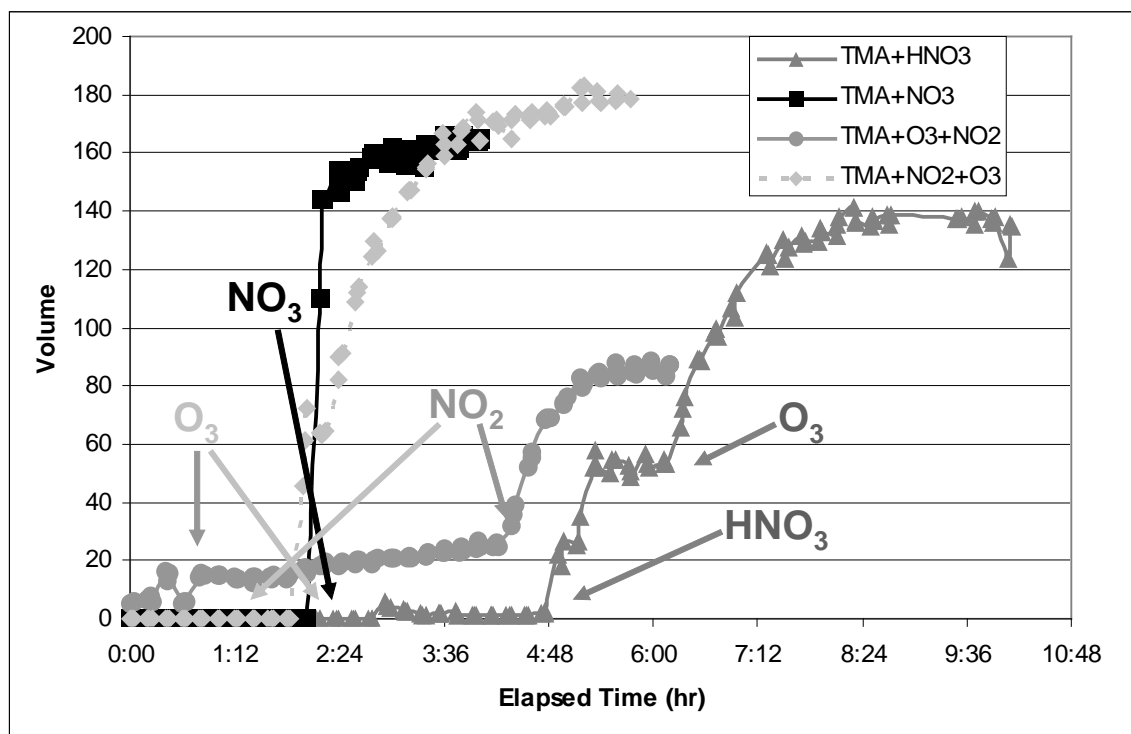
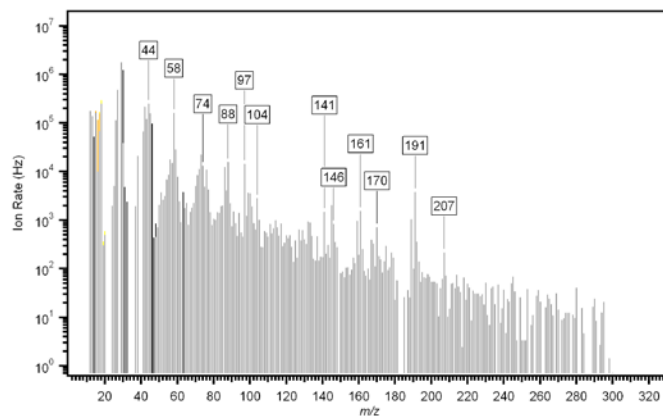
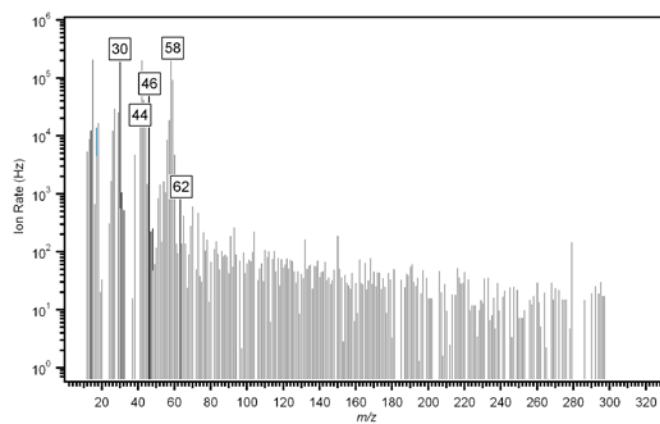


**Figure B.3** Time profiles of SMPS volume concentrations for four smog chamber experiments involving TMA reactions with NO<sub>x</sub>, O<sub>3</sub>, HNO<sub>3</sub>, and N<sub>2</sub>O<sub>5</sub>. Volume concentrations are wall-loss corrected.

A)



B)



C)

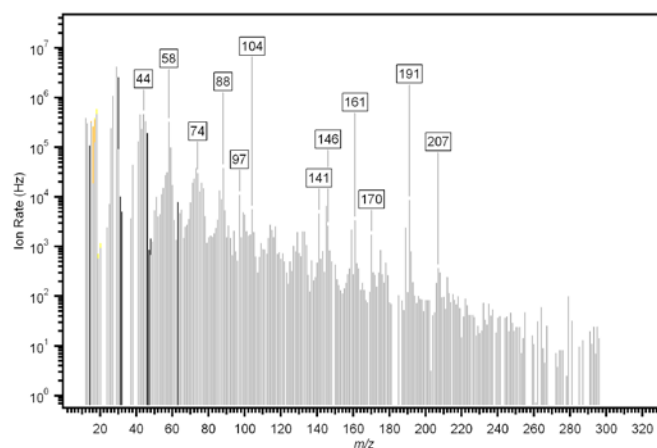


**Figure B.4** Mass spectra of particles formed from trimethylamine smog chamber reactions. A) TMA+O<sub>3</sub>+NO<sub>x</sub>. B) TMA + HNO<sub>3</sub> C) TMA+NO<sub>3</sub>.

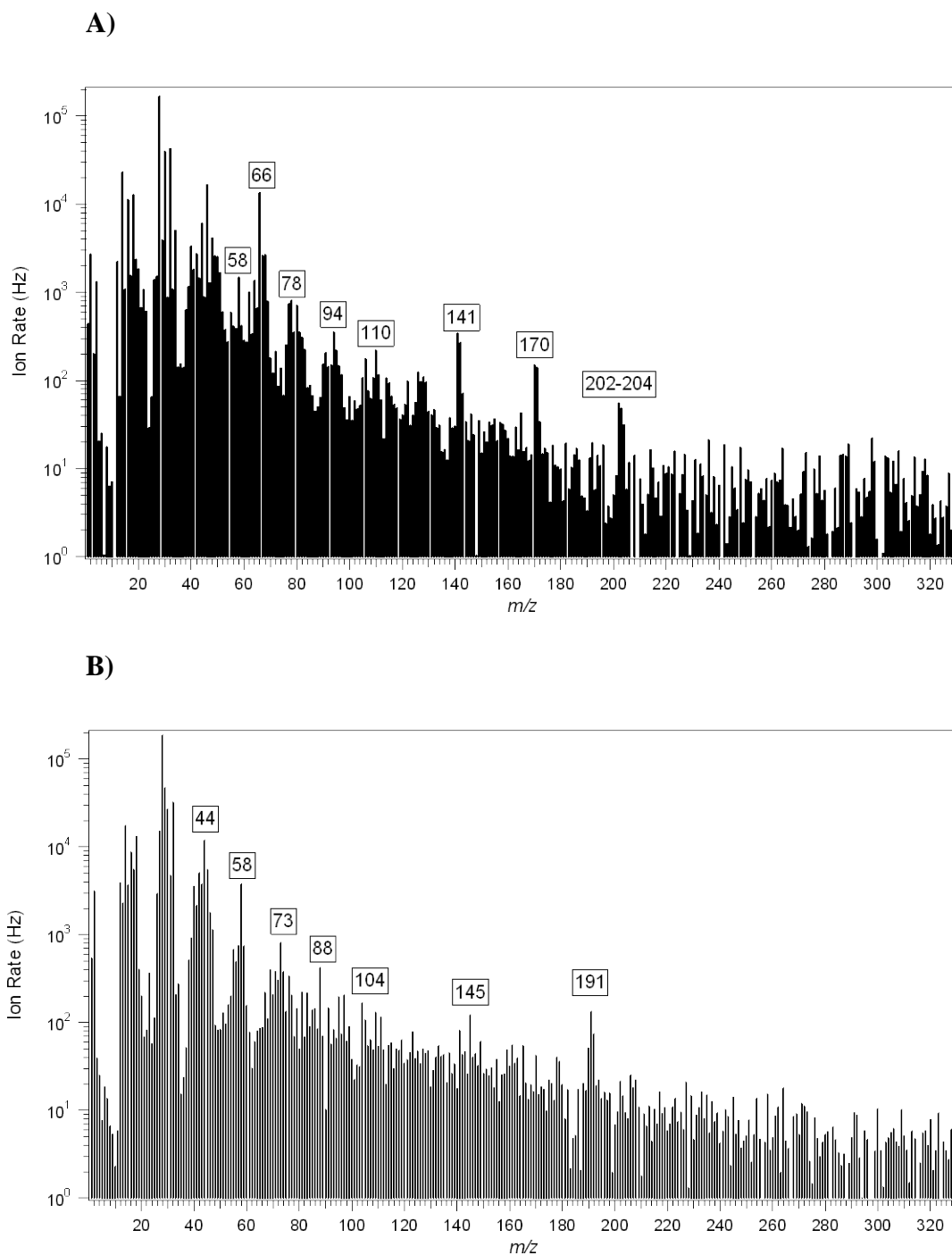


**Figure B.5** Mass spectra of particles formed during isotope-labeled experiments. A) Mass spectrum from deuterated trimethylamine (TMA-d9) and  $O_3/NO_x$ . B) Mass spectrum from trimethylamine and  $O_3/^{15}NO_x$ .

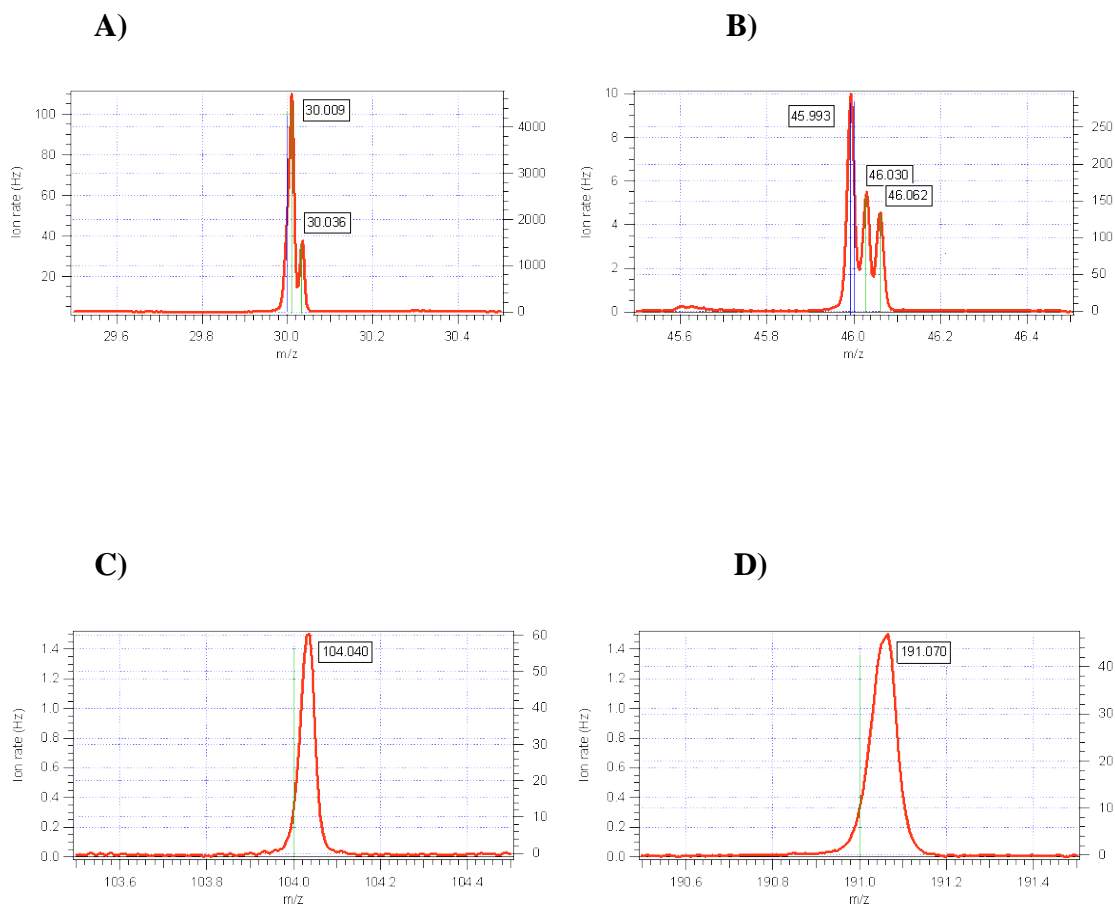


**Figure B.6** High resolution mass spectral peaks from HR-ToF-AMS. A)  $m/z$  30. B)  $m/z$  46. C)  $m/z$  104. D)  $m/z$  191.

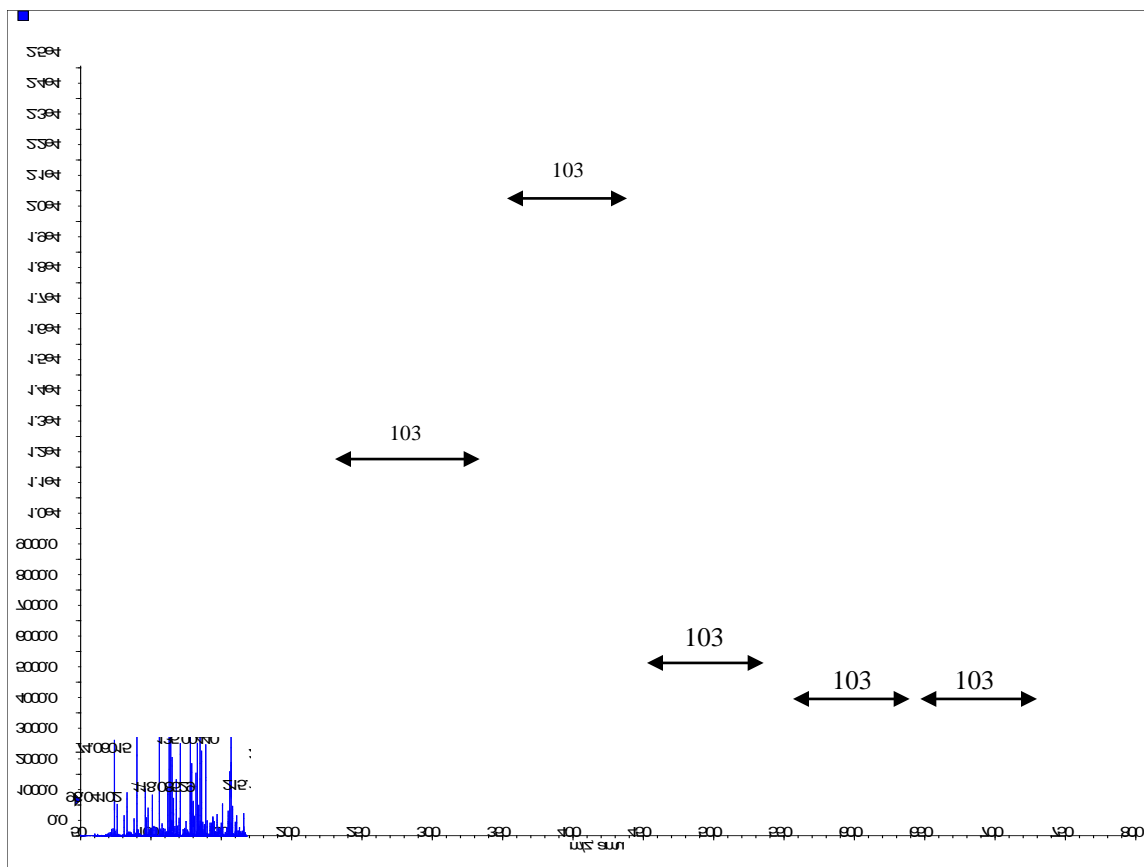


**Figure B.7** High resolution APCI mass spectrum of water-soluble particulate matter from reaction of trimethylamine and ozone/NO<sub>x</sub> photochemical system.

## Appendix C

### **Real-Time Aerosol Density Determination Utilizing a Modified Scanning Mobility Particle Sizer – Aerosol Particle Mass Analyzer System**

Reference: Malloy, Q.G.J., Nakao, S., Qi, L., Austin, R., Stothers, C., Hagino, H., and Cocker, D.R.III, 2009. *Aerosol Science and Technology* 43, 673-678.

## Introduction

In environmental chamber experiments, aerosol density is required to convert size distribution data into mass concentrations. Early environmental chambers, in the absence of density measurements, estimated mass loadings assuming an aerosol density equal to 1 g/cm<sup>3</sup>. Many SOA studies have characterized SOA (Jaoui et al. 2004; Surratt et al. 2006; Yu et al. 1999). However, the data concerning the density associated with these aerosol are limited and vary widely. Recent studies have estimated secondary organic aerosol (SOA) densities ranging from 0.9 g/cm<sup>3</sup> to 1.6 g/cm<sup>3</sup> for a variety of SOA forming systems (Bahreini et al. 2005; Jaoui et al. 2004; Kalberer et al. 2000; Kostenidou et al. 2007; Surratt et al. 2006; Yu et al. 1999; Zelenyuk et al. 2008). Of particular interest is the wide variability in reported data from similar experimental conditions. For example, Bahreini et al (2005) have reported the density from a  $\beta$ -pinene ozonolysis in unseeded experiments of 1.20 g/cm<sup>3</sup>. However, Kostenidou et al. (2007) reported the average aerosol density from this same system under similar experimental conditions as 1.41-1.50 g/cm<sup>3</sup> (Bahreini et al. 2005; Kostenidou et al. 2007).

The first aerosol density measurements were obtained using pycnometers, however the data collection was slow and of low quality (Hanel et al. 1977). Kelly and McMurry (1992) used a combination of a Differential Mobility Analyzer (DMA) and impactor allowing for size segregated densities to be determined with fairly good accuracy (Kelly et al. 1992). More recently, density is reported using particle time of flight (PTOF)–SMPS and APM–SMPS comparisons (Jimenez et al. 2003; Kostenidou et al. 2007; McMurry et al. 2002; Song et al. 2007). Furthermore, recent work by Shilling et



al has shown aerosol vacuum effective densities from  $\alpha$ -pinene ozonolysis are a function of the mass loading (Shilling et al. 2008). The relationship between mass loading and aerosol density is thought to arise from the relative contribution of highly oxygenated species to the total aerosol mass. Shilling et al. reported densities ranging from 1.73 g/cm<sup>3</sup> at a mass loading of 0.46  $\mu\text{g}/\text{m}^3$  to 1.23 g/cm<sup>3</sup> at mass loadings of 15.9  $\mu\text{g}/\text{m}^3$ . This work evaluates high time resolution density evolution for SOA as it evolves for two classic SOA experiments. We also evaluate density estimates using AMS-SMPS to the more direct APM-SMPS measurements.

### **Vacuum Effective Density**

Use of PTOF instruments for measurement of aerosol size has been in existence for some time (Sinha 1984). Aerosol mass spectrometers such as the Aerosol Time of Flight Mass Spectrometer (ATOFMS, TSI) and the AMS (Aerodyne) are two common instruments with PTOF modes that report vacuum aerodynamic diameter. Used in combination with a SMPS, these time of flight sizing instruments allow for determination of the vacuum effective density based upon the electrical mobility diameter (SMPS, operating in the transition regime) and the vacuum aerodynamic diameter (operating in free molecular regime) using the following equation (DeCarlo et al. 2004)

$$\frac{d_m}{C_c(d_m)} = \frac{d_{va} \chi^v \chi^t \rho_0}{\rho_p C_c \left( \frac{d_{va} \chi^v \rho_0}{\rho_p} \right)} \quad \text{Eq 1.}$$

where  $d_m$  is the electrical mobility diameter as measured by the SMPS,  $C_c$  is the Cunningham slip correction factor,  $d_{va}$  is the vacuum aerodynamic diameter,  $\chi^v$  is the

vacuum dynamic shape factor,  $\chi'$  is the transition regime dynamic shape factor,  $\rho_0$  is unit density (1 g/cm<sup>3</sup>), and  $\rho_p$  is the particle density. In the free molecular regime, the Cunningham slip correction factor is approximated as

$$C_c(d) \approx \frac{2\lambda}{d}(\alpha + \beta) \quad \text{Eq 2.}$$

where  $\lambda$ ,  $\alpha$ , and  $\beta$  are empirically determined constants (Allen et al. 1982).

Chamber aerosol is commonly assumed to be spherical, leading equation 1 to simplify to (DeCarlo et al. 2004)

$$\rho_p = \frac{d_{va}}{d_m} \rho_0. \quad \text{Eq 3.}$$

### **DMA-APM Density Calculation Theory**

Ehara and Shin (1996) developed an aerosol particle mass analyzer (APM) which enables selection of aerosol based on mass by balancing the centrifugal and electrostatic forces on a particle passing through a small annular gap between two cylinders (Ehara et al. 1996). A differential voltage applied between the two cylinders with the outer cylinder rotating at a set angular momentum, classifies particles according to mass described by the following equation (Ehara et al. 1996)

$$m_p \omega^2 r = \frac{\pi d_m^3}{6} \rho_p \omega^2 r = neE_{APM} = \frac{neV}{r \ln\left(\frac{r_1}{r_2}\right)} \quad \text{Eq 4.}$$

where  $m_p$  is the mass of the particle,  $\omega$  is the angular rotational speed,  $r$  is the radial distance from the axis of rotation to the annular gap,  $d_m$  is the mobility diameter,  $\rho_p$  is the particle density,  $n$  is number of elementary charges per particle,  $e$  is the unit electrical charge,  $E_{APM}$  is the magnitude of the electric field applied between the two

cylinders,  $V$  is the voltage applied to the APM,  $r_1$  is the radius of the outer cylinder, and  $r_2$  is the radius of the inner cylinder.

The APM, in series with a DMA, allows for direct determination of mobility effective density.

$$\rho_{eff} = \frac{m_p}{\frac{\pi d_m^3}{6}} \quad \text{Eq 5.}$$

Traditionally, the DMA has been placed ahead of the APM to first select the aerosol based on electrical mobility followed by the APM mass to charge classification (Figure C.1).

The DMA-APM configuration was successfully utilized by McMurry et al. (2002) who sampled ambient particles from Atlanta and laboratory generated particles. However, when diameters are changing rapidly, as in aerosol chamber experiments, the DMA-APM setup suffers from the slow APM response due to long settling times when  $\omega$  or applied voltage is changed. For example, an  $\alpha$ -pinene/ozone (100 ppb  $\alpha$ -pinene/ 350 ppb ozone) experiment will have particle diameter growth rate of change of approximately 2 nm/min during the first 2-3 hours of an experiment. The traditional DMA-APM transmission curve incorporates discrete data points associated with step changes in the applied voltage within the APM, after which, one must wait for the CPC to produce a reading. Therefore, in order to obtain an APM transmission curve, a time of approximately 35 minutes is required using default parameters. An additional problem commonly encountered in environmental chamber experiments using the traditional

DMA-APM is the low signal to noise ratio due to the narrow transfer function of the DMA.

### **Modified APM-SMPS System**

We have reversed the order of the traditional DMA-APM system to reduce sampling time, reduce the need to vary  $\omega$  or  $V$ , and to take advantage of the rapid classifying properties of the SMPS (Figure C.2).

An additional advantage of this setup is that it makes use of the broader transfer function of the APM to increase the system signal to noise ratio. The SMPS used is built in house (scan time = 60 sec, voltage range negative 40 to negative 7000, TSI 3081L DMA, TSI 3077 Kr<sup>85</sup> neutralizer, and TSI 3771 particle counter), allowing for sizing of particles from 28-730 nm. The APM (Kanomax model 3600) is capable of angular rotation speeds up to 10000 rpm and electrical potential up to 5000 V, enabling selection of particles as light as 0.01 fg (particles of ~ 26 nm assuming unit density and perfect spheres). In addition to reversing the SMPS and APM order, custom Labview<sup>®</sup> programming was developed to enable continuous operation of both the APM and SMPS.

Signal to noise is improved by utilizing a independent SMPS, which identifies the mode particle diameter of the aerosol sampled and relays this information to the APM-SMPS. The mass of the particles to be transmitted through the APM is estimated using the information of the mode particle diameter from the independent SMPS and an initial assumed density (typically 1.2 to 1.4 g/cm<sup>3</sup>). This estimated mass is then used to set  $\omega$  and  $V$  of the APM, which are re-evaluated every 4 minutes during the course of an experiment. The mobility aerosol density is then determined from the mass selected by

the APM (Eq 4.) and the peak diameter from a second SMPS located directly downstream of the APM.

### **Data Reduction**

Mobility size distributions are recorded every 78 seconds along with the corresponding mass of particles which the APM transmitted. Custom Matlab<sup>®</sup> programming enables for automated fitting of a lognormal curve to the mobility distribution from the SMPS located downstream of the APM and determination of the mode diameter. The mode diameter as determined from the lognormal curve is then combined with the recorded corresponding APM mass to calculate a mobility effective density using equation 5.

### **Evaluation**

The APM-SMPS system performance was first evaluated with 100 nm (as selected by a DMA) dry ammonium sulfate particles (Sigma-Aldrich, purity > 99%,  $\rho=1.77 \text{ g/cm}^3$ ), which were transmitted to the APM-SMPS system in order to ensure the method of estimating initial densities does not bias the final density calculations. Initial densities were varied from 1.4-2.2  $\text{g/cm}^3$  in 0.2  $\text{g/cm}^3$  increments. Figure C.3 (frame A) shows a sample of the raw output from this testing with an assumed density of 1.80  $\text{g/cm}^3$ , results from this testing revealed no inherent bias in the APM-SMPS, with measured densities (1.78 to 1.81  $\text{g/cm}^3$ , Figure C.3 frame B).

Reasons for the slight over estimation of ammonium sulfate is unknown, however it should be noted that the APM does not have a shape effect. Never the less, the results from the ammonium sulfate are in reasonable agreement with the published density.

Accurate APM-SMPS performance was also confirmed with polystyrene latex spheres (Duke Scientific,  $\rho=1.05 \text{ g/cm}^3$ ) and aerosolized dioctyl phthalate (Sigma-Aldrich, purity > 99%,  $\rho=0.985 \text{ g/cm}^3$ ) in order to evaluate its performance with solid and liquid aerosol (Table C.1).

## **Experimental**

### **Chamber Experiments**

The APM-SMPS system sampled SOA generated from a series of environmental chamber experiments conducted at the UCR/CE-CERT environmental chamber facility. The UC-Riverside/CE-CERT Environmental Chamber has been described in detail elsewhere (Carter et al. 2005). Briefly the facility consists of two  $90 \text{ m}^3$  Teflon reactors located in a temperature controlled room, which is continuously flushed with purified air. The reactors are attached to a rigid collapsible frame to minimize diffusion of contaminants into the reactors by maintaining a positive differential pressure with respect to the chambers surroundings. The chamber has two banks of black lights (80 lights in total). Each light source emits a sufficiently high 360 nm wavelength photon flux to drive  $\text{NO}_2$  photolysis. Connected to the chamber are two in house built SMPS's identical to the one detailed above, along with an AMS and APM-SMPS. Compounds of interest are introduced to the chamber by passing a stream of pure  $\text{N}_2$  over a known volume liquid contained in a glass injection manifold or by flushing pure  $\text{N}_2$  through a calibrated glass bulb filled with the gaseous compound to the desired partial pressure. In cases where a ozonolysis experiment was performed, ozone was introduced into the dark chamber by passing 20 psig of pure air through two UV ozone generators,  $\text{CO}$  was added in

sufficient quantities to consume >99 % of the hydroxyl radicals produced. All experiments were conducted in the absence of seed. In all experiments, the relative humidity (RH) was below 0.1%.

## Results

### **$\alpha$ -Pinene-Ozone SOA Density**

An  $\alpha$ -pinene ozonolysis experiment was conducted at 27 °C (400 ppb  $\alpha$ -pinene/ 800 ppb O<sub>3</sub>/ excess CO as the hydroxyl scavenger). Mass loadings from this experiment were in excess of 2000  $\mu\text{g}/\text{m}^3$  as measured by an SMPS. This mass loading is especially high; however during this experiment, the SMPS was programmed to remain at a single voltage (essentially a DMA) so as to transmit only a single diameter particle to the AMS located downstream. Due to the narrow transmission curve of the DMA, large mass loadings were needed to obtain a substantial signal from the AMS. The mobility aerosol density remained a nearly constant  $1.24 \pm 0.03 \text{ g}/\text{cm}^3$  throughout the course of the experiment (~ 7 hrs) (Figure C.4).

During the course of the same experiment, the vacuum effective density was also determined from a DMA-AMS setup as described above and found to be  $1.26 \pm 0.03 \text{ g}/\text{cm}^3$ . This effective density value closely matches that determined previously from Bahreini et al. (2005), Zelenyuk et al. (2008), and Shilling et al (2008) at mass loadings > 15  $\mu\text{g}/\text{m}^3$ . It is worth noting that in the experiments of Bahreini et al., initial hydrocarbon concentrations were approximately an order or magnitude lower than that reported here and used seed particles, while the experiments of Shilling et al had initial hydrocarbon concentrations even lower. In addition to these differences, the experiments of Shilling et

al. contained dry ammonium sulfate seed particles and a relative humidity of 40%. The work of Zelenyuk contained no seed and was conducted at an RH below 1%. Despite these dramatic differences in experimental conditions, the aerosol density reported here matches extremely well with that of Shilling et al. (1.23 g/cm<sup>3</sup>), Zelenyuk et al (1.198 g/cm<sup>3</sup>), and Bahreini et al. (1.19 g/cm<sup>3</sup>). As mentioned previously, Shilling et al. has shown aerosol density to be a function of the mass loadings, while work of Zelenyuk and Bahreini do not indicate final mass loadings, it is assumed that they are much lower than those reported here. Therefore, this may explain the small differences between our results and those of Zelenyuk and Bahreini.

#### ***m*-Xylene NO<sub>x</sub> SOA Density**

Additional chamber experiments were carried out to examine the aerosol density of SOA formed from the irradiation of *m*-xylene and NO<sub>x</sub> (70 ppb *m*-xylene, and 11 ppb NO), resulting in a final mass loading of 25 µg/m<sup>3</sup>. The experiment was conducted in the same manner to that of the α-pinene/O<sub>3</sub> however, the irradiation necessary for the reaction was provided by the 80 black lights. Additionally, the vacuum effective density during this experiment was determined using an SMPS in parallel with the AMS. This setup enabled collection of data from the AMS under the low mass loadings encountered in this experiment, which would not have been possible with the SMPS upstream of the AMS. The aerosol density measured by both the APM-SMPS and SMPS-AMS follows the α-pinene/O<sub>3</sub> trend with little change in the density throughout the experiment except for a slight decrease during the first 4 hours. Similar to the α-pinene/O<sub>3</sub> experiments, the APM-SMPS recorded density matched that of the SMPS-AMS, reaching a plateau at a



value of  $1.35 \pm 0.03 \text{ g/cm}^3$  compared to a value of  $1.36 \pm 0.03 \text{ g/cm}^3$  as measured by the SMPS-AMS.

For similar aromatic systems, Alfarra et al. (2006) have reported aerosol density values of  $1.35\text{-}1.40 \text{ g/cm}^3$  from 1,3,5-trimethylbenzene photo-oxidation with  $\text{NO}_x$ , while Martin-Reviejo et al. (2005) reported the density of aerosol generated from benzene at  $1.35 \text{ g/cm}^3$  (Alfarra et al. 2006; Martin-Reviejo et al. 2005). The only work in which density was reported from *m*-xylene was performed by Song et al. (2007) who found the density of the aerosol as  $1.41 \text{ g/cm}^3$  (Song et al. 2007). It should be noted that the work of Song et al. also employed an APM for density measurements. However, differences in the experimental conditions under which the experiments of Song et al. were performed, namely the absence of  $\text{NO}_x$  in the reaction system, make drawing conclusions based on differences in these two experiments difficult.

## **Summary and Discussion**

We have demonstrated the applicability of a modified APM-SMPS system for the real-time density analysis of chamber generated SOA. This new system obtains data 30 times faster than a traditional DMA-APM setup. Very little change in aerosol density was observed for  $\alpha$ -pinene ozonolysis experiments with densities measured by our APM-SMPS and SMPS-AMS agreeing well over the course of the entire experiment ( $1.24$  and  $1.26 \text{ g/cm}^3$  respectively), while in *m*-xylene experiments a slight decrease in aerosol density was observed during the initial course of the experiment with both an SMPS-APM and SMPS-AMS ( $1.35$  and  $1.36 \text{ g/cm}^3$ , respectively) determined densities agreeing throughout the experiment. Furthermore, in environmental chamber applications, use of

the SMPS-AMS is found to be more than adequate for aerosol density determination, with vacuum effective densities agreeing extremely well with those determined from an APM-SMPS setup. Deployment of the APM-SMPS for ambient measurements would present difficulties not encountered here due the externally mixed nature of ambient aerosol. In particular, the broad transfer function of the APM would lead to transmission of multiple masses to the SMPS, additionally the SMPS would observe aerosol with a varied distribution of mobility diameters. However, the results reported here are consistent with previously reported ambient particle densities of 1.0-1.5 g/cm<sup>3</sup> (Pitz et al. 2003; Spencer et al. 2007). Furthermore, this method utilizing both AMS and APM data can be extended to examine particle shape factors as described by Schmid et al., in which a DMA+APM+AMS are setup in series (Schmid et al. 2007). This method would allow for determination of the mobility and vacuum effective density simultaneously from direct measurements of  $d_m$ ,  $m_p$ , and  $d_{va}$ .

## References

- Alfarra, M. R., Paulsen, D., Gysel, M., Garforth, A. A., Dommen, J., Prevot, A. S. H., Worsnop, D. R., Baltensperger, U. and Coe, H. (2006). A mass spectrometric study of secondary organic aerosols formed from the photooxidation of anthropogenic and biogenic precursors in a reaction chamber. *Atmos. Chem. Phys.* 6:5279-5293.
- Allen, M. D. and Raabe, O. G. (1982). Re-Evaluation of Millikan Oil Drop Data for the Motion of Small Particles in Air. *J. Aerosol Sci.* 13(6):537-547.
- Bahreini, R., Keywood, M. D., Ng, N. L., Varutbangkul, V., Gao, S., Flagan, R. C., Seinfeld, J. H., Worsnop, D. R. and Jimenez, J. L. (2005). Measurements of secondary organic aerosol from oxidation of cycloalkenes, terpenes, and m-xylene using an Aerodyne aerosol mass spectrometer. *Environ. Sci. Technol.* 39(15):5674-5688.
- Carter, W. P. L., Cocker, D. R., Fitz, D. R., Malkina, I. L., Bumiller, K., Sauer, C. G., Pisano, J. T., Bufalino, C. and Song, C. (2005). A new environmental chamber for evaluation of gas-phase chemical mechanisms and secondary aerosol formation. *Atmos. Environ.* 39(40):7768-7788.
- DeCarlo, P. F., Slowik, J. G., Worsnop, D. R., Davidovits, P. and Jimenez, J. L. (2004). Particle morphology and density characterization by combined mobility and aerodynamic diameter measurements. Part 1: Theory. *Aerosol Sci. Tech.* 38(12):1185-1205.
- Ehara, K., Hagwood, C. and Coakley, K. J. (1996). Novel method to classify aerosol particles according to their mass-to-charge ratio - Aerosol particle mass analyser. *J. Aerosol Sci.* 27(2):217-234.
- Hanel, G. and Thudium, J. (1977). Mean Bulk Densities of Samples of Dry Atmospheric Aerosol-Particles - Summary of Measured Data. *Pure Appl. Geophys.* 115(4):799-803.
- Jaoui, M., Kleindienst, T. E., Lewandowski, M. and Edney, E. O. (2004). Identification and quantification of aerosol polar oxygenated compounds bearing carboxylic or hydroxyl groups. 1. Method development. *Anal. Chem.* 76(16):4765-4778.
- Jimenez, J. L., Bahreini, R., Cocker, D. R., Zhuang, H., Varutbangkul, V., Flagan, R. C., Seinfeld, J. H., O'Dowd, C. D. and Hoffmann, T. (2003). New particle formation from photooxidation of diiodomethane (CH<sub>2</sub>I<sub>2</sub>). *J. Geophys. Res. [Atms.]* 108(D10)

- Kalberer, M., Yu, J., Cocker, D. R., Flagan, R. C. and Seinfeld, J. H. (2000). Aerosol formation in the cyclohexene-ozone system. *Environ. Sci. Technol.* 34(23):4894-4901.
- Kelly, W. P. and McMurry, P. H. (1992). Measurement of Particle Density by Inertial Classification of Differential Mobility Analyzer Generated Monodisperse Aerosols. *Aerosol Sci. Tech.* 17(3):199-212.
- Kostenidou, E., Pathak, R. K. and Pandis, S. N. (2007). An algorithm for the calculation of secondary organic aerosol density combining AMS and SMPS data. *Aerosol Sci. Tech.* 41(11):1002-1010.
- Martin-Reviejo, M. and Wirtz, K. (2005). Is benzene a precursor for secondary organic aerosol? *Environ. Sci. Technol.* 39(4):1045-1054.
- McMurry, P. H., Wang, X., Park, K. and Ehara, K. (2002). The relationship between mass and mobility for atmospheric particles: A new technique for measuring particle density. *Aerosol Sci. Tech.* 36(2):227-238.
- Pitz, M., Cyrys, J., Karg, E., Wiedensohler, A., Wichmann, H. E. and Heinrich, J. (2003). Variability of apparent particle density of an urban aerosol. *Environ. Sci. Technol.* 37(19):4336-4342.
- Schmid, O., Karg, E., Hagen, D. E., Whitefield, P. D. and Ferron, G. A. (2007). On the effective density of non-spherical particles as derived from combined measurements of aerodynamic and mobility equivalent size. *J. Aerosol Sci.* 38(4):431-443.
- Shilling, J. E., Chen, Q., King, S. M., Rosenoern, T., Kroll, J. H., Worsnop, D. R., DeCarlo, P. F., Aiken, A. C., Sueper, D., Jimenez, J. L. and Martin, S. T. (2008). Loading-dependent elemental composition of  $\alpha$ -pinene SOA particles. *Atmospheric Chemistry and Physics Discussions* 8:15343-15373.
- Sinha, M. P. (1984). Laser-Induced Volatilization and Ionization of Microparticles. *Rev. Sci. Instrum.* 55(6):886-891.
- Song, C., Na, K., Warren, B., Malloy, Q. and Cocker, D. R. (2007). Secondary organic aerosol formation from m-xylene in the absence of NO<sub>x</sub>. *Environ. Sci. Technol.* 41(21):7409-7416.
- Spencer, M. T., Shields, L. G. and Prather, K. A. (2007). Simultaneous measurement of the effective density and chemical composition of ambient aerosol particles. *Environ. Sci. Technol.* 41(4):1303-1309.

- Surratt, J. D., Murphy, S. M., Kroll, J. H., Ng, N. L., Hildebrandt, L., Sorooshian, A., Szmigielski, R., Vermeylen, R., Maenhaut, W., Claeys, M., Flagan, R. C. and Seinfeld, J. H. (2006). Chemical composition of secondary organic aerosol formed from the photooxidation of isoprene. *J. Phys. Chem. A* 110(31):9665-9690.
- Yu, J. Z., Cocker, D. R., Griffin, R. J., Flagan, R. C. and Seinfeld, J. H. (1999). Gas-phase ozone oxidation of monoterpenes: Gaseous and particulate products. *J. Atmos. Chem.* 34(2):207-258.
- Zelenyuk, A., Yang, J., Song, C., Zaveri, R. A. and Imre, D. (2008). A New Real-Time Method for Determining Particles' Sphericity and Density: Application to Secondary Organic Aerosol Formed by Ozonolysis of alpha-Pinene. *Environ. Sci. Technol.* 42(21):8033-8038.

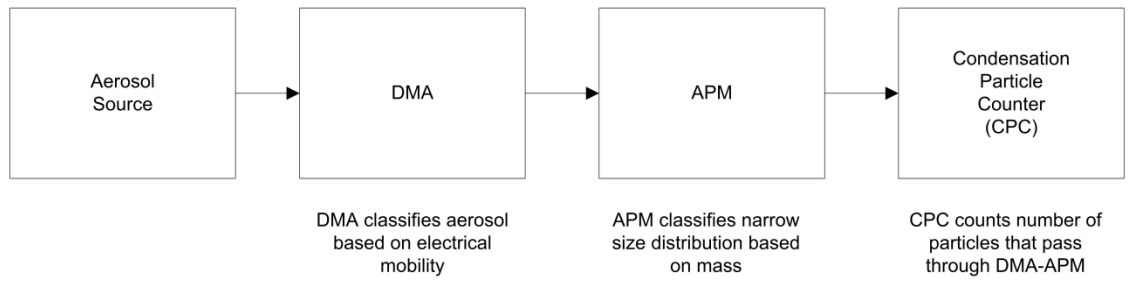


**Figure C.1** Typical DMA-APM setup indicating units and functions of each unit

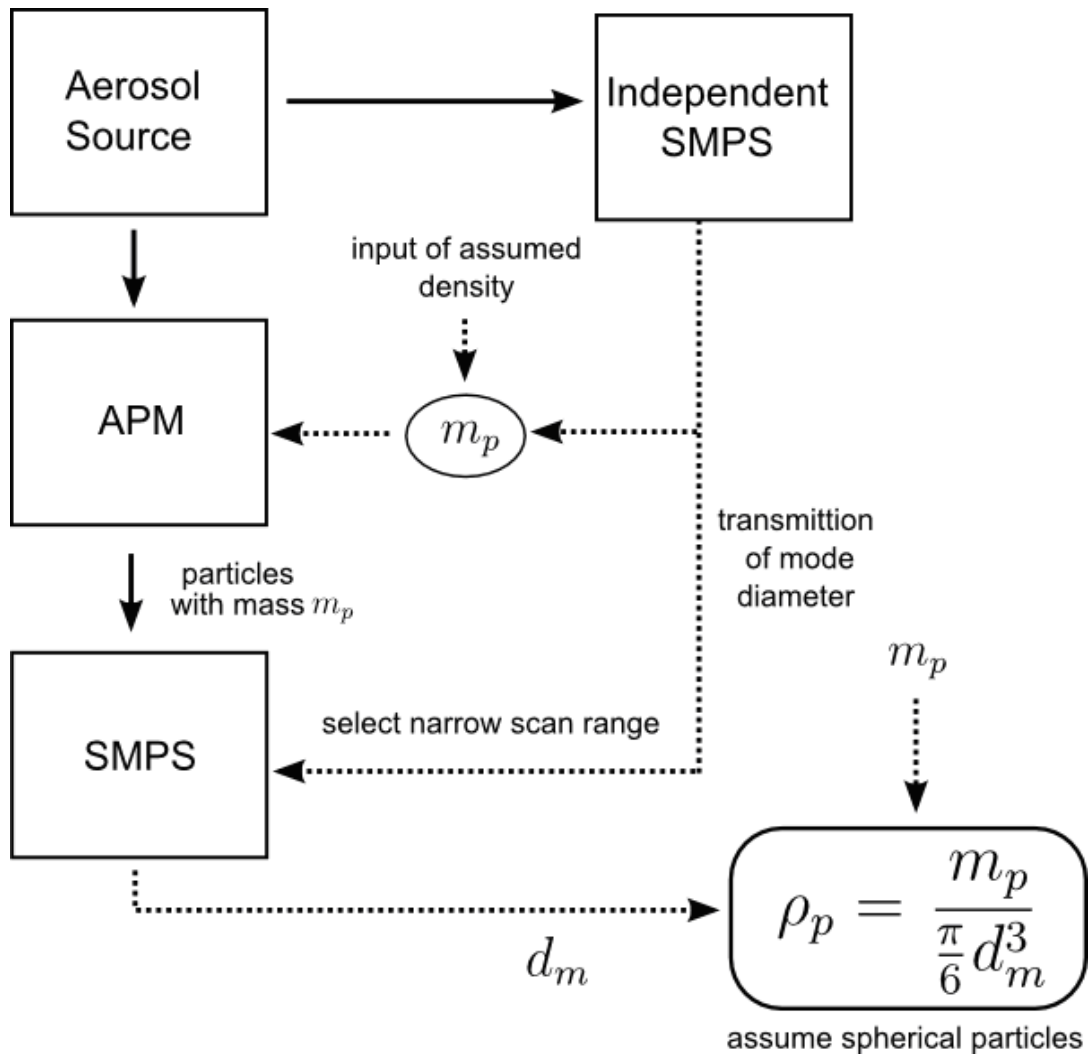


**Figure C.2** Modified APM-SMPS setup indicating placement of units and functions of each unit along with inputs needed. Solid lines indicate flow of aerosol, dotted lines represent flow of data. Note  $\rho_p$  is only equal to the true particle density if the aerosol is spherical, otherwise it is the mobility effective density

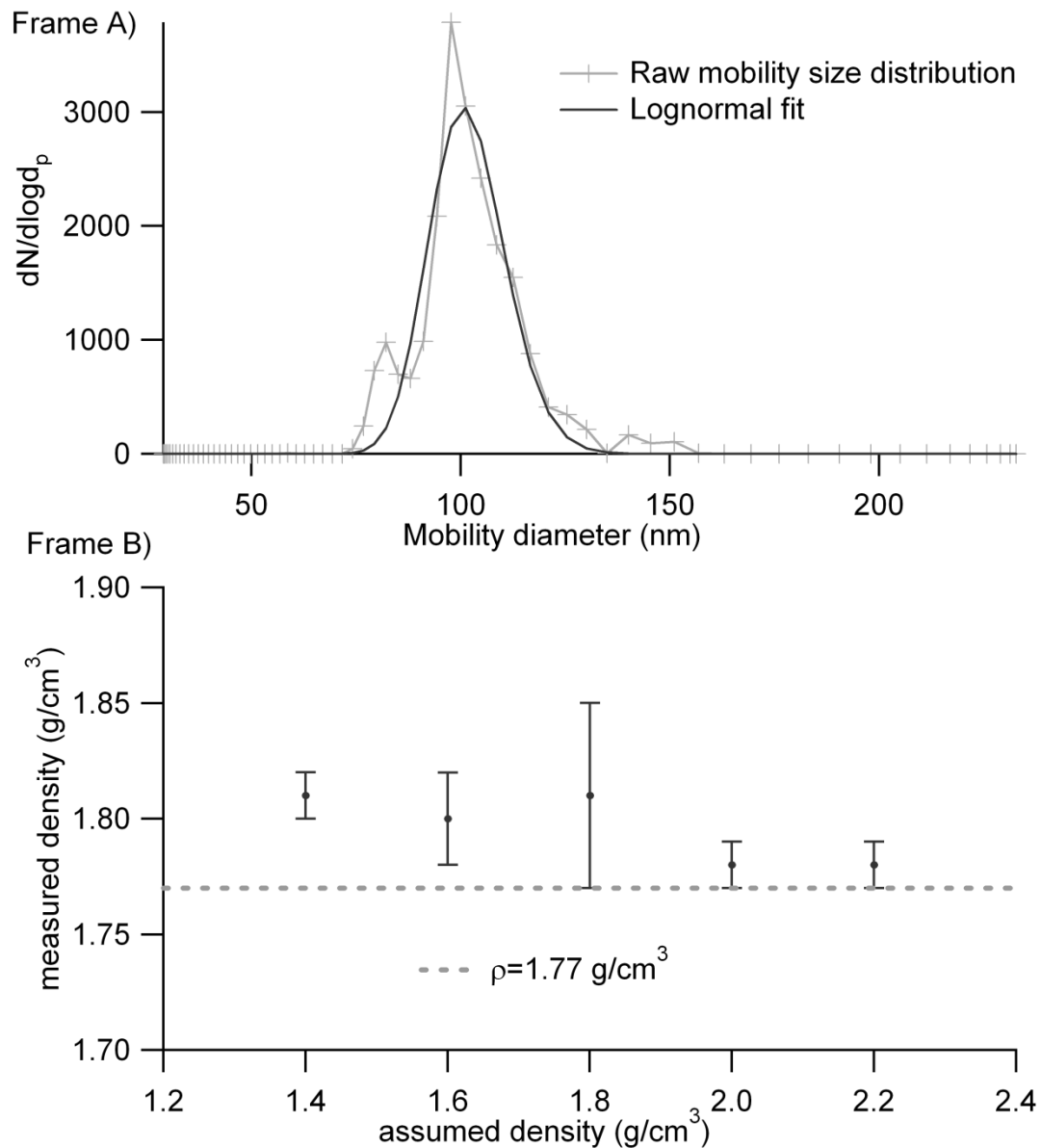


**Figure C.3** Frame A) Mobility size distribution of 100 nm ammonium sulfate particles (assumed density  $1.80 \text{ g}/\text{cm}^3$ ) after passing through an APM set to transmit particles of 0.942 fg. Frame B) APM-SMPS validation results indicating good agreement between measured density and true density of dry ammonium sulfate and insensitivity of system to initial assumed density.



**Table C.1** Comparison of densities of various laboratory generated particles as measured by the modified APM-SMPS and the SMPS-AMS.

<i>APM-SMPS</i>	Ave. (g/cm <sup>3</sup> )	S.D. (g/cm <sup>3</sup> )	n	RSD (%)	reported density (g/cm <sup>3</sup> )	error (%)
(NH <sub>4</sub> )SO <sub>4</sub>	1.81	0.04	15	2.0	1.77	2.4
PSL	1.04	0.02	18	2.0	1.05	-0.8
DOP	0.97	0.01	7	1.3	0.99	-2
<i>SMPS-AMS</i>						
PSL	1.07		9		1.05	1.9
DOP	0.98	0.03	4	3.3	0.99	-0.8

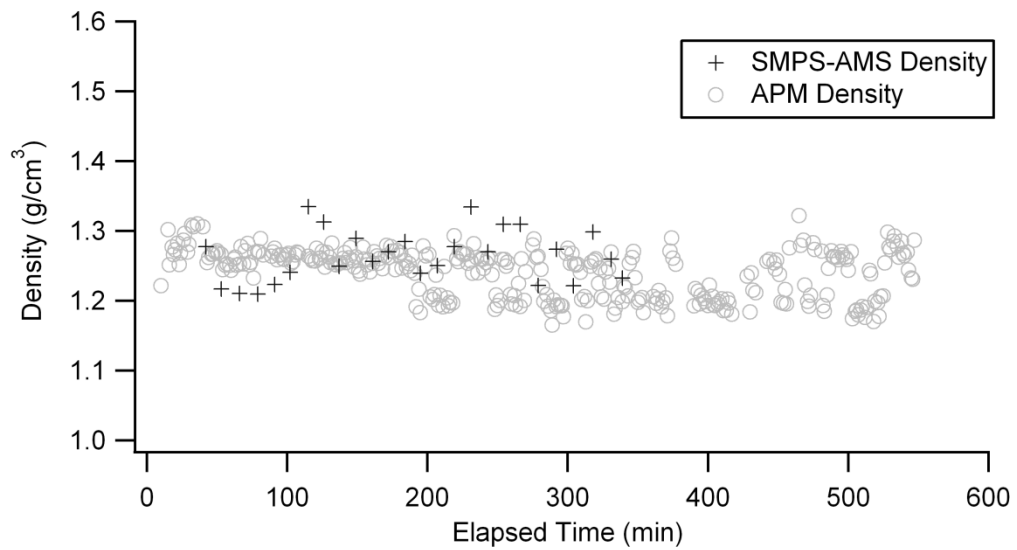


**Figure C.4** Aerosol density for a  $\alpha$ -pinene/ $O_3$  experiment as measured by the APM-SMPS and an SMPS-AMS setup.

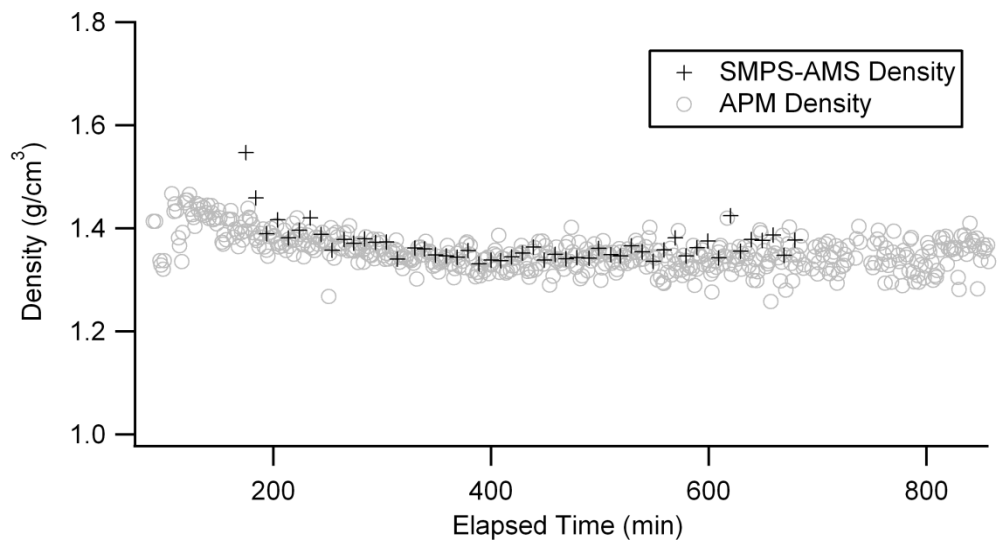


**Figure C.5** Aerosol density for an *m*-xylene/NO<sub>x</sub> experiment as measured by the APM-SMPS and an SMPS-AMS setup.